

# The Two-body Photodisintegration of Deuterium from 200 MeV to 600 MeV

Rebecca Crawford

Presented as a Thesis for the Degree of Doctor of Philosophy

Department of Physics and Astronomy,  
University of Glasgow,  
August 1994.

©Rebecca Crawford, 1994.

ProQuest Number: 11007898

All rights reserved

INFORMATION TO ALL USERS

The quality of this reproduction is dependent upon the quality of the copy submitted.

In the unlikely event that the author did not send a complete manuscript and there are missing pages, these will be noted. Also, if material had to be removed, a note will indicate the deletion.



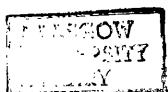
ProQuest 11007898

Published by ProQuest LLC (2018). Copyright of the Dissertation is held by the Author.

All rights reserved.

This work is protected against unauthorized copying under Title 17, United States Code  
Microform Edition © ProQuest LLC.

ProQuest LLC.  
789 East Eisenhower Parkway  
P.O. Box 1346  
Ann Arbor, MI 48106 – 1346



thesis  
9997  
C071

## Abstract

This thesis presents an experimental study of the  $D(\gamma,p)n$  breakup channel of the photodisintegration of deuterium in which both the total cross section  $\sigma_{tot}$ , and the differential cross section,  $d\sigma/d\Omega$ , have been measured over the photon energy range 200–600 MeV. The experiment was performed at the recently completed tagged photon facility of the 855 MeV Microtron MAMI-B, at the Mainz Institut für Kernphysik, Germany. The experiment used the GLASGOW tagging spectrometer in conjunction with the large acceptance detector DAPHNE achieving systematic and statistical errors of a few percent and extending the range of photon energies previously studied. Data taking started in May 1992, as part of the first round of approved experiments at MAMI-B.

The GLASGOW tagging spectrometer was used to determine the photon energy with a resolution of about 2 MeV at intensities up to  $5 \cdot 10^5$  photons per channel. Photon flux normalisation was determined to  $\pm 2\%$ . A 270 mm long cryogenic target filled with liquid deuterium was placed coaxially with the beam. Protons were detected in the large acceptance tracking detector DAPHNE ( $3.7\pi$  steradians) whose coverage of the azimuthal angle was complete and whose polar angular range was  $21^\circ$ – $159^\circ$ . The central vertex detector of DAPHNE provided good definition of charged particle angles; the polar angular resolution was  $< 1^\circ$  and the azimuthal resolution  $< 2^\circ$ . The precise angular information together with the good definition of photon energy defines the reaction kinematics without the need to rely on experimentally determined proton energies. This redundancy of information allows a good rejection of background events.

The Monte Carlo code GEANT was used to simulate the experiment in order to evaluate systematic corrections to be applied to the data. Included in the GEANT simulation are the effects of detector geometry and thresholds. In addition the physical processes resulting from the interaction of protons with the detector materials are considered, including energy deposition in the target and detecting layers, non-linear light response of the scintillators, multiple scattering and nuclear interactions of the protons.

The extensive data are presented in the form of twenty-one angular distribu-

tions and their corresponding integrated total cross sections at photon energies in the range 200 to 600 MeV, in steps of 20 MeV. The total systematic error is estimated to be less than 4%. Previous experimental work is reassessed in the light of the present results and the results compared with two very recent theoretical calculations by the Mainz group.

## **Declaration**

The data presented in this thesis were obtained in collaboration with colleagues from the INFN - sezione di Pavia, the CEA-SPhN of Saclay and the Mainz Institut für Kernphysik. I participated fully in the execution of the experiment and the analysis of these data is entirely my own work. This thesis was composed by myself.

**Rebecca Crawford**

## Acknowledgements

Firstly, I wish very much to thank my supervisor, Dr Jim Kellie for all his patient help over the past three or so years. Many thanks are equally due to Dr Paolo Pedroni who has been of invaluable assistance during the time I have spent working at the INFN in Pavia, Italy.

I owe my gratitude to the Insitut für Kernphysik at Mainz, Germany, for allowing the use of the accelerator and maintaining an excellent beam. I am indebted to all the members of the DAPHNE group for allowing me to take part in their experimental programme. Also for all their hard work in setting up and running the experiments, and their advice and guidance during the analysis.

I am beholden to give a benediction of reverence, esteem, veneration and great genuflexion, paying obeisance to each gracious member of the Kelvin Laboratory for their unique role in a genial and interesting environment. I have always enjoyed the company and conversation both at the lab and on our various extracurricular excursions. Dr Ian Anthony and Mr Andy Sibbald deserve many thanks for their constant help with things computing. I extend my sincerest thanks to Professor R.O.Owens for all his advice and encouragement. Dr Gillian Cross has done well to survive these years of office sharing. I am grateful for her friendship, tolerance and leveling influence. I am also grateful for being let in on the essential supplies of pancakes and clouty dumpling from her mother.

I wish to thank the Science and Engineering Research Council for providing me with a grant and with travelling expenses.

Finally, I dedicate this thesis to my Mother, Father, Melvyn, Gary, Jane and James.

# Contents

<b>1</b>	<b>The Two-body Photodisintegration of Deuterium from 200 to 600 MeV</b>	<b>2</b>
1.1	General Introduction . . . . .	3
1.2	Theoretical Background . . . . .	7
1.2.1	Overview . . . . .	7
1.2.2	Elementary Calculations . . . . .	10
1.2.3	Meson Exchange Currents and Isobar Configurations . .	16
1.2.4	Relativistic Effects and the $0^\circ$ Cross Section . . . . .	19
1.2.5	Other Recent Calculations . . . . .	19
1.3	Review of Existing Measurements . . . . .	21
1.3.1	Measurements with Bremsstrahlung Beams . . . . .	23
1.3.2	Neutron Capture Experiments . . . . .	25
1.3.3	Recent Measurements . . . . .	27
1.4	Review of Photon Tagging Techniques . . . . .	31
1.5	The Present Measurement – Theoretical and Experimental Justification . . . . .	33
<b>2</b>	<b>The Experimental System</b>	<b>34</b>
2.1	Introduction . . . . .	35

2.2	The Accelerator and Beamline . . . . .	35
2.2.1	Accelerator Characteristics . . . . .	35
2.2.2	Accelerator Monitoring and Control . . . . .	40
2.2.3	Beamline Transport Design . . . . .	40
2.3	The Tagging Spectrometer and the Photon Beamline . . . . .	41
2.3.1	The Bremsstrahlung Radiator . . . . .	41
2.3.2	The Magnet System of the Tagging Spectrometer . . . . .	43
2.3.3	The Focal Plane Array . . . . .	46
2.3.4	The Tagger Electronics . . . . .	48
2.3.5	Photon Beam Collimator . . . . .	49
2.3.6	Photon Beam and Electron Beam Monitoring . . . . .	50
2.3.7	Photon Flux Normalisation / Tagging Efficiency . . . . .	51
2.4	The DAPHNE Detector . . . . .	55
2.4.1	General Layout . . . . .	55
2.4.2	The Wire Chambers and Track Reconstruction . . . . .	62
2.4.3	The A B C D E F Scintillator Layers . . . . .	69
2.4.4	The Cryogenic Target . . . . .	70
2.4.5	Electronics and Event Triggers . . . . .	71
2.4.6	Data Acquisition . . . . .	72
<b>3</b>	<b>Energy Calibrations and Particle Identifications</b>	<b>74</b>
3.1	Introduction . . . . .	75
3.2	Energy Calibration of the Scintillators . . . . .	75
3.3	Particle Identification . . . . .	77
3.3.1	Particle Discrimination using Plots of $dE/dx$ Loci . . . . .	78

3.3.2	The Range Method . . . . .	81
3.4	The GEANT Simulation . . . . .	85
<b>4</b>	<b>Data Analysis</b>	<b>86</b>
4.1	Introduction . . . . .	87
4.2	General Comments . . . . .	89
4.2.1	Data Reduction . . . . .	89
4.2.2	Data Analysis . . . . .	90
4.2.3	Reconstruction of 2-body Kinematics . . . . .	92
4.2.4	GEANT Simulations . . . . .	94
4.3	Data Analysis $E_\gamma=200, 220$ and $240$ MeV . . . . .	96
4.4	Data Analysis $E_\gamma=240-480$ MeV . . . . .	101
4.4.1	Introduction . . . . .	101
4.4.2	Specific Kinematics and Mechanisms for the $D(\gamma,p)n\pi^0$ Competing Process . . . . .	106
4.5	Data Analysis $E_\gamma=480-600$ MeV . . . . .	112
4.5.1	Analysis of Events which fail the Particle Separation Check in the Range Method Analysis . . . . .	112
4.5.2	Analysis of Events which pass the Particle Separation Check in the Range Method Analysis . . . . .	118
4.6	Corrections to the Data . . . . .	120
4.6.1	Efficiency Correction . . . . .	120
4.6.2	Dead Angle Correction . . . . .	121
4.6.3	Real/Random Correction . . . . .	122
4.6.4	Multiple Tagger Hits . . . . .	123
4.6.5	Correction for the Effective Length of the Target . . . . .	125

<b>5</b>	<b>Experimental Results</b>	<b>127</b>
5.1	Introduction . . . . .	128
5.2	Calculation of Differential Cross Section . . . . .	128
5.3	Experimental Results . . . . .	129
<b>6</b>	<b>Comparison with Other Measurements and Theory</b>	<b>138</b>
6.1	Comparison with Other Measurements . . . . .	139
6.1.1	Introduction . . . . .	139
6.1.2	Phenomenological Fits up to $E_\gamma=440$ MeV . . . . .	140
6.1.3	Comparison with Recent Data to $E_\gamma=440$ MeV . . . . .	144
6.1.4	Comparison with the Existing Data Set above $E_\gamma=440$ MeV	154
6.2	Comparison with Recent Theoretical Calculations . . . . .	157
<b>7</b>	<b>Conclusions</b>	<b>168</b>
7.1	Conclusions . . . . .	169
<b>A</b>	<b>The Range Method</b>	<b>172</b>
<b>B</b>	<b>Cross Section Results</b>	<b>196</b>
<b>C</b>	<b>Coherent Bremsstrahlung Trials</b>	<b>206</b>

# List of Figures

1.1	Existing total cross section data . . . . .	4
1.2	Recent total cross section measurements . . . . .	5
1.3	Relative contributions to $\sigma_{tot}$ . . . . .	7
1.4	Contributions from E1 and M1 transitions to the total cross section	12
1.5	Instantaneous interchange of an n-p pair . . . . .	15
1.6	Pion exchange current diagrams . . . . .	17
1.7	$\Delta$ contribution diagrams . . . . .	17
1.8	Effective operators . . . . .	18
1.9	Examples of existing differential cross section data $E_\gamma = 200$ MeV	24
2.1	The Experimental System . . . . .	36
2.2	The Mainz Microtron MAMI-B . . . . .	38
2.3	The Quadrupole/Dipole Design . . . . .	45
2.4	The Focal Plane Detector . . . . .	47
2.5	A typical TDC spectrum . . . . .	49
2.6	Vertex reconstruction . . . . .	51
2.7	Tagging efficiency measurement . . . . .	53
2.8	The Pair Detector . . . . .	54
2.9	Pair Detector efficiency . . . . .	55

2.10	Planar and transverse views of DAPHNE . . . . .	56
2.11	Overall view of DAPHNE . . . . .	57
2.12	The transverse and longitudinal views of a wire chamber . . . . .	63
2.13	Impact point reconstruction . . . . .	65
2.14	Impact point degeneracy . . . . .	65
2.15	Angular region in which MWPC's are searched . . . . .	66
2.16	Triangle formed by the 3 MWPC points . . . . .	67
2.17	The variation of longitudinal position resolution with $\theta$ . . . . .	68
2.18	Polar angular resolution . . . . .	68
2.19	The Target Cell . . . . .	70
3.1	Calibration of one of the B layer scintillators . . . . .	76
3.2	Particle identification stop B layer events . . . . .	79
3.3	Particle identification D layer . . . . .	80
3.4	Rate of energy loss versus range for protons and pions in plastic scintillator . . . . .	82
3.5	Example of Range Method fit for typical sample of events . . . . .	83
4.1	D( $\gamma, p$ )n event, cross-sectional view of DAPHNE . . . . .	88
4.2	Comparison $E_{theo}$ and $E_{meas}$ at $E_\gamma=320$ MeV . . . . .	92
4.3	$E_{theo}-E_{meas}$ from two-body kinematics for $E_\gamma=260-330$ MeV . . . . .	93
4.4	$E_{theo}-E_{meas}$ from two-body kinematics, Data and GEANT simu- lations of D( $\gamma, p$ )n events . . . . .	95
4.5	$E_{theo}-E_{meas}$ from two-body kinematics , Data and GEANT sim- ulation $E_\gamma=200$ MeV . . . . .	97
4.6	$E_\gamma=200$ MeV, $\theta=62.5^\circ-82.5^\circ$ Data and GEANT simulation . . . . .	98

4.7	$E_\gamma=200$ MeV, $\theta=62.5^\circ-82.5^\circ$ Background evaluation . . . . .	99
4.8	$E_\gamma=200$ MeV, $\theta=62.5^\circ-82.5^\circ$ Data with background subtracted and GEANT simulation . . . . .	99
4.9	$E_{theo}-E_{meas}$ from two-body kinematics for $E_\gamma=190-470$ MeV . .	102
4.10	$E_{theo}-E_{meas}$ from two-body kinematics at $E_\gamma=320$ MeV . . . . .	104
4.11	$E_{theo}-E_{meas}$ from two-body kinematics at $E_\gamma=400$ MeV . . . . .	105
4.12	Maximum proton energy from the $D(\gamma,p)n\pi^\circ$ and proton energy from the $p(\gamma,p)\pi^\circ$ reaction compared with that from the $D(\gamma,p)n$ reaction . . . . .	107
4.13	$E_{theo}-E_{meas}$ spectra from two-body kinematics showing $D(\gamma,p)n\pi^\circ$ threshold at $E_\gamma=320$ MeV . . . . .	109
4.14	Classification $D(\gamma,p)n$ or $D(\gamma,p)n\pi^\circ$ by comparison to $D(\gamma,p)n$ and then $H(\gamma,p)\pi^\circ$ kinematics . . . . .	111
4.15	Analysis of events which fail the particle separation check in the Range Method analysis . . . . .	113
4.16	Kinematic region of events which fail the particle separation check in the Range Method analysis . . . . .	114
4.17	GEANT Simulation of $D(\gamma,p)n$ Events which fail the particle separation check in the Range Method analysis . . . . .	115
4.18	B energy loss against 'crude range' . . . . .	116
4.19	$\chi^2$ proton versus $\chi^2$ pion . . . . .	117
4.20	Remaining $D(\gamma,p)n$ events and GEANT simulation . . . . .	118
4.21	$E_{theo}-E_{meas}$ from two-body kinematics at $E_\gamma=500$ MeV . . . . .	119
4.22	Range Method efficiency correction . . . . .	120
4.23	Dead angle correction . . . . .	121
4.24	A typical TDC spectrum . . . . .	122
4.25	Neighbouring multiple tagger hits correction . . . . .	124

4.26	Effective target length . . . . .	126
5.1	Total Cross Section Results . . . . .	131
5.2	Differential cross sections 200,220,240,260 MeV . . . . .	132
5.3	Differential cross sections 280,300,320,340 MeV . . . . .	133
5.4	Differential cross sections 360,380,400,420 MeV . . . . .	134
5.5	Differential cross sections 440,460,480,500 MeV . . . . .	135
5.6	Differential cross sections 520,540,560,580 MeV . . . . .	136
5.7	Differential cross sections 600 MeV . . . . .	137
6.1	The first four Legendre Polynomials . . . . .	140
6.2	Total cross sections – Present data and parameterisation . . . . .	142
6.3	Legendre Polynomial coefficients of data and of parameterisation . . . . .	143
6.4	Total cross sections – Present and Recent data . . . . .	145
6.5	Differential cross sections 200,220,240,260 MeV . . . . .	147
6.6	Differential cross sections 280,300,320,340 MeV . . . . .	148
6.7	Differential cross sections 360,380,400,420 MeV . . . . .	149
6.8	Legendre coefficients DAPHNE and Bonn data . . . . .	151
6.9	Legendre coefficients DAPHNE, MIT and LEGS data . . . . .	152
6.10	Differential cross sections 440,460,480,500 MeV . . . . .	155
6.11	Differential cross sections 520,540,560,580 MeV . . . . .	156
6.12	Theoretical Calculations of $\sigma_{tot}$ . . . . .	158
6.13	Differential cross sections 200,220,240,260 MeV . . . . .	159
6.14	Differential cross sections 280,300,320,340 MeV . . . . .	160
6.15	Differential cross sections 360,380,400,440 MeV . . . . .	161

6.16	Differential cross sections 480,520,560,600 MeV . . . . .	162
6.17	Comparison of Legendre coefficients from DAPHNE and the Impulse Approximation calculation . . . . .	164
6.18	Comparison of Legendre coefficients from DAPHNE and the Coupled Channel calculation . . . . .	165
C.1	Scan through azimuthal angle . . . . .	209
C.2	Relative intensity of coherent to incoherent contributions . . . . .	210

# List of Tables

1.1	Existing $D(\gamma, p)n$ below 450 MeV . . . . .	22
1.2	Existing $D(\gamma, p)n$ data extending above 450 MeV . . . . .	23
1.3	Existing $p(n, \gamma)D$ data . . . . .	26
2.1	Microtron Characteristics . . . . .	39
2.2	840 MeV Photon Tagging Spectrometer parameters QD design .	44
2.3	Principal characteristics of DAPHNE . . . . .	60
2.4	The characteristics of the 3 MWPC chambers . . . . .	64
4.1	Deuterium break-up channels . . . . .	88
5.1	Additional Systematic Error . . . . .	130
B.1	Differential Cross Sections $E_\gamma = 200, 220, \text{and } 240$ MeV . . . . .	197
B.2	Differential Cross Sections $E_\gamma = 260, 280, \text{and } 300$ MeV . . . . .	198
B.3	Differential Cross Sections $E_\gamma = 320, 340, \text{and } 360$ MeV . . . . .	199
B.4	Differential Cross Sections $E_\gamma = 380, 400, \text{and } 420$ MeV . . . . .	200
B.5	Differential Cross Sections $E_\gamma = 440, 460, \text{and } 480$ MeV . . . . .	201
B.6	Differential Cross Sections $E_\gamma = 500, 520, \text{and } 540$ MeV . . . . .	202
B.7	Differential Cross Sections $E_\gamma = 560, 580, \text{and } 600$ MeV . . . . .	203
B.8	Total Cross Section Results . . . . .	204
B.9	Legendre Polynomial Coefficients . . . . .	205

# Chapter 1

## The Two-body Photodisintegration of Deuterium from 200 to 600 MeV

## 1.1 General Introduction

The latest generation of electron accelerators in Europe and in the United States offer new electron and photon beam facilities for the study of nuclear systems using the electromagnetic probe. For example, they provide the experimentalist with the opportunity to gain information on the different components of the nuclear force and on baryon resonances. Photonuclear reaction cross sections are relatively small so their measurement requires high photon fluxes. These new photon beam facilities offer such intensities with good definition of both flux and photon energy. As a nuclear probe the photon has the advantage that its interaction is described by the theory of QED and so is in principle well understood. In addition the electromagnetic interaction is weak compared with the strong interaction between nucleons, consequently it is only a small perturbation to the system and can thus explore all the nuclear volume.

The deuteron is the most basic nuclear system, and the understanding of it represents a fundamental challenge in nuclear dynamics. The study of its bound state properties and reactions complements the study of  $N - N$  scattering to provide information on the  $N - N$  interaction. One of the simplest reactions involving it is its two-body photodisintegration,  $D(\gamma,p)n$ . In principle this fundamental process is exactly calculable, although the theory involves an understanding of the electromagnetic interactions and a knowledge of the nature of the nuclear forces. The photodisintegration of this simple two-body system therefore offers the possibility of testing the ingredients of theoretical calculations such as  $N - N$  and  $N - \Delta$  potentials, coupling constants and form factors. It also provides insight on how to treat meson exchange currents, delta excitation and final state interactions.

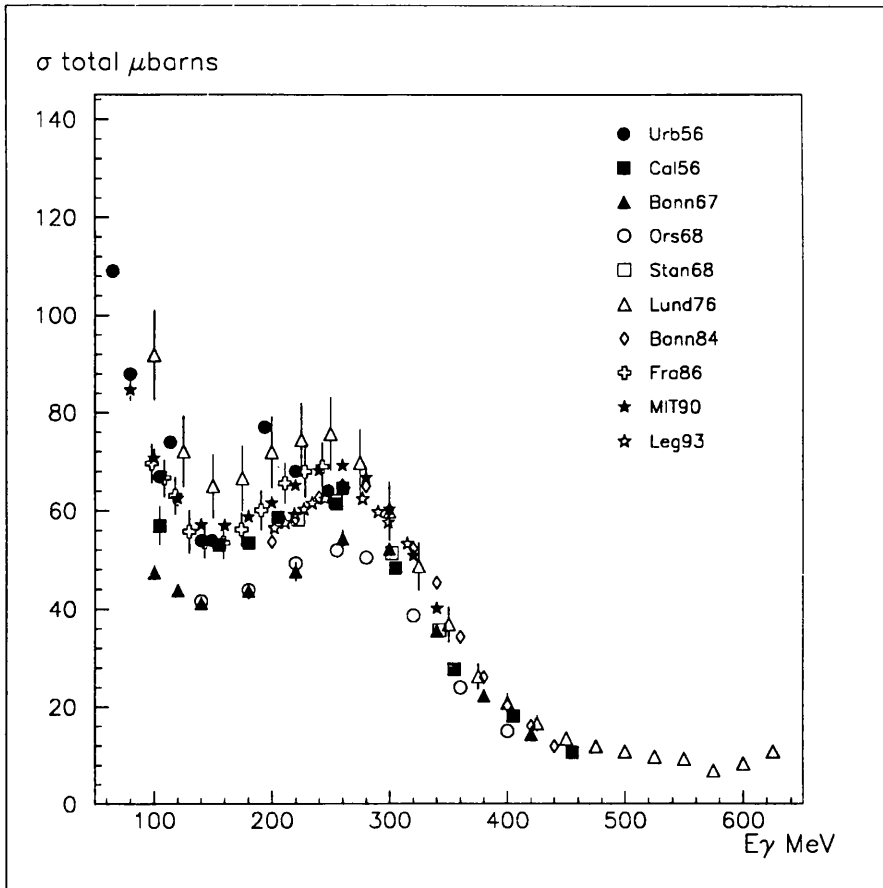


Figure 1.1: *Existing total cross section data*

The importance of deuteron photodisintegration in photonuclear physics has meant that it has been the subject of a great number of experiments since it was first studied by Chadwick and Goldhaber in 1934 [1]. However, the history of these  $D(\gamma, p)n$  measurements has been characterised by large discrepancies among experiments and this has often precluded a reliable comparison between theory and experiment.

The existing total cross section data in the photon energy region above 100 MeV are shown in figure 1.1. It is clear there is a lack of consistency, which is outwith the quoted normalisation uncertainties of 5–10%. For example, in the intermediate energy region at around 100 MeV there exists differences of

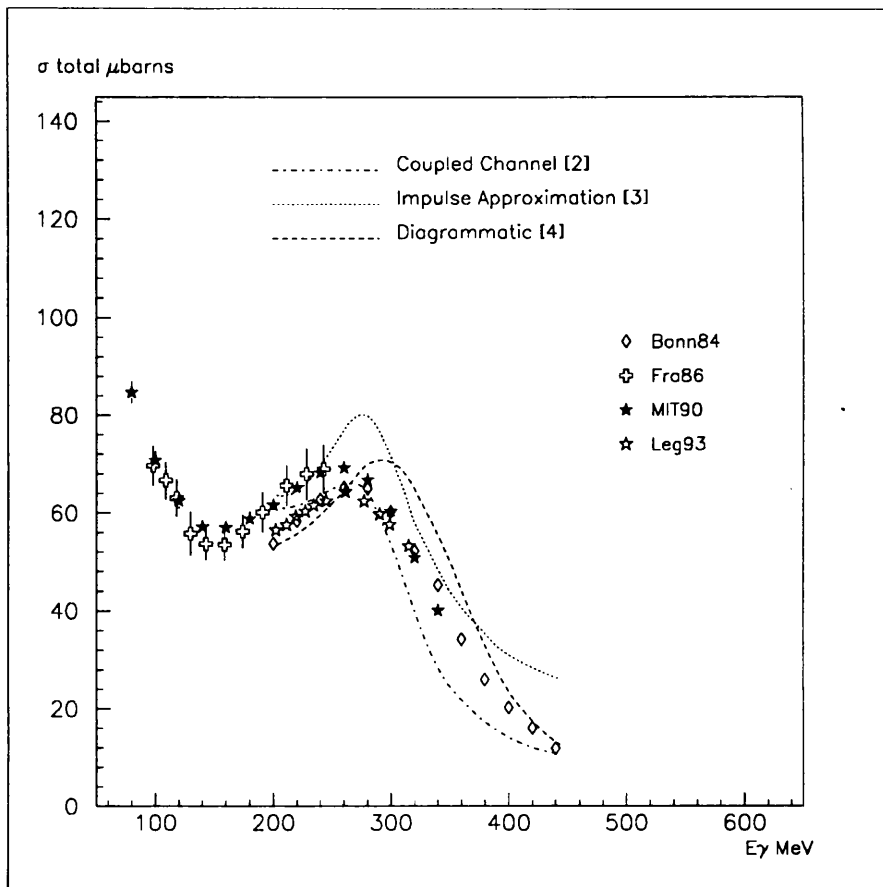


Figure 1.2: *Recent total cross section measurements*

60% and the discrepancy in the region of the  $\Delta$  resonance is as large as 40%.

However, if data from experiments performed at several laboratories in recent years are selected, as is shown in figure 1.2, although discrepancies still exist, the situation is much improved, with excellent agreement being found at low energies. Whilst it can be seen there is reasonable agreement above 300 MeV there is still relatively poor agreement around the 150–300 MeV range. For example, there is a systematic discrepancy of about 15% around 200 MeV between the Frascati and Bonn data. At these energies the theoretical predictions of the cross section contemporary to the data, some of which are also displayed in figure 1.2, give quite different results, varying in magnitude by  $\sim 15\text{--}20\%$ , mainly

due to the different treatments of the  $\Delta$ . Therefore, even with recent advances in experimental techniques, the differences are still too large to allow a discrimination between different calculations. Two of the theoretical calculations shown, the coupled channel approach [2], and the impulse approximation [3], have very recently been updated, and are reported in new references [5], [6] and [7], respectively. This recent data set together with the results from the present experiment are compared to the new theoretical results in Chapter 6.

In order to address the uncertainties in the data and discriminate between the theoretical treatments, a critical review of the problems associated with past measurements is necessary to identify and assess the sources of error. New experiments need high accuracy to achieve any benefit. For example at lower energies, for the data to distinguish between otherwise acceptable  $N - N$  potentials, an accuracy of about 4% is required. Cross sections with low systematic errors over a large energy range are needed, aiming for consistency between experiments within their quoted accuracy and between different techniques.

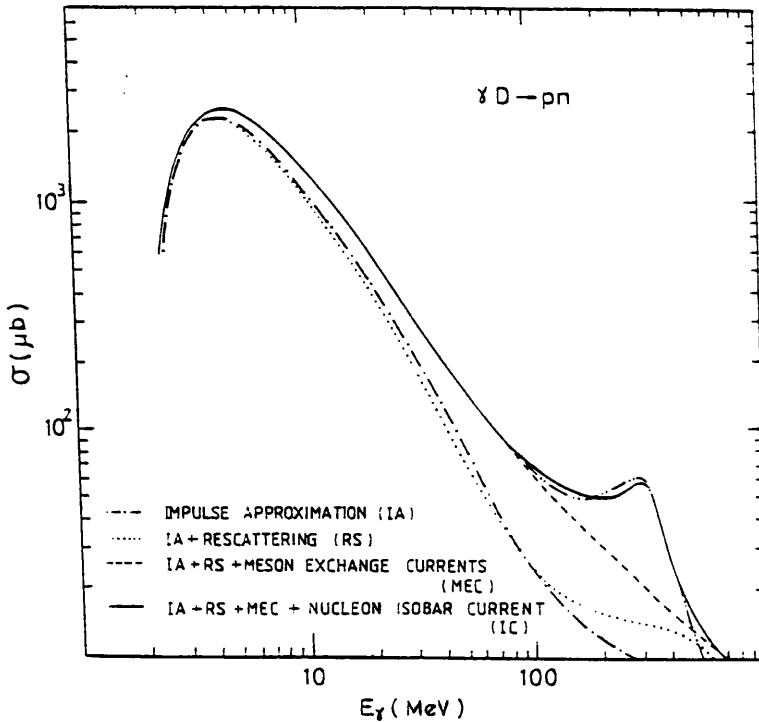


Figure 1.3: *Relative contributions to  $\sigma_{tot}$*

## 1.2 Theoretical Background

### 1.2.1 Overview

The importance of deuteron photodisintegration has meant that alongside the extensive experimental effort there has been much theoretical interest. Indeed, this basic two-body system has served as a testing ground each time new theoretical ideas concerning the nature of the nucleon-nucleon interaction have developed.

Figure 1.3 shows the relative importance of different photon absorption mechanisms thought to contribute to the total cross section [8]. There is a peak around a few MeV, within which absorption is mostly 1-body. Above this the cross section falls off with increasing photon energy and 2-body exchange mechanisms gain in importance. During the early study of the reaction at low energies, where the cross section is dominated by one nucleon absorption, good

agreement amongst data and with theory was found. Surprisingly simple theoretical calculations that successfully predict the experimental data can be made using the concepts of the zero range approximation and effective range theory [9]. The elementary approaches use non-relativistic perturbation theory, and wave functions are obtained by solving the Schrödinger equation for a simple  $N - N$  potential. Simple forces can be assumed, as at these energies the details of the nuclear force are relatively unimportant. The interaction of the photon with the nucleon-nucleon system is described by a multipole expansion considering only lowest multipoles. At higher energies, as the wavelength of the photon approaches the same magnitude as the range of the nuclear force, the details of the forces become important. Calculations progressed by including more realistic forces, more complicated wave functions and higher multipole transitions.

In complex nuclei for photon absorption at low energies ( $E_\gamma=10-30$  MeV) the cross section is dominated by the giant dipole resonance. This is due to one nucleon absorption (1N), but there is coherent addition of 1N amplitudes of all the protons in the nucleus. It can be shown that this dipole absorption obeys a sum rule with a particularly simple form. If the electric dipole cross section is integrated over all photon energies the result, known as the TRK (Thomas-Reich-Kuhn) sum rule is given by:

$$\int_0^\infty \sigma_{E1}(E_\gamma)dE_\gamma = 60 \frac{NZ}{A} \text{ [MeV mb]} \quad (1.1)$$

As photon energy increases one-body and two-body photoabsorption mechanisms are of increasing importance relative to the collective excitation of the giant dipole resonance. The photon interacts with all the charges and currents present in the nuclear system. It is found these can include not only the nu-

cleons but also meson exchange currents (MEC) and the internal degrees of freedom of the nucleons themselves (for example excitation of isobars in the nuclear medium such as the  $\Delta$ ).

Above 50 MeV, from the experiments of the 1950's, came indications that the total integrated cross section was appreciably larger than that predicted from the TRK sum rule. This led to an understanding of the importance of exchange mechanisms. Since the sum rule significantly underestimates the observed total cross section, it was suggested that this excess strength was due to the presence of charged mesons and could be explained in terms of exchange mechanisms. As the photon energy increases, one-body photoabsorption mechanisms become less important than photoabsorption mechanisms involving more than one nucleon. This arises from the inherent mismatch in momentum and energy associated with photon absorption on a single nucleon. Conservation of energy implies the photon energy provides the nucleon kinetic energy. However, a nucleon having this amount of kinetic energy has much more momentum than the original photon. This momentum mismatch is much larger than the Fermi momentum of the initial bound nucleon, which implies the participation of two nucleons in the photon absorption process. In photon absorption associated with both resonant exchange mechanisms, such as  $\Delta$  excitation, and non-resonant exchange mechanisms, such as meson exchange currents, the photon energy is shared between two nucleons which emerge approximately back to back and thereby readily satisfy the requirement for conservation of momentum.

Exchange mechanisms are even more important for the deuteron, since its large radius implies a lack of high momentum components in the Fermi distribution, and thus the importance of two-body photoabsorption mechanisms is

enhanced. In the photon energy range of this experiment, the formation of the  $\Delta$  resonance is important in the  $E_\gamma=200\text{--}400$  MeV region. After its formation, the  $\Delta$  decays to a nucleon by the emission of a pion which is subsequently re-absorbed by the other nucleon. This sequence provides the mechanism for the momentum to be shared between the two nucleons.

Recent experiments examined the  $0^\circ$  cross section and initially the theory was unable to account for its finite magnitude. This inability of the simple pure S-state deuteron calculation to predict the  $D(\gamma, p)n$  cross section at  $0^\circ$ , lead to an understanding of the importance of the D-state component in the deuteron wave function, and of the necessity of a proper treatment of relativistic effects. Modern calculations have shown that there exist several types of relativistic effect which significantly contribute to the cross section.

Different theoretical approaches of increased complexity have developed, successfully describing the data and extending our understanding to higher energies. Until recently, these calculations only implicitly included meson exchange currents. However, modern calculations including the formation of the  $\Delta$  resonance and MEC explicitly have been performed [2],[4].

The development of these different theoretical approaches to the description of the two nucleon system, and its interaction with the electromagnetic force is now outlined.

### 1.2.2 Elementary Calculations

The assumptions and approximations made for a simple one nucleon absorption calculation for low photon energies are now described below [9].

- i) Non-relativistic perturbation theory is used and the Schrödinger equation is solved for a simple N-N potential.
- ii) The assumption of a deuteron system comprising only a neutron and a proton is made.
- iii) The interaction of photons with the deuteron is described by an expansion of the transition operator in electric and magnetic multipoles.
- iv) Only E1 and M1 transitions from a pure S state deuteron in the long wavelength limit are considered.
- v) The N – N interaction used is a zero-range approximation, modified with an effective range treatment to account for finite range effects.

In the long wavelength limit the photon wavelength is much greater than the range of the potential and so the use of a zero range force is sufficient. The resulting angular distribution from this simple model, has the form:

$$\frac{d\sigma}{d\Omega} = \frac{d\sigma^{E1}}{d\Omega} + \frac{d\sigma^{M1}}{d\Omega} \quad (1.2)$$

$$\frac{d\sigma^{E1}}{d\Omega} = \alpha \frac{\sqrt{MB}}{1 - \sqrt{MB}r_t} \frac{\omega - B^{3/2}}{M} \frac{1}{\omega^3} \sin^2\theta_p \quad (1.3)$$

$$\frac{d\sigma^{M1}}{d\Omega} = \frac{\alpha}{6} (\mu_p - \mu_n)^2 \frac{\sqrt{B(\omega - B)}}{\omega M^2} \frac{(\sqrt{MB} - \beta)^2}{M(\omega - B) + \beta^2} \quad (1.4)$$

where:

B = deuteron binding energy

M = mean of neutron and proton masses

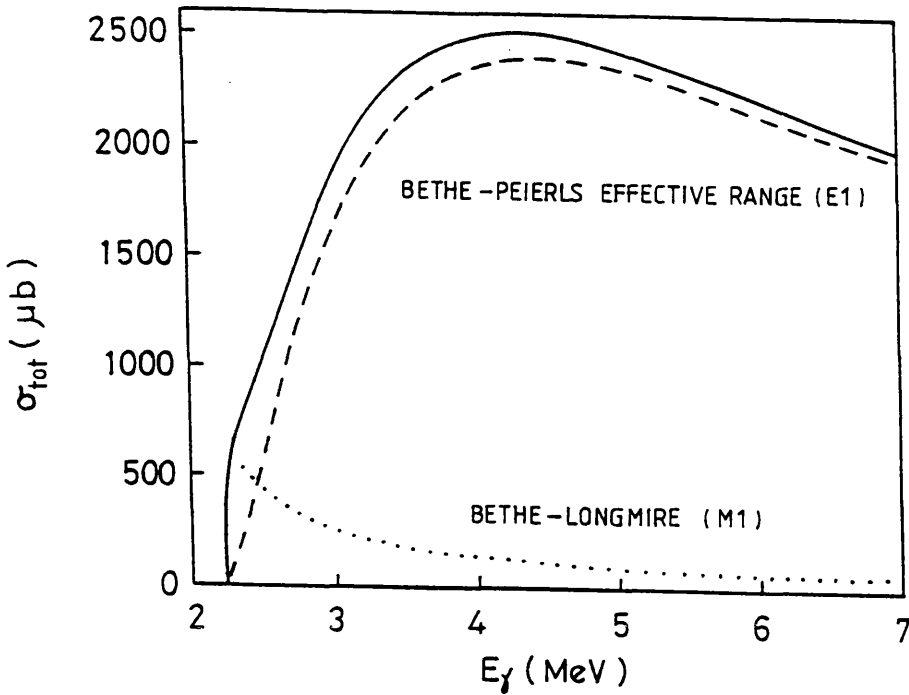


Figure 1.4: Contributions from E1 (dashed line) and M1 (dotted line) transitions to the total cross section (full line)

$\mu_p$  = proton magnetic moment

$\mu_n$  = neutron magnetic moment

$\theta_p$  = proton polar angle

$\omega$  = photon energy

$r_t = 1.76$  fermi = triplet range

$\beta$  = inverse of the singlet n-p scattering length

$\alpha = \frac{e^2}{4\pi} =$  fine structure constant

$\hbar = c = 1$

It features a  $\sin^2\theta$  term produced by E1 transition from  $^3S_1$  to  $^3P_1$ , and an isotropic term produced by M1 spin-flip transition from  $^3S_1$  to  $^1S_0$ . Figure 1.4 indicates the relative contributions from each of these two terms, the E1 term is seen to be dominant and the M1 contribution is only important just above

threshold. A more careful elementary non-relativistic calculation was made by [10] using a mixture of S-state and D-state. This calculation was expanded to include also higher electric and magnetic multipoles. Subsequent developments in the theory are conveniently described in terms of the T-Matrix formalism.

## The Interaction Hamiltonian

The non-relativistic Hamiltonian has the form

$$H_{NR} = H_0 + H \quad (1.5)$$

where

$$H = T + V \quad (1.6)$$

The  $H_0$  term represents the centre-of-mass motion, and the terms  $T + V$  refer to the intrinsic relative kinetic energy and the internal potential energy of the nuclear system.

## The T-Matrix Approach

Transition probabilities and hence cross sections can be expressed in terms of the T-matrix elements  $T_{fi}$ . In first order perturbation theory

$$T_{fi} = \sqrt{\frac{\alpha}{2\pi^2}} \langle f | J_\gamma(0) | i \rangle \quad (1.7)$$

with  $J_\gamma(0) = \epsilon^\mu(\gamma) J_\mu(0)$  representing the interaction of the photon with the charges and magnetic moments of the deuteron system which results in the change from initial to final states. The photon is completely defined by the polarisation vector,  $\epsilon^\mu(\gamma)$ , and  $J_\mu(0)$  is the nuclear current density operator.

The formalism is developed by separating the centre of mass motion from the rest frame of the system with respect to which the internal wavefunctions of the initial and final states are defined.

$J_\gamma(0)$  is written as an expansion in terms of electric and magnetic multipole operators of order  $L$  represented as  $\hat{T}_{e/m}^{[L]}$  which are defined in terms of electric and magnetic multipole fields  $\vec{A}^{[L]}(m)$  and  $\vec{A}^{[L]}(e)$ , and an explicit reference to the nuclear current  $\vec{j}(\vec{x})$ .

$$\hat{T}_{e/m}^{[L]} = \int d^3x \vec{j}(\vec{x}) \cdot \vec{A}^{[L]}(e/m) \quad (1.8)$$

For the electric operators the following treatment is possible.

The electric term  $\vec{A}^{[L]}(e)$  can be expressed mathematically as two terms, the dominant one of which is the gradient of a scalar field  $\Phi$  and the other one a remainder  $A'$ . If the conservation equation for the nuclear current is applied,

$$\vec{\nabla} \cdot \vec{j}(\vec{x}) + i[H, \rho(\vec{x})] = 0 \quad (1.9)$$

(cf  $\vec{\nabla} \cdot \vec{j} + \frac{d\rho}{dt} = 0$  in classical electromagnetism for a current density  $\vec{j}$  and charge density  $\rho$ ), one may substitute for the nuclear current  $\vec{j}(\vec{x})$  where it appears explicitly in the electric part of the transition matrix element using (1.9) and obtain,

$$\langle f | \hat{T}_e^{[L]} | i \rangle = \frac{-i^L}{w} (E_f + B) \int d^3x \langle f | \rho(\vec{x}) | i \rangle \Phi_L Y^{[L]} + \int d^3x \langle f | \vec{j}(\vec{x}) | i \rangle \vec{A}'^{[L]}(e) \quad (1.10)$$

$\rho(\vec{x})$  is the nuclear charge density,  $H$  the intrinsic Hamiltonian,  $\vec{j}(\vec{x})$  the intrinsic nuclear current,  $E_f$  the final state energy and  $B$  the deuteron binding energy. The term involving  $\rho(\vec{x})$  is known as the Siegert operator.

The important point to note is that the dominant part of the electric transition matrix element can be derived from the nuclear charge density and does

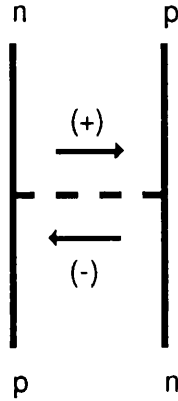


Figure 1.5: *Instantaneous interchange of an n-p pair*

not require an explicit knowledge of the nuclear current. This result is known as the Siegert theorem and has allowed the effects of nuclear currents, including meson exchange currents, to be incorporated into a theoretical treatment in which only the nuclear charge distribution needs to be specified. However, for the small remainder term  $\int d^3x \langle f | \vec{j}(\vec{x}) | i \rangle \cdot \vec{A}^{\prime[L]}(e)$  and the magnetic term  $\hat{T}_m^{[L]}$ , explicit currents are still required.

The way in which the meson exchange currents enter can be seen by writing the nuclear current and charge density as one-body and two-body operators  $[\vec{j}_{(1)}(\vec{x}), \vec{j}_{(2)}(\vec{x}), \rho_{(1)}(\vec{x}), \rho_{(2)}(\vec{x})]$ . The continuity equation can be written as:

$$\vec{\nabla} \cdot \vec{j}_{(1)}(\vec{x}) + i[T, \rho_{(1)}(\vec{x})] = 0 \quad (1.11)$$

$$\vec{\nabla} \cdot \vec{j}_{(2)}(\vec{x}) + i[T, \rho_{(2)}(\vec{x})] + i[V, \rho_{(1)}(\vec{x})] = 0 \quad (1.12)$$

where  $H = T + V$ .

The second equation is simplified by applying Siegert's hypothesis; that the two-body exchange charge density  $\rho_{(2)}(\vec{x})$  vanishes in the non-relativistic limit. This is illustrated in figure 1.5. This instantaneous interchange of an n-p

pair creates an instantaneous two-body current  $\vec{j}_{(2)}$  but not a charge density. The current  $\vec{j}_{(2)}$  associated with meson exchange and other two body effects is necessarily present if the potential  $V$  does not commute with  $\rho_{(1)}(\vec{x})$ , which is usually the case.

The use of Siegert operators to calculate deuteron photodisintegration cross sections and thereby include the effects of meson exchange currents implicitly, was adopted by various theorists including DeSwarth and Marshak and Partovi. The calculations of Partovi [11], which extended up to 140 MeV, gave a good fit to the total cross section and a very reasonable fit to the differential cross section given the experimental uncertainties existing at the time.

### 1.2.3 Meson Exchange Currents and Isobar Configurations

As previously mentioned at energies above 50 MeV exchange mechanisms become increasingly important and must be included in theoretical calculations. The calculations outlined in section 1.2.2 culminated in detailed calculations within the framework of classical non-relativistic nuclear theory but without taking into account explicit meson exchange currents or isobar excitations.

The interaction of the photon with meson exchange currents or isobar configurations can be represented diagrammatically. The contributions to the two-body electromagnetic current from one pion exchange are shown as Feynmann diagrams in figure 1.6a and 1.6b. The role played by  $\Delta$ 's within the nuclear medium and as participants in the electromagnetic interaction can be described in terms of 'effective operators' which are illustrated in figures 1.7a-c. Figure 1.7a describes the virtual excitation of a  $\Delta$  in the nuclear medium and figures

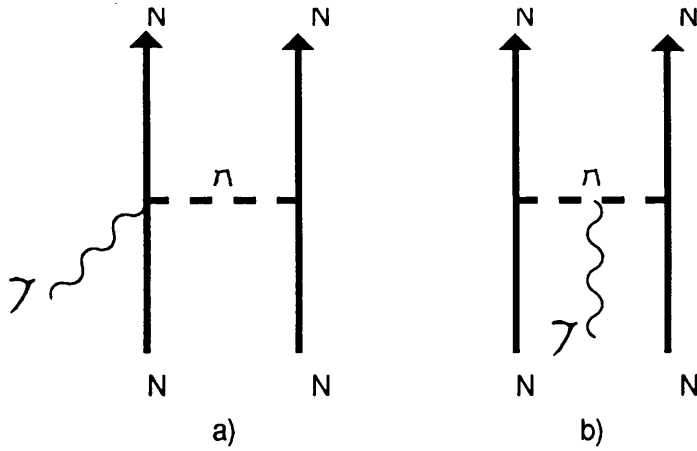


Figure 1.6: *Pion exchange current diagrams*

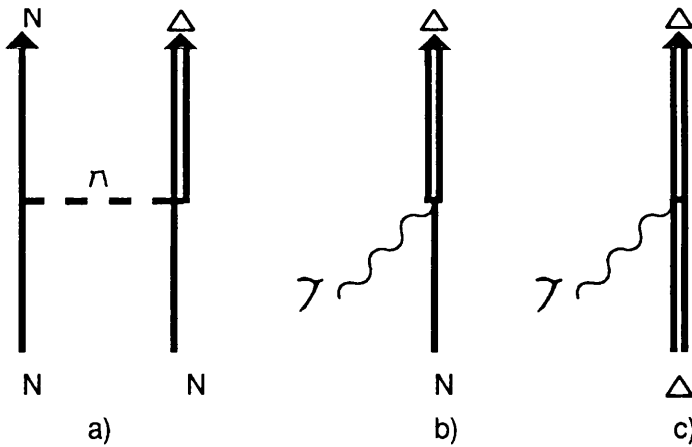


Figure 1.7:  *$\Delta$  contribution diagrams*

1.7b and 1.7c illustrate interactions between an incoming photon and  $\Delta$  configurations. These effective operators are expressed as combinations of Feynmann diagrams as shown in figure 1.8. Alternatively isobars can be introduced explicitly into the nuclear wave function. In this case the isobar propagation is automatically included in the isobar components of the nuclear wavefunction. The most accurate determination of the wavefunctions is by direct solution of the coupled equations for the nucleon and isobar states – the coupled channel approach.

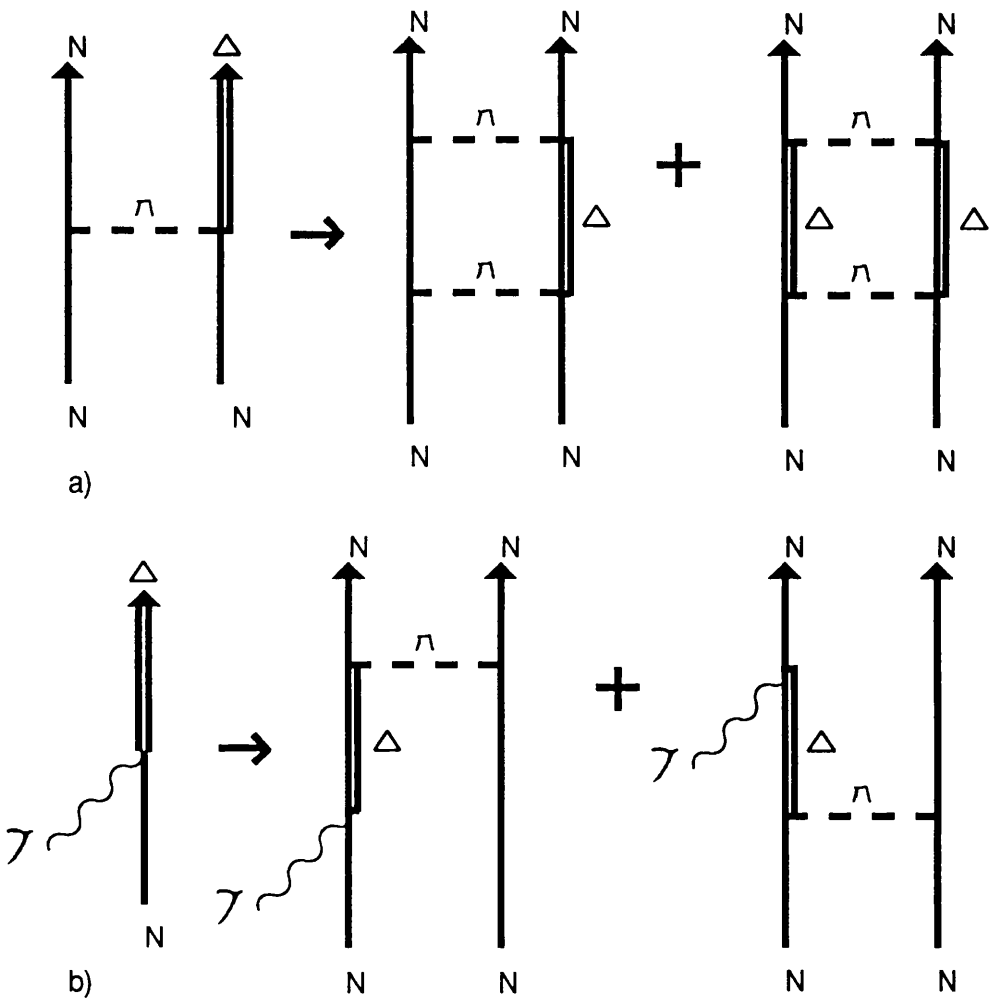


Figure 1.8: *Effective operators*

### 1.2.4 Relativistic Effects and the $0^\circ$ Cross Section

Several modern calculations have shown that there exist relativistic effects which significantly modify the photodisintegration cross section even at quite low photon energies. During the studies of the  $D(\gamma, p)n$  process at  $0^\circ$  in the 1970's the importance of low-order relativistic effects was first indicated. In the simplest model of the reaction, in which only E1 and M1 transitions from the  $^3S_1$  state are considered, the calculation does not predict the experimentally observed  $0^\circ$  cross section. The E1 transition from the  $^3S_1$  state does not contribute at  $0^\circ$  as this is forbidden by angular momentum conservation and although M1 transitions do contribute at  $0^\circ$  their effect is too small to account for the observed magnitude. It has been found a complete treatment of low-order relativistic effects is necessary to predict the  $0^\circ$  cross section even at energies as low as 20 MeV [12]. This situation arises since it turns out the dominant E1 transitions to the  $^3P_1$  states interfere destructively at  $0^\circ$  and consequently the  $0^\circ$  cross section is particularly sensitive to small effects such as the spin-orbit contribution to the charge density.

### 1.2.5 Other Recent Calculations

As discussed in section 1.2.3 recent theoretical studies have concentrated on subnuclear degrees of freedom to account for meson exchange and  $\Delta$  excitation (rather than the N - N interaction via potential models).

In addition to the general outline of the theoretical developments already presented, there have been many refinements and several alternative approaches adopted. These have included:

- a) the incorporation of relativistic effects [12],
- b) the incorporation of retardation effects where finite propagation time of the exchanged mesons are considered [13],
- c) the adoption of a diagrammatic approach to describe the reaction, in which techniques developed in high energy physics using a restricted set of Feynmann diagrams are employed [4],
- d) treating the deuteron as a six quark bag [14].

The results of this large number of calculations of the total and differential cross sections for the two-body photodisintegration of the deuteron extend across a fairly wide range of values. The present data are compared with a representative selection of these calculations but in particular with two very recent calculations, one by Arenhövel and Schwamb [5], the other by Wilhelm and Arenhövel [6]. The first is an impulse approximation calculation including explicit meson-exchange currents beyond the Seigert operators for NN, N $\Delta$ , and  $\Delta\Delta$  configurations. In the second across the  $\Delta$  resonance region, the final state interaction is treated within an NN - N $\Delta$  coupled channel approach which includes explicit pion degrees of freedom. The Wilhelm and Arenhövel approach provides probably the most comprehensive treatment which includes nucleon, isobar and meson effects in configuration space of the two-body photodisintegration of the deuteron. It does not however, include relativistic corrections or take into account quark degrees of freedom.

### 1.3 Review of Existing Measurements

Many different experimental techniques have been utilised. Mainly these have used untagged photon facilities, but more recently several measurements have employed photon beams of known energy. When examining different photon energy regions, it is apparent there are varying degrees of disagreement, which often exceed the quoted errors, between measurements of both the total and differential cross sections. However, in general, there is fair agreement in the general features of the angular distribution shapes, although large discrepancies exist in absolute normalisation.

In the older measurements, uncertainties in normalisation due to the lack of well defined photon fluxes, and difficulties associated with the clean rejection of other reactions and background, have proved to be the most persistent problems. The majority of these older experiments have used untagged Bremsstrahlung, and have been subject to uncertainties in the determination of both the photon flux and photon energy. Typically the photon energy is not known independently, but is determined from the measured values of proton energy and angle using the  $D(\gamma,p)n$  two-body reaction kinematics. The resulting lack of precision in defining the reaction variables, has led to the inclusion of other reaction channels and background events in the yield. Below pion threshold, the proton yield can provide an unambiguous measurement of the  $D(\gamma,p)n$  cross section, but as the photon energy increases above production thresholds, protons from other channels may be included. Indeed it is possible to count pions as protons if inadequate particle separation techniques are used.

Many of these difficulties are removed by photon tagging, which, due to the requirement of a tagging coincidence, in effect counts individual photons. The

Reference	$E_\gamma$ [ MeV ]	$\theta$ range (degrees)	Uncertainty	Photon System	Target	Proton Detector
[15]Urbana56	60 – 250	30-150	10% stat. 10-25% tot.	Bremsstrahlung	$D_2$ liquid	nuclear emulsions
[16]Caltech56	105 – 450	40-140	8% syst. 5% stat.	Bremsstrahlung	$D_2$ gas	plastic telescope
[17]Berkeley56	150 – 290	36-140	10% syst. 10-25% stat.	Bremsstrahlung	$D_2$ liquid	plastic telescope
[18]Indiana58	190 – 240	11,100,176	10-20% tot.	Bremsstrahlung	$D_2$ liquid	plastic telescope
[19]Bonn67	100 – 420	40-140	5-10% syst. 3% stat.	Bremsstrahlung	$D_2$ liquid	plastic telescope
[20]Orsay68	100 – 400	30-130	4% syst. 2.5% stat.	Bremsstrahlung	$D_2$ liquid	spectrometer
[21]Glasgow68	100 – 320	30-140	3% syst.	Bremsstrahlung	$D_2$ liquid	plastic telescope
[22]Stanford68	222 – 342	20-160	7% syst. 1% stat.	Bremsstrahlung	$D_2$ liquid	spectrometer
[23]Cornell68	240 – 320	24-130	5% syst. 3% stat.	Bremsstrahlung	$D_2$ liquid	spark chamber
[24]Lund77	74 – 241	40-140	10% syst. 8% stat.	Bremsstrahlung	$D_2$ liquid	plastic telescope
[25]Bonn84	200 – 440	18-145	6% syst. 6% stat.	tagged Bremsstrahlung	$D_2$ liquid	time of flight spectrometer
[26]Frascati86	100 – 255	32-130	5% syst. 3% stat.	$e^+$ annihilation	$D_2$ liquid	plastic telescope
[27]Frascati89	98 – 243	0,90,180	4.4% syst. 5-10% stat.	$e^+$ annihilation	$D_2$ liquid	plastic telescope
[28]MIT90	50 – 350	20-160	4.8% syst.	improved Bremsstrahlung	$D_2$ gas	spectrometer
[29]LEGS93	200-315	16 – 160	4.2% syst. 2% stat.	laser back- scattering	$D_2$ liquid	various

Table 1.1: Existing  $D(\gamma, p)n$  below 450 MeV

technique provides a reliable flux determination and an accurate determination of the photon energy. The knowledge of the photon energy allows an overdetermination of the reaction kinematics, which usually facilitates a clean rejection of background.

The existing measurements covering the photon energy range of this experiment are summarised; for  $E_\gamma < 450$  MeV in table 1.1, and for  $E_\gamma > 450$  MeV in table 1.2. The energy and angular ranges are shown and the experimental technique indicated. The majority of the existing measurements cover the

Reference	$E_\gamma$ [ MeV ]	$\theta$ range (degrees)	Uncertainty	Photon System	Target	Proton Detector
[30]Cal61	500 – 900	80-140	15-100%	Bremsstrahlung	$D_2$ liquid	plastic telescope
[31]Lund76	139 – 832	37-140	5% syst. 3.1-7.6% stat.	Bremsstrahlung	$D_2$ liquid	plastic telescope
[32]Tokyo82	180 – 600	15-72	10-18% syst. 5% stat.	tagged Bremsstrahlung	$D_2$ liquid	spectrometer
[34]Bonn83	180 – 730	180	6% syst. 6% stat.	tagged Bremsstrahlung	$D_2$ liquid	telescope

Table 1.2: Existing  $D(\gamma, p)n$  data extending above 450 MeV

photon energy range up to 350 MeV, with several experiments to 450 MeV and a few measurements extending higher.

A critical review of past and recent experiments follows, and it is shown that, even accounting for recent developments, there remains the need for reliable data.

### 1.3.1 Measurements with Bremsstrahlung Beams

The early experiments of the 1950's (Caltech[16], Berkeley[17], Indiana[18]) established the general features of the reaction and indicated the importance of meson exchange current contributions to the cross section above 50 MeV. Although they all reported a cross section which disagreed with contemporary calculations, there was also poor agreement among their results, casting doubt on the absolute normalisations of the experiments. These discrepancies can be identified as being due to the characteristics noted above and discussed further below, which were common in these early measurements and in many of the experiments that followed. There is also disagreement in the shape of the

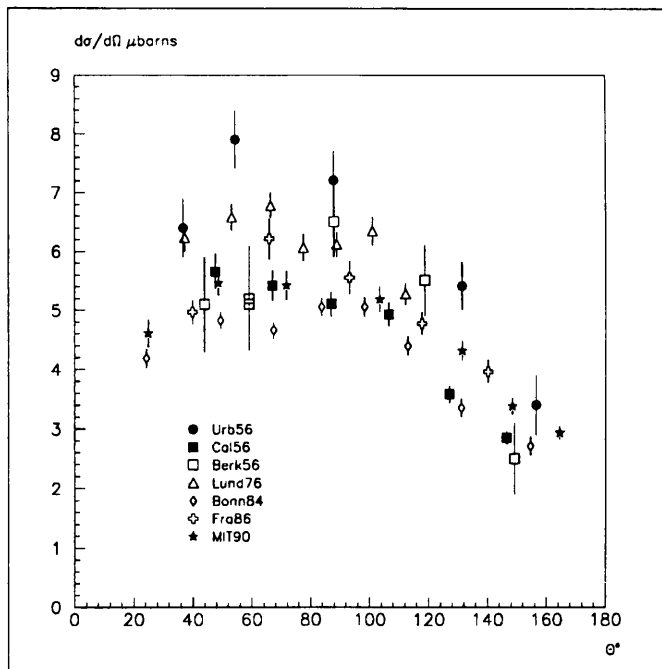


Figure 1.9: *Examples of existing differential cross section data  $E_\gamma=200$  MeV*

differential cross sections from these measurements as is clear from the example of figure 1.9.

All measurements before 1980 utilised collimated Bremsstrahlung beams, relied on theoretical assumptions about Bremsstrahlung shapes and monitored only the integrated beam intensity. In general, the flux normalisation has been obtained by measuring the total integrated photon intensity over all photon energies, typically with an ionisation chamber. Theoretical intensity and angular distributions are then assumed, and the relative intensity for each photon energy calculated. The dependence of this technique on theoretical assumptions and the uncertainty in the measurement of the integrated photon flux, have proved to be serious disadvantages as is clear from the discrepancies in the data set. Various designs of ionisation chamber were employed, the calibration of which proved problematic, eg. Urbana [15] reported two different methods of

determining the detection efficiency which disagreed by 15%.

The Bremsstrahlung spectra were often calculated according to the Schiff formula [35], which is known to be only approximately correct, differing significantly from the full Bethe-Heitler formula [36]. Reasonable confidence can be placed in the shape of the theoretical photon energy dependence, however, the angular distributions are only approximately correct, and the effects of collimation are not necessarily properly accounted for.

All these measurements rely on a knowledge of the experimental value of the detected proton momentum, which together with the two-body kinematics of the reaction, allow the photon energy to be determined. This does not provide a very satisfactory technique of distinguishing the two-body photodisintegration process from other channels at higher energies. There is a suspicion from some of the angular distribution data, for example the Lund experiment [31], that pion channels have been included. Protons from the pion production channel,  $D(\gamma, p)n\pi^0$  are forward peaked and any failure to perform a clean rejection of these protons results in spurious forward/backward asymmetries. The data analysis of the present experiment described in Section 4.4, makes clear the difficulties in the separation of  $D(\gamma, p)n\pi^0$  from  $D(\gamma, p)n$ , even with the extra information available from the overdetermined kinematics in the present experiment and this tends to confirm the suspicions about this problem in the earlier work.

### 1.3.2 Neutron Capture Experiments

Several experimental studies have been performed on the inverse reaction to deuteron photodisintegration, neutron capture  $p(n, \gamma)D$ . High energy neutrons

Reference	$E_n$ [ MeV ]	$\theta$ range (degrees)	Target
[37]Princeton71	475 – 750	10-160	$D_2$ liquid
[38]Berkeley71	300 – 720	30-150	$D_2$ liquid
[39]Freiburg83	190 – 590	10-65	$D_2$ liquid

Table 1.3: Existing  $p(n, \gamma)D$  data

incident upon a hydrogen target are captured by protons to form deuterons and this is accompanied by the emission of radiation which is detected. The principle of detailed balance is used to transform the radiative capture reaction cross sections into the photodisintegration frame of reference. These cross sections can then be included in the data set. As one would expect from time reversal invariance there is good agreement between these converted cross sections and the photodisintegration data at lower photon energies, where the cross section is known accurately.

The existing data corresponding to the photon energy range of the present experiment are shown in table 1.3. The experiments at Princeton and Berkeley [37],[38], are relative measurements therefore only the shapes of the angular distributions can be compared. Within the errors, the angular distributions from the neutron capture data are found to be self-consistent, and good agreement is found with the photodisintegration data. When comparing the magnitude of the absolute measurement of Freiburg [39] with photodisintegration data, it is found to agree best with Bonn [25].

A major source of uncertainty with these measurements is neutron flux de-

termination. Generally the data provide useful knowledge of the shape of the angular distributions but are less reliable in determining magnitudes.

### 1.3.3 Recent Measurements

It is evident that the accuracy of the subset of most recent experiments in figure 1.2 is an improvement on that of the previous measurements. The better consistency amongst the data is attributable to the recent significant progress, which has been made in the design of photon sources. The selection includes the Bonn [25], Frascati [26], MIT [28], LEGS [29] and Tokyo [32] experiments performed with either quasi-monoenergetic photons or with improved untagged Bremsstrahlung techniques.

The advantage common to all of the experimental methods included in this subset is that each to some degree has a redundancy of information. The MIT experiment used a magnetic spectrometer to make an accurate measurement of proton energy and angle; hence they could distinguish other channels more effectively. The Bonn, Frascati, LEGS and Tokyo experiments all determined photon energy independently. The knowledge of the photon energy overdetermined the reaction kinematics allowing a rejection of other channels, such as  $D(\gamma, p)n\pi^0$ .

The experimental system at MIT used an untagged Bremsstrahlung beam but employed new techniques to overcome some of the associated problems of photon flux and energy determination. The experiment covered the photon energy range 50–350 MeV, the angular range  $20^\circ$ – $160^\circ$  and the results gave an estimated total uncertainty of 5%. The photon beam was not collimated and therefore the uncertainty from theoretical assumptions concerning the Brem-

strahlung angular distribution were avoided. The experimental procedure for determining the photon flux involved monitoring the electron current and using a theoretical Bremsstrahlung cross section, thus avoiding the use of an ionisation chamber, the calibration of which is difficult. By repeating measurements using different Bremsstrahlung end point energies a check of the calculated Bremsstrahlung shape used to analyse the data was made. A magnetic spectrometer with wire chamber and scintillation detectors was used to determine proton energy and angle precisely. The use of the spectrometer compares extremely favourably with a scintillator telescope measurement with respect to resolution and particle identification. Furthermore, the large corrections which arise from nuclear interactions in the telescope medium are avoided, although there are still (smaller) corrections for nuclear interaction losses in the thin  $dE/dx$  particle identification scintillators. A deuterium gas target was used for ease of obtaining an accurate measurement of the target thickness and also to minimise energy loss corrections and hence uncertainties in the reconstruction of  $E_p$ . The good definition of  $E_p$  and  $\theta_p$  permits confidence to be placed in the angular distributions presented by this experiment. However, as it is a measurement using untagged Bremsstrahlung, questions concerning the absolute magnitude remain since the absolute cross sections are based on the calculated absolute intensity of the Bremsstrahlung spectrum. A check is made by measuring the  $p(\gamma, \pi^0)p$  cross section and comparing it with previous measurements.

The Bonn experiment employed a photon tagging system which provided monochromatic photons and a good definition of the photon flux. Measurements cover the range 200–440 MeV at 8 lab angles from  $18^\circ$ – $145^\circ$  with an estimated overall uncertainty of 4%. The tagging spectrometer determined the photon energy to 10 MeV, and 8 time-of-flight spectrometers consisting of scintillation

counters were used to measure the proton energy. The spectrometers were equally spaced around the target, each having a geometrical solid angle of 32 msr. The  $D(\gamma, p)n\pi^0$  channel was rejected by using a determination of missing mass to separate the reactions. Two peaks were obtained, the  $D(\gamma, p)n$  peak was distributed around the neutron mass, and the pion production peak had missing mass greater than the sum of the neutron mass plus the pion mass. For the most forward spectrometer, which having the longest time-of-flight has the best proton energy determination, the overall resolution of the  $D(\gamma, p)n$  peak was  $\sim 5\%$ . The peak from the pion production events was a factor ten greater in magnitude, and had a tail extending under, the  $D(\gamma, p)n$  events. A clean separation of the pion production channel was further complicated by events for which the reaction products had undergone nuclear interactions. A fit was made to this plot to account for the overlap of the two distributions.

The Tokyo group also employed a tagging spectrometer with a resolution of 7 MeV. The experiment was designed to investigate the possibility of the existence of the dibaryon resonance, the photon energy range was 180–600 MeV and lab angles from  $15^\circ$ – $72^\circ$  were covered with a systematic uncertainty of 10–18%. Charged particles were detected in a hadron spectrometer consisting of an analyzer magnet, four sets of multiwire proportional chambers, and three sets of time-of-flight scintillation counters. The magnetic spectrometer was used to measure the proton energy precisely, and the momentum resolution was typically 3%. Protons were separated from other particles using a scatter plot of time-of-flight against particle momentum, and  $D(\gamma, p)n$  events selected by imposing kinematical restraints. The problems encountered with the poor energy resolution of plastic telescopes, and of the degradation of proton energy information due to nuclear interactions in the scintillator medium are greatly

reduced since the proton momenta are determined by the magnetic spectrometer. However, corrections are still needed as some events are still lost due to interactions in the time-of-flight scintillators.

The experiment carried out at Frascati used a quasi-monochromatic photon beam produced by positron in-flight annihilation on a hydrogen target. The photon beam comprised a mixture of a Bremsstrahlung spectrum with a peak at the high photon energy end due to positron annihilation. The energy range 100–255 MeV was studied with  $\theta_p$  from  $32.5^\circ$ – $130^\circ$ , with a total error of 5%. Determination of the photon energy scale came from an online pair spectrometer, and the proton energy was measured in a plastic telescope.

The Bonn, Frascati and Tokyo experiments all used liquid deuterium targets. With liquid targets there are difficulties in determining the target thickness accurately. There may be uncertainties in the knowledge of deuterium density due to the target boiling, however, this is a well understood problem and there are known ways to cope.

The LEGS experiments were conducted with linearly polarized photons. Three independent measurements with three different detector systems and two different liquid deuterium targets were performed. The experiment L3a(P) used a phoswich detector system. Total and differential cross sections were measured within the photon energy range 200–315 MeV with tagged photons. Data were taken simultaneously at 8 angles in the polar angular range  $16^\circ$ – $160^\circ$ . The L3a(S) measurements were performed simultaneously with the L3a(P) measurements with both detector systems viewing the same liquid deuterium target. A Si- $\mu$ strip/NaI/Plastic detector system was used and data were taken sequentially at three different angles. The photon energy was not determined from the

tagging spectrometer but was instead reconstructed from the experimental values of proton energy and angle and the  $D(\gamma,p)n$  two-body reaction kinematics.

In the L3b(N) experiment, which used a large Drift chamber/NAI/Plastic detector system, tagged data with good statistical precision were taken with a large angular acceptance centred near 90 degrees in the CM system using a different target.

## 1.4 Review of Photon Tagging Techniques

In tagged photon experiments, a continuous energy spectrum of photons is initially produced from a beam of high energy electrons. Several tagging techniques are used, but in all the energy of a photon inducing a nuclear reaction is determined by requiring a coincidence between a reaction product detector and a detector which both identifies one of the final state particles involved in the process that produced the photon and allows the photon energy to be deduced. The principal photon tagging techniques are:

1) Bremsstrahlung:  $e^- \rightarrow e^- + \gamma$ , high energy electrons incident on a very thin target radiate in the presence of the Coulomb field of the target nuclei. The residual electron is used to tag the photon, the photon energy is given by,  $E_\gamma = E - E'$ , since the energy of the recoil nucleus is negligible.

2) Positron annihilation:  $e^+ + e^- \rightarrow \gamma + \gamma$ , high energy positrons collide with atomic electrons in a very thin target producing a spectrum of annihilation radiation consisting of 2 photons. The low energy photon is used to tag the high energy one, whose energy can be deduced from the angle of its low energy partner.

3) Laser backscattering:  $e^- + \gamma \rightarrow e^- + \gamma'$ , laser photons Compton scatter off high energy electrons. The residual electron is used to tag the photon, the photon energy is given by,  $E_\gamma = E - E'$ .

The MAMI-B facility utilises the Bremsstrahlung tagging technique, and in order to determine the Bremsstrahlung photon energy the photon/residual electron coincidence is observed. Electron Bremsstrahlung by the electron beam passing through a thin radiator, produces photons with known energy  $E_\gamma = E - E'$  since the incident electron energy  $E$  and that of the residual scattered electron  $E'$  can be determined. In practice the energy of the recoil electron is measured in a magnetic analyser and the incident energy is well determined by the microtron accelerator. This essentially simple technique removes many of the difficulties associated with untagged Bremsstrahlung photon beams for which an accurate determination of the photon energy was invariably problematic.

Furthermore, in previous photonuclear work photon flux normalisation, necessary to determine absolute cross sections, proved to be another major source of uncertainty. The photon tagging technique, by effectively counting each photon in the beam provides a reliable flux determination, and also circumvents this disadvantage of untagged photons. The present experiment by presenting absolute total and differential cross sections covering a broad range of energies will demonstrate the power of the tagging technique.

## 1.5 The Present Measurement – Theoretical and Experimental Justification

By using DAPHNE with its large acceptance ( $3.7\pi$  steradians), good angle definition and particle identification in conjunction with the high intensity Glasgow tagger with its good definition of flux and of photon energy, high precision results with small systematic errors are achievable. MAMI-B extends the range of photon energies previously studied, the experimental system can detect the  $D(\gamma,p)n$  reaction over a large photon energy range from 100–800 MeV. The experimental system not only extends the photon energy but by providing accurate and overdetermined kinematic information needed to detect and identify the  $D(\gamma,p)n$  reaction, is able to achieve a significant improvement in background rejection compared to most previous measurements.

Reliable data are currently needed as the differences in the data sets are still too large to allow a discrimination between the different theoretical models. Data are needed for both differential and total cross sections, and also for  $0^\circ$  and  $180^\circ$  and the polarisation observables. Together they will be able to constrain all of the presently uncertain parameters in the theory. In addition to the present measurement of extensive total and differential cross sections, in the near future, the experimental system will be used for the measurement of polarisation observables. The Tagged Photon Facility will be extended by the provision of a flux of tagged photons having a high degree of linear polarisation. The DAPHNE detectors' complete coverage in azimuthal angle means it is ideally suited to the measurement of polarisation observables. The future development of the production of polarised photons is discussed in Appendix C.

## **Chapter 2**

# **The Experimental System**

## 2.1 Introduction

The tagged real photon beam is one of the major experimental facilities available at the Institut für Kernphysik, Universität Mainz, Germany. This experiment used the photon facility together with the large acceptance detector DAPHNE. The complete experimental layout is shown in figure 2.1. The 855 MeV Mainz Microtron MAMI-B provides a 100% duty cycle electron beam, which is used to produce the photon beam by the Bremsstrahlung process in a thin ( $3 \cdot 10^{-4}$  radiation lengths) radiator. The photon beam is then collimated before reaching the target. The photon energy is determined by a tagging spectrometer which analyses the recoil momentum of the electron. The tagging spectrometer, installed by the Glasgow group comprises 2 parts, a quadrupole/dipole magnetic focussing system and a 352 channel focal plane detector. It is able to tag photons in the range from 42 to 792 MeV with a resolution of about 2 MeV at intensities up to  $5 \cdot 10^5$  photons per channel. The spectrometer directs electrons which do not radiate away from the experimental area to a Faraday cup located outside the experimental hall to minimize background. The electron beam before and after the radiator is shielded by concrete walls and measurements of the room background have shown it to be small.

## 2.2 The Accelerator and Beamline

### 2.2.1 Accelerator Characteristics

The 855 MeV Mainz Microtron MAMI-B is a new continuous electron beam facility at the Institut für Kernphysik, Universität Mainz, Germany [40] [41]. The design philosophy of MAMI-B was to provide a high duty cycle, good energy

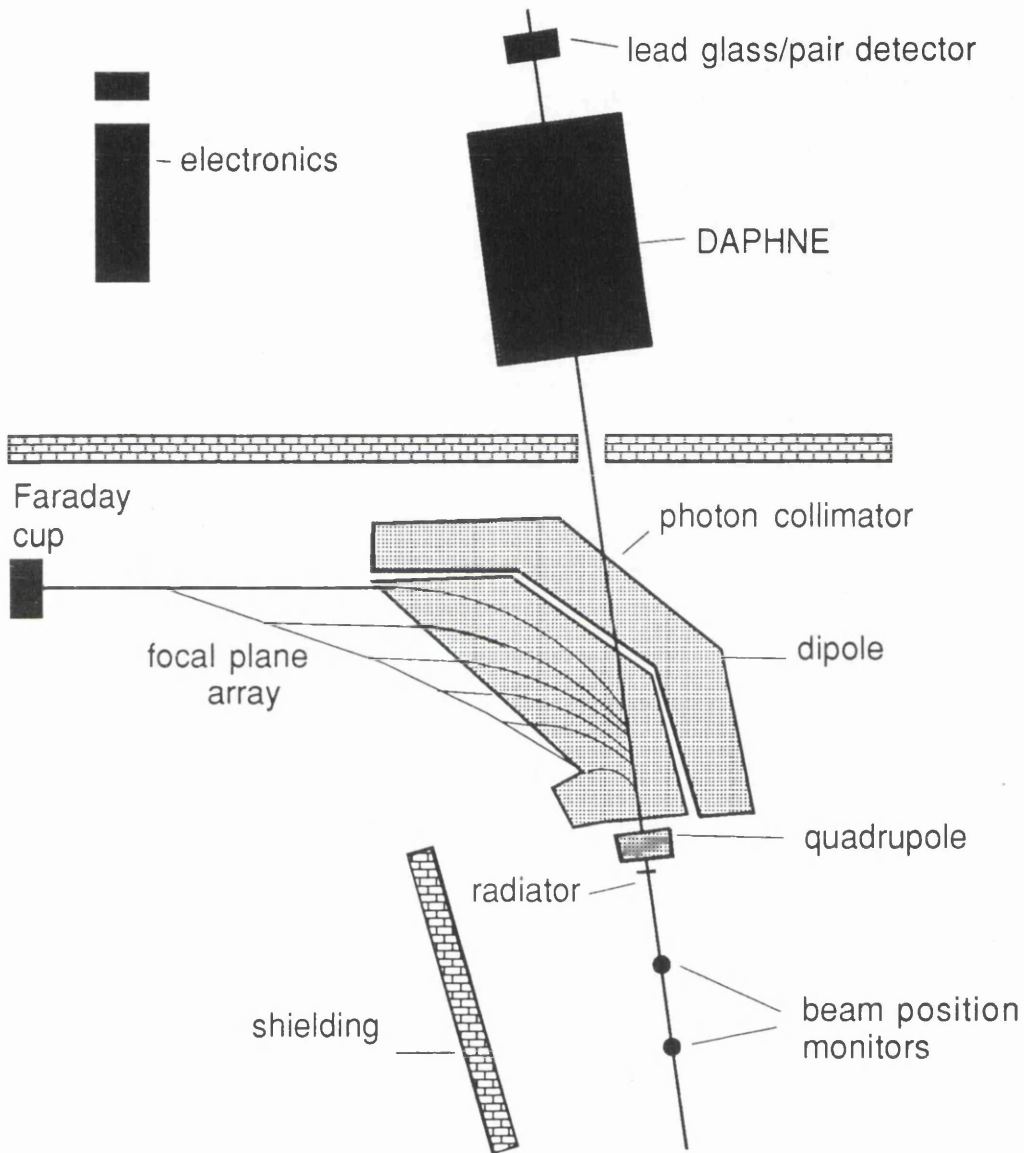


Figure 2.1: The Experimental System

resolution electron beam for use as an interdisciplinary facility at reasonable cost. The accelerating scheme recirculates an electron beam through linac sections in a cascaded racetrack electron microtron to provide a 100% duty cycle beam of energy 855 MeV, with a resolution of 60 KeV at currents of up to about 100  $\mu$ A.

The system, shown schematically in figure 2.2, comprises an electron source which delivers an initial beam to an injection linac followed by three cascaded racetrack microtrons RTM1 ,RTM2 and RTM3.

A racetrack microtron consists of a linear accelerator (linac) situated between 2 uniform field bending magnets which recirculate the electrons through the accelerating section. In the linac the electrons are accelerated by the axial electric component of a standing wave in a series of standing wave cavities, whose radio frequency power is generated by a set of phase locked klystrons. For each microtron, as the electron energy increases in each recirculation through the linac, the radius of orbit in the magnetic field of the dipoles increases and thus each return path is spatially separated. The higher energy electrons in an outer return path have a larger orbit to circulate than those of lower energy in an inner path, and the difference in path lengths is arranged to be one RF wavelength to ensure the electrons are all sent into the accelerator at the same phase.

An important feature of the operation of a racetrack microtrons is its inherent phase correction, the characteristic responsible for compressing the energy spread of the MAMI-B final beam to  $\Delta E \sim 60$  KeV. If an electron becomes displaced from the resonant energy, as a result of energy loss by synchrotron radiation for example, an automatic re-adjustment takes place as there is a con-

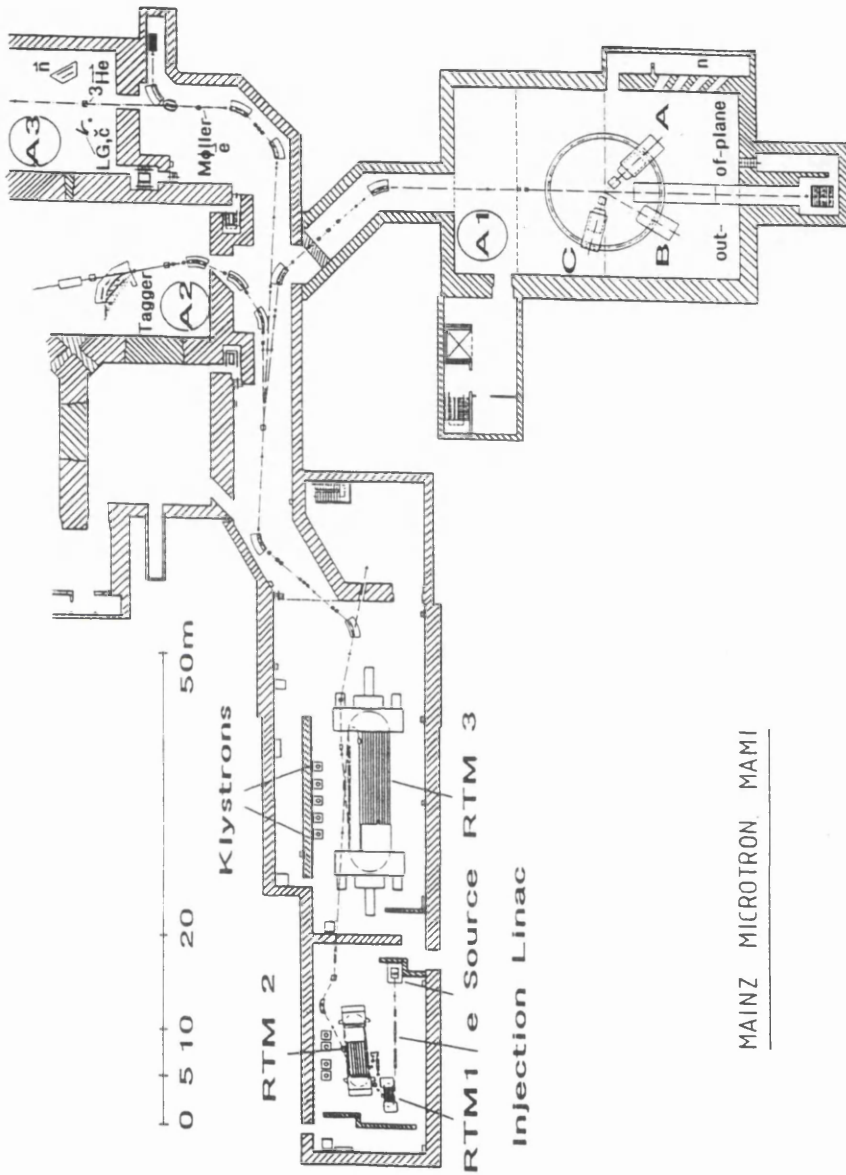


Figure 2.2: The Mainz Microtron MAMI-B

General			
Stage No.	I	II	III
Input Energy MeV	3.46	14.39	179.8
Output Energy MeV	14.39	179.8	855
No. of recirculations	18	51	90
Magnet System			
Magnet distance (m)	1.67	5.60	12.86
Flux density (T)	0.1028	0.5553	1.2842
Max orbit diam. (m)	0.97	2.17	4.43
Weight per magn. (to)	1.3	43	450
Gap width (cm)	6	7	10
R.F System			
No. of Klystrons	1	2	5
Linac length (el.) (m)	0.80	3.55	8.87
R.F power dissip. (kW)	8	48	103
R.F beam power (kW)	1.1	17	68
Energy gain (MeV)	0.6	3.24	7.5
Beam (100 $\mu$ A)			
Energy width (keV)	$\pm 9$	$\pm 18$	$\pm 60$
Emittance vertical ( $\mu$ m)	$<0.17\pi$	$<0.014\pi$	$<0.04\pi$
Emittance horizontal ( $\mu$ m)	$<0.17\pi$	$<0.014\pi$	$<0.14\pi$
Injection:	100 KeV gun and 3 linac sections fed by another klystron		
Extraction:	From each even numbered return path of RTM3,ie in steps of 15 MeV		
R.F.structure:	On-axis coupled biperiodic standing wave vacuum based OFIIC copper		
Klystrons:	Thomson TII 2075 50 kW c.w. max., 2449.6 MHz.		

Table 2.1: *Microtron Characteristics*

tinual interplay between electrons defocussed in energy and focussed in phase. For example, if an electron's energy is low, it follows a shorter recirculation path and reaches the linac early, advanced in phase, and thus is accelerated more than the main beam and approaches the correct energy.

The excellent design parameters of the accelerator are listed in table 2.1. The electrons are recycled through the RTM's many times to produce the maximum output energy of 855 MeV, and so only a relatively modest energy gain is needed from the linacs in each recirculation. The final energy is reached by a combination of the 3.5 MeV linac, and the gain of each of the 3 RTM stages; the 14 MeV 18-turn first stage, the 180 MeV 51-turn second stage and finally

the 855 MeV 90-turn third stage. The low power requirement in the accelerator cavities permits d.c operation producing a 100% duty cycle electron beam. In fact, the beam does have the pulsed micro-structure corresponding to the R.F. frequency of 2.45 GHz but within the time resolution of the photoreaction experiments it is effectively d.c. In past photonuclear experiments, low duty cycle machines with short high current output pulses have inevitably produced higher random backgrounds and dead times in experimental measurements.

Measurements show that the accelerator performance is at least as good as the design values. The phase space emittance is  $0.04\pi$  mm.mrad in both the vertical and horizontal directions, and the variation of beam intensity with position and angle exhibits a sharp cut off with an extremely small halo.

### 2.2.2 Accelerator Monitoring and Control

Each return path of the RTM's may be individually steered by means of transverse deflection coils, and a separate magnet is used to extract the beam. There exist various position and phase monitoring devices and computer aids to help set up and control the beam, such as the synchrotron radiation monitors at the RTM magnets.

### 2.2.3 Beamline Transport Design

The beamline system is designed to transport the beam from after its extraction from RTM3, through various dipole steering and quadrupole focussing elements to the A2 hall photon facility, with the requirements that the beam transport is achromatic, and that the phase space (the product of beam spot size and beam divergence) of the beam is the same at the A2 Bremsstrahlung radiator as it

was leaving RTM3. This transport involves several large angular deflections accomplished by dipole-quadrupole systems which are achromatic in both the horizontal and vertical planes. The spatial dependence of electrons in the beam before the dipoles is independent of their energy and so the dispersive nature of the dipoles has to be corrected for by quadrupole focussing/defocussing elements between the two dipoles.

## 2.3 The Tagging Spectrometer and the Photon Beamline

### 2.3.1 The Bremsstrahlung Radiator

The electron beam is focussed on to and passes through a radiator, situated just before the tagging spectrometer. The electrons radiate by the Bremsstrahlung process producing a continuous photon energy spectrum up to a maximum energy equal to the kinetic energy of the incident electrons. The photon beam flux depends on the electron beam current and the thickness of the radiator (measured in radiation lengths). As the electron beam traverses the radiator the beam divergence is increased due to electron multiple scattering. To maximise the photon flux, which passes through the photon collimator it is necessary to keep  $\theta_{mult.sc}$  significantly less than  $\theta_{Brem}$ , the angular spread of the Bremsstrahlung process, and therefore thin radiators are desirable. The requirement to minimise Möller scattering, which produces signals in the focal plane detector without a corresponding photon in the beam, demands high  $Z$  materials. Materials of very high  $Z$  cannot easily be used since targets of a suitable thickness in radiation lengths are too fragile. Nickel foil radiators are a good compromise for many experiments and a 1 mm diameter gold spot deposited on a thin alu-

minium backing is used when it is worthwhile to limit the effective area of the radiator.

The tagged photon spectrometer is provided with a set of radiators of various materials and thicknesses and viewing screens which are mounted on a ladder. The ladder has a vertical movement controlled by a stepping motor which allows the interchange or removal of the radiators. In addition the ladder mechanism can be used to install a goniometer, capable of rotation about 3 orthogonal axes with high resolution. The goniometer defines the alignment of a thin diamond crystal radiator (0.0008 radiation lengths, 100  $\mu\text{m}$ ) with an angular precision of 0.002 mrad. This radiator is used for the production of linearly polarised photons by the coherent Bremsstrahlung process. The advantages of using linearly polarised photons to study the two body photodisintegration of deuterium are discussed in Appendix C which considers future developments.

In the present measurement a 1  $\mu\text{m}$  thick gold spot radiator was used ( $3 \cdot 10^{-4}$  radiation lengths). The small diameter (1 mm) of the gold spot ensures that the beam alignment with respect to the radiator, spectrometer and photon collimator can be monitored with high sensitivity and good reproducibility. The gold spot was used as it was feared the electron beam size might have been bigger than 1 mm and/or unstable. By using the gold spot radiator any drift in the beam would be seen immediately as a drop in photon beam intensity. In fact, neither fear materialised and the beam diameter was  $< 0.5$  mm and was very stable in position. The angular divergence of the electron beam in the radiator from multiple scattering is given by:

$$\theta_{mult.sc} = \frac{21}{E} \sqrt{t} \text{mrad} \quad (2.1)$$

(t in radiation lengths, E in MeV), and so the resulting divergence for the

radiator used is 0.25 mrad which is significantly less than the Bremsstrahlung characteristic angle ( $\theta_{Brem} = m/E = 0.6$  mrad), where  $m$  is the electron rest mass.

### 2.3.2 The Magnet System of the Tagging Spectrometer

The magnet system momentum analyses the Bremsstrahlung scattered electrons, focussing the different energies along a focal plane which has the form of a shallow curve [42]. It is equipped with a focal plane detector of length 4.2 metres, which accepts electrons in the energy range  $(E'_{min}/E):(E'_{max}/E) \sim 0.05:0.93$ , corresponding to photon energies of 42 to 792 MeV for the normal 855 MeV accelerator output energy. When an electron of energy  $E'$  is detected in the focal plane in coincidence with a photonuclear event, the energy  $E_\gamma$  of the photon responsible for the event can then be obtained using  $E_\gamma = E - E'$ , where  $E$  is the energy of the incoming electrons. The spectrometer also transports the main electron beam to a Faraday cup located in a separate room from the experimental area. The general design requirements of the tagging spectrometer are:

- i) a momentum acceptance covering a large fraction of the incident electron momentum,
- ii) energy resolution of the order of 120 KeV,
- iii) compactness - for minimum radiator-to-photonuclear target distance to provide a small beamspot size,
- iv) sufficient angular acceptance - accept  $\geq 99\%$  of residual electrons which have radiated and have an energy within its focal plane acceptance range,

<b>General :</b>	
momentum acceptance	8:1
solid angle acceptance	$\sim 8$ msr
angular acceptance	$\pm 50$ mrad
dispersion	$\sim 1$ cm/%
first order optics in radial plane	point to point
momentum range	50–800 MeV/c
object distance	0.1m
quadrupole/dipole separation	0.25m
<b>Quadrupole :</b>	
Max. pole tip field	3 kGauss
Aperture diameter	3 cm
Length	0.15 m
<b>Dipole :</b>	
Magnetic field	1.00 Tesla
Entrance and exit face radii	0.18m – 8.0m
Gap height	5 cm
Weight	$\sim 65$ tons
Bend radius (main beam)	2.8 m
Bend angle (main beam)	$80^\circ$
Entrance and exit angle (main beam)	$16.7^\circ$ – $58.8^\circ$

Table 2.2: *840 MeV Photon Tagging Spectrometer parameters QD design*

v) uniform field (for simplicity of construction).

The quadrupole/dipole design adopted is shown in figure 2.3, and table 2.2 lists the important parameters.

The magnet optics comprise a 'QD' system. To improve the angular acceptance the quadrupole focusses vertically and defocusses horizontally before the dipole disperses. The dipole also has edge focussing designed to improve the overall focussing characteristics in the focal plane. It also directs the beam which has not radiated to the beam dump. An NMR probe set up inside the dipole monitors the field constantly.

## The Experimental System

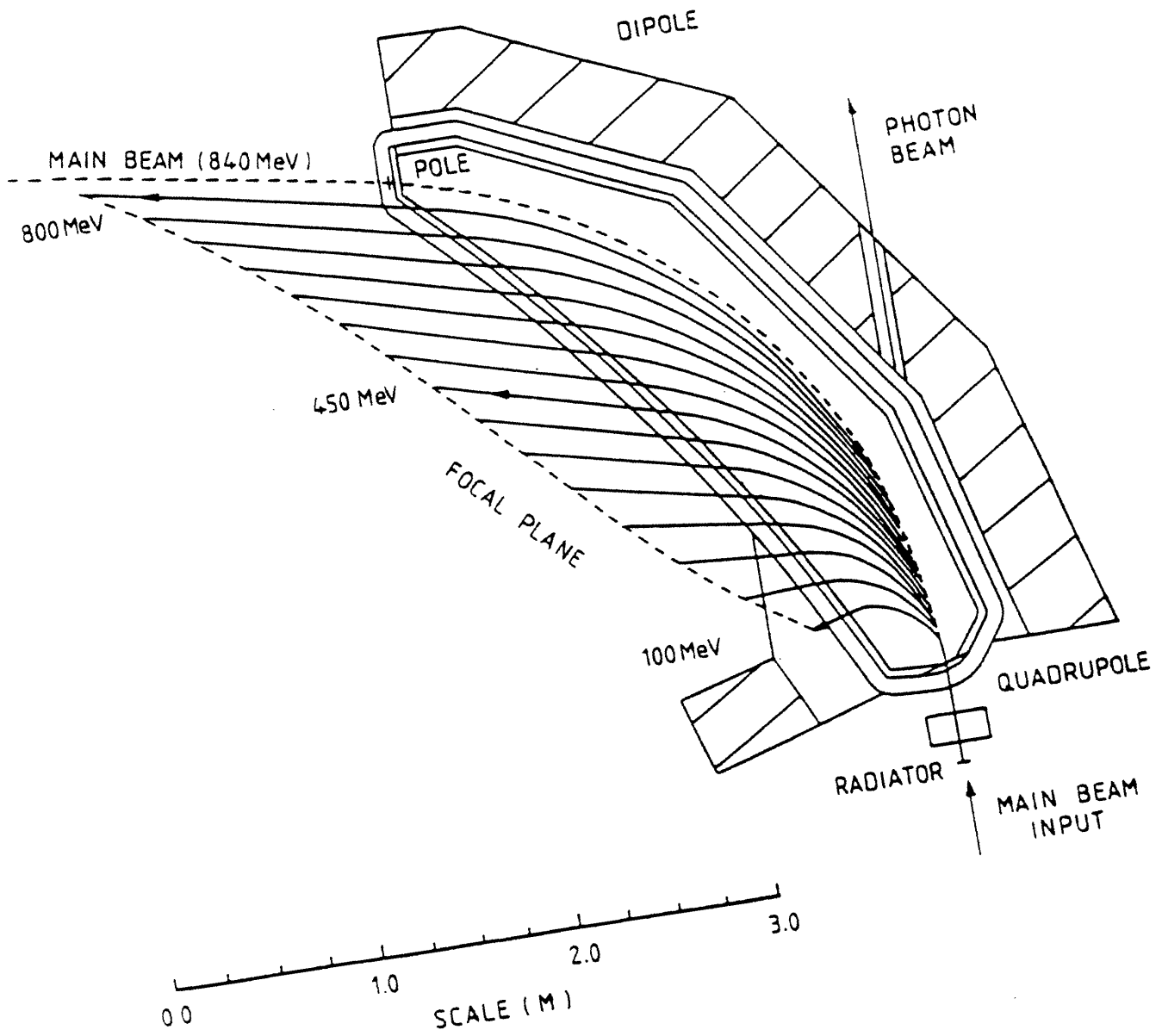


Figure 2.3: The Quadrupole/Dipole Design

### 2.3.3 The Focal Plane Array

Although the intrinsic resolution of the tagging spectrometer is always better than 0.2 MeV it was too costly to install a focal plane array with this resolution and wide coverage. For general use it was reasonable to design a focal plane detector system (FPD) with an average energy resolution of 2 MeV. The general specifications of the FPD are:

- (i) ability to handle total counting rates of the order of  $10^8$  Hz,
- (ii) position resolution compatible with a 2 MeV energy resolution,
- (iii) good timing ( $\leq 1$  nsec),
- (iv) a lifetime of at least several years operation,
- (v) reasonably straightforward to construct and maintain,
- (vi) not be too expensive,
- (vii) overlapping adjacent detecting elements for background rejection via a coincidence requirement,
- (viii) high detection efficiency for electrons.

A section of the detector system which was chosen to satisfy these requirements is shown in figure 2.4.

The average photon energy resolution of 2 MeV per channel is achieved using an array of 352 overlapping scintillator elements. Each element comprises a scintillator/lightguide assembly attached to a photomultiplier tube and its base electronics. The 2 mm thick NE111 plastic scintillators form an array with a half-width overlap between adjacent channels. A thixotropic gel is used as

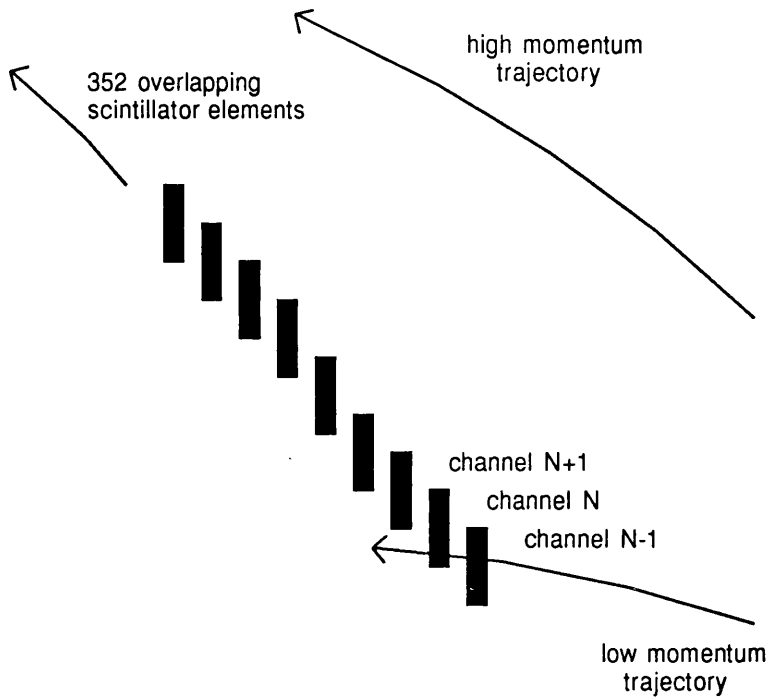


Figure 2.4: *The Focal Plane Detector*

optical couplant between the lightguide and the phototube. Hamamatsu R1635 phototubes satisfy the lifetime requirements and were chosen for their miniature size necessary to achieve the required position resolution. The phototubes are assembled onto cards containing their base resistor chain and signal electronics which consist of a threshold discriminator and an edge triggered AND unit to give a coincidence with the adjacent overlapping detector.

The coincidence identifies an ionizing particle and reduces  $\gamma$  and neutron background. A minimum ionizing electron deposits a mean energy of  $\sim 460$  keV in each 2 mm scintillator. The chosen scintillator thickness is a compromise between light output and electron multiple scattering effects. It was necessary to keep the mean angular divergence in the scintillator due to multiple scattering minimal as if an electron scatters, for example, in the first scintillator, it could miss the second and therefore not satisfy the coincidence. The pulse height spectrum from the detectors has a good separation between the electron

detection pulses and the noise, consequently a threshold may be used to cut off the noise without the fear of losing electrons, so that the elements have an electron detection efficiency of 100%. On detection of an electron a logic pulse is sent to the tagger electronics.

The detector design allows for a future development which would increase the number of channels to 650 thus improving the photon energy resolution by a factor of 2. The ladder detectors are mounted behind a plane in which best focus is obtained so this improved resolution can be obtained later over part of the plane by mounting a small high resolution array in the best focus plane.

### **2.3.4 The Tagger Electronics**

When an electron is detected in the focal plane the signal is recorded and used to test for a coincidence with the DAPHNE detector. The hardware comprises 3 linked bus systems, VME-bus, CAMAC, and FASTBUS. Each of the 352 channels has its own associated scaler and TDC in high density FASTBUS crates. All electron hits in the focal plane produce an ECL logic pulse which is sent to be recorded in TDCs and pattern units and also to a free running scaler. A logic pulse derived from an OR output of all 352 channels is produced to test for a coincidence between an electron and a trigger coming from the main experiment signalling a photoreaction product. The TDC is recorded if this coincidence requirement is satisfied; it is needed to determine whether or not a real coincidence has occurred between the product detector i.e. DAPHNE and the electron or if in fact it is a random coincidence.

Figure 2.5 shows a typical TDC spectrum in which there is a prompt peak superimposed on an extremely small random background. The random plateau

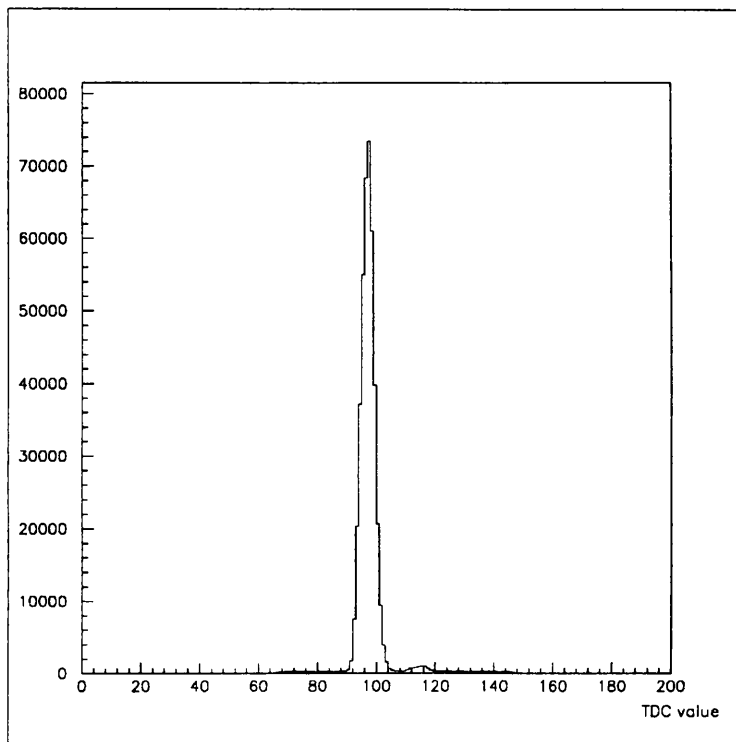


Figure 2.5: A typical TDC spectrum

is small as the DAPHNE experiment runs at a low electron beam current. Since the ladder signal comes much earlier than the trigger from DAPHNE, all signals from the ladder are delayed by 400 nsec before being fed to the TDC. The TDC is started by the DAPHNE electronics and stopped by its corresponding electron detector. The tagger electronics are controlled by a VME processor which itself is controlled by the VME processor in the data acquisition system of DAPHNE.

### 2.3.5 Photon Beam Collimator

The photon beam is collimated in order to produce an approximately circular well defined beamspot at the target. The collimator consists of a 5 mm diameter hole through 2 lead blocks each of thickness 50 mm and is situated 2.5 metres downstream from the radiator. The Bremsstrahlung, which is strongly forward peaked is contained within a cone about the electron direction of semi-angle

about 2 characteristic angles. With this collimation about 50% of the Bremsstrahlung photons pass through the collimator and reach the target. This effect is taken into account in the tagging efficiency discussed in section 2.3.7. The DAPHNE target is situated 8.2 metres from the radiator and the collimation produces a beamspot diameter of 17 mm.

### **2.3.6 Photon Beam and Electron Beam Monitoring**

A photon beam monitor (comprising an image intensifier and TV camera which views light from a piece of 3 mm thick BC430 plastic scintillator) is used for the initial alignment of the photon beam. The centre of the Bremsstrahlung photon cone should be aligned with the collimator axis to obtain maximum transmitted photon flux, best stability and optimum real to random ratio. The camera provides an image of the beamspot downstream of the photoreaction experiment. This gives an online image whilst adjustments to radiator position and alignments to direct the electron beam along the collimator axis are made. To monitor the stability of the beam position and direction the camera is viewed regularly throughout the experiment and realignment made when necessary.

The central vertex detector of DAPHNE is also used to monitor the photon beam. Events are selected from which the trajectories of two charged particle tracks can be determined, thereby allowing the accurate reconstruction of the reaction position. Although this offers no immediate online capability to monitor of the photon beam, it does allow the beam profile to be measured precisely, and enable a sensitive check for any beam halo to be made. An example of this vertex reconstruction is shown in figure 2.6. It is apparent there is a central core to the beam with a diameter of less than 4 mm surrounded by a halo which at

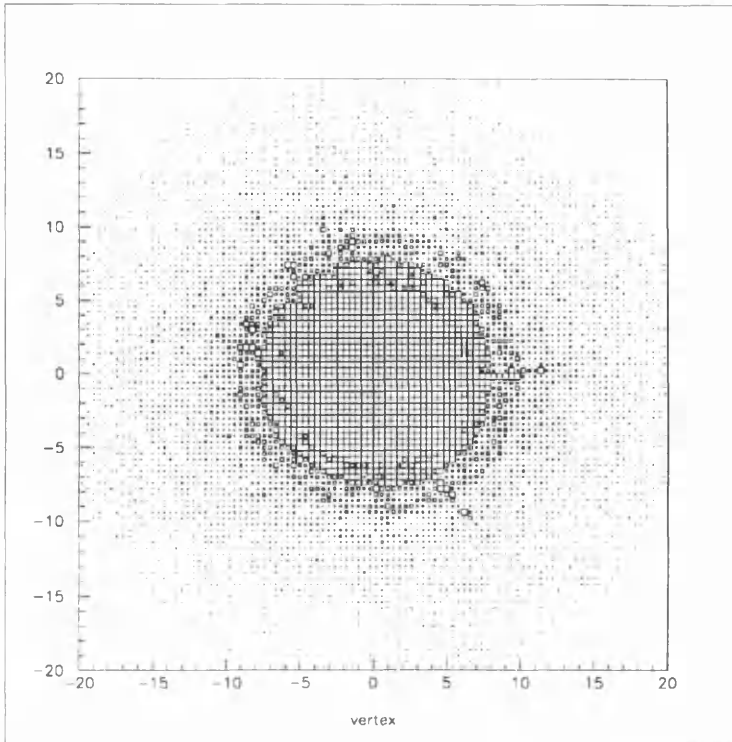


Figure 2.6: *Vertex reconstruction*

most extends out from the centre of the core by 8 mm. Since the deuterium target has a diameter of 20 mm it is clear the photon flux is completely contained within the target volume.

### 2.3.7 Photon Flux Normalisation / Tagging Efficiency

In a tagged photon experiment the determination of the total  $\gamma$  flux, relies on an accurate measurement of the tagging efficiency. The tagging efficiency,  $\epsilon_{tag}$ , is defined as the probability that a tagging electron detected in the focal plane detector has a corresponding Bremsstrahlung photon which has passed through the collimator and reached the target.

The value of  $\epsilon_{tag}$  is less than unity mainly due to the collimation of the photon beam and is almost independent of  $E_\gamma$ . Möller scattering, which can produce electron signals in the focal plane without any photon in the beam,

can also be responsible for a reduction in  $\epsilon_{tag}$  which does depend strongly on electron (and hence apparent photon) energy. However, its effect is negligible for the conditions of this experiment.

For each photon energy bin (for each tagger channel), the number of photons  $N_\gamma$  is obtained by counting the corresponding tagged electrons and correcting for the tagging efficiency.

$$N_\gamma = N_{elec.} \cdot \epsilon_{tag} \quad (2.2)$$

The actual value of  $\epsilon_{tag}$  is measured by placing a photon detector in the beam, and recording coincidences between this and the focal plane detector. Then the tagging efficiency for a particular ladder channel is:

$$\epsilon_{tag} = \frac{N_{coin}}{N_{elec}} \quad (2.3)$$

where  $N_{coinc}$  is coincidence rate between the photon detector and that ladder channel, and  $N_{elec}$  is number of electrons recorded by the free running scaler counting signals from that tagger channel. More exactly,  $N_{elec}$  is corrected for background, ie. the number of electrons detected by the free running scaler without the radiator in the beam. An example of tagging efficiency measurements for each ladder channel, ie. as a function of photon energy, is shown in figure 2.7.

These normalisation measurements were made frequently by introducing a lead glass Cerenkov detector into the photon beam. A very reduced current was necessary to avoid pile-up in the lead glass detector. In order to be able also to monitor  $\epsilon_{tag}$  during normal data taking, a low efficiency pair spectrometer was placed in the beam downstream of DAPHNE. This provides a continuous measurement of the photon flux and also allows the photon beam stability to be monitored.

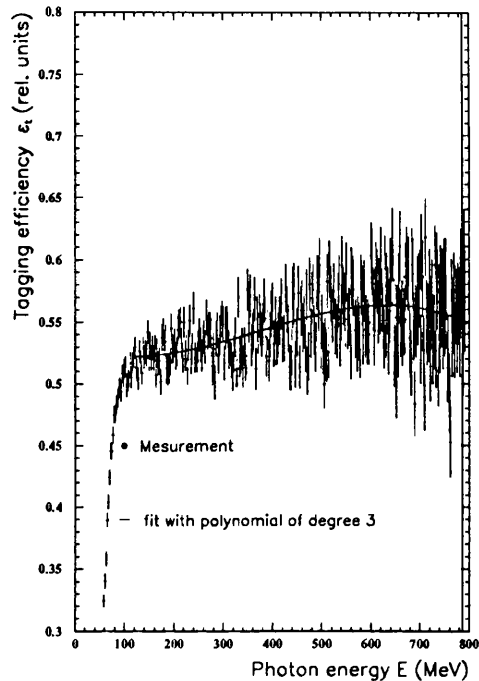


Figure 2.7: *Tagging efficiency measurement*

The lead glass (25 X 25 X 25 cm, ie. 30 radiation lengths) is large enough to totally absorb all photons in the energy range 42 to 792 MeV incident upon it and was therefore considered to be 100% efficient. This was checked by observing its pulse height spectrum which was found to have good separation from any noise, therefore a threshold could be applied without fear of losing photon signals. At the low intensities used, both the singles rate in the focal plane detector without radiator and the number of random coincidences between the focal plane and the lead glass were negligible.

The pair spectrometer comprises a radiator followed by 2 thin scintillators separated by an absorption layer to reduce coincidences due to very low energy untagged photons. It is shown in figure 2.8. A third scintillator placed before the radiator operates in anticoincidence and serves as a veto of the electromagnetic background produced inside the DAPHNE target. The efficiency of the pair detector was then calibrated relative to the lead glass and as can be seen in

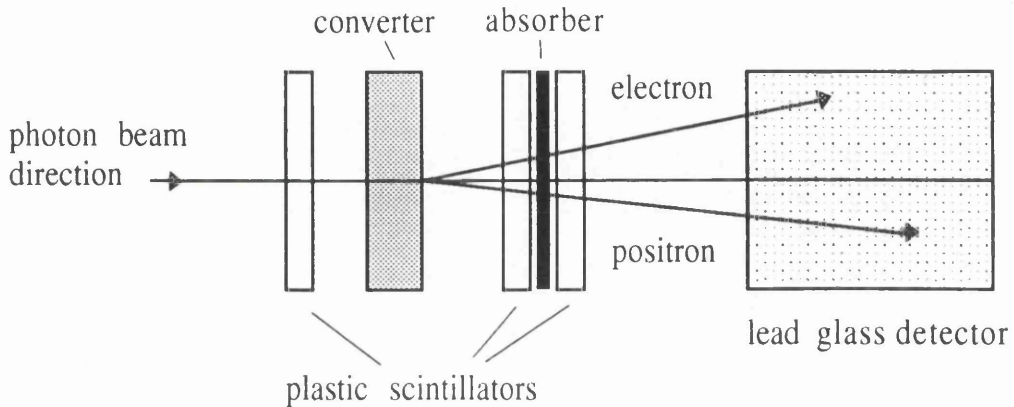
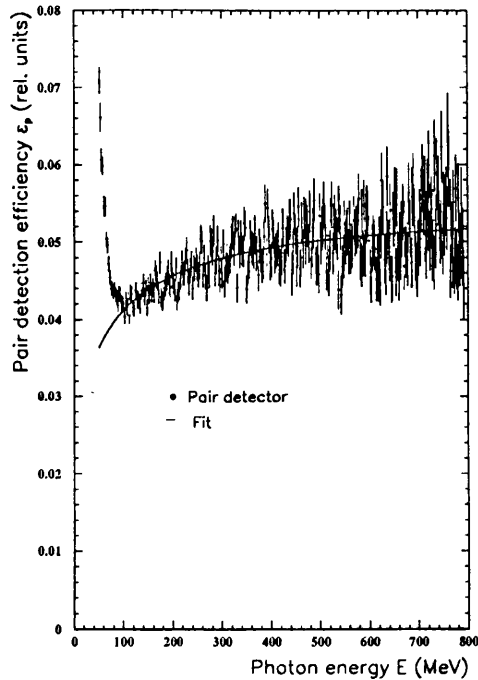
Figure 2.8: *The Pair Detector*

figure 2.9 was found to be  $\sim 5\%$ . This efficiency was assumed to be independent of beam current. The absolute normalisation uncertainty is estimated to be less than 3%. To calculate  $\epsilon_{tag}$  during each run, the number of coincidences is counted between the pair spectrometer and 8 of the tagger channels which sample the whole tagged range, and a best fit made.

Random contributions to the pair detector/tagger coincidence rate must be evaluated and corrected for. Also multiple counts in the tagger due to an electron which undergoes multiple scattering in one ladder detector and then fires additional detectors artificially increases the number of electrons recorded by the scalers. This effect is discussed more fully in section 4.6.4.

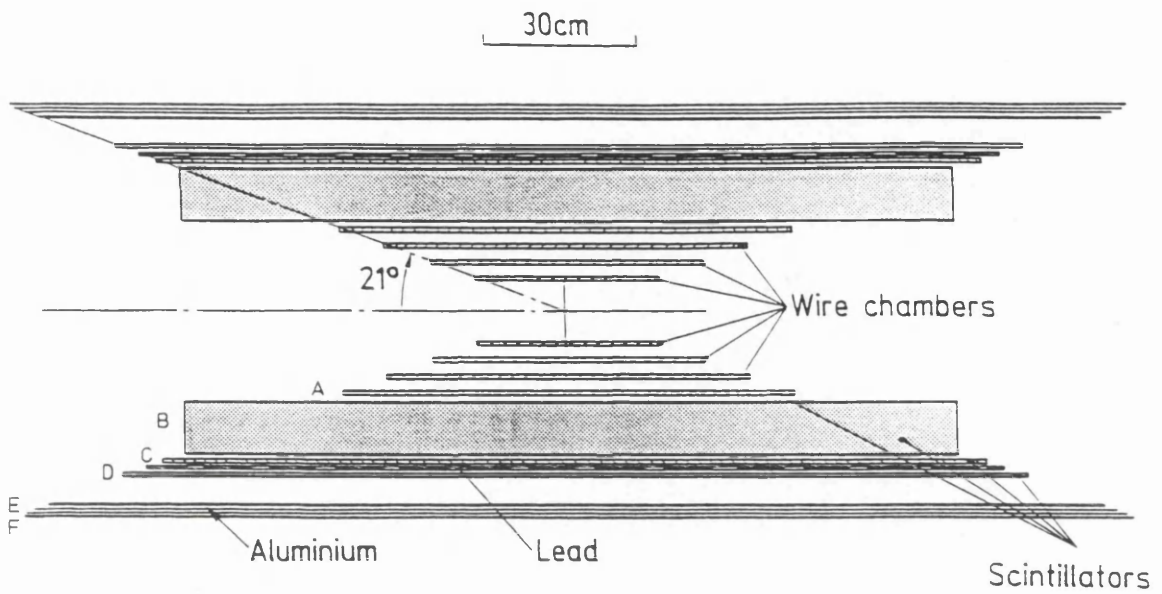
Figure 2.9: *Pair Detector efficiency*

## 2.4 The DAPHNE Detector

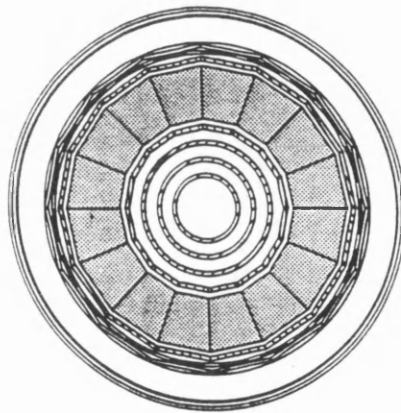
### 2.4.1 General Layout

The DAPHNE (Detecteur a grande Acceptance pour la physique PHoto-Nucleaire Experimentale) detector, which has been developed by the INFN - sezione di Pavia and the CEA-SPhN of Saclay, is a large solid angle detector ( $3.7\pi$  steradians) for tracking charged particles. Figure 2.10 shows a planar and a transverse view of the detector. Figure 2.11 shows an overall view of DAPHNE.

DAPHNE was built in order to study a variety of photonuclear reactions involving light nuclei. Hence, it is well suited for investigating the properties of baryon resonances and for several experiments which aim to examine different components of the nuclear force over a wide range in energies. The principal requirements and considerations that led to the DAPHNE design were:



longitudinal view of DAPHNE



transverse view of DAPHNE

Figure 2.10: *Planar and transverse views of DAPHNE*

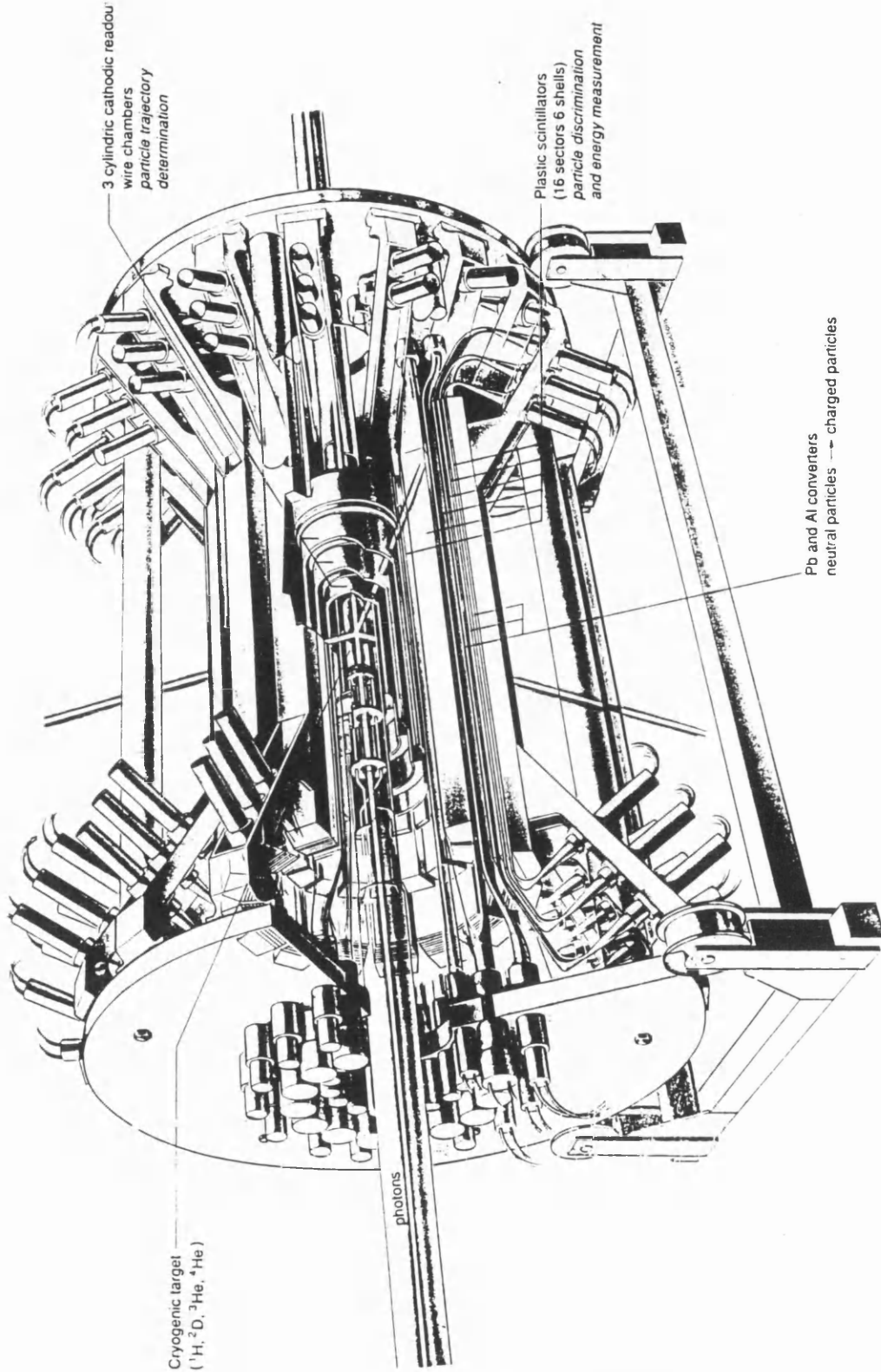


Figure 2.11: Overall view of DAPHNE

- i) very large angular and momentum acceptance,
- ii) good particle identification,
- iii) precise measurement of charged particle angles,
- iv) segmentation to allow final states with particle multiplicity up to 5 to be detected without ambiguity,
- v) good trigger selectivity.

In addition, it was desirable that it should also provide moderate neutral particle detection efficiency with some momentum resolution.

The philosophy of the DAPHNE design is to use the accurate angular information from the tracking detectors to reconstruct the kinematics of the detected reaction products without the need to rely heavily on the pulse height information from its plastic scintillators. Direct measurement of the particle energies is not of primary importance and the principal function of the scintillators is the identification and separation of charged particles by means of  $dE/dx$  energy loss measurement.

The main characteristics and performance of the detecting system are summarized below. Its components are:

- A 270 mm long cryogenic target

The cryogenic target is a 270 mm long thin walled Mylar cylinder, 43 mm in diameter placed coaxially with the beam. It can be filled with liquid hydrogen, deuterium,  $^3\text{He}$  and  $^4\text{He}$ .

- A central vertex detector

This consists of 3 coaxial cylindrical multiwire proportional chambers with anode wire and cathode strip readout. The wire chambers are devoted to charged particle tracking and by giving a position resolution of better than 0.5 mm provide good angular definition.

– **A segmented cylindrical calorimeter**

The vertex detector is surrounded by 3 segmented cylindrical layers for charged particle identification and energy measurement. The telescope consists of plastic scintillator layers of thickness 10 mm (A layer), 100 mm (B layer) and 5 mm (C layer) and each comprises 16 azimuthal segments. The 10 cm thick B layer has also a useful efficiency for the detection of neutrons. The light produced when a particle releases energy in the scintillators is detected by photomultiplier tubes at each end of the layers (except for the case of the A layer which due to restrictions in space is read only at one end). The two TDC's allow a crude position determination by time difference between the signals from each end. The scintillator layers have light guides to ensure uniform light collection close to each end, and optimise pulse height and timing resolution.

– **A scintillator - absorber sandwich**

The outer layers form a lead-aluminium-scintillator sandwich designed to enhance the detection efficiency for  $\pi^0$ 's which decay by 2 photon emission. The 16-fold azimuthal segmentation is continued in the layers of lead, scintillator (D layer), lead, scintillator (E layer), aluminium and finally scintillator (F layer). Like the B and C layers the D E and F scintillators are read out at both ends.

The main features of DAPHNE are summarized in table 2.3. The coverage of the azimuthal angle is complete and the polar angular range is  $21^\circ$ – $159^\circ$ :

ANGULAR ACCEPTANCE		
94% of $4\pi$ :		
Polar angle:	$21^\circ < \theta < 159^\circ$	
Azimuthal angle:	$0^\circ < \phi < 360^\circ$	
CHARGED PARTICLE DETECTION THRESHOLDS		
Pions:	T = 12 MeV	(p = 60 MeV/c)
Protons:	T = 23 MeV	(p = 220 MeV/c)
MAX ENERGY OF PARTICLES STOPPED IN THE SCINTILLATORS (A,B,C)		
Pions		
$\theta=90^\circ$ :	T = 23 MeV	(p = 138 MeV/c)
$\theta=21^\circ$ :	T = 120 MeV	(p = 219 MeV/c)
Protons		
$\theta=90^\circ$ :	T = 125 MeV	(p = 500 MeV/c)
$\theta=21^\circ$ :	T = 225 MeV	(p = 688 MeV/c)
NEUTRAL PARTICLE DETECTION EFFICIENCIES		
Photons (70 MeV)	Neutrons	
$\theta=90^\circ$	$\epsilon=46\%$	$\epsilon=10\%$
$\theta=21^\circ$	$\epsilon=82\%$	$\epsilon=30\%$
Neutral Pions	(two $\gamma$ 's detected)	$\epsilon \sim 20\%$

Table 2.3: *Principal characteristics of DAPHNE*

thus the solid angle is ( $3.7\pi$  steradians). A complete description of DAPHNE is given in [43].

## 2.4.2 The Wire Chambers and Track Reconstruction

### General Characteristics

The vertex detector is designed for charged particle tracking. It consists of three cylindrical multiwire chambers (MWPC) having 192, 288 and 354 wires at radii of 64, 96, and 128 mm respectively. The transverse and longitudinal views of a chamber are shown in figure 2.12.

Each chamber itself comprises 3 cylindrical shapes. The central is formed by the  $20\mu\text{m}$  diameter tungsten anode wires which lie parallel to the axis of the chamber. The inner and outer are formed by the cathode strips. The characteristics of each of the 3 chambers are listed in table 2.4. This arrangement gives an anode interwire spacing of 2 mm, thus the presence of an anode wire signal provides the azimuthal angle for a track. The excellent position resolution is achieved from the analogue read out signals from the cathode strips. The inner and outer cathode strips are wound helically at  $+45^\circ$  and  $-45^\circ$  to the chamber axis respectively. The distance between the strips is 0.5 mm. The anode to cathode gap is 4 mm. The gas medium is of argon (74.5%), ethane (25%) and freon (0.5%) at about 1 atmosphere.

### Impact Point Reconstruction

Charged particle tracks fire clusters of neighbouring strips and so the mean strip position in such a cluster must be determined. The impact point is defined by the centre of gravity of the analogue signals from the cathode strips. From the intersection of the inner and outer helically wound cathode strips the azimuthal angle and the z coordinate along the chamber axis are both determined, as

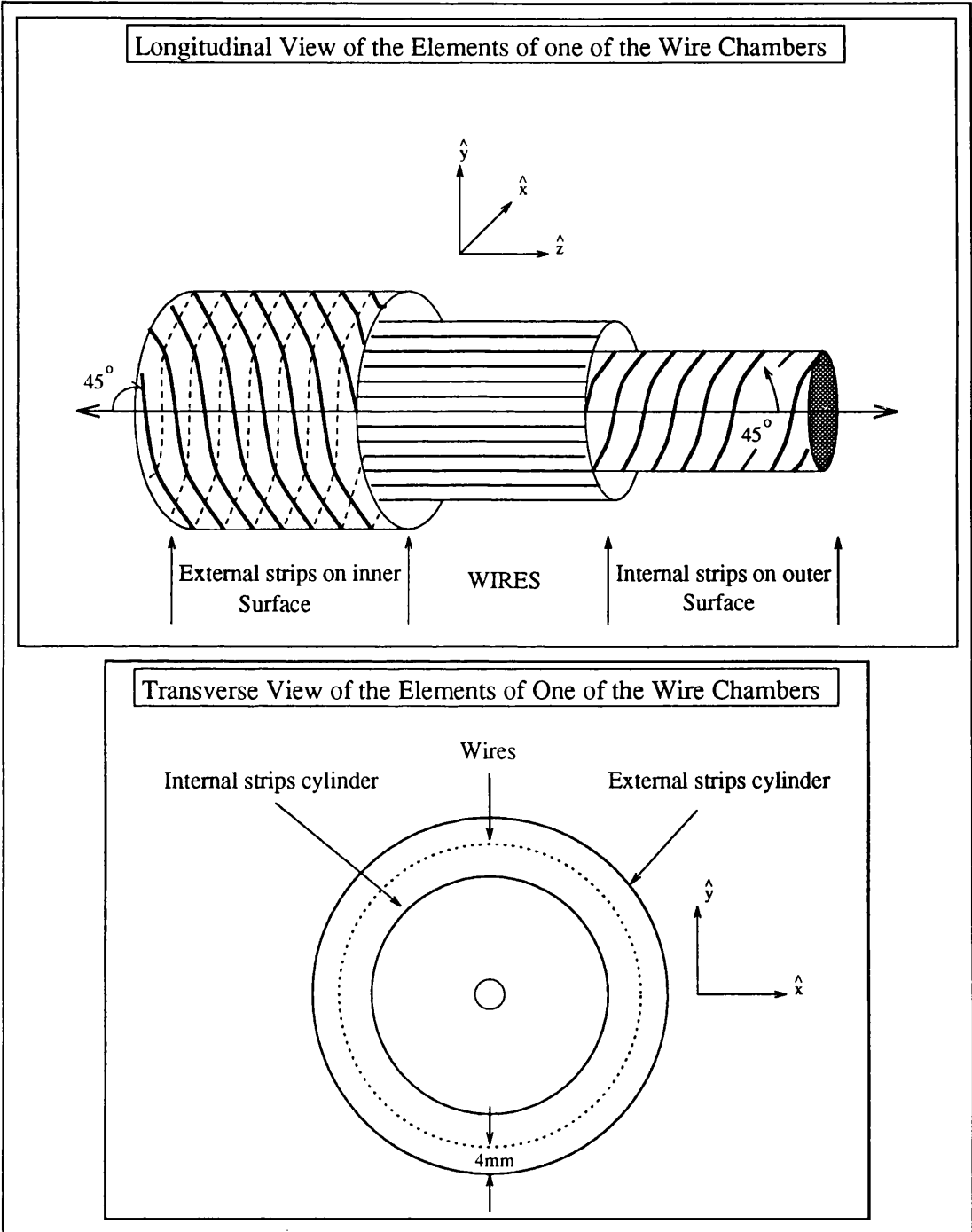


Figure 2.12: *The transverse and longitudinal views of a wire chamber*

	CH 1	CH 2	CH 3
Length (mm)	370	570	770
Int radius (mm)	60	92	124
Ext radius (mm)	68	100	132
No. of wires	192	288	384
No. of int strips	60	92	124
No. of ext strips	68	100	132
wires- int strips gap(mm)	4	4	4
wires- ext strips gap(mm)	4	4	4

Table 2.4: *The characteristics of the 3 MWPC chambers*

shown in figure 2.13.

In some instances there may be two intersections for a particular pair of cathode strips. This ambiguity is resolved and the correct solution is determined by using the separate determination of azimuthal angle provided by the anode wires. That is:

$$\phi_F = 2\pi \cdot \frac{\text{no. identifying wire fired} - 1}{\text{total no. of wires of the chamber}} \quad (2.4)$$

where wire number one is defined along the x axis. An example of the two possible impact points, and the resolution of the ambiguity is shown in figure 2.14. When there is more than one particle all possible intersections are determined and compared to all the azimuthal angles from the wires.

## Track Reconstruction

The general procedure for track reconstruction of charged particles is now described. For each A layer sector that has fired a search is made for a triplet



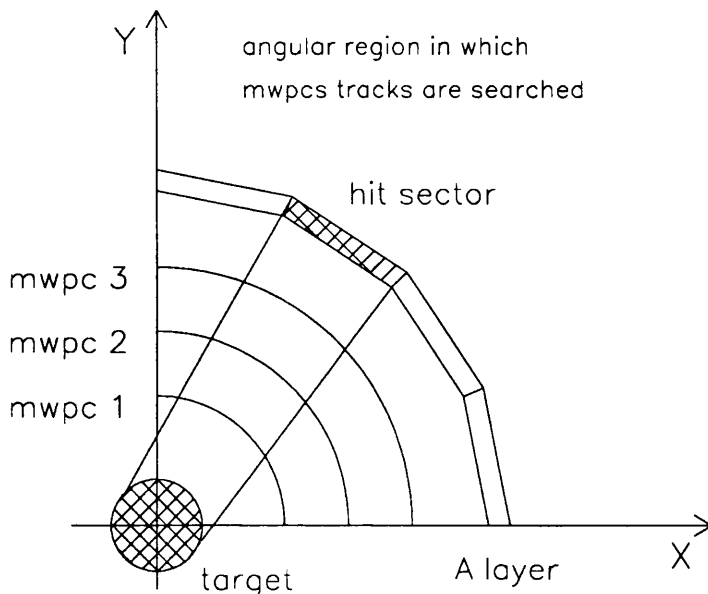


Figure 2.15: *Angular region in which MWPC's are searched*

of reconstructed points, one on each of the MWPC's, that form a line that intercepts the target and the A layer sector. Figure 2.15 shows the MWPC angular region, in the XY plane, covered by particles coming from the target. This region is checked to see if there is at least one reconstructed point on each MWPC.

The 3 MWPC points of such a triplet in this a region form a triangle as shown in figure 2.16. The cosine of the angle  $\beta$  is calculated and if  $\cos 172^\circ > \cos \beta > -1$ , the triplet is assumed to come from the same physical trajectory.

## Experimental Position Resolutions

The error on the longitudinal coordinate is calculated using a formula derived experimentally from cosmic ray tests. Cosmic rays intersect each of the chambers twice providing six points, to five of which a line is fitted. Solving the

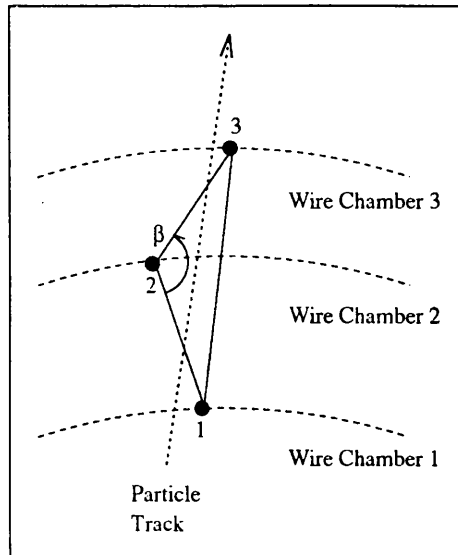


Figure 2.16: *Triangle formed by the 3 MWPC points*

resulting equation for the sixth point provides a measure of the longitudinal position error,  $\Delta z$ , through the difference between experimental and fitted points.

Figure 2.17 shows the variation of longitudinal position resolution with charged particle polar angle. It can be seen that it is very precise at  $90^\circ$  where the position resolution (FWHM) is  $255 \mu\text{m}$ . This deteriorates at more extreme angles but it remains better than 1 mm over most of the polar angle range. The resulting polar angular resolution is shown in figure 2.18.

Cosmic ray tracks were also used to determine the azimuthal resolution, the discrete wire spacing results in an uncertainty of  $\Delta\phi=2^\circ$ .

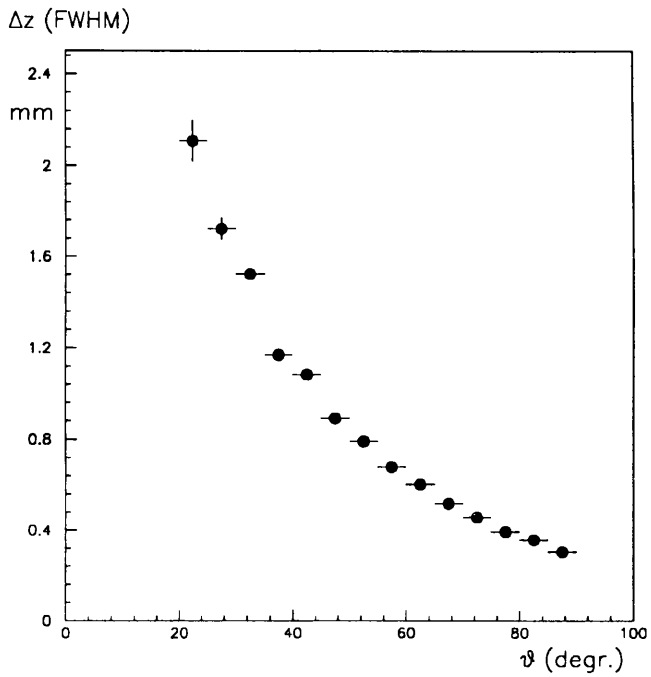


Figure 2.17: *The variation of longitudinal position resolution with  $\theta$*

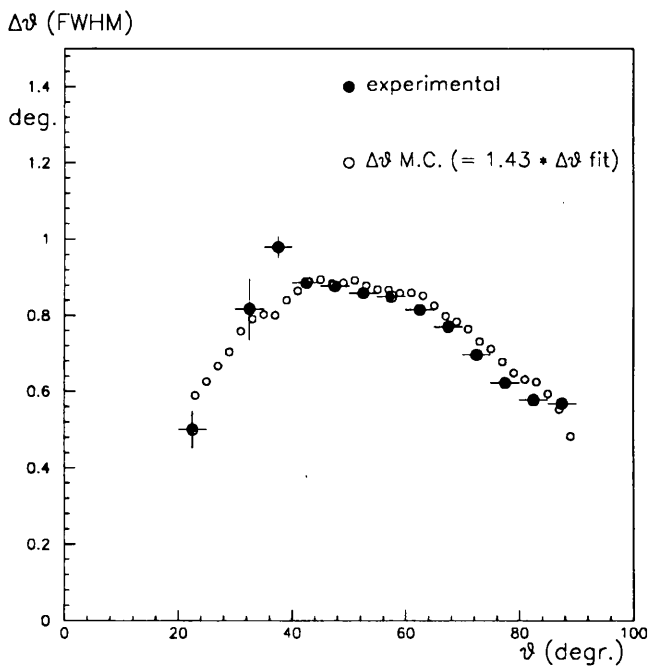


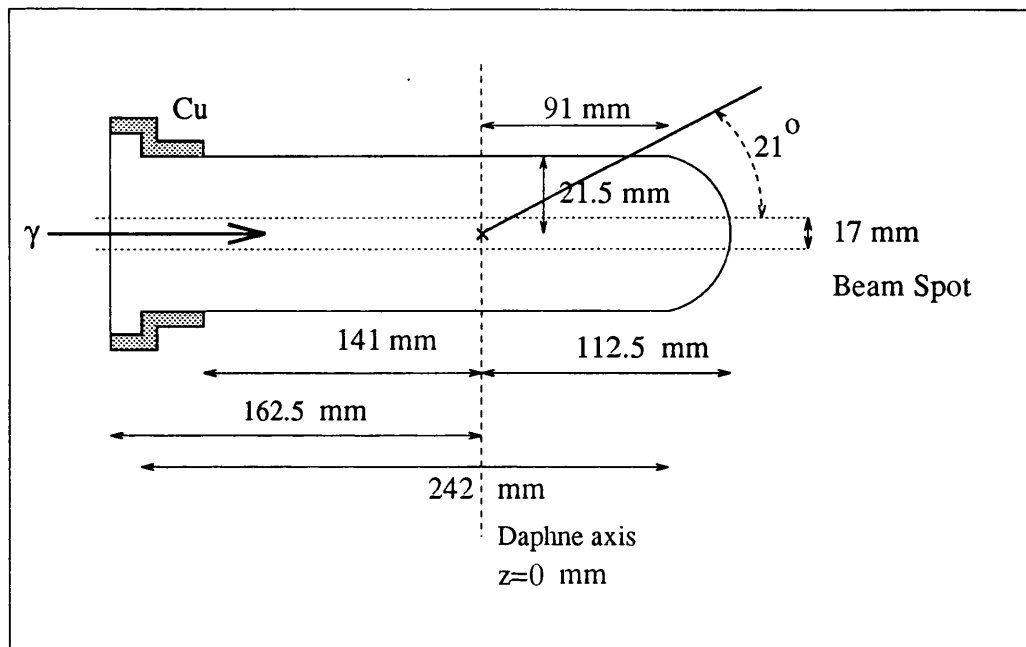
Figure 2.18: *Polar angular resolution*

### 2.4.3 The A B C D E F Scintillator Layers

Although the A,B,C scintillators (thicknesses 10,100 and 5 mm respectively), are principally used to identify and separate charged particles by means of  $dE/dx$  determinations, they also provide energy information with a modest resolution and within a limited energy range. In addition the B layer provides a modest but useful neutron detection capability although with no energy determination and poor angular resolution (a polar angle can be calculated from the TDC time difference signals and a rough azimuthal determined from the 16-fold segmentation).

After the C layer is the outer lead - scintillator - aluminium sandwich, which is designed for  $\pi^0$  detection. It comprises a 6 mm layer of lead, 5 mm of scintillator (D layer), lead, 5 mm of scintillator (E layer), 6 mm aluminium and finally 5 mm of scintillator (F layer). Since the  $\pi^0$  has a lifetime of  $8.7 \cdot 10^{-17}$ s it decays into two photons effectively at its point of production. On reaching the lead layers the two photons can form electron-positron pairs which are subsequently detected in the outer scintillator layers. The efficiency for detecting a single photon from the  $\pi^0$  decay is about 40%. The 16-fold segmentation provides crude azimuthal information for the neutral particles.

The results of an analysis of cosmic ray data were used in matching the gains of the sectors of each scintillating layer, a cosmic event being classified as opposite sectors firing and no tagger coincidence. The gains of the photomultiplier tubes were monitored throughout the runs and were found to drift randomly over a period of a few days by approximately 10%. This was investigated and run-by-run correction factors for gain stability obtained which were applied to the data during analysis.

Figure 2.19: *The Target Cell*

#### 2.4.4 The Cryogenic Target

The cryogenic target consists of a long thin walled Mylar cylinder, 270 mm in length and 43 mm in diameter and is shown in figure 2.19. It is situated on the axis of the wire chambers (coaxially with the beamline) and is surrounded by vacuum. The target can be filled with liquid hydrogen, deuterium, Helium-3 and Helium-4. The refrigeration system comprises two stages, a Gifford MacMahon refrigerator coupled to a Joule - Thomson valve and can reach temperatures below 2.8 K. Liquefaction for each target is achieved through one (H, D, He-4) or both (He-3) stages. The Gifford MacMahon standard commercial refrigerator cools to 17 K by thermal exchange with gaseous Helium-4 pumped throughout the system. Further cooling is achieved by the Joule - Thomson valve which comprises a small aperture through which the gas flows. The molecules of the gas lose kinetic energy in expanding through the aperture and a drop in

temperature is observed provided the system is below its inversion temperature. An automatic control system monitored and regulated the target temperature and pressure and these were kept constant to 10 mK and  $< 1$  mbar respectively. The target density was stable to the order of 0.5%.

### 2.4.5 Electronics and Event Triggers

The analogue pulse from each separate photomultiplier is sent to a dedicated ADC and TDC. The TDC has been started by the A layer and is stopped by the pulse from the photomultiplier. The pulse is also sent to the logic circuitry which decides the types of events to be recorded. Various event triggers can be formed and used to test for a coincidence with a tagger channel. The ADC's and TDC's are only recorded if there is a coincidence with the tagger, otherwise a fast clear signal is generated and clears the ADC's and TDC's before they are read out. DAPHNE is used with various light nuclei targets and different triggers depending on whether an exclusive channel or total photodisintegration is being studied. Single or multiple charged particle triggers are formed by a coincidence between the A ( $\Delta E$ ) and B (E) layers signals. A more sophisticated charged particle trigger can be formed reducing pion and/or electron contamination by the choice of an appropriate electronic threshold. Electromagnetic cross sections are high relative to photonuclear cross sections so DAPHNE sees not only photoreaction products but also a large number of electrons produced by photons interacting with atomic electrons (in the target walls etc). The on-line electron/pion reject allows the fraction of data taking on the channel of interest to be maximised and computer dead time to be kept minimal. Neutral particle triggers are also available and might be, for example, signals coming from only the outer layers after the lead converter, signalling a neutral pion.

The ADC's and TDC's convert the analogue pulse height and timing information into a digital form which is recorded by the data acquisition system if the event has a coincidence with the tagger.

### 2.4.6 Data Acquisition

The DAPHNE data acquisition system comprises VME and CAMAC systems. The VME computer controls the electronic modules and provides the coupling between DAPHNE and the tagger. In order to minimize dead time when reading out a DAPHNE event only the CAMAC modules containing a recorded event are read. The information from the CAMAC crates are read out on FERA (Fast Encoding and Readout ADC's). This information is then transferred to one of two buffer memories HSM1 (High Speed Memory 1) and HSM2, one of which is read out while the other is being filled. The raw data for each event are finally written to exabyte magnetic tape. Some online analysis is displayed on a SUN workstation enabling a check on the overall features of the data.

The relatively large intensity of lower energy photons present in the Bremsstrahlung spectrum generates undesirable forward peaked background in the wire chambers. This unwanted component to the interrupt rate sets a limit on the photon beam intensity if saturation of the wire chambers is to be avoided. Furthermore, since a typical event in DAPHNE involves reading on average 2000 ADC's and TDC's the ensuing dead time for each event imposes a severe restriction on the counting rate. The tagged photon beam intensity is set taking consideration of these restrictions, and is dependent on the event trigger used and the magnitudes of cross sections under study. In this measurement the beam current was 1.2nA, corresponding to  $10^6$  photons/sec over the tagged

photon energy range. This limited the data acquisition rate to  $\sim 125$  events/sec giving a deadtime of  $\sim 25\%$ .

## **Chapter 3**

# **Energy Calibrations and Particle Identifications**

### 3.1 Introduction

This chapter describes the way in which the proton energy calibration of DAPHNE was established and provides a general discussion of the techniques used to identify and separate protons from other particles detected in DAPHNE. The ways in which these techniques were used to separate protons from the  $D(\gamma,p)n$  reaction from the often overwhelming background of pions and protons from other reactions are presented in the following chapter. The Monte Carlo GEANT simulation of the detector response, which can be used to provide corrections for events lost during the analysis, for example, during particle identification, is discussed.

### 3.2 Energy Calibration of the Scintillators

The calibration of the correspondence between energy deposited in the scintillator layers in MeV and the resulting ADC signals from the scintillators was accomplished [44] by exploiting the fully determined kinematics of various 2-body breakup channels, that is, of  $H(\gamma,\pi^+)n$ ,  $H(\gamma,p)\pi^0$ , and  $D(\gamma,p)n$ . Using the accurate knowledge available of photon energy  $E_\gamma$ , provided by the tagger, and of the polar angle  $\theta_p$ , from DAPHNE's wire chambers, these reactions provide protons and pions entering DAPHNE whose total energies can be calculated reliably.

For each particle, the expected energy loss in each of the DAPHNE layers was then calculated and a plot of this energy loss against the experimentally observed ADC value made. An example of a calibration graph for one of the B scintillators, for a calibration using protons and for a calibration using pions, is

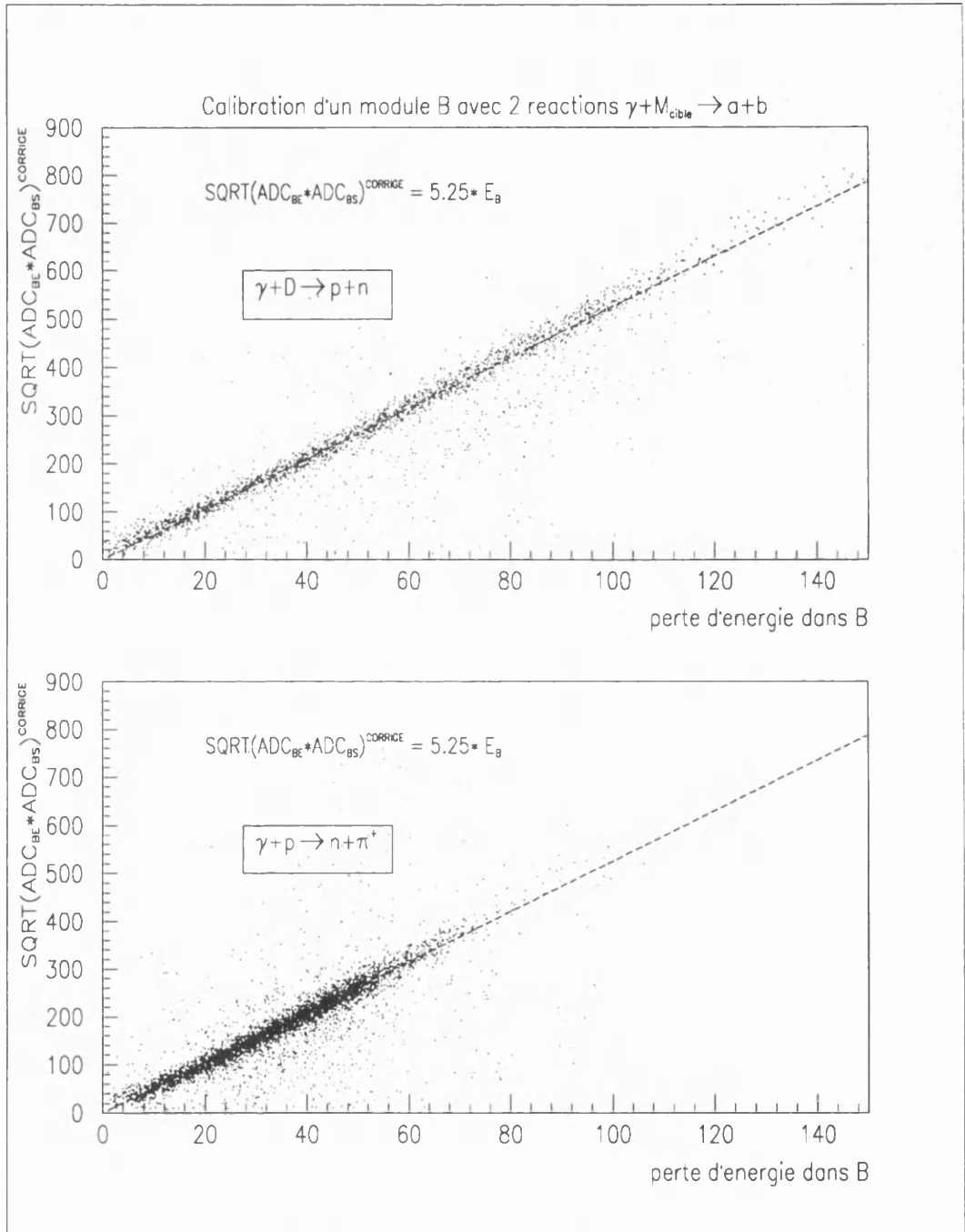


Figure 3.1: Calibration of one of the B layer scintillators

shown in figure 3.1. Allowances were made for the energy losses in the material traversed by the particle before reaching the layer, for the B layer, that is, the target, wire chambers and the A layer. The graph passes through the origin, this gives an experimental verification that this thickness is known. For protons, the scintillator light output is not strictly a linear response to energy loss and a correction has been made to allow for this non-linearity.

The relationship between ADC signal and energy loss is further complicated as the signal arriving at a photomultiplier tube depends on where along the length of the scintillator the light is produced. This is due to the attenuation of the light in the scintillator and reflection at its surfaces. Attenuation coefficients for each scintillator sector in each of the layers were determined using cosmic rays and used to correct the ADC values. The geometrical mean of the two ADCs connected to the opposite ends of each scintillator was taken in order to reduce this position dependence. The correlation shown in figure 3.1, is that obtained after removing the remaining position dependence. On the y-axis the corrected geometrical mean is plotted and along the x-axis the theoretical energy loss in the B scintillator in MeV electron equivalent.

The data were then fitted to a linear function and this used for calibration. The separate calibrations shown, using the pion and proton events which stop in the B layer, agree well, and this validates the function used to predict the effects of non-linear response of NE102 scintillator to protons.

### **3.3 Particle Identification**

Several different techniques for particle identification have been developed to cope with particles of all energies. These can be applied to events in which the

charged particles stop in any of DAPHNE's 6 scintillator layers or pass through the whole of the detector.

Particles are identified by observing their energy loss in the various detector layers. This can be predicted using the Bethe-Bloch formula, or in its integrated form, the Range-Energy relationship. The rate of energy loss in material for charged particles is dependent on the particle mass, and by comparing the measured energy losses with those predicted, particle separation, for example between pions and protons, can be made. At higher energy these energy loss identifications become more problematic as the particles deposit less energy, and the effects of hadronic interactions, which degrade the identifying information, are greater. In addition, relativistic protons and pions have energy losses not different by much more than the scintillator resolution.

The main requirement of this analysis is that of separating protons from pions. Two methods are used to do this. In the first, over a series of limited photon energy ranges, different particle types can be successfully identified by using the appropriate plot of two quantities derived from the measured energy losses. Two examples are given below in section 3.3.1. A Range Method analysis [45] described in section 3.3.2 provides a more elegant and versatile particle identification and particle energy determination and can be used over a wide energy range.

### **3.3.1 Particle Discrimination using Plots of $dE/dx$ Loci**

At lower photon energies for events that stop in B layer particle discrimination is at its most straightforward. Protons and pions are unambiguously separated using energy loss information from the A and B layer signals in the standard

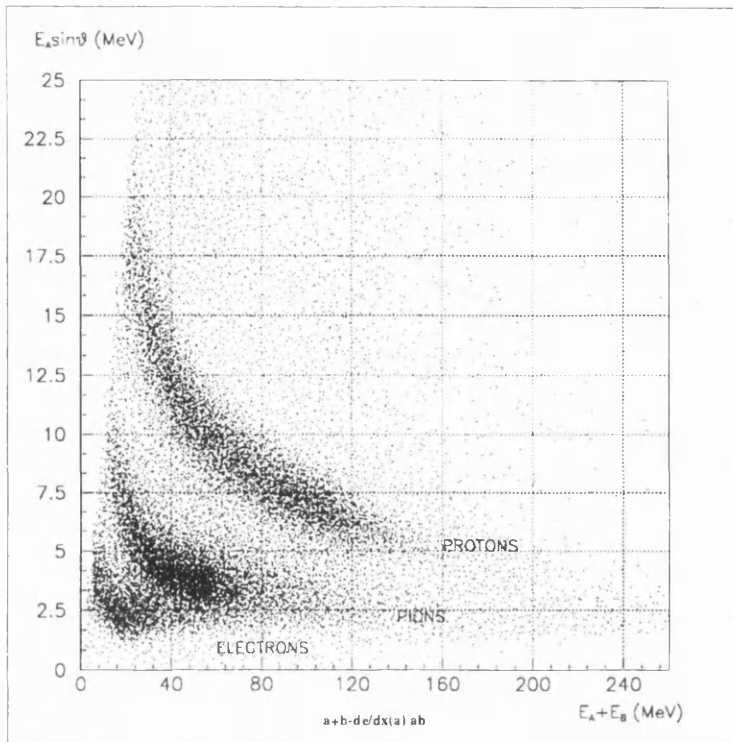


Figure 3.2: Particle identification stop B layer events

way. Figure 3.2 shows a typical scatter plot of  $E_A + E_B$ , the sum of the energies deposited in A and B, against  $E_A \sin \theta$  (the energy calibrations for A and B are those described in section 3.2 and the polar angle  $\theta$  is determined using the techniques in section 2.4.2 of the previous chapter). The quantity  $E_A \sin \theta$  is plotted along the y-axis to represent the  $dE/dx$  signal in the A layer, i.e. the signal which would have been produced had the particle passed normally through the layer. There are two well defined concentrations of events, which are cleanly identified as being either protons or pions. A loose proton ridge cut is applied to the data at this stage of the analysis.

Particle discrimination becomes more difficult for higher energy particles which pass through the B layer depositing less energy in the scintillators. However, another plot is generally useful in separating protons from pions. For each of the outer layers, if the thickness of the material traversed by the particle (obtained from a knowledge of the layer in which the particle has stopped and

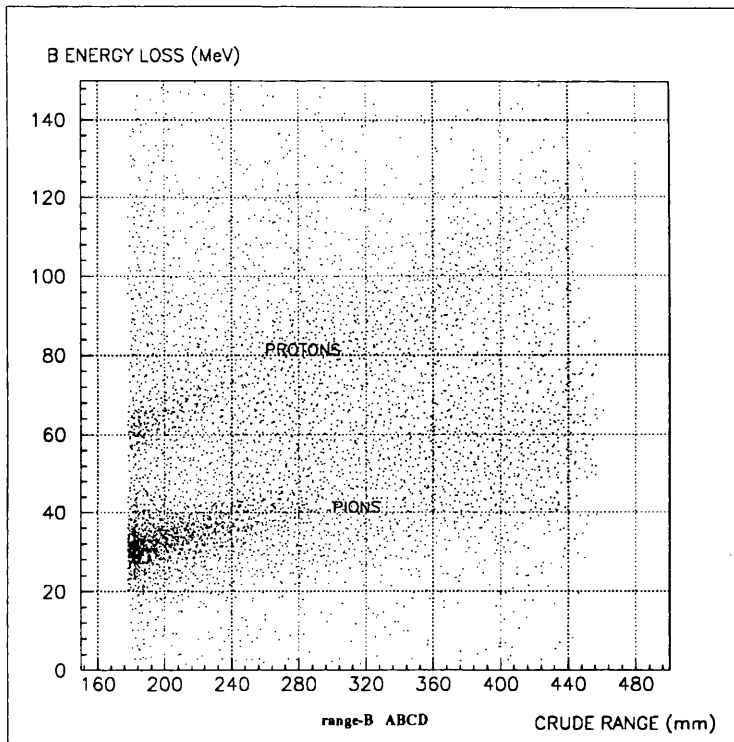


Figure 3.3: *Particle identification D layer*

its polar angle) is expressed in terms of equivalent plastic scintillator, a separation is possible from a plot of the energy loss information from the B layer signal against this thickness. In figure 3.3, for particles stopping in the D layer, the B signal (representing an energy loss) is plotted along the vertical axis, and the approximate thickness of material in the particle path (representing a crude estimate of range, ie a quantity related to the energy of the particle) is plotted along the horizontal axis. Separate concentrations of events are identifiable and there is a reasonable separation on which a loose cut can be based.

### 3.3.2 The Range Method

The Range Method extends the range over which particle identification and energy determination can be accomplished easily to much higher energies. It is more successful than the methods described in 3.3.1 in discriminating particle type and determining particle energy for the momentum range 300 - 900 MeV/c.

The important feature of the method is its simultaneous use of all the experimentally measured energy losses for each incident particles path. This information can be used to obtain several points on a graph of rate of energy loss,  $dE/dx$ , versus distance travelled for each incident particle. As shown in figure 3.4, the shape of this curve obtained from the Bethe-Bloch equation depends on both the particle type and its initial energy. Comparison with the measured data therefore allows protons to be separated from pions and also gives an estimate of their initial energy.

The procedure for determining the particle type and energy for each event is based on a goodness-of-fit ( $\chi^2$ ) minimisation routine. Using the angle information from the wire chambers the thickness of each layer in DAPHNE traversed by the particle is calculated. For each traversed scintillator layer of the detector the mean value of  $dE/dx$  is calculated (energy released/path inside the layer) together with the corresponding distances along the particles path. First assuming that the particle is a proton an approximate value for its initial energy  $E_o$  is obtained from its range in DAPHNE. Using this energy the theoretical specific energy losses for a proton at each position along its track are calculated from the Bethe-Bloch equation and used to predict the energy loss,  $\Delta E_i$ , in each of the scintillators layers. A goodness-of-fit  $\chi_p^2$  for this hypothesis (proton of energy  $E_o$ ) is then obtained:

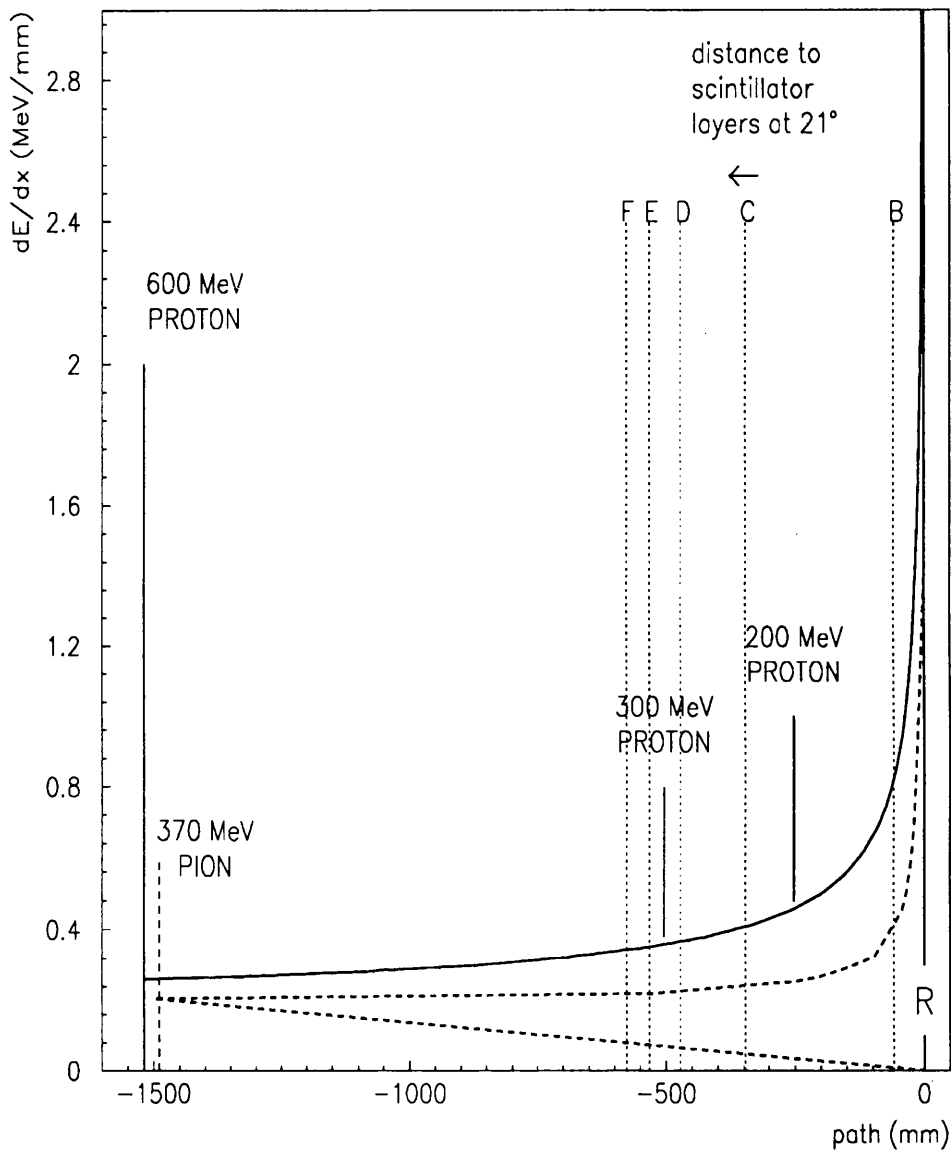


Figure 3.4: Rate of energy loss versus range for protons and pions in plastic scintillator

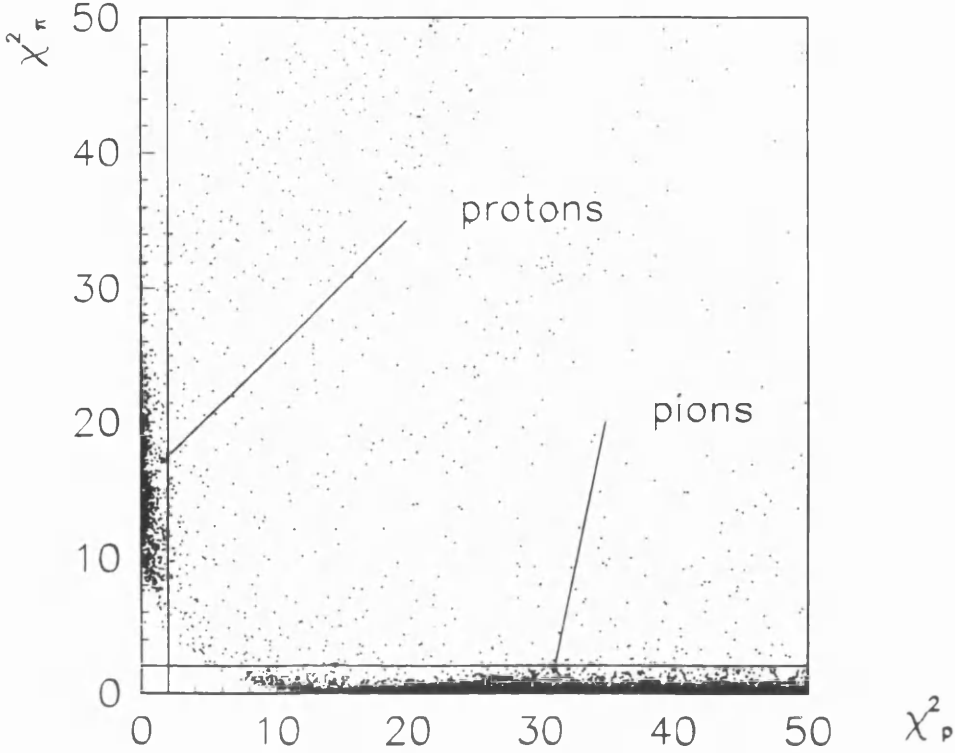


Figure 3.5: Example of Range Method fit for typical sample of events

$$\chi^2 = \frac{1}{N-1} \sum_{i=1}^N \frac{|\Delta E_i - \Delta E_i^{exp}|^2}{\sigma_i^2} \quad (3.1)$$

from the difference between the predicted,  $\Delta E_i$ , and the measured energy losses,  $\Delta E_i^{exp}$ , where  $\sigma_i$  is the resolution of the measured loss in the  $i^{th}$  scintillator layer. The predicted scintillator output signals are corrected to take account of quenching, the non-linear response of scintillators to protons. The initial energy is then allowed to vary in order to minimise  $\chi^2_p$  and determine the most probable incident proton energy. The minimisation is then repeated for the hypothesis that the incident particle was a pion and the best fit  $\chi^2_\pi$  is determined (no quenching correction is needed for pions). The  $\chi^2$  values for the two fits can then be used to distinguish between protons and pions. Figure 3.5 shows the distribution of the two  $\chi^2$  values obtained for a typical sample of events; the regions corresponding to good protons and good pions are indicated. The large majority of events have an acceptable  $\chi^2$  for one hypothesis (proton or pion)

but not for the other. Only a small fraction of events fails the Range Method analysis with large values for  $\chi_p^2$  and  $\chi_\pi^2$ . A limit is set on the acceptable  $\chi_p^2$  for a proton, and the Monte Carlo code GEANT used to calculate efficiencies to correct for events lost in the identification due to hadronic interactions or multiple scattering moving a particle outside the pion and proton regions.

Within the momentum range 300 - 900 MeV/c, the proton momentum reconstruction has a resolution  $\Delta P/P = 2.5 - 10 \%$ , and the pion contamination amongst events identified as protons has been found to be less than 1% of true pions. For higher energy protons the energy losses in the DAPHNE layers are lower, not very different from pion energy losses and the Range Method does not work as well. More pions are wrongly identified as protons (and vice versa) and more particles fail the analysis with large values of  $\chi_p^2$  and  $\chi_\pi^2$ . A quantitative limit for the acceptable use of the Range Method for identifying protons was worked out by using it to analyse particles known to be pions from the  $p(\gamma, \pi^+)n$  reaction. These particles were assumed to be protons and an upper limit on reconstructed momentum was found above which more than 0.5% of the pions were accepted as protons. The maximum momentum depended on polar angle (path length) in DAPHNE according to:

$$P_{max}(MeV/c) = 810 + \frac{(\theta - 90)^2}{40} \quad (3.2)$$

For particles of higher momenta the Range Method can still be used but extra cuts are needed to reject pions without reducing the proton detection efficiency.

A more detailed discussion of the Range Method has been published in [45] and this is reproduced in Appendix A.

### 3.4 The GEANT Simulation

A Monte Carlo simulation of detector response was made using the GEANT code [46] in order to understand and interpret the experimental data and also to evaluate systematic corrections. The simulation allows corrections due to various physical detector effects and also due to software cuts that may be made during an analysis to be applied to the data points. Included in the simulation are the effects of detector geometry, detector resolution and thresholds. In addition the physical processes resulting from the interaction of particles with the detector materials are considered, allowing for example the energy deposition in the defined experimental set-up, such as DAPHNE's target, wire chambers and active scintillator layers to be evaluated.

The most important physical processes for charged particles are collision energy losses (accounting for the effects of straggling), nuclear interactions and multiple scattering. For each scintillator, light attenuation and non-linear light output response must be taken into account. Corrections can be evaluated and applied for events lost during the analysis due, for example, to cuts on  $dE/dx$  or  $\chi^2$  plots in the Range Analysis. In both cases events may be lost from the accepted regions due to hadronic interactions and multiple scattering.

Comparison between the simulated and measured detector response is shown in figure 4.4, of section 4.2.4, and is found to confirm the accuracy with which GEANT can model the detector and the physical processes which take place in it.

# **Chapter 4**

## **Data Analysis**

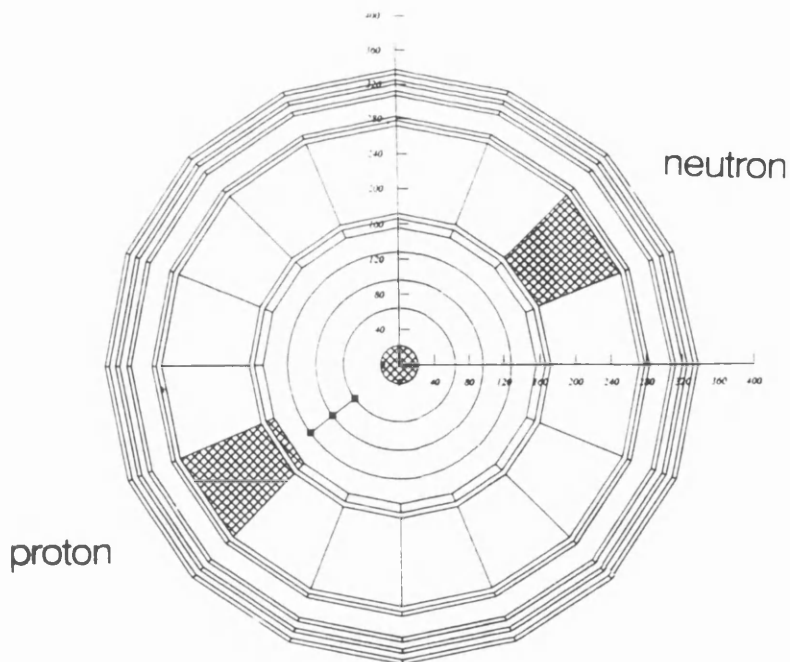
## 4.1 Introduction

The data on the  $D(\gamma,p)n$  reaction presented in this thesis were taken as part of a general investigation of the photodisintegration of deuterium using the DAPHNE detector. In order to collect data simultaneously on all of the breakup channels listed in table 4.1, DAPHNE was set up so that only a charged particle or a neutral trigger is needed for the data acquisition system to record the event. The  $D(\gamma,p)n$  events have to be extracted from the complete data set, which contains an increasingly large fraction of events due to other competing channels as the photon energy increases beyond the threshold for the one and two pion breakup modes.

The main task of the data analysis is the discrimination and selection of the two-body  $D(\gamma,p)n$  events from those due to other competing reactions. The first step is the selection of events in which only a single charged particle is detected. In principle it is also possible to require the detection of the neutron in coincidence; for example, the event shown in figure 4.1 is one in which both the proton and neutron are detected, the  $180^\circ$  difference between the neutron and proton azimuthal angle being characteristic of the  $D(\gamma,p)n$  reaction. However it is preferable to use the single charged particle trigger requirement in order to collect more events. This minimises the statistical error and also avoids a large uncertainty in the result due to the neutron detection efficiency.

Once the single charged particle trigger events are separated, it is necessary to make a charged particle identification to distinguish between protons and charged pions from the one charged pion reactions included in table 4.1. There are in addition some background events due to atomic interactions which result in an electron being detected. Most of these events are eliminated by an on-line

One charged particle	Q value	Three charged particles	Q value
$D(\gamma, p)n$	2.2 MeV		
$D(\gamma, p)n\pi^0$	137.16 MeV	$D(\gamma, pp\pi^-)$	140.47 MeV
$D(\gamma, \pi^+)nn$	143.05 MeV		
$D(\gamma, p)n\pi^0\pi^0$	272.12 MeV	$D(\gamma, p\pi^+\pi^-)n$	281.32 MeV
$D(\gamma, \pi^+)nn\pi^0$	278.01 MeV	$D(\gamma, pp\pi^-)\pi^0$	275.43 MeV

Table 4.1: *Deuterium break-up channels*Figure 4.1:  $D(\gamma, p)n$  event, cross-sectional view of DAPHNE

electron veto and do not produce a trigger; the remainder are easily identified by the scintillator signals and can be rejected.

Once the scintillator signals have been used to identify single proton events, it is necessary to rely on the reaction kinematics to separate  $D(\gamma, p)n$  events and allow a further rejection of other proton producing channels and background. Because the kinematics of the 2-body breakup are completely determined for each event by the measured values of  $E_\gamma$  and  $\theta_p$ , this separation can be done by comparing the measured and predicted proton energies.

## 4.2 General Comments

This section contains general comments concerning the analysis. Details of the various procedures needed in different photon energy regions are contained in subsequent sections.

### 4.2.1 Data Reduction

An initial data reduction is performed to select the required subgroup of events for input to the detailed analysis. At this stage raw scintillator and wire chamber signals are converted into energies and momenta and information on the particle track. A tagger calibration is used to convert tagger channel into photon energy. The subgroup selection is carried out by requiring events to satisfy the following cuts and conditions:

- i) There is only one reconstructed charged particle track and this particle reaches and triggers at least the A layer scintillators.
- ii) The event must fall within the prompt peak of the tagger TDC spectrum.

- iii) The event must pass a cut for electron rejection, safely keeping all protons and pions, applied to a plot of the type shown in figure 3.2.
- iv) The event must have an azimuthal angle outside the 'dead' regions defined by small misalignments of the scintillators (more fully discussed in section 4.6.2).
- v) The polar angle must lie within the limits  $21^\circ < \theta < 159^\circ$ , the acceptance range of DAPHNE for events originating in the target cell.
- vi) The track of the event as reconstructed from the wire chamber coordinates must pass through the target cell.

#### 4.2.2 Data Analysis

In the early stages of the analysis several different techniques of the type discussed in section 3.3.1, which use different combinations of the energy losses in the DAPHNE scintillator layers, were developed to identify protons. It was found that by basing the identification on the successive use of two or more such plots, an unambiguous identification could be made, but different plots had to be used in different  $E_\gamma$  and  $\theta_p$  ranges. The development of the Range Method described in section 3.3.2 simplified and improved this stage of the analysis. It is less subjective and gives better identification for most photon energies.

At photon energies from  $E_\gamma=200-480$  MeV, protons are extracted from the charged particle events just using the Range Method. Above  $E_\gamma=480$  MeV additional proton identification methods are required. Once protons are identified, the principal challenge is then the separation of the  $D(\gamma,p)n$  yield from that due to other reaction channels in which a single proton may be detected in DAPHNE. The major competing background is from the  $D(\gamma,p)n\pi^0$  reaction,

which, over the photon energy range of the experiment, produces a proton yield varying from the same order to many times that of  $D(\gamma,p)n$ .

For particles stopping in DAPHNE (this corresponds, for protons, to energies of  $E_p=200$  MeV at  $\theta=90^\circ$  and  $E_p=350$  MeV at  $\theta=21^\circ$ ), the Range Method successfully discriminates particle type and determines particle energy. For significantly higher energy events that pass through DAPHNE the identification is complicated because relativistic pions and protons have, within the scintillator resolution, the same energy loss. As a result the Range Method has a proton energy upper limit, above which it is unable to distinguish protons from pions unambiguously. This limit is  $E_p=350$  MeV at  $\theta=90^\circ$  and  $E_p=460$  MeV at  $\theta=21^\circ$  (see section 3.3.2, equation 3.2).

The analysis techniques required therefore vary as the photon energy increases. For  $E_\gamma < 480$  MeV all  $D(\gamma,p)n$  protons are within the energy limit of the Range Method, so that the analysis principally involves the rejection of the other proton channels. The pion contamination amongst events identified as protons by the Range Method has been investigated [45] and found to be less than 1% of true pions. As the photon energy increases, the pion background, from for example  $D(\gamma,\pi^+)nn$ , also increases, however for  $E_\gamma < 480$  MeV the remaining pions not removed by the Range Method are eliminated by the kinematics reconstruction discussed in section 4.2.3. For  $E_\gamma > 480$  MeV additional identification methods are needed for the protons whose energies are too great for the Range Method identification. For this region also the separation of  $D(\gamma,p)n$  relies heavily on the reconstruction of the 2-body kinematics.

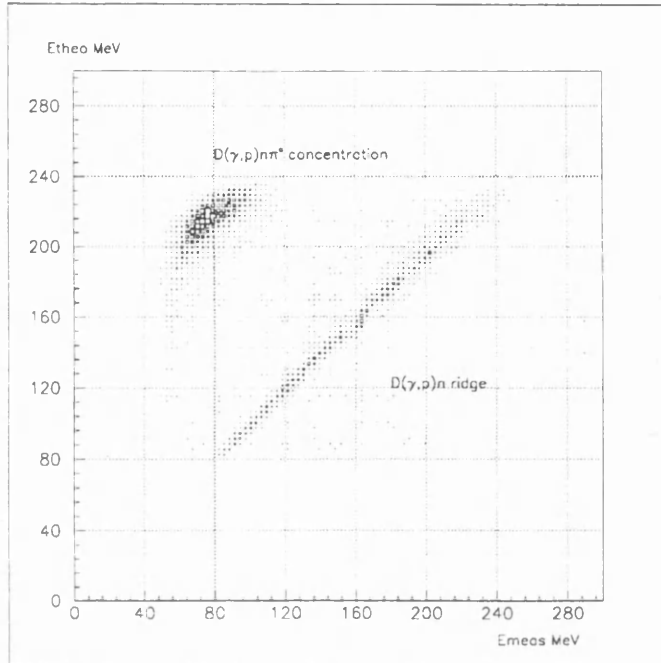


Figure 4.2: Comparison  $E_{theo}$  and  $E_{meas}$  at  $E_{\gamma}=320$  MeV

### 4.2.3 Reconstruction of 2-body Kinematics

As  $D(\gamma,p)n$  is a 2-body reaction, the well determined kinematics of the reaction can be used to assist in its separation from other channels. After proton events have been identified and their energy determined (using the Range Method for example), a consistency check is performed on the proton energy to see if the event is from the  $D(\gamma,p)n$  reaction. The experimentally determined proton energy is compared with the energy obtained from the kinematics of the 2-body photodisintegration of deuterium using the photon energy  $E_{\gamma}$  and the polar angle  $\theta_p$  of the particle. The tagging spectrometer determines the photon energy to  $\sim 2$  MeV and DAPHNE's wire chambers determine polar angle with a resolution of less than  $1^{\circ}$ .

Figure 4.2 shows a typical comparison between the measured proton energy and the calculated theoretical proton energy. The correlation between the mea-

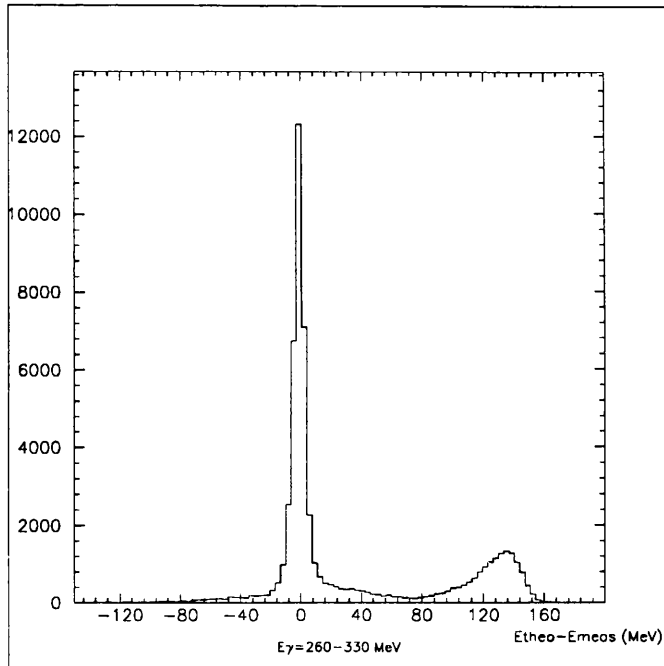


Figure 4.3:  $E_{theo} - E_{meas}$  from two-body kinematics for  $E_{\gamma} = 260 - 330$  MeV

sured and calculated energies for the  $D(\gamma,p)n$  events is clear and produces a concentration of events along a line at  $45^{\circ}$  to the axis. This allows a reliable check to be carried out to see if a particular event is truly from  $D(\gamma,p)n$ . In figure 4.2 for events produced by 320 MeV photons, there is a concentration of  $D(\gamma,p)n\pi^{\circ}$  events well separated from the  $D(\gamma,p)n$  events and a more widespread distribution of background protons.

Figure 4.3 shows the difference between the  $D(\gamma,p)n$  theoretical energy and the experimentally determined energy for  $E_{\gamma} = 260 - 330$  MeV. The  $D(\gamma,p)n$  events are seen as a peak centred around zero superimposed on a spectrum of  $D(\gamma,p)n\pi^{\circ}$  events and other background.

#### 4.2.4 GEANT Simulations

GEANT simulations of  $D(\gamma,p)n$  events were made in order to evaluate systematic corrections to the data for events lost during the analysis, and to estimate a correction for background events erroneously included in the yield. The response of DAPHNE to  $D(\gamma,p)n$  protons was simulated as a function of  $\theta_p$  and  $E_\gamma$ . These variables determine  $E_p$  and a sample of protons of this energy are tracked through the detector. For each proton the simulated energies deposited in the scintillator layers are used as input information for the Range Method and an apparent "measured" energy is reconstructed. The dashed curve in figure 4.4 shows the difference between the proton energy input to the GEANT simulation and the "measured" proton energy from the Range Method for a selection of proton energy values. Superimposed for comparison are the corresponding DAPHNE data, showing, for real events, the difference between the "theoretical"  $D(\gamma,p)n$  proton energy calculated from the measured values  $E_\gamma$  and  $\theta_p$ , and the experimentally determined energy from the Range Method.

The plots for proton energies of 130 MeV and 150 MeV show comparisons in regions where  $D(\gamma,p)n$  data selection is at its cleanest. It can be seen that for these proton energies there is good agreement for the peak to tail ratio. The tail simulates the number of events outwith the peak due to hadronic interactions and multiple scattering. For the higher proton energies, 250 MeV and 300 MeV, the DAPHNE  $D(\gamma,p)n$  data plot includes some background events which are necessarily absent from the simulation. The plots nevertheless make clear the good agreement between the simulation and the data in the region of the main peak.

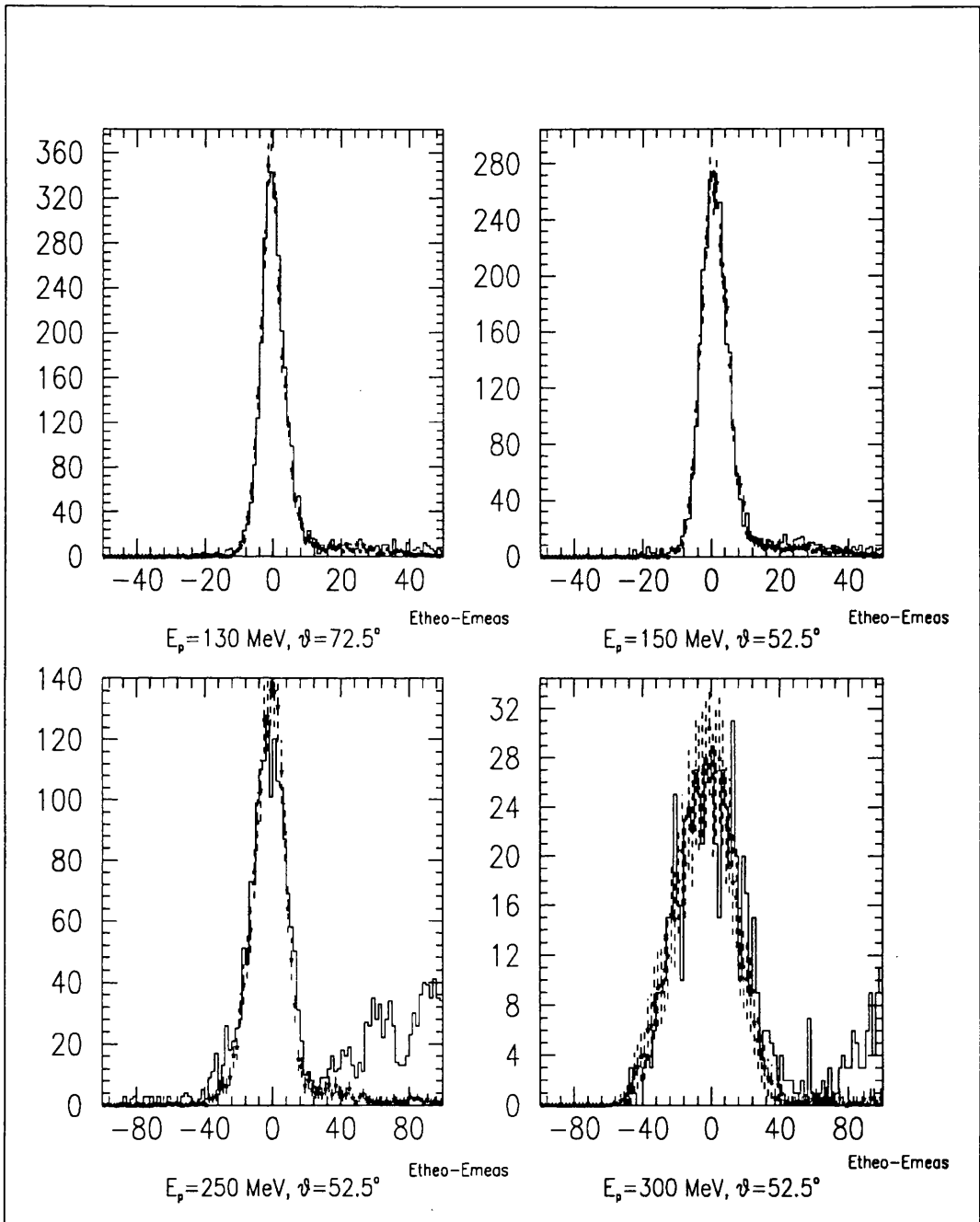


Figure 4.4:  $E_{theo} - E_{meas}$  from two-body kinematics, Data and GEANT simulations of  $D(\gamma, p)n$  events

### 4.3 Data Analysis $E_\gamma=200, 220$ and $240$ MeV

The determination of the cross sections for  $E_\gamma=200, 220$  and  $240$  MeV proved to be reasonably straightforward. All events stop before, or in, the B layer and so particle discrimination is at its simplest and the effects of competing channels are small. At these low energies pions are successfully identified by the Range Method. There exists no competing reaction where a proton is detected, since  $D(\gamma,p)n\pi^0$  protons have insufficient energy to reach the scintillators and trigger the electronics. The analysis for these energies involves constructing the  $E_{theo}-E_{meas}$  spectra as discussed in section 4.2.3 and binning them in increments of 20 MeV in photon energy and  $20^\circ$  in angle. The spectra for  $E_\gamma=200$  MeV together with the GEANT simulations are reproduced in figure 4.5.

It can be seen in the figure there is a small background of varying magnitude extending under the peak. The energy deposition in the  $E - dE/dx$  layers for these events has led the Range Method to identify them as good protons and their energy discrepancy,  $E_{theo}-E_{meas}$ , for  $D(\gamma,p)n$  kinematics is fairly close to zero. However, on close inspection of all the information available event by event, there is evidence this background comes from low energy negatively charged pion events, for example, from the  $D(\gamma,\pi^-)pp$  channel. At 200 MeV, the  $D(\gamma,\pi^-)pp$  channel is not far above its threshold and there is little energy available to the particles. The two protons have insufficient energy to reach the detecting layers of DAPHNE and the event is seen as only one charged particle. The energy losses in the scintillators are anomalous due to the formation of pionic atoms in the scintillator material. The pion is subsequently captured by the nucleus and the 135 MeV rest mass energy is given to nucleons which can deposit energy in the scintillator. Associated with these events is often

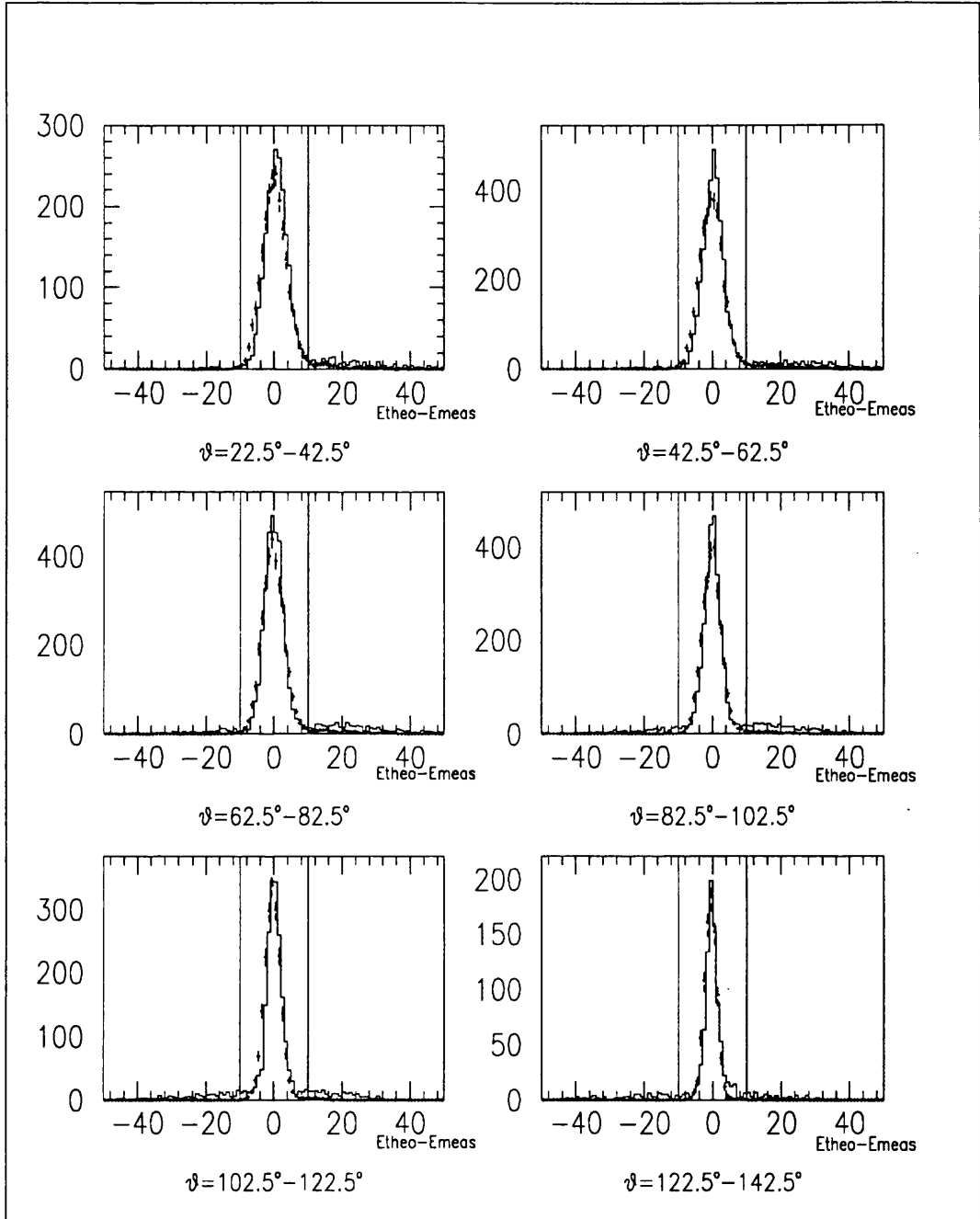


Figure 4.5:  $E_{theo} - E_{meas}$  from two-body kinematics, Data and GEANT simulation  $E_\gamma = 200$  MeV

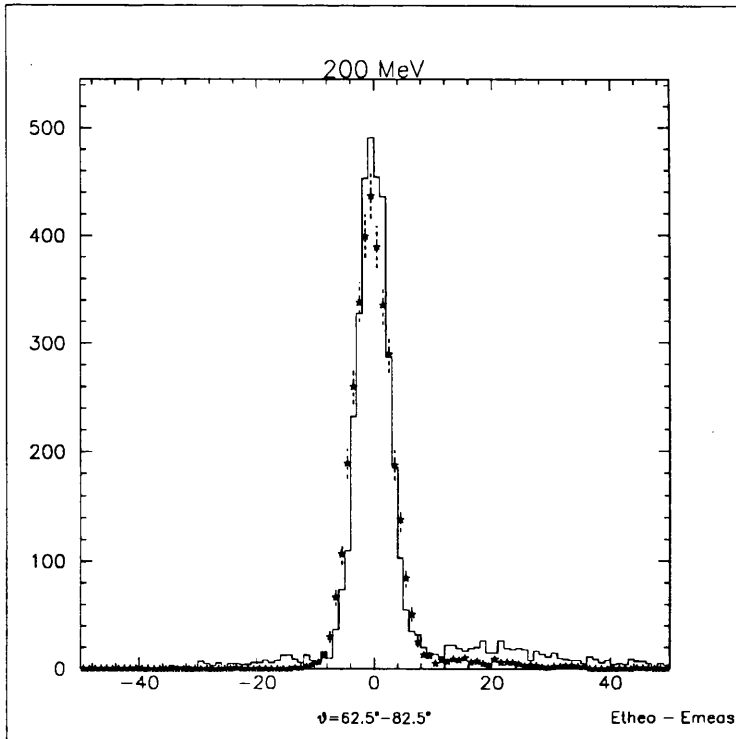


Figure 4.6:  $E_\gamma=200\text{ MeV}$ ,  $\theta=62.5^\circ-82.5^\circ$  Data and GEANT simulation

a second charged particle track passing through the wire chambers obliquely, not originating from the target, possibly corresponding to a charged particle involved in the pion capture reaction. Furthermore, the magnitudes of the wire chamber signals are generally smaller than those for standard proton events, which also strongly suggests these events are pions.

Cuts are then made to select a region around the peak of each spectrum in figure 4.5, rejecting the unwanted background whilst retaining the majority of genuine  $D(\gamma,p)n$  events. The GEANT simulations provide a correction for the number of  $D(\gamma,p)n$  events lost in the tails of the spectra, and are also used to assess the number of background events still included in the peak region.

Figure 4.6 shows the data and GEANT simulation for  $E_\gamma=200\text{ MeV}$ , and  $\theta=62.5^\circ-82.5^\circ$ . The data and GEANT peaks are first normalised to equal areas within the range of values of  $E_{theo}-E_{meas}$  from  $-10\text{ MeV}$  to  $+10\text{ MeV}$ . The

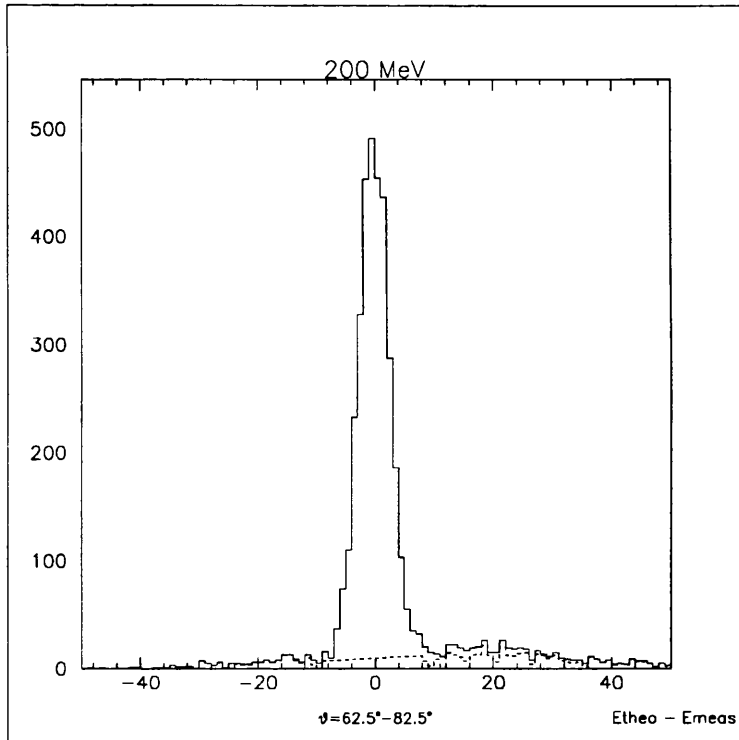


Figure 4.7:  $E_\gamma = 200 \text{ MeV}$ ,  $\theta = 62.5^\circ - 82.5^\circ$  Background evaluation

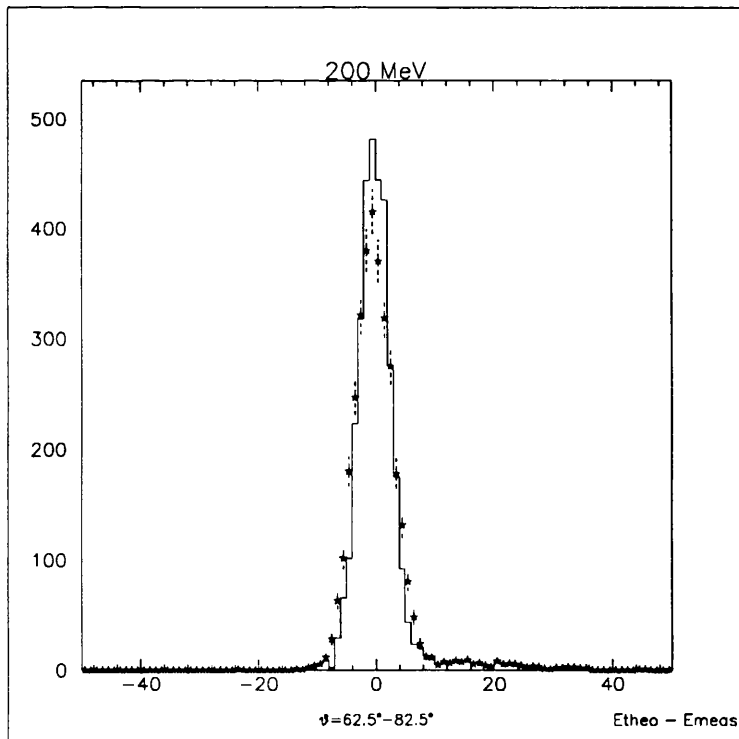


Figure 4.8:  $E_\gamma = 200 \text{ MeV}$ ,  $\theta = 62.5^\circ - 82.5^\circ$  Data with background subtracted and GEANT simulation

GEANT spectrum is then subtracted from the data in the region outside the peak. The remainder gives the background spectrum outside the peak which is then used to evaluate a contribution extending underneath the peak. This is shown as the dashed line in figure 4.7. Thus GEANT helps provide a complete background spectrum which is then subtracted from the data. The final  $D(\gamma,p)$  experimental spectrum with the background subtracted and the corresponding GEANT simulation are shown in figure 4.8.

## 4.4 Data Analysis $E_\gamma=240-480$ MeV

### 4.4.1 Introduction

Since the Range Method successfully discriminates particle type for photon energies  $E_\gamma=240-480$  MeV, the principal problem is the rejection of  $D(\gamma,p)n\pi^0$  events. In general, protons from the  $D(\gamma,p)n\pi^0$  reaction have considerably less energy than those from  $D(\gamma,p)n$  as 135 MeV rest mass is needed for pion production. This is seen in figure 4.9, which shows plots of the difference between expected proton energy from the  $D(\gamma,p)n$  reaction and the experimentally determined proton energy. The events from the  $D(\gamma,p)n\pi^0$  reaction generally lie to the right of the  $D(\gamma,p)n$  peak, (ie experimentally measured energy is less than theoretically determined energy assuming two-body kinematics), however, a tail in the  $D(\gamma,p)n\pi^0$  distribution certainly extends underneath the  $D(\gamma,p)n$  peak by an unknown amount.

The plots in figure 4.9 show the data in 70 MeV photon energy intervals and include all proton angles. They do not give a good indication of the degree to which the two reactions can be resolved in the analysis. For the analysis, the data were again split into 20 MeV photon energy bins and then further into angular bins of  $20^\circ$ . It was found that the nature of the background changes rapidly with these variables. There is a large variation in the relative magnitudes of the peaks, in their separation and in the extent to which the two distributions overlap. For the majority of the data the separation is far better than that shown in figure 4.9. In general, the magnitude of the  $D(\gamma,p)n$  peak relative to  $D(\gamma,p)n\pi^0$  peak is larger for angles greater than  $40^\circ$ , and is worse only for a restricted range of forward angles. The  $D(\gamma,p)n\pi^0$  background is very forward peaked.

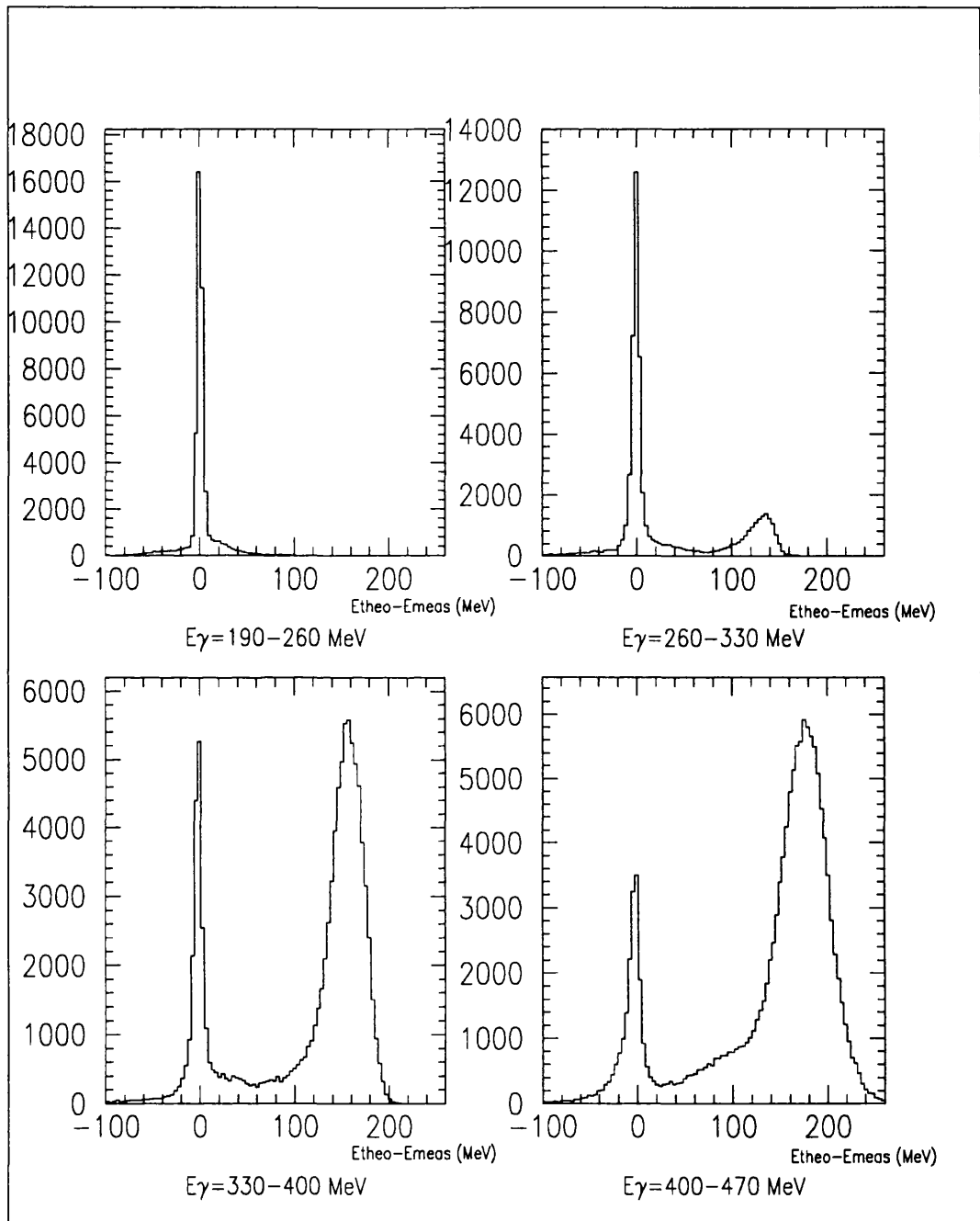


Figure 4.9:  $E_{theo} - E_{meas}$  from two-body kinematics for  $E_\gamma = 190 - 470$  MeV

Figures 4.10 and 4.11 show representative examples of  $E_{theo}-E_{meas}$  spectra. Figure 4.10 shows, for  $E_{\gamma}=320$  MeV the proton angular ranges  $22.5^{\circ} - 42.5^{\circ}$  and  $62.5^{\circ} - 82.5^{\circ}$  and figure 4.11, for  $E_{\gamma}=400$  MeV,  $62.5^{\circ} - 82.5^{\circ}$  and  $122.5^{\circ} - 142.5^{\circ}$ . The ratios of the events in the  $D(\gamma,p)n$  and  $D(\gamma,p)n\pi^{\circ}$  peaks and their separation are seen to be markedly different.

Generally the analysis was carried out using GEANT in a way similar to that for the lower energies. Cuts were applied to the  $E_{theo}-E_{meas}$  plot to reject the background whilst retaining the majority of  $D(\gamma,p)n$  events, and GEANT was used to simulate the data and provide a correction for the number of events lost due to the cut. However it was useful also to consider the kinematical limitations on the proton energy spectrum from the  $D(\gamma,p)n\pi^{\circ}$  reaction and also the way in which the mechanism of the reaction affects the shape of the proton spectrum. These help to identify cases in which the  $D(\gamma,p)n\pi^{\circ}$  distribution is likely to extend under  $D(\gamma,p)n$  peak and to establish the shape of this tail in the  $D(\gamma,p)n\pi^{\circ}$  distribution.

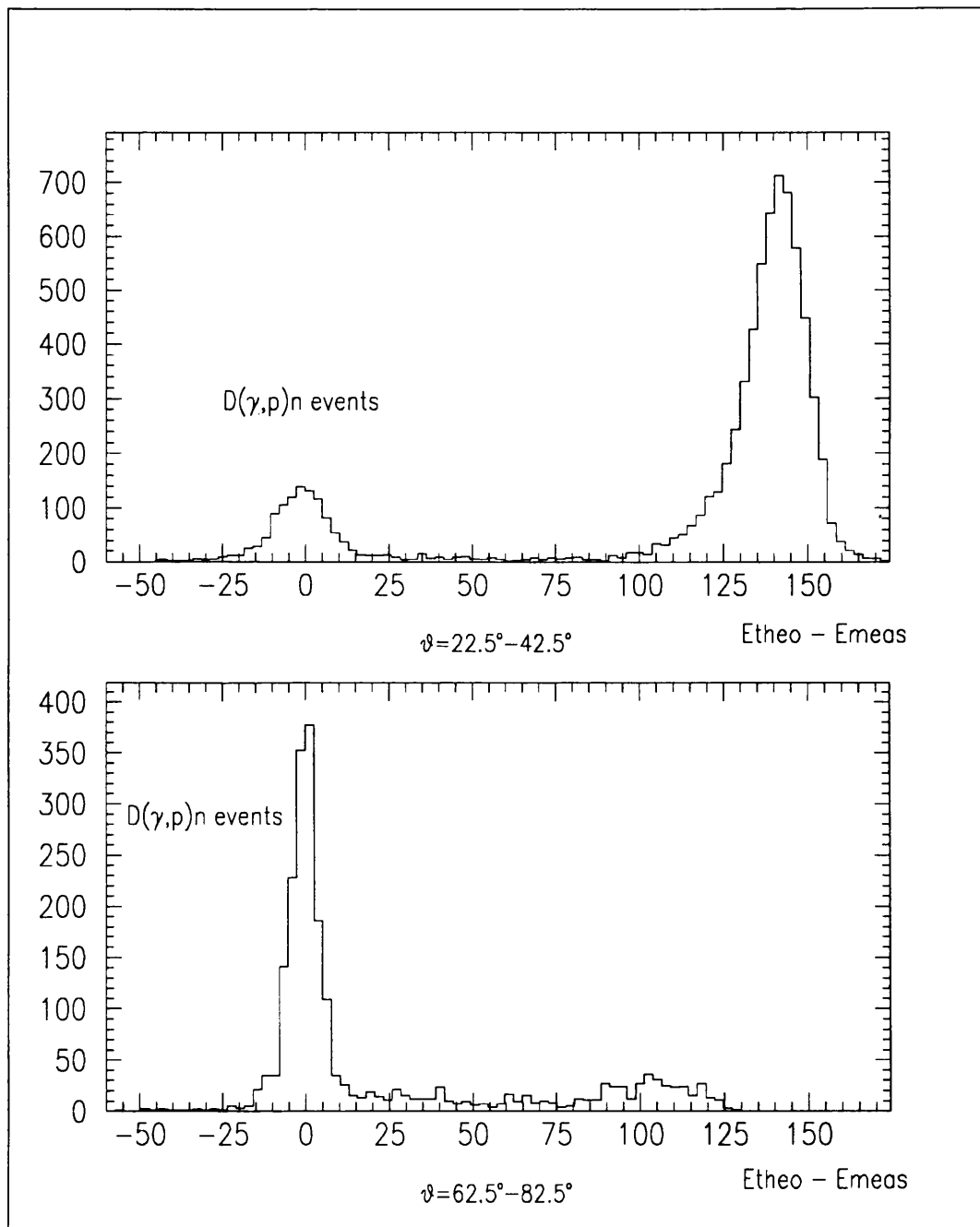


Figure 4.10:  $E_{theo} - E_{meas}$  from two-body kinematics at  $E_\gamma = 320$  MeV

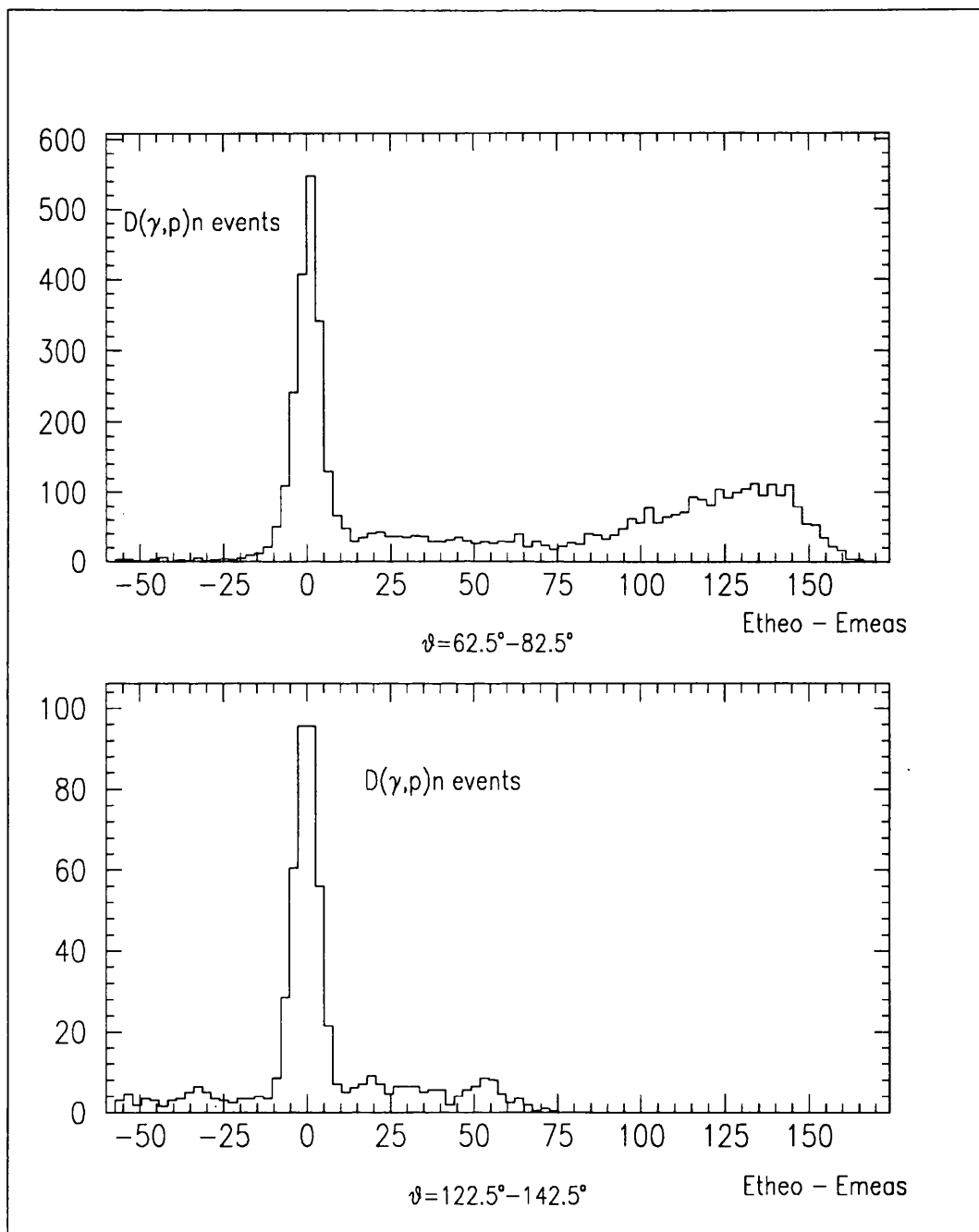


Figure 4.11:  $E_{theo} - E_{meas}$  from two-body kinematics at  $E_\gamma = 400$  MeV

#### 4.4.2 Specific Kinematics and Mechanisms for the $D(\gamma,p)n\pi^0$ Competing Process

Two specific kinematics of pion production are of interest. They are the limiting case when the proton has its maximum possible energy and the kinematics of quasi-free  $D(\gamma,p)n\pi^0$  process in which the neutron is a spectator. In figure 4.12 the relations between proton kinetic energy and polar angle for these two specific kinematics are shown along with the  $D(\gamma,p)n$  kinematics for  $E_\gamma=300$  and 500 MeV.

#### The Maximum Proton Energy for $D(\gamma,p)n\pi^0$

The maximum energy a proton from  $D(\gamma,p)n\pi^0$  can have at any given  $E_\gamma$  and  $\theta_P$  occurs when the neutron and pion emerge as 'one particle' with the same velocity in the same direction. This energy is given by the curves labelled  $\gamma + D \rightarrow p + (n\pi^0)$  in figure 4.12. Events of this type define a theoretical lower limit in the  $E_{theo}-E_{meas}$  plot, corresponding to the case in which a proton from the  $D(\gamma,p)n\pi^0$  looks most like a proton from  $D(\gamma,p)n$ . Therefore a useful guide in determining cuts to the spectra is obtained by evaluating this end point for  $D(\gamma,p)n\pi^0$  in order to provide a point below which it is theoretically not possible to have  $D(\gamma,p)n\pi^0$  events.

Figure 4.13 shows the data for  $E_\gamma=320$  MeV,  $\theta=22.5^\circ - 42.5^\circ$  and  $\theta=62.5^\circ - 82.5^\circ$ , together with the GEANT simulations and the  $D(\gamma,p)n\pi^0$  end points. There is good agreement between the simulations and the data in the region of the main peak and the  $D(\gamma,p)n\pi^0$  theoretical thresholds appear to provide reasonable estimates to the end points of the  $D(\gamma,p)n\pi^0$  spectra. However, there is a small background, possibly extending under the peaks, from pion contami-

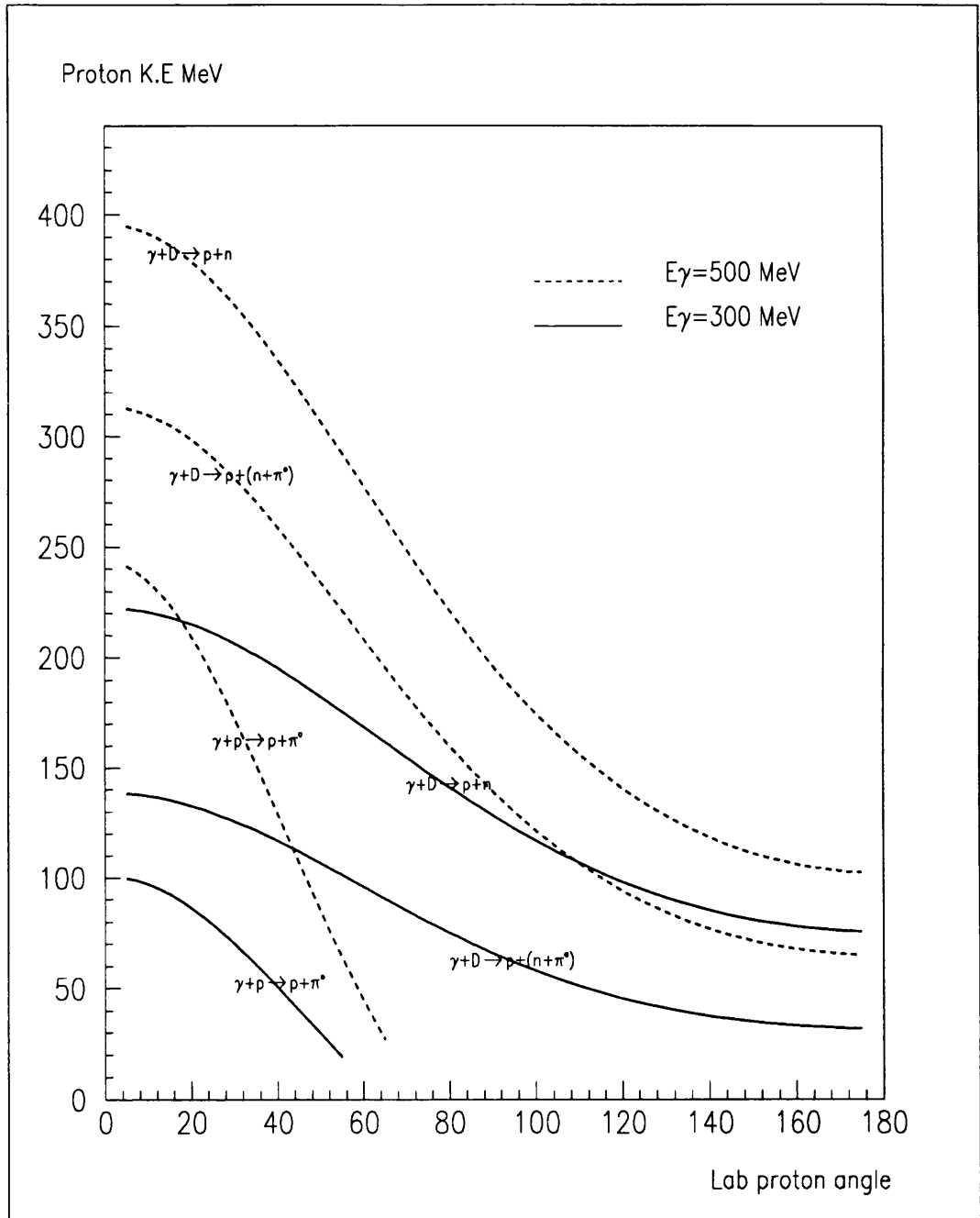


Figure 4.12: Maximum proton energy from the  $D(\gamma, p)n\pi^0$  and proton energy from the  $p(\gamma, p)\pi^0$  reaction compared with that from the  $D(\gamma, p)n$  reaction

nation and  $D(\gamma,p)n\pi^0$  protons. These  $D(\gamma,p)n\pi^0$  protons have, due the effects of hadronic interactions, multiple scattering and detector resolution a higher reconstructed proton energy. This end point should therefore be considered as a guide rather than a definite limit. The data and the GEANT simulation are normalised to equal areas within the region of the main peak, a cut is made rejecting the  $D(\gamma,p)n\pi^0$  events and other background, and GEANT provides a correction for the number of  $D(\gamma,p)n$  events lost. The GEANT spectrum is then subtracted from the data in the region outwith the cut. The remaining background spectrum is then interpolated underneath the  $D(\gamma,p)n$  peak to provide an estimate of the background to be subtracted from the  $D(\gamma,p)n$  events.

### Quasi-free $D(\gamma,p)n\pi^0$ kinematics

A large part of the strength of the  $D(\gamma,p)n\pi^0$  reaction is expected to be due to quasi-free pion production, in which pion photoproduction takes place on the proton whilst the neutron is a spectator. The momentum of the outgoing proton in a particular event depends on the Fermi momentum of the initial neutron, but an indication of the average energy can be obtained by taking the case of a stationary initial neutron.

To a sufficient accuracy this can be approximated by the two-body kinematics of single pion photoproduction on hydrogen and the results are labelled  $\gamma + p \rightarrow p + \pi^0$  in figure 4.12. These events are only significant at angles forward of  $60^\circ$  and the protons have at least 135 MeV less energy than those from  $D(\gamma,p)n$  protons at the same polar angle.

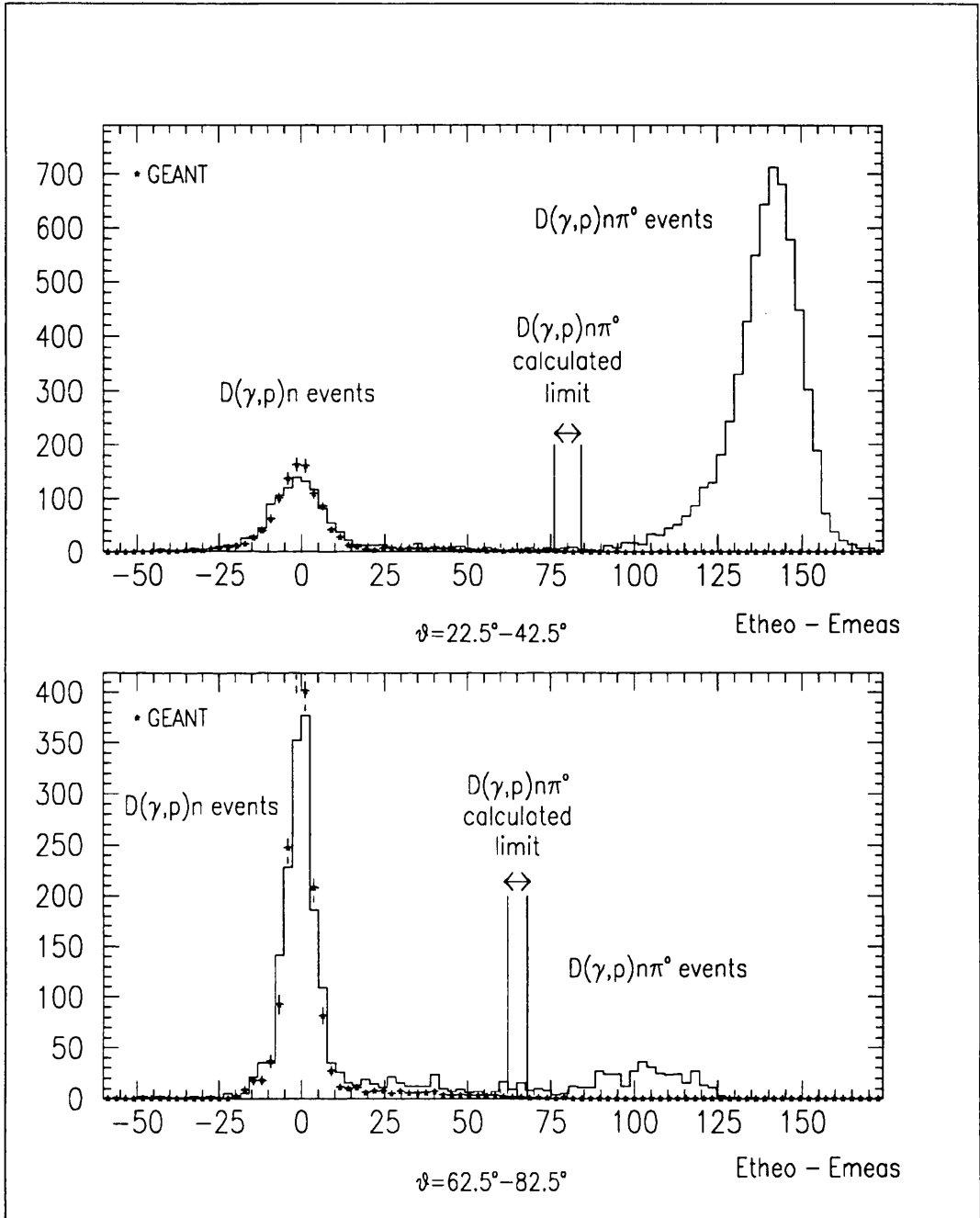


Figure 4.13:  $E_{theo} - E_{meas}$  spectra from two-body kinematics showing  $D(\gamma, p)n\pi^0$  threshold at  $E_\gamma = 320$  MeV

## The proton energy spectrum for $D(\gamma,p)n\pi^0$

The quasi-free process is expected to be the dominant contribution to the  $D(\gamma,p)n\pi^0$  reaction, although other mechanisms are possible which would lead to a more equal sharing of energy between the outgoing particles, in particular to a higher proton energy. If the quasi-free process is dominant one can perhaps assume that all observed proton events are produced by either  $D(\gamma,p)n$  or quasi-free  $D(\gamma,p)n\pi^0$  reactions. Making this assumption, a procedure for separating the two possible types of event is to check the proton energy in each event against that predicted by the 2-body kinematics of first the  $D(\gamma,p)n$  and then the  $H(\gamma,p)\pi^0$  reactions.  $E_{theo}-E_{meas}$  can be calculated for each hypothesis and the event classified according to which gave a value closest to zero. The results are shown in figure 4.14, the dashed line peaks centred on zero are those events classified as  $D(\gamma,p)n$ , the solid line those as  $D(\gamma,p)n\pi^0$ . The method appears fairly successful in isolating  $D(\gamma,p)n$  events up to  $\sim E_\gamma=400$  MeV and provides a useful cross check for the "maximum proton energy" approach at lower energies. At higher energies unphysical bumps appear in the  $D(\gamma,p)n$  spectra arising from events which are clearly not  $D(\gamma,p)n$  but have been classified as such. It seems probable that these events come from more complex interactions in which the neutron is not a spectator. In an attempt to understand and reproduce these peaks the three body phase space generator GENBOD [47] was used to model the final state. This simulation produced peaks having a systematic behaviour similar to that observed for the data. This strongly suggested that the events associated with the additional peaks are from non quasi-free pion production and that any attempt to remove the  $D(\gamma,p)n\pi^0$  background assuming a quasi-free mechanism will produce suspect results.

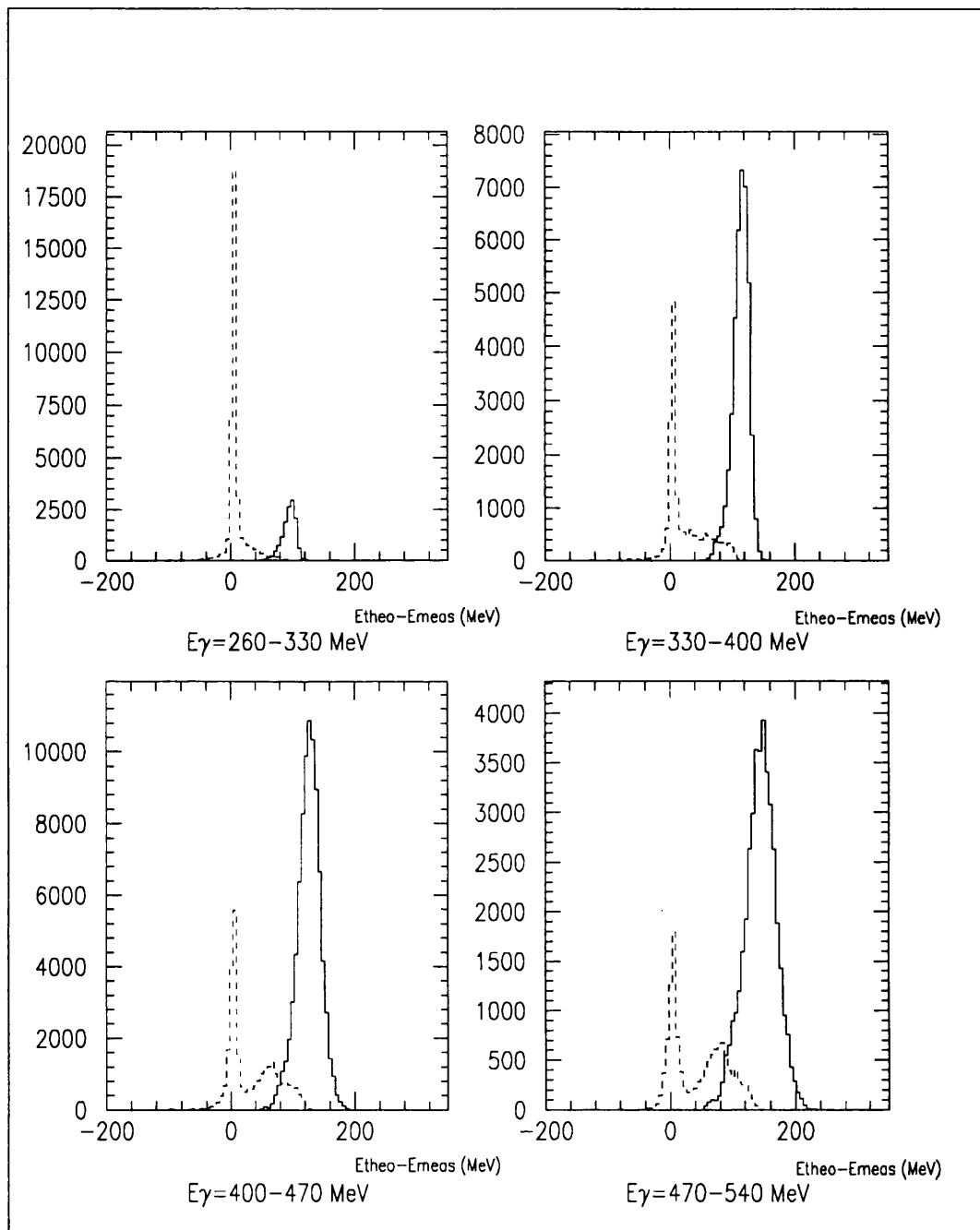


Figure 4.14: Classification  $D(\gamma,p)n\pi^0$  or  $D(\gamma,p)n$

## 4.5 Data Analysis $E_\gamma=480-600$ MeV

In this region the Range Method is not on its own sufficient to separate protons and pions. As  $E_\gamma$  increases above 480 MeV many of the reaction products have sufficient energy to pass through all of the DAPHNE layers. A large fraction of these particles have energies above the limit for which protons can be distinguished from pions. The events are checked against the condition for satisfactory particle separation at the conclusion of the Range Method analysis and many events fail. This is particularly significant since the single charged particle events in this photon energy region are predominantly pions; the  $D(\gamma,p)n$  protons are only a small fraction of the total.

Events which pass the particle separation check are treated as before; an example is given in section 4.5.2. The treatment of events which fail the check is described in the following section.

### 4.5.1 Analysis of Events which fail the Particle Separation Check in the Range Method Analysis

The solid line in figure 4.15 is the distribution of  $E_{theo}-E_{meas}$ , assuming  $D(\gamma,p)n$  kinematics for all events at  $E_\gamma=560$  MeV, which fail the particle separation check. There is a very large peak for negative values of  $E_{theo}-E_{meas}$ , which is caused by pions, mainly from  $D(\gamma,\pi^+)nn$ , which "look rather like" high energy protons (the  $E_{theo}-E_{meas}$  spectra previously discussed for  $E_\gamma < 480$  MeV had peaks for positive values due to  $D(\gamma,p)n\pi^0$  protons). There is however a small  $D(\gamma,p)n$  peak centred on zero and the analysis to extract these events involves developing methods for the rejection of a large pion background especially any tail of the background extending under the  $D(\gamma,p)n$  peak. Other plots shown in

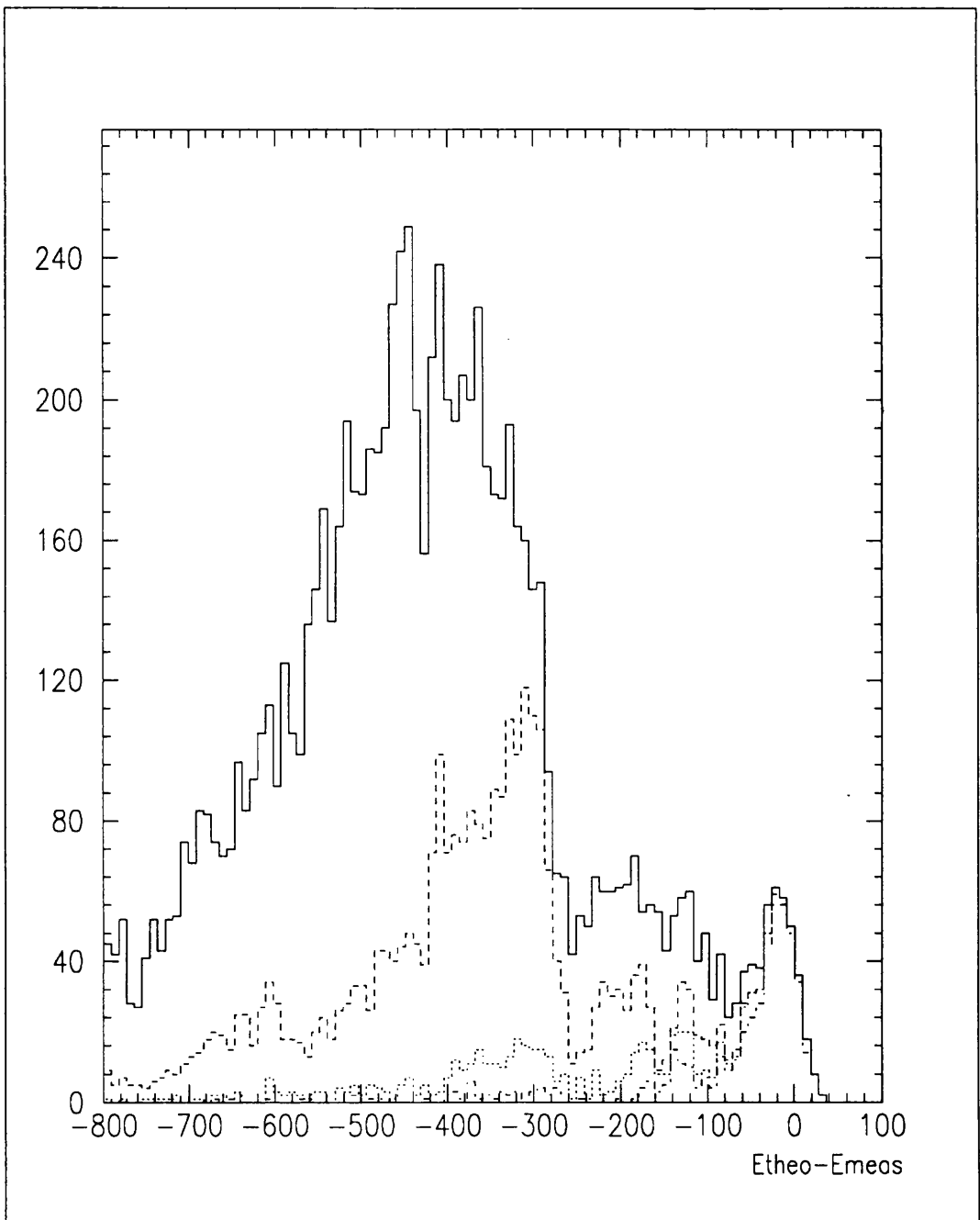


Figure 4.15: *Analysis of events which fail the particle separation check in the Range Method analysis*

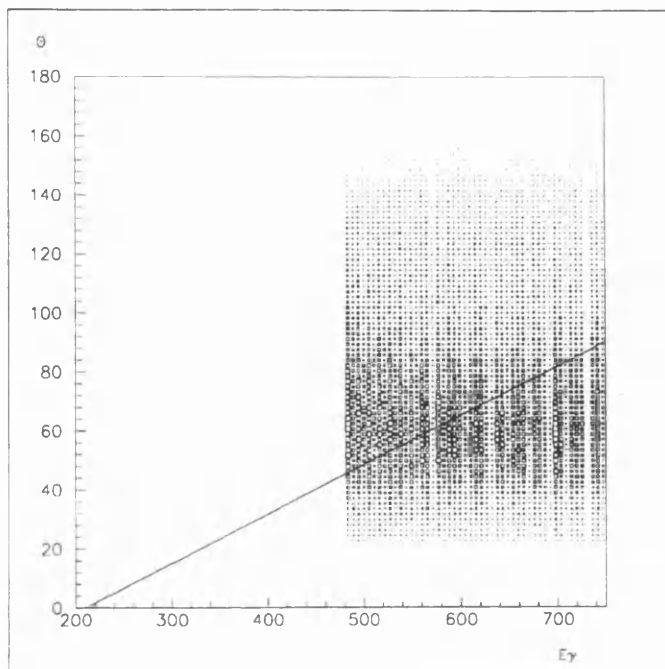


Figure 4.16: *Events which fail the particle separation check in the Range Method analysis*

the figure are of events remaining after successive cuts for rejecting pions have been applied to the data. These cuts are now discussed.

Events which fail the particle separation check are predominantly pions which are not adequately rejected by the Range Method. In this energy range these pions are fitted by the Range Method as very high energy protons. This is illustrated in figure 4.15, which contains data for  $E_\gamma=560$  MeV analysed by the Range Method on the hypothesis that the particle is a proton.

The methods developed to remove pions from the data rely on knowing the kinematic regions in which protons from the  $D(\gamma,p)n$  which fail the particle separation check will be confined. This is illustrated in figure 4.16. In this figure all events for  $>480$  MeV which fail the particle separation check are shown on a scatter plot of polar angle against photon energy. The events cover the whole kinematic region but the high energy protons from  $D(\gamma,p)n$  which the analysis

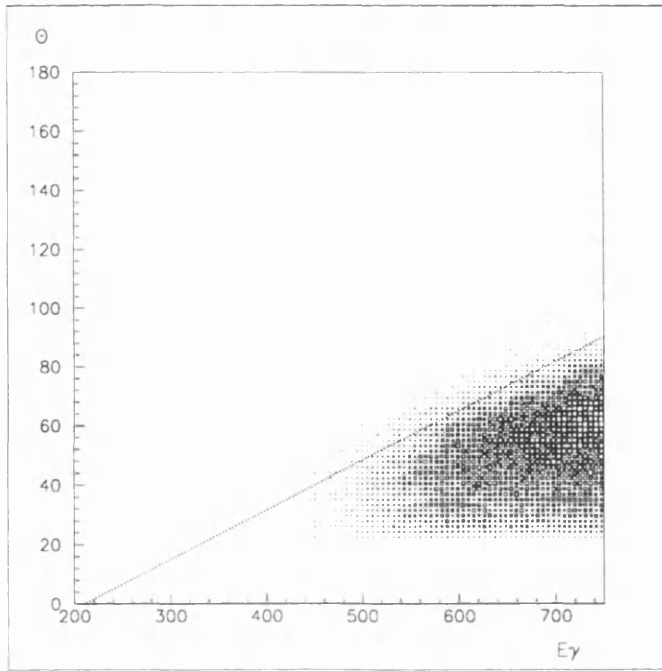


Figure 4.17: *GEANT Simulation of  $D(\gamma,p)n$  Events which fail the particle separation check in the Range Method analysis*

has to select will be concentrated in the high  $E_\gamma$ , low  $\theta_p$  region. This is shown in figure 4.17 which contains solely  $D(\gamma,p)n$  events as simulated by GEANT, which is used to track  $D(\gamma,p)n$  protons over the whole kinematic region and then analyse them with the Range Method. The events shown in figure 4.17 are those that fail the particle separation check. This identifies the region in figure 4.16 that could contain such  $D(\gamma,p)n$  events, and shows it is associated as expected with the highest energy protons, which are found in the forward part of the  $D(\gamma,p)n$  angular distribution. As the photon energy increases the angular region for which  $D(\gamma,p)n$  protons fail the separation check covers a greater angular range backward of  $21^\circ$ . However, it is clear from figure 4.17 a well defined cut, shown as the diagonal line, can be applied to the data confidently selecting  $D(\gamma,p)n$  events while at the same time rejecting a considerable pion background. The effect of this cut on the  $E_\gamma=560$  MeV data is shown as the

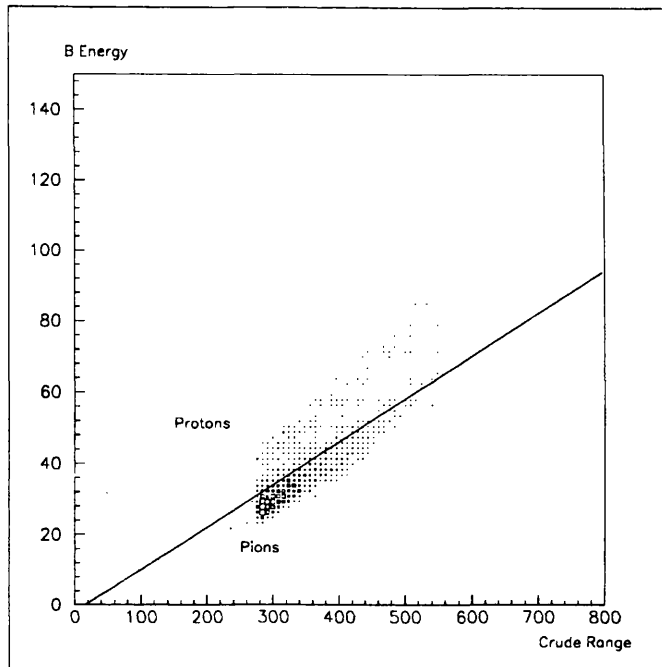


Figure 4.18: *B energy loss against 'crude range'*

dashed line in figure 4.15 and clearly rejects considerable pion background.

The GEANT simulated  $D(\gamma,p)n$  protons which fail the separation check were then used to generate a plot of B energy loss versus the 'crude range' discussed in Chapter 3, section 3.2.1. This was used as a guide to determine another safe cut to be applied to the remaining pion and proton events. As an example, a selection of the events, which fail the separation check for  $E_\gamma=560$  MeV, is shown in figure 4.18 together with the cut. The effect of this cut in separating protons and pions is shown as the dotted line in figure 4.15. The cuts applied up to now have resulted in  $\sim 5\%$  of events in the  $D(\gamma,p)n$  peak around zero being removed.

It is now useful to examine the  $\chi_p^2$  and  $\chi_\pi^2$  distribution of the remaining events. Figure 4.19 shows a scatter plot of  $\chi_\pi^2$  for the hypothesis of an event being a pion plotted against  $\chi_p^2$  for the hypothesis it was a proton. The sepa-

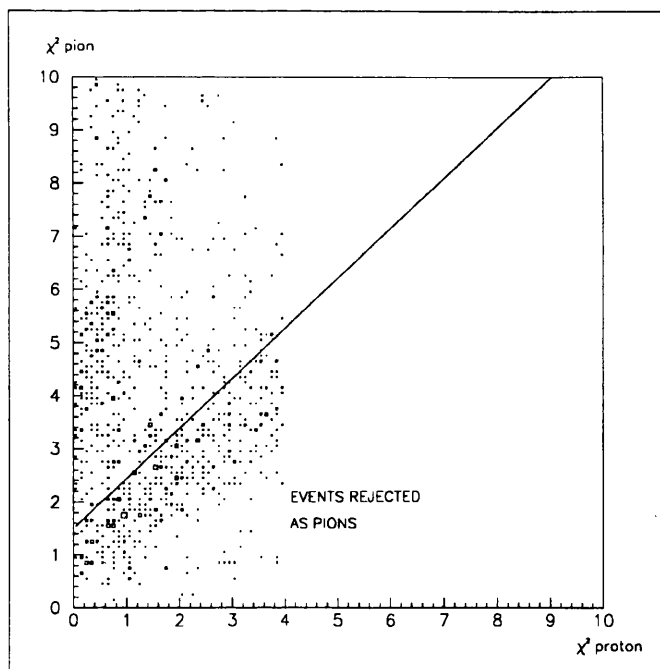


Figure 4.19:  $\chi^2$  proton versus  $\chi^2$  pion

ration is clearly poor compared to figure 3.5 of Chapter 3. However, the plot is still useful. Two rather imprecise distributions can be seen. All the events have a reasonably good  $\chi_p^2$  for the proton hypothesis, but there is a greater range in  $\chi_\pi^2$  pion values. The cut shown in figure 4.19 rejecting the cluster of events with a low  $\chi_\pi^2$ , was determined as before from the GEANT simulated  $D(\gamma,p)n$  protons. It removes most of the events in the pion bump in figure 4.15 whilst the  $D(\gamma,p)n$  peak centred around zero remains relatively unchanged. The events remaining after this final cut are shown as the dash-dotted line of figure 4.15. Although there is still a pion tail extending underneath the peak it clearly accounts for only a small fraction of genuine events. Finally, an evaluation and rejection of this background is made by making a comparison with a suitably normalised simulated GEANT  $E_{theo}-E_{meas}$  spectrum. This is shown in figure 4.20. The GEANT simulation allows a further cut to be applied to the data at  $E_{theo}-E_{meas} = -120$  MeV with the confidence that although pions are rejected

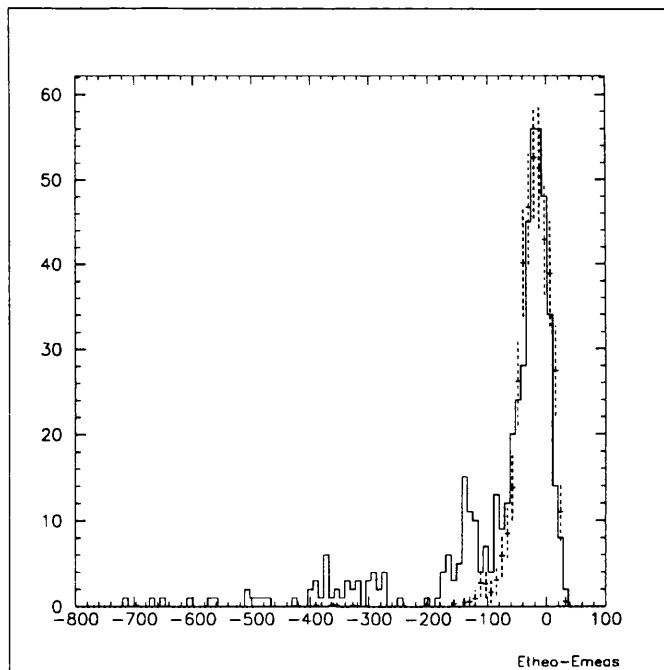


Figure 4.20: Remaining  $D(\gamma,p)n$  events and GEANT simulation

the majority of  $D(\gamma,p)n$  protons are retained. This is apparent from a comparison of the  $D(\gamma,p)n$  peak in figures 4.15 and 4.20 which shows that after the sequence of background subtractions the percentage reduction in the peak region due to the rejected pion events is  $\sim 5\%$ . GEANT simulations were made to evaluate the fraction of proton events that are lost due to the cuts applied during the foregoing analysis. The estimated loss is typically 10%, mainly from the tail region to the left of the peak in the  $E_{theo}-E_{meas}$  spectrum.

#### 4.5.2 Analysis of Events which pass the Particle Separation Check in the Range Method Analysis

There are many events even in the  $E_\gamma=480-600$  MeV region for which the Range Method can successfully separate protons from pions. These events are mainly the lower energy protons in the backward part of the  $D(\gamma,p)n$  angular distribution and they pass the particle separation check (equation 3.2 in section

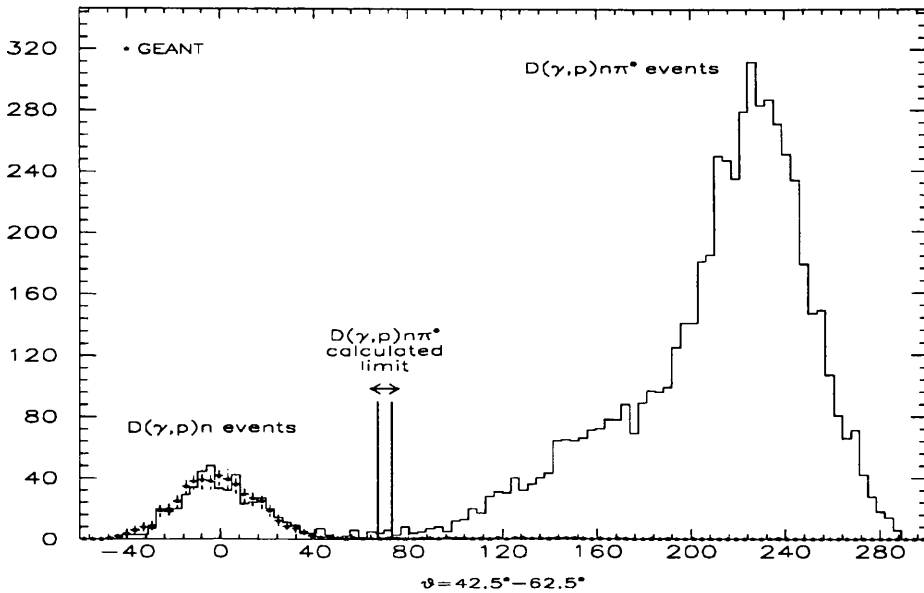


Figure 4.21:  $E_{theo} - E_{meas}$  from two-body kinematics at  $E_\gamma = 500$  MeV

3.3.2) at the end of the Range Method. These events are treated in the same way described for the  $E_\gamma < 480$  MeV data in section 4.4. The  $E_{theo} - E_{meas}$  spectra are binned in 20 MeV photon energy and  $20^\circ$  angle increments.

Figure 4.21 shows a plot of those events which have passed the particle separation check for  $E_\gamma = 500$  MeV,  $\theta = 42.5^\circ - 62.5^\circ$ . To the right of the  $D(\gamma, p)n$  peak there are events from the  $D(\gamma, p)n\pi^0$  reaction. These  $D(\gamma, p)n\pi^0$  protons have lower energies and therefore are unambiguously separated from pions by the Range Method. The relative number and separation of the two reactions is not significantly worse than was found at lower photon energies. Also shown is the GEANT simulation of the  $D(\gamma, p)n$  events. It is clear the simulation is very successful in reproducing the data even for such a particular subgroup of events.

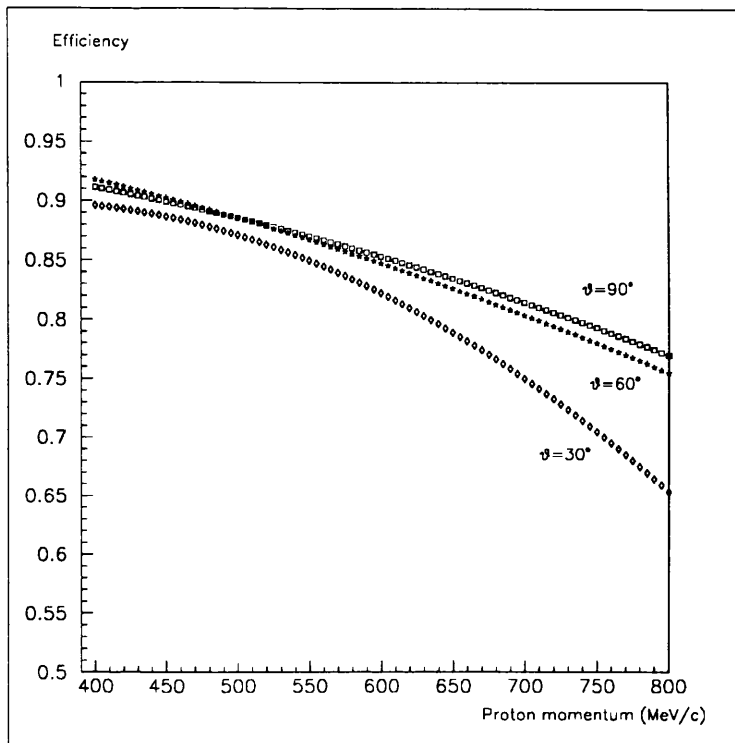


Figure 4.22: Range Method efficiency correction

## 4.6 Corrections to the Data

### 4.6.1 Efficiency Correction

The Range Method uses cuts on the  $\chi^2$  loci (discussed in detail in Appendix B) to identify protons. However, some proton events are lost as a result of hadronic interactions or multiple scattering. The efficiency for proton detection as a function of proton momentum and angle, is needed to apply the appropriate corrections to the data. These were evaluated with the GEANT code. As an example, the correction factors for a range of angles, as a function of proton momentum are shown in figure 4.22.

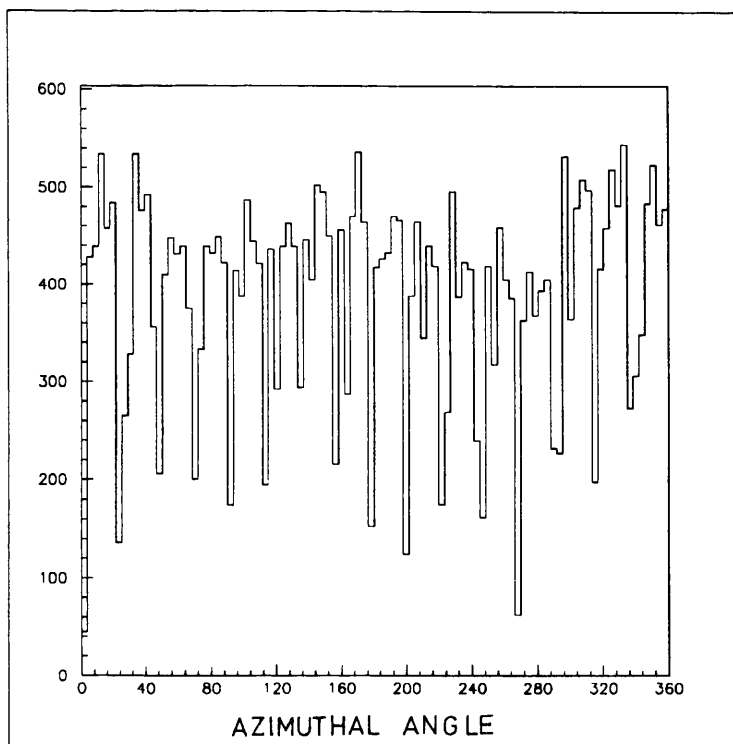


Figure 4.23: *Dead angle correction*

## 4.6.2 Dead Angle Correction

It is necessary to apply a dead angle correction to the data due to the segmented construction of the scintillator layers. This causes some particles whose tracks lie at the junctions between the segments to be lost. This can happen due to the misalignments between the layers or because a particle loses energy in two segments of the B layer. Figure 4.23 shows the experimental distribution in azimuthal angle for events which stop in the B layer. Sixteen regularly spaced dips can be seen in an otherwise approximately isotropic background due to the gaps between the 16 segments. Most of the dips are defined by a lack of counts in only one channel. However, some of the dips, for example at  $160^\circ$  are characterised by two separated channels, while the dip around  $340^\circ$  covers 3 contiguous channels. It was found that these gaps do not exactly overlap from layer to layer due to small misalignments of the sectors. Limits were defined

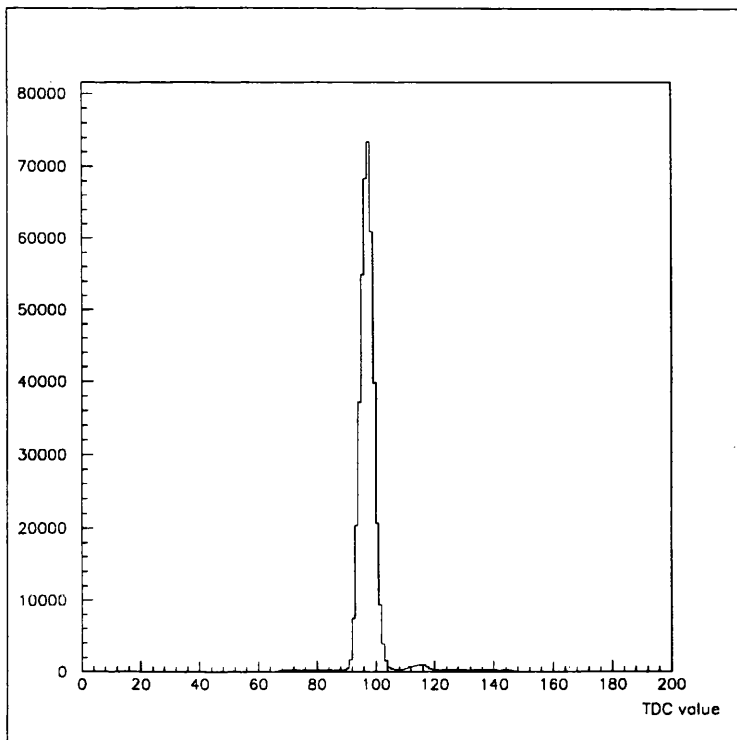


Figure 4.24: *A typical TDC spectrum*

and events having an azimuthal angle within these dead zones were rejected. A correction of 17% was applied later.

### 4.6.3 Real/Random Correction

A typical TDC spectrum, measuring the time difference between the DAPHNE trigger and the "coincident" electron in the focal plane of the tagger is shown in figure 4.24. It comprises a prompt peak superimposed on a random background. The prompt peak is from the true coincidence of tagging electron and photoreaction product and the plateau from accidental coincidences. The smaller second prompt peak is due to neutral photoreaction products for which the DAPHNE trigger is slightly delayed as the particles are detected in the outer layers. The prompt peaks for individual channels have to be aligned to compensate for the relative time differences arising from various cable delays. A correction for the

real/random rate was then evaluated. As the photon flux was relatively low due to the limit on the data acquisition rate, this correction proved to be small. The correction is dependent on the photon energy and is at its maximum for low photon energies (the increase in the Bremsstrahlung intensity distribution at low  $E_\gamma$  produces an increased electron count rate in the focal plane and a corresponding increased random background). For this worst case the correction is less than 1%.

The main analysis was performed taking only events that fell in a time window of 20 ns around the prompt region of this spectrum. The analysis was then repeated with an equivalent time window set for events in the random plateau, thus giving a measure of the contribution to the yield by random events within the prompt peak, and allowing this contribution to be subtracted. However, the low photon flux and clean rejection of background in the analysis meant this correction was negligible over most of the photon energy range.

#### 4.6.4 Multiple Tagger Hits

Multiple counts in the tagger fall into two categories. In the first a single electron detected in the tagger focal plane undergoes multiple scattering in one detector and then fires more than one channel in the focal plane so that the photon flux deduced from the focal plane scalers is too high. This proves straightforward to correct for. The signature of this multiplicity is two or more neighbouring channels firing. The lowest of the channel numbers that has fired is taken to give the correct photon energy (from the geometry of the overlapping elements these events hit the true element and scatter to higher channel numbers). Figure 4.25 shows the correction for this effect to the tagger counts as a function

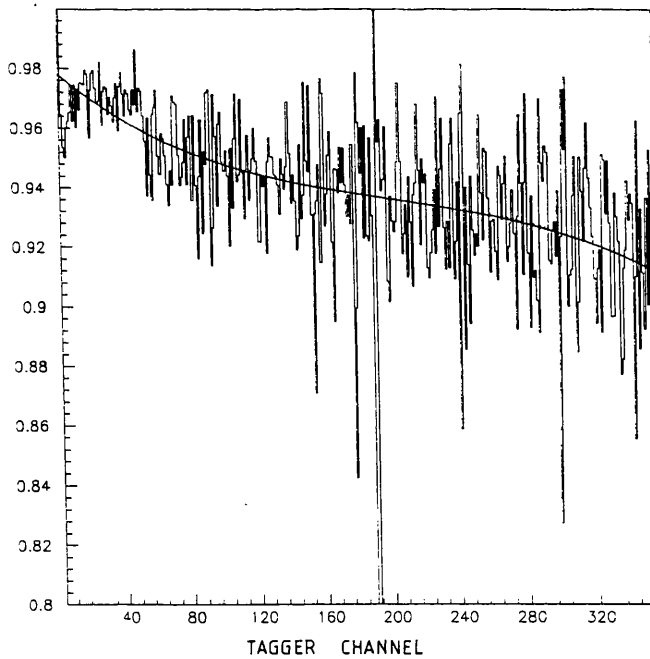


Figure 4.25: *Neighbouring multiple tagger hits correction*

of tagger channel number. It can be seen that the correction is largest at low photon energies, ie higher tagger channel numbers where the intensity of electrons hitting the focal plane is largest. The apparent very large correction around channel 190 is due to a 'dead' channel.

The accumulated scaler counts from all tagger channels are summed to obtain the total tagger scaler count used to determine the flux normalisation. The multiplicities from multiple hits are therefore erroneously included. A correction can be evaluated from the channel-by-channel multiplicity correction shown in figure 4.25 and the spectrum of the tagger scaler counts as a function of channel number.

If more than one tagger channel has fired and the channels are not neighbouring there is the problem of determining the correct photon energy and of correcting the tagger count. For these events the signal from each tagger channel which had fired was analysed as a separate event. This was done no

matter where the event fell in the TDC spectra of the channel which had fired, thus ensuring it is correctly included in the random subtraction for all such channels. As the photon flux was relatively low due to the limit on the data acquisition rate, the mean tagger multiplicity is close to one and corrections for these non-neighbouring multiple events are small.

#### **4.6.5 Correction for the Effective Length of the Target**

As a consequence of DAPHNE's extended target and detector geometry the probability of detection for a particle depends on the position at which it was produced along the target length and on its polar angle. Figure 4.26, illustrates the extreme cases to be considered. Particle trajectories at  $90^\circ$  will be detected with a uniform probability along the target length. For events at very forward angles, only those originating from the upstream end of the target will be detected. Trajectory 1 is safely within DAPHNE's acceptance. Trajectory 2 is the downstream limit for which a particle at this extreme forward angle will be detected, and as such it defines an effective maximum length of the target. Trajectory 3 further downstream will not be detected. The converse is true for backward angles, that is, only events originating from the downstream part of the target will be detected. This defines an effective length of the target for events at this angle and gives a correction which can be applied to the events when they are binned as a function of angle.

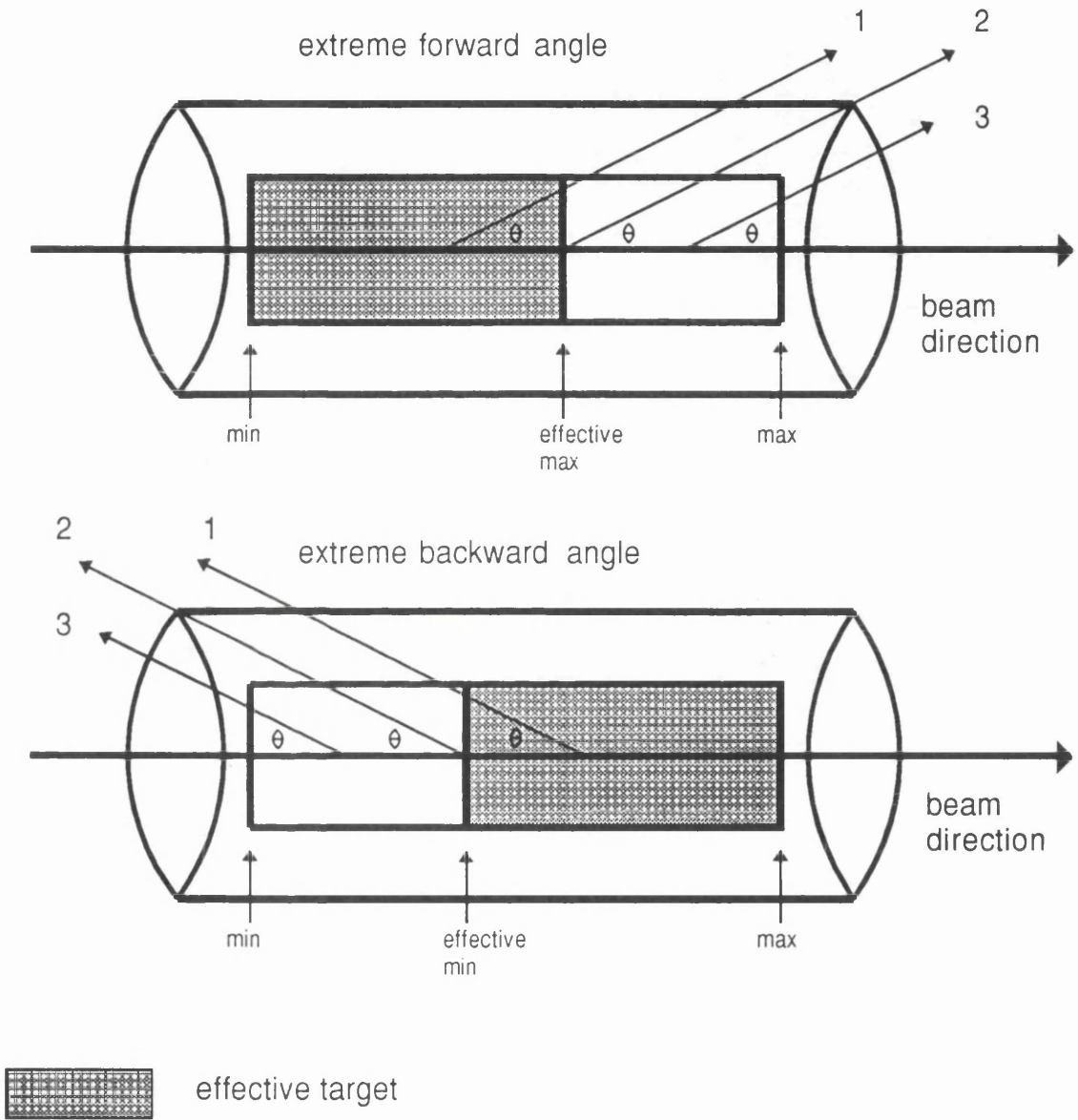


Figure 4.26: *Effective target length*

# **Chapter 5**

## **Experimental Results**

## 5.1 Introduction

The total and the differential cross sections for the  $D(\gamma,p)n$  breakup of the photodisintegration of deuterium have been measured over the photon energy range 200–600 MeV. The extensive data are presented in the form of twenty-one angular distributions together with their corresponding integrated total cross sections. The differential cross sections were evaluated in  $5^\circ$  bins within  $21^\circ < \theta < 159^\circ$ . The corrections discussed in Chapter 4, section 4.6 were applied and the cross sections were converted from the lab frame to the centre of mass frame. Total cross sections were obtained from the  $A_0$  coefficient determined from fourth order Legendre Polynomial fits to the angular distribution.

## 5.2 Calculation of Differential Cross Section

The differential cross section formula is given by:

$$\frac{d\sigma}{d\Omega} = \frac{Yield}{N_\gamma N_{target} \Delta\Omega} \quad (5.1)$$

$N_{target} = (N_A \rho t) / A$  is the number of target nuclei per unit area ( $N_A$  is Avogadro's number,  $\rho$  is the target density,  $t$  is target thickness and  $A$  is atomic weight).

$N_\gamma$  is the total number of photons, calculated for each photon energy bin by summing the corresponding tagger channels and correcting for tagging efficiency and electron multiple hits as explained in Chapter 4, section 4.6.4.

$\Delta\Omega$  is the solid angle given by:

$$\Delta\Omega = \int_{\phi_1}^{\phi_2} \int_{\theta_1}^{\theta_2} \sin(\theta) d\theta d\phi = 2\pi(\cos(\theta_1) - \cos(\theta_2)) \quad (5.2)$$

### 5.3 Experimental Results

The differential cross sections in the centre of mass were fitted by a fourth order Legendre Polynomial expansion, given by:

$$\frac{d\sigma}{d\Omega} = \sum A_l(E_\gamma) P_l \cos(\theta) \quad (5.3)$$

where  $\theta$  is the c.m angle between the incoming photon and outgoing proton. The coefficients were calculated from a least squares fit. The statistical and systematic errors were evaluated, added in quadrature and used in the fit. The total cross sections were obtained from the  $A_0$  coefficient:

$$\sigma_{tot} = 4\pi A_0 \quad (5.4)$$

and are shown in figure 5.1. The errors are too small to be shown on the scale used. The resulting differential cross sections from this analysis are shown in the centre of mass system in figures 5.2–5.7, together with the fits. The total and differential cross sections together with the fitted Legendre Polynomial coefficients are given in tables 1–9 of Appendix B.

The systematic uncertainties included in figures 5.2–5.7 are those dependent on proton angle. This includes the error associated with the efficiency correction and that with the effective length of target correction discussed in section 4.6. Also included are the uncertainties in corrections due to cuts applied and functions fitted to the  $E_{theo}-E_{meas}$  spectra. An additional global systematic error from the sources listed in table 5.1 is estimated to be  $\pm 3\%$ . To observe the influence of experimental errors on the fit an additional systematic error of 10% was included and the fit redone. The values of the coefficients remained unchanged.

Source	Systematic error
$\gamma$ flux normalisation	$\pm 2\%$
Target density	$\pm 1\%$
Target length	$\pm 2\%$
Dead angle correction	$\pm 1\%$
Total	$\pm 3\%$

Table 5.1: *Additional Systematic Error*

In previous work it has been usual to fit deuteron photodisintegration data with Legendre Polynomials due to their physical correspondence with multipole magnitudes, and also the expansion has the advantage that the  $A_0$  coefficient relates directly to the total cross section. The fitting to higher orders and the cut off in order has in the past, not been significant as the number of data points was few. However, the present data's  $5^\circ$  binning means that fitting to fourth order can introduce spurious fluctuations. Structure appears in the fourth order function fitted to the angular distribution arising from statistical fluctuations in the data. Although, the inclusion of higher orders may prevent spurious fluctuations, it has to be done with great care, and this approach will be left to the future development of the analysis. It will be necessary to consider if a weighted Legendre polynomial fit will be required, by taking into account the manner in which theory says the higher order components decrease with respect to each other, as photon energy increases. It is anticipated this form of analysis will be independent from nuclear physics input to the theory.

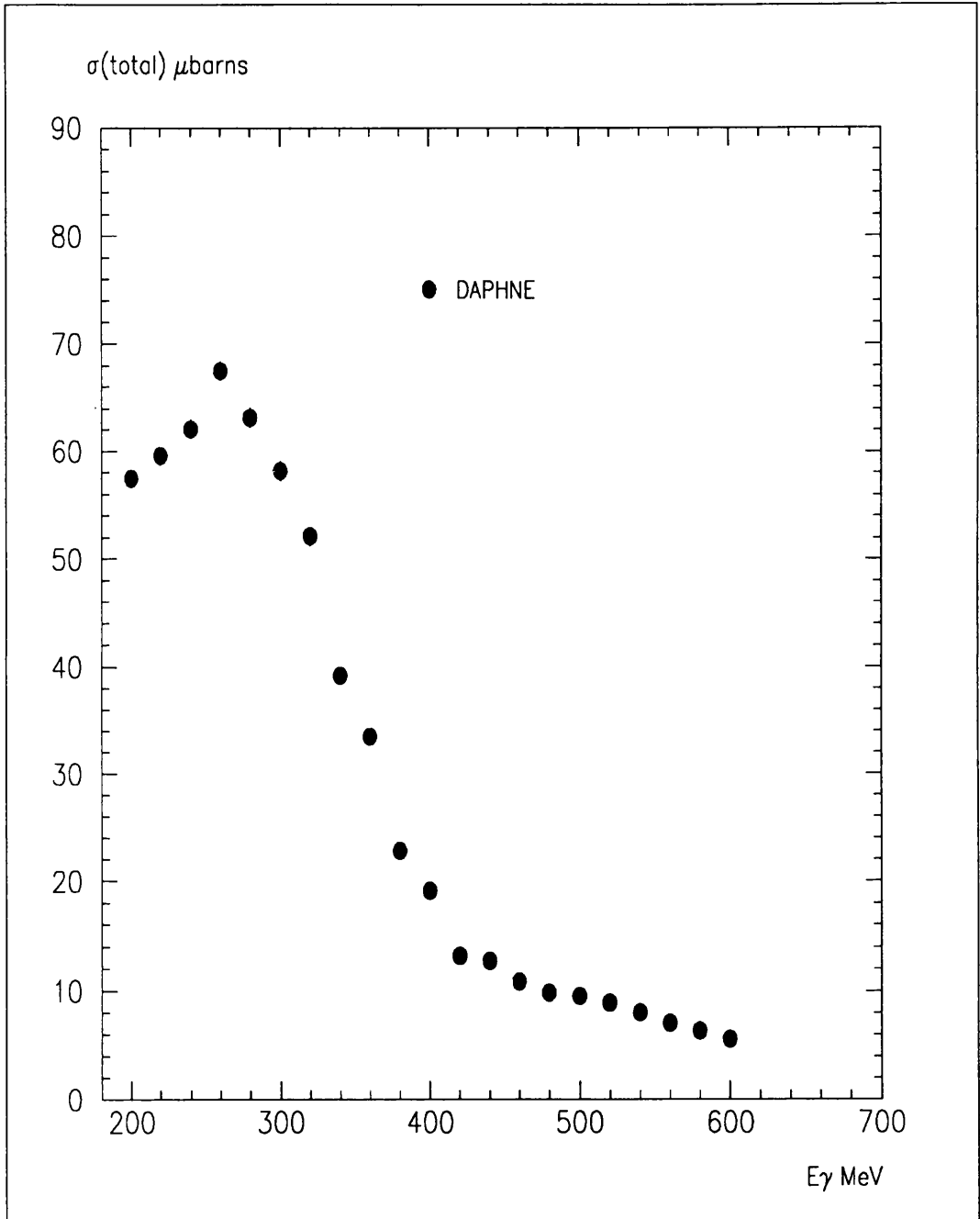


Figure 5.1: *Total Cross Section Results*

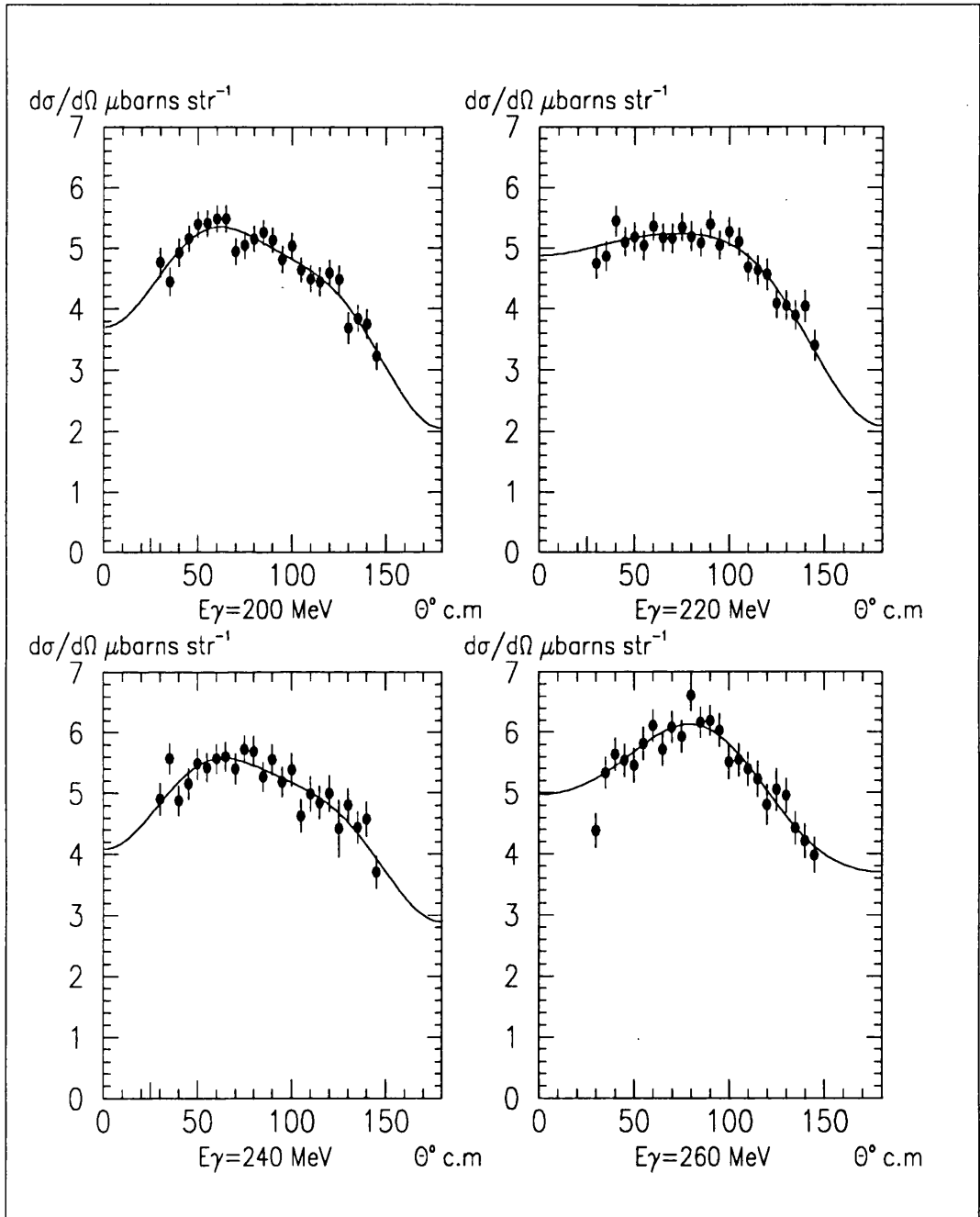


Figure 5.2: *Differential cross sections 200,220,240,260 MeV*

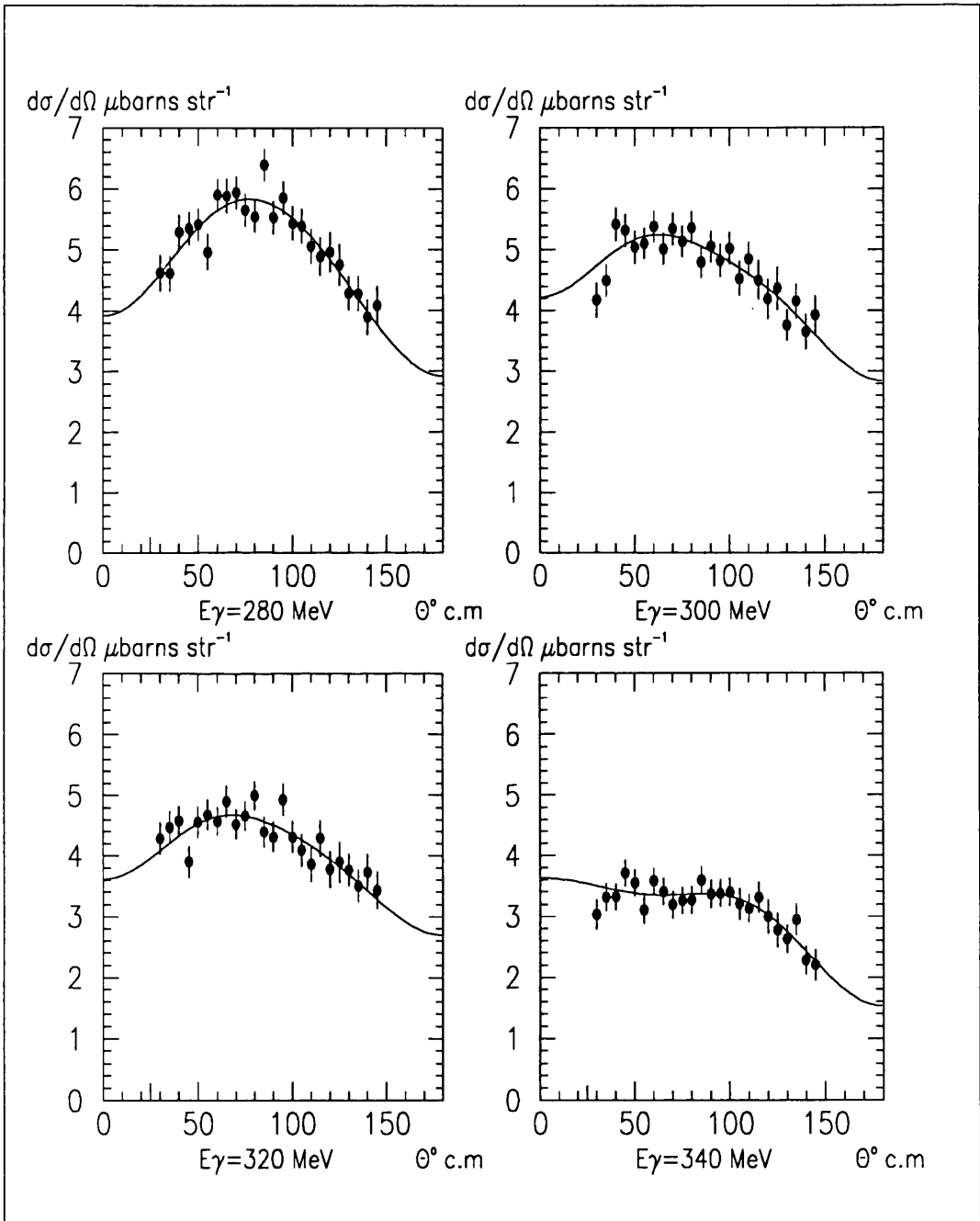


Figure 5.3: Differential cross sections 280,300,320,340 MeV

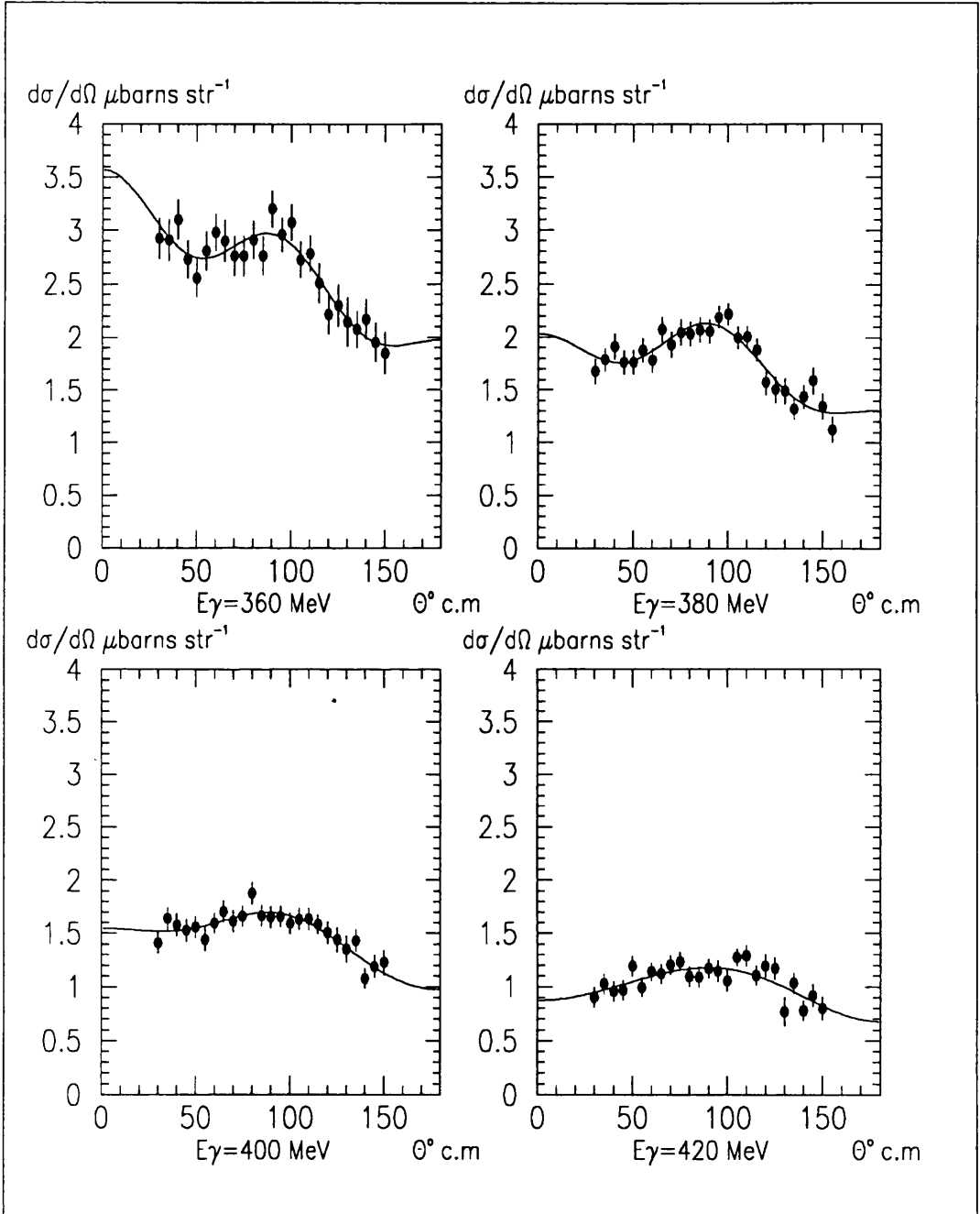


Figure 5.4: *Differential cross sections 360,380,400,420 MeV*

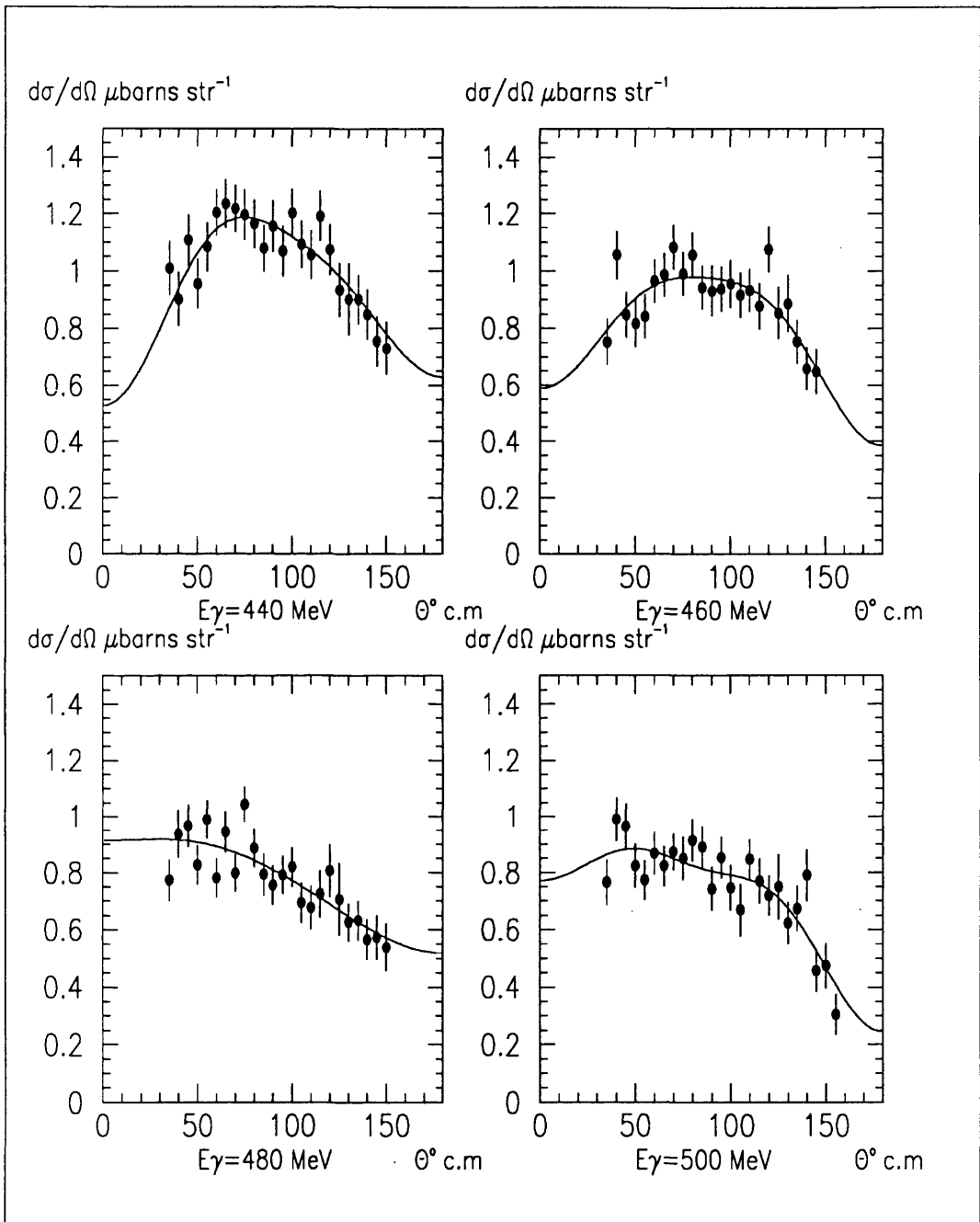


Figure 5.5: *Differential cross sections 440,460,480,500 MeV*

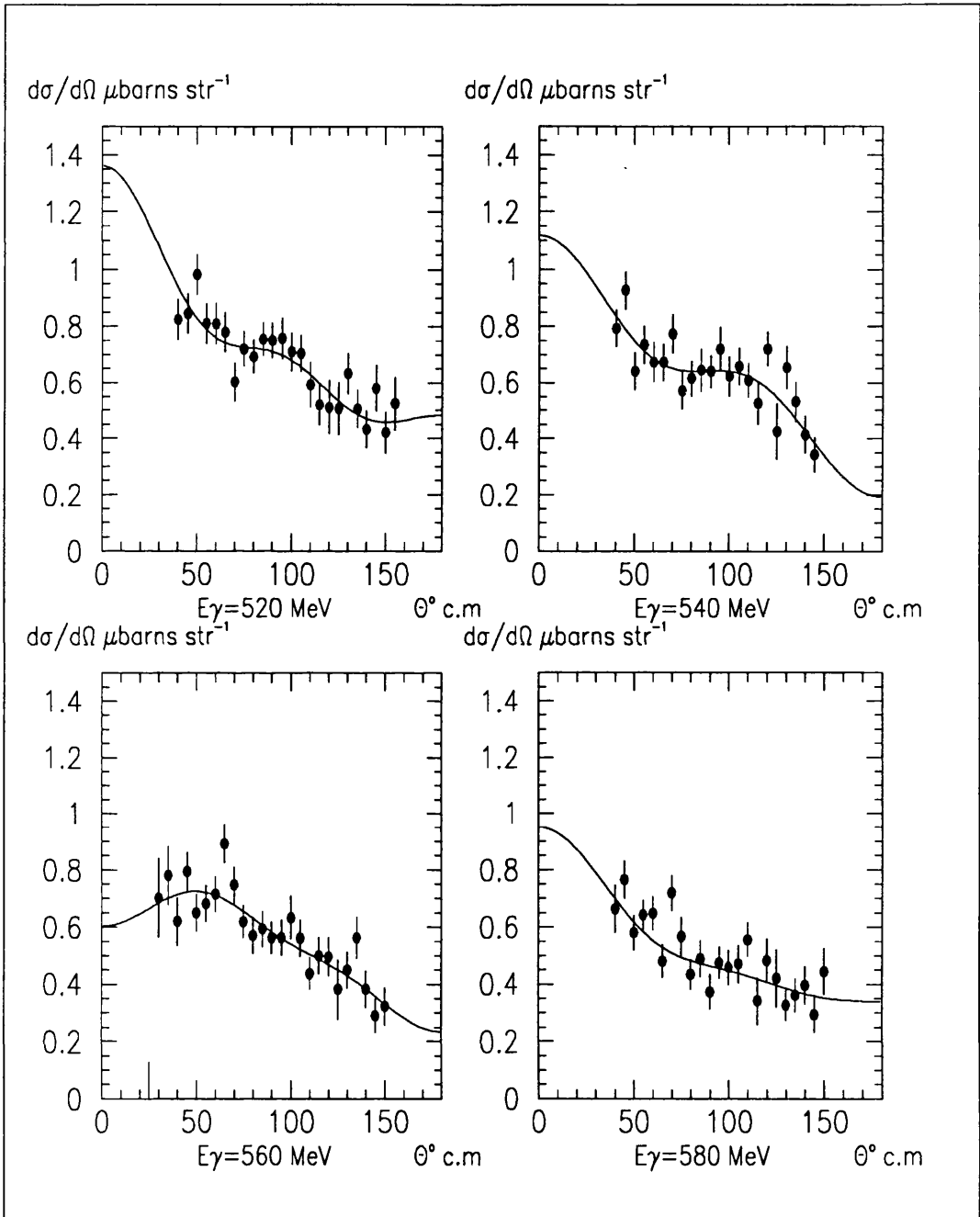


Figure 5.6: *Differential cross sections 520,540,560,580 MeV*

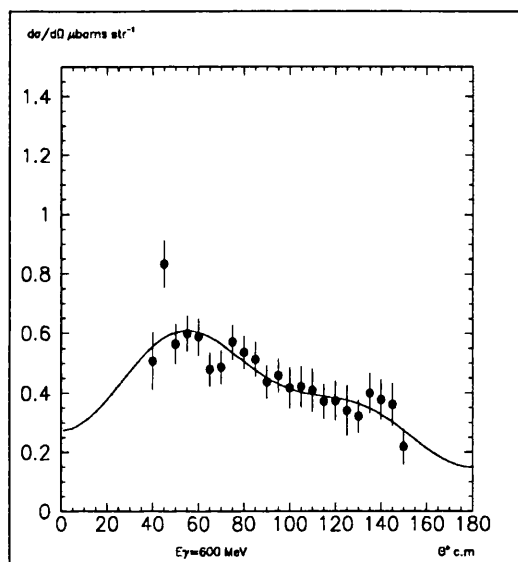


Figure 5.7: *Differential cross sections 600 MeV*

## **Chapter 6**

# **Comparison with Other Measurements and Theory**

## 6.1 Comparison with Other Measurements

### 6.1.1 Introduction

The DAPHNE data are now compared to other early and recent experimental work. The present measurements cover the extensive photon energy range 200–600 MeV, whereas the majority of existing data extend only to 350 MeV. This section, therefore, considers first the comparison with the large number of measurements at the lower photon energy range and then examines the degree of consistency with the few, very partial data sets extending higher.

Various phenomenological fits of the existing data set have been obtained, for example, by Rossi *et al* [48] and by Jenkins *et al* [49]. These are discussed and used in order to perform a general comparison to the majority of previous work. Since these parameterisations are derived from fits to all existing data sets, in the light of the criticisms made of early data in Chapter 1, section 1.3, a more detailed comparison is made with the recent subset discussed in Chapter 1, section 1.3.3. General comment on the degree of similarity between the present data and the data included in the subset is initially made in a fairly qualitative way. However, in order to look more closely at the differences in shape in the distributions at these and higher energies, it is constructive to examine Legendre polynomial coefficients fitted to each of the data sets. The coefficients represent the magnitude of the various contributing shapes as shown to fourth order in figure 6.1.

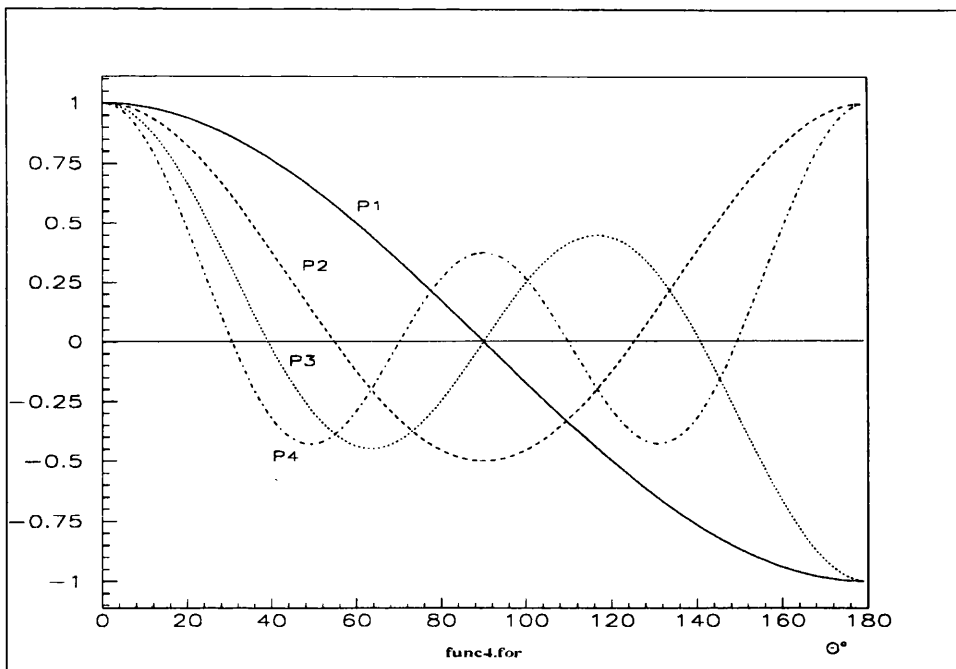


Figure 6.1: *The first four Legendre Polynomials*

### 6.1.2 Phenomenological Fits up to $E_\gamma=440$ MeV

Rossi *et al* [48] used all previous differential cross section data in the photon energy range 20 to 440 MeV and fitted it to a simple phenomenological function. The Bremsstrahlung data were re-normalised to the total cross section obtained by fitting only the data from monoenergetic photon experiments. The function used for the fit to the differential cross section in the centre-of-mass frame is a fourth order Legendre polynomial with coefficients  $A_l(E_\gamma)$ , ie:

$$\frac{d\sigma}{d\Omega} = \sum A_l(E_\gamma) P_l \cos(\theta) \quad (6.1)$$

where  $\theta$  is the c.m angle between the incoming photon and outgoing proton. The parameters in the function were varied to obtain a best fit in both energy and angle, to the data. The reduced  $\chi^2=0.9$  of the fit gives a measure of the level of consistency between experiments, this value indicating a very good agreement between the data and the phenomenological function. However, Jenkins *et al*

[49], commenting that the Rossi analysis used an incomplete treatment of errors have redone the fit, also to fourth order, using a method of  $\chi^2$  minimisation that accounts properly for statistical and systematic errors. They rejected extremely inconsistent data and obtained a  $\chi^2=2.0$ , which gives a better indication of the level of consistency in the data set and the agreements between the function and the data.

The present measurement total cross sections are shown together with the Jenkins [49] parameterisation up to  $E\gamma=440$  MeV in figure 6.2. The coefficients from the Legendre polynomial fits to the data are shown in comparison to the Jenkins coefficients in figure 6.3 (the  $A_0$  coefficient is omitted as it is directly proportional to the total cross section of figure 6.2). The values of the coefficients are given in Appendix B.

It can be seen from the total cross sections and the coefficients that both the absolute value and the shape of the differential cross sections are in reasonable agreement with the fit to previous published data. However, this is not a particularly meaningful comparison since the parameterisation has been obtained from sets of data among which there are still significant discrepancies. A far more meaningful comparison is with the subset of recent measurements discussed in Chapter 1, section 1.3.3. This comparison is examined in more detail in the next section. The parameterisation, however, as the average of many varying results may represent a fairly accurate guide. In figure 6.2, it is seen the DAPHNE data are lower than the parameterisation in the 200–260 MeV region where there exist the largest discrepancies in the overall data. However, there is good agreement within errors in the 260–350 MeV region where the greatest consistency has been observed in previous data.

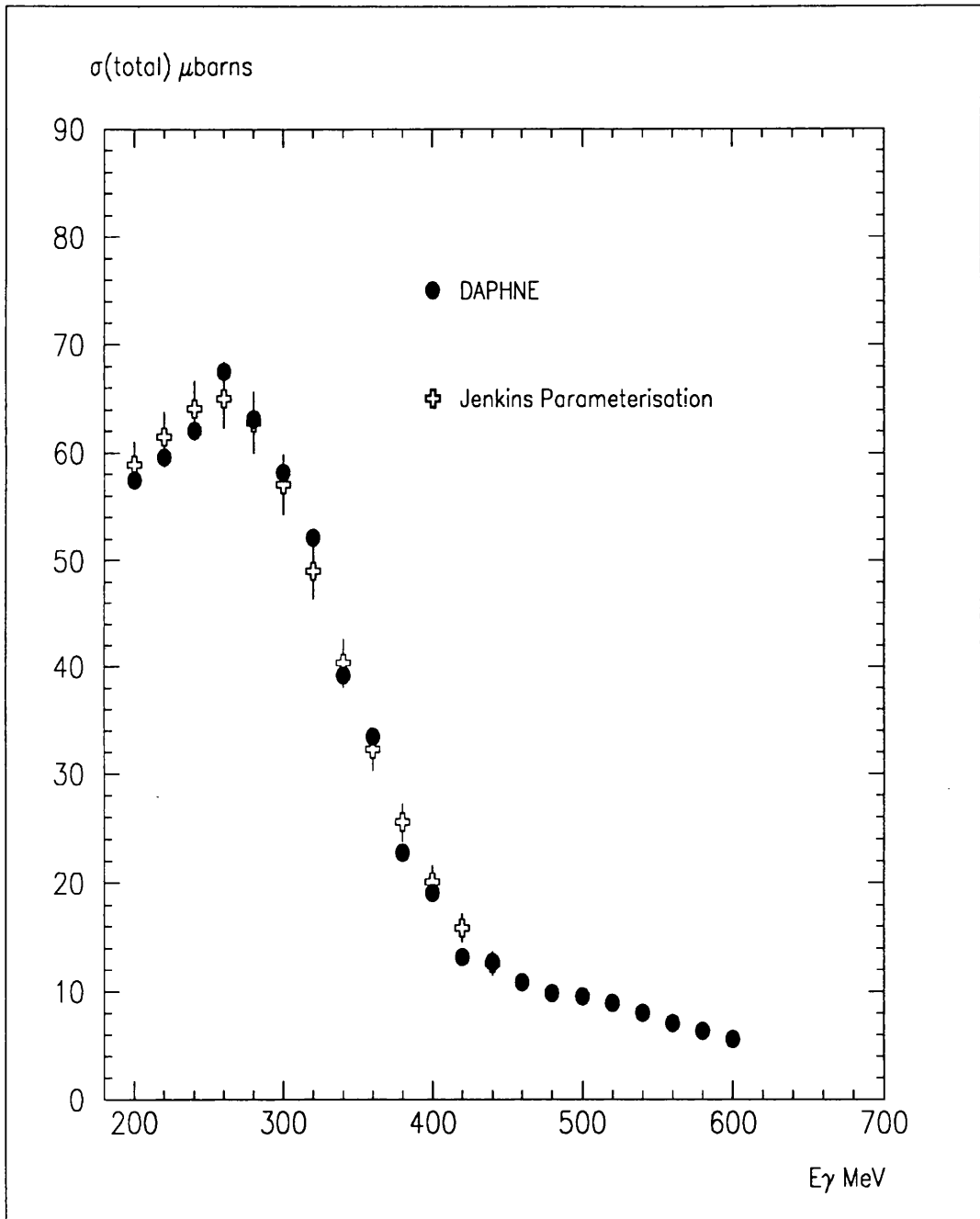


Figure 6.2: Total cross sections – Present data and parameterisation

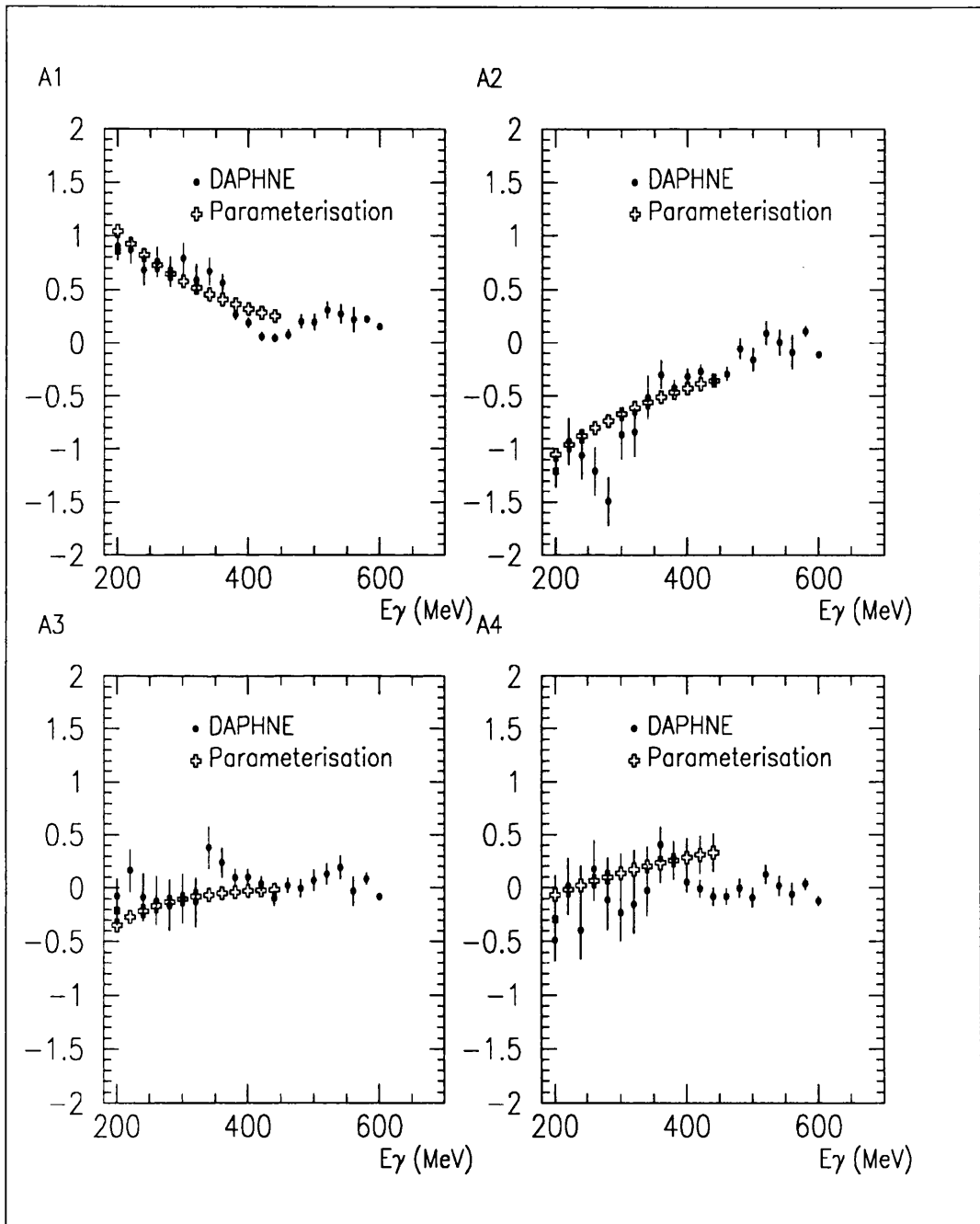


Figure 6.3: Legendre Polynomial coefficients of data and of parameterisation

### 6.1.3 Comparison with Recent Data to $E_\gamma=440$ MeV

The recent data subset in the photon energy range of this present experiment comprises data from the Bonn [25], Frascati [26], MIT [28], LEGS[29], and Tokyo [32] experiments. The Bonn data covers  $E_\gamma=200-440$  MeV, Frascati from 200–240 MeV, MIT is from 200–340 MeV, the LEGS measurements cover  $E_\gamma=200-260$  MeV and the Tokyo data are from 200–600 MeV. With the exception of the Tokyo measurements which comprise 3 or 4 data points at forward polar angles, all the data sets cover roughly the same angular range as the present measurement, from  $\sim 20^\circ$  to  $\sim 160^\circ$ . However, each of these sets of data comprises 7 or 8 angular measurements at about  $20^\circ$  intervals, whereas DAPHNE's large angular acceptance allowed the whole range to be covered simultaneously, with statistics permitting a  $5^\circ$  binning.

The total cross section measurements from this experiment are shown together with the other recent data in figure 6.4. The Lund data is included although it is not a recent experiment since it goes up to higher  $E_\gamma$  than other experiments. The situation within the recent data subset prior to the present experiment, was that there was reasonable agreement above 300 MeV but still relatively poor agreement in the 150–300 MeV region. In general, it is observed that the comparison of the present data with the Bonn, MIT, and Lund data in the photon energy range 300–440 MeV further reinforces the already good agreement. Below 300 MeV the present data agrees well with two of the measurements, LEGS and Bonn, within the quoted errors, whilst disagreeing with the others by 10–20 %, which is outwith their quoted uncertainty.

The differential cross sections from this experiment are compared with the subset in figures 6.5, 6.6, and 6.7. Only the statistical error and that system-

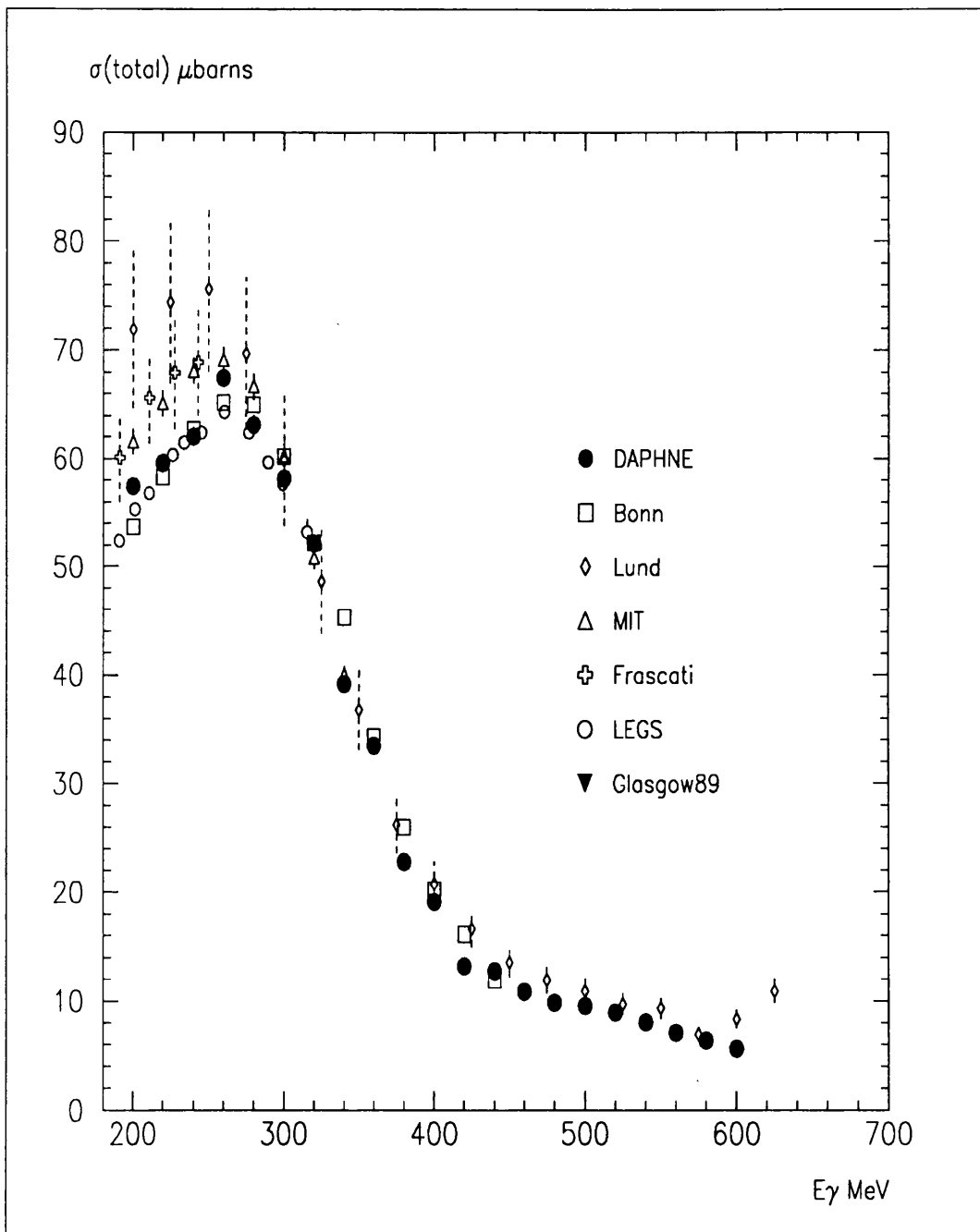


Figure 6.4: Total cross sections – Present and Recent data

atic error dependent on proton angle are shown. Since the measurements were not made at the same photon energies for each of the experiments, some interpolation of the data has been necessary. With reference to figure 6.5, for which  $E_\gamma=200-260$  MeV, in general, at these energies the shapes of the present differential cross sections are in reasonable agreement (to within 10%) with all the recent data sets. The major discrepancy is in absolute magnitude, and as already noted DAPHNE agrees better with the Bonn and LEGS data but has a 10-20% discrepancy with respect of the MIT and Frascati measurements.

At  $E_\gamma=260$  MeV, all the data sets agree very well in both shape and magnitude. There is only a slight discrepancy at forward angle, with LEGS and DAPHNE in good agreement but  $\sim 10\%$  lower than MIT and Bonn. In figure 6.6, for  $E_\gamma=280, 300$  and  $320$  MeV it is seen, the present data, MIT, and Bonn, and LEGS generally all agree fairly well, with the present data tending to be slightly lower at forward angles and again in best agreement with LEGS. For  $E_\gamma=340$  MeV (figure 6.6) and  $E_\gamma=360-420$  MeV (figure 6.7) larger discrepancies in comparison with the Bonn data appear. For 360 MeV and above, there is now  $15^\circ, 30^\circ, 40^\circ,$  and  $72^\circ$  Tokyo data but otherwise the Bonn data is the only other measurement to cover these photon energies. However, at 340 MeV which is the photon energy limit of the MIT experiment, DAPHNE and MIT agree well but are very different from Bonn which is more peaked in the middle angles. This is the characteristic difference that is seen as the photon energy increases. At  $E_\gamma=360$  MeV and 380 MeV, at forward angles the Tokyo data tends to be in better agreement with the present data than with Bonn. The angular distributions above 420 MeV are discussed in the next section but there is again the same feature apparent in the comparison of the present data with Bonn. The Bonn data at  $E_\gamma=440$  MeV are found to have several pronounced

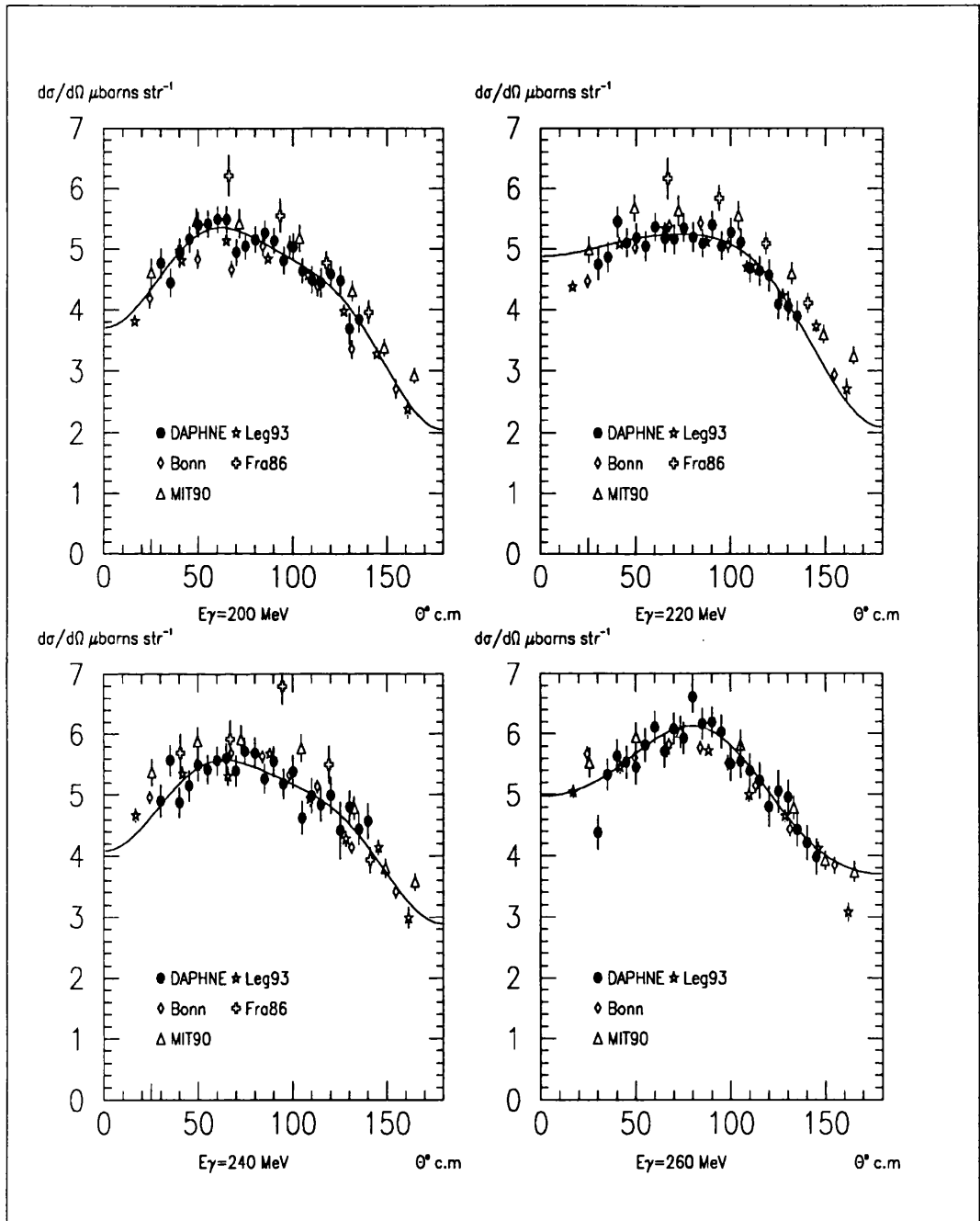


Figure 6.5: *Differential cross sections 200,220,240,260 MeV*

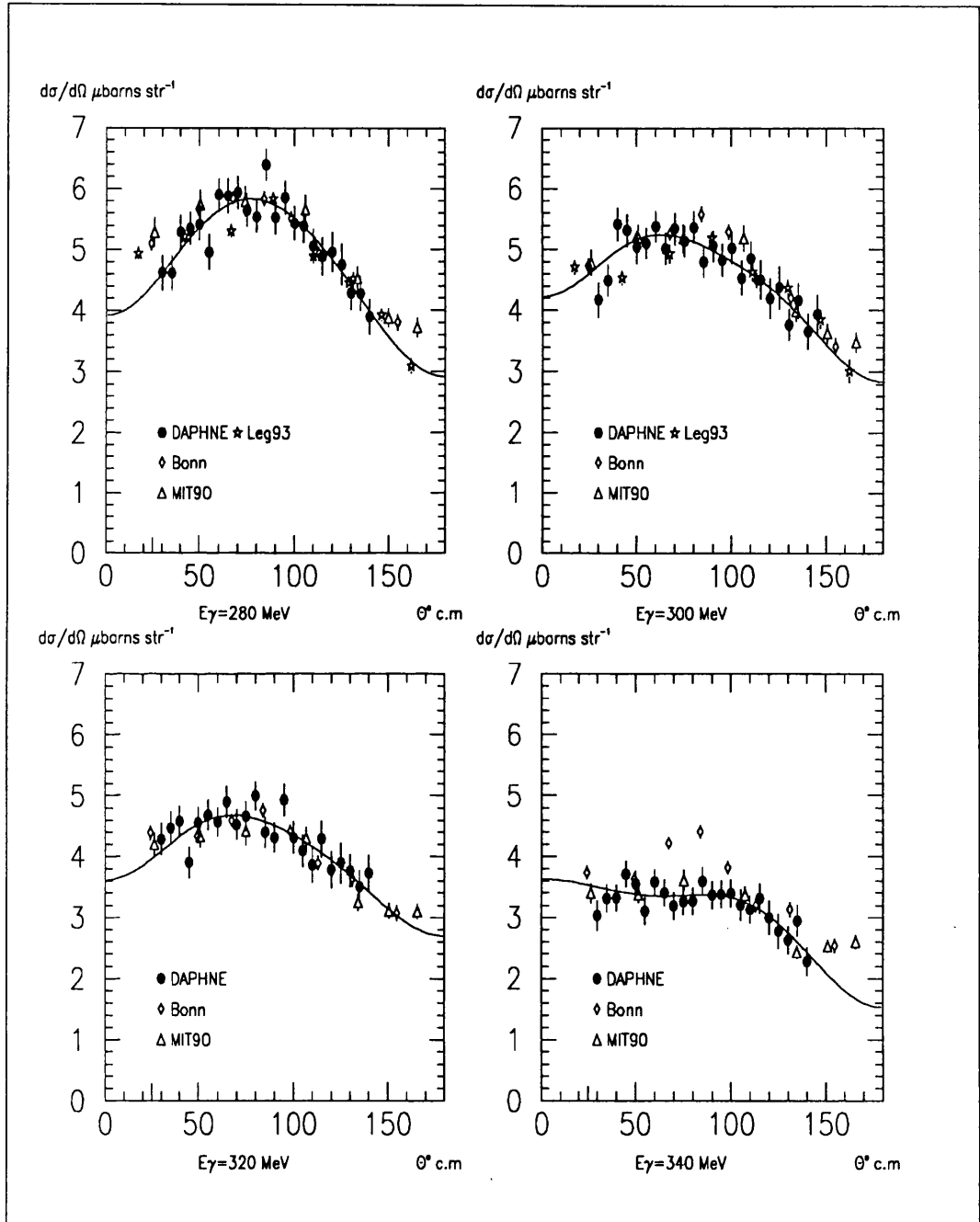


Figure 6.6: *Differential cross sections 280,300,320,340 MeV*

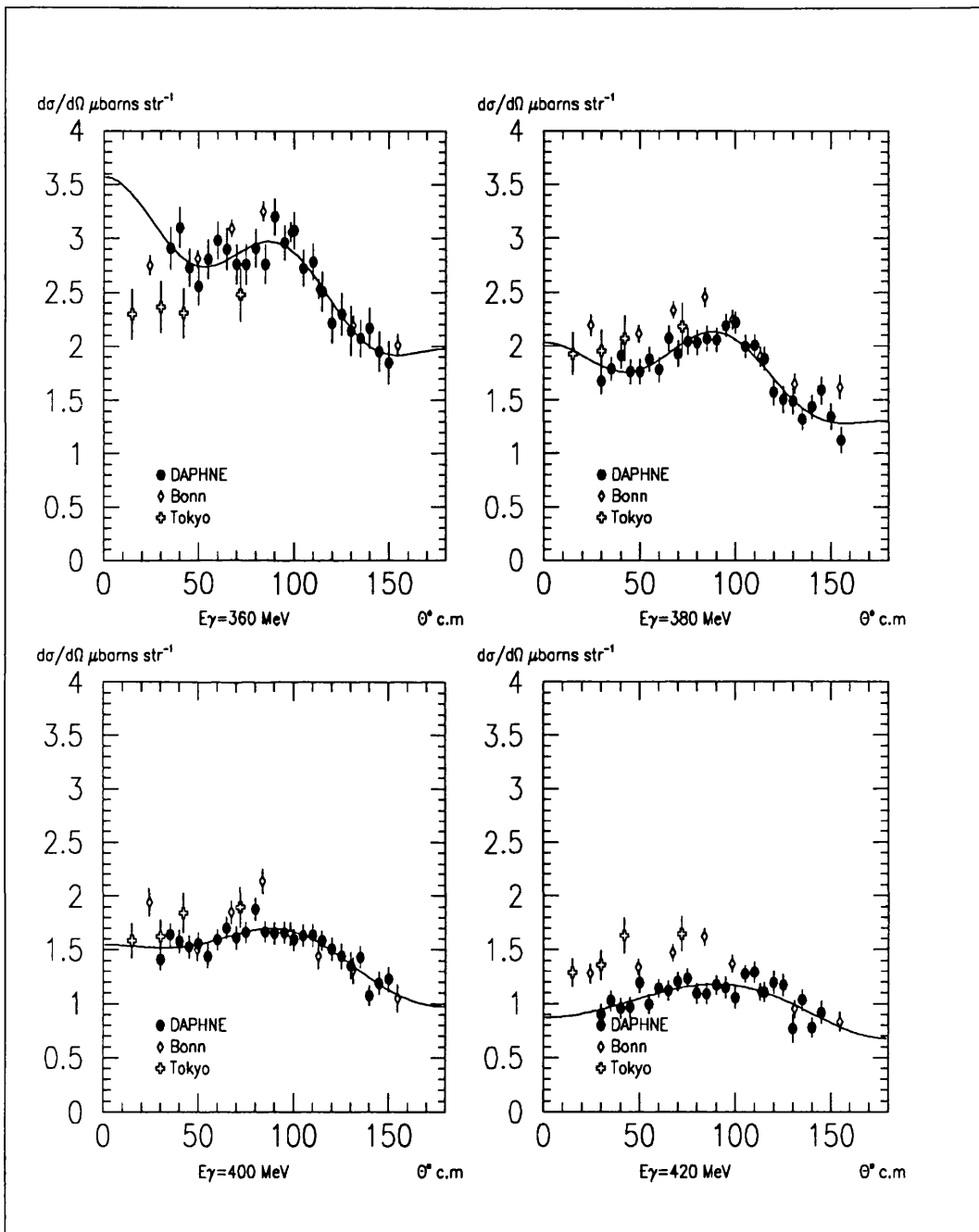


Figure 6.7: *Differential cross sections 360,380,400,420 MeV*

peaks, whereas the DAPHNE and the two other experiments, Lund [31] and Tokyo [32] are characterised by a single peak lying approximately in the middle of the angular range.

In order to look more closely at the difference in shape in the distributions Legendre polynomials were fitted to the MIT, Bonn, and LEGS data. This could not be done for the Tokyo data since it comprises only four points in a limited angular range. The coefficients are shown in figure 6.8 and allow a more quantitative comparison of the shapes.

A general remark that can be made on examining these coefficients is that the level of agreement among the measurements is better than that between any of the measurements and the parameterisation. The Bonn results have an  $A_4$  coefficient greater in magnitude than that for the present data. With reference back to figure 6.1, the  $A_4$  coefficient is characteristic of an angular distribution which is peaked in the centre and at extreme forward and backward angles, this corresponding to the difference in angular distribution between Bonn and DAPHNE for energies greater than 340 MeV.

The recent experiments can now be reassessed in the light of these comparisons. There is a better consistency amongst this recent data subset than amongst the complete set of existing data. This is attributable to the former having been performed with either quasi-monoenergetic photons or with improved untagged Bremsstrahlung techniques. The LEGS and Bonn experiments with which the present data agrees in magnitude within the region that previously had the largest discrepancies, both utilised tagged photons. The significant differences between the DAPHNE and Bonn angular distributions occur at photon energies where the  $D(\gamma, p)n\pi^0$  cross section is at its largest. This sug-

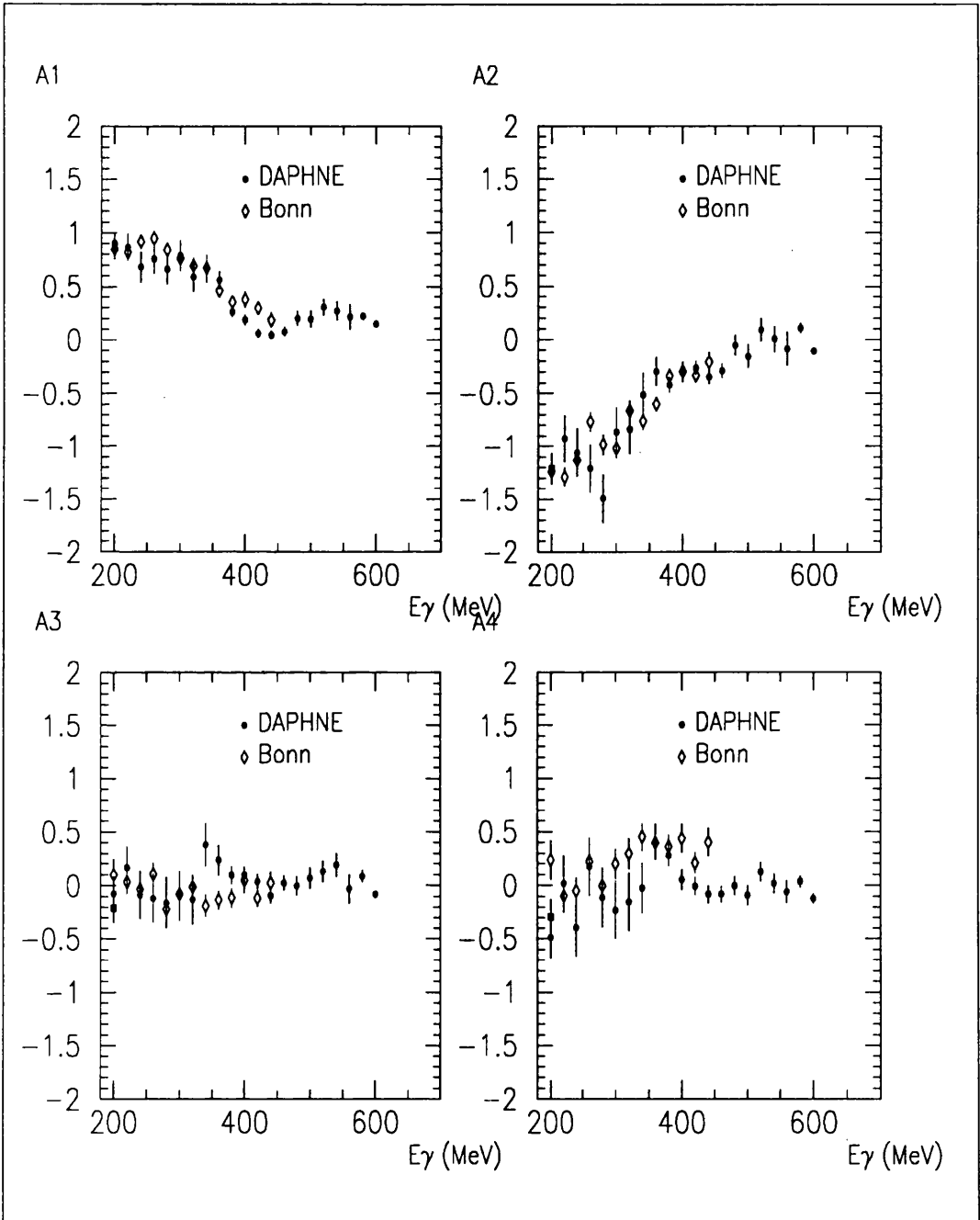


Figure 6.8: Legendre coefficients DAPHNE and Bonn data

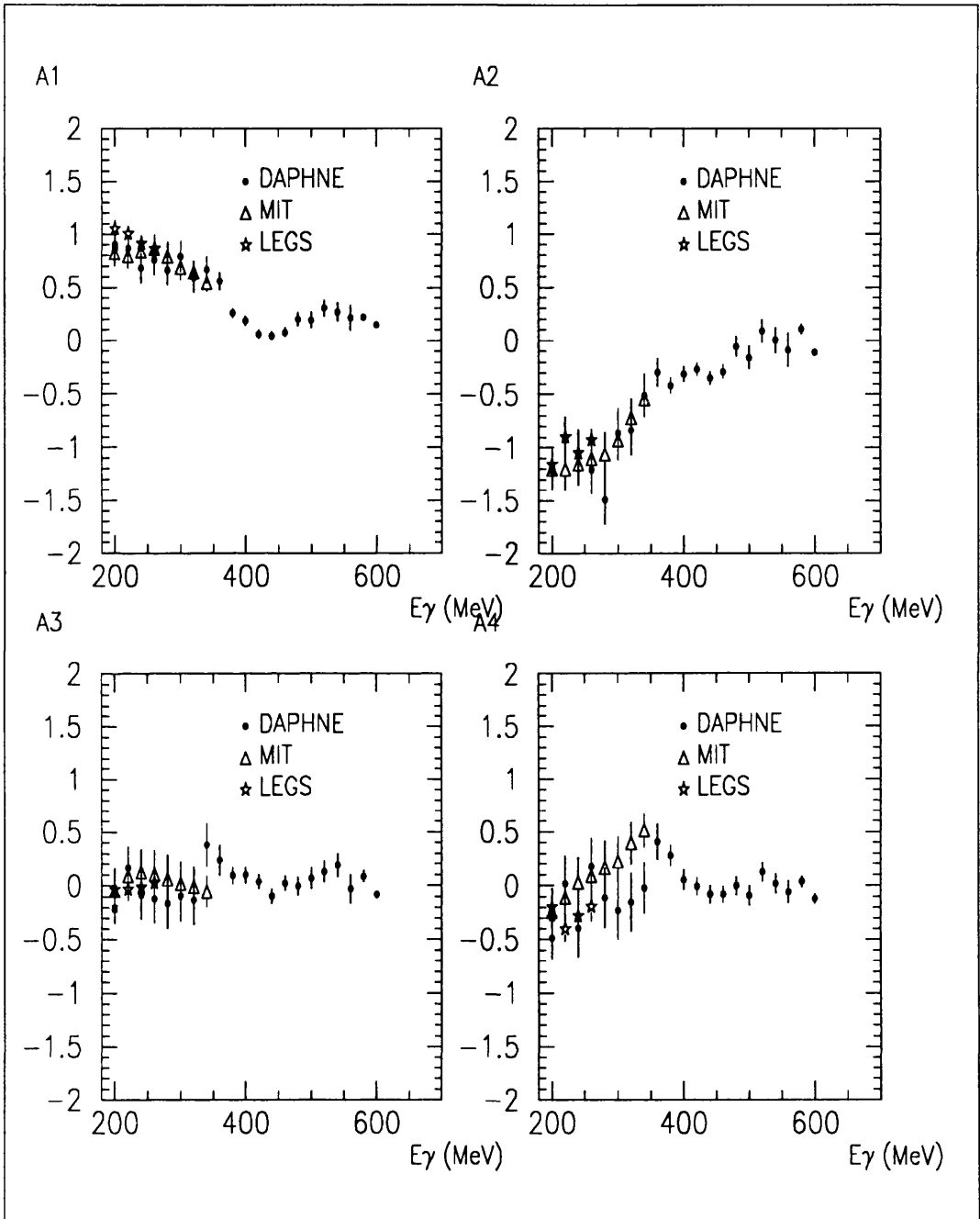


Figure 6.9: Legendre coefficients DAPHNE, MIT and LEGS data

gests they may not have separated  $D(\gamma, p)n\pi^0$  properly, although the example of a missing mass plot in their paper [25] shows a perfectly adequate separation. However, the example given was for an extreme forward angle detector and the discrepancies are largest for middle angles. The disagreement with MIT's absolute magnitude is probably due to the MIT measurement using untagged Bremsstrahlung. Their results are liable to have uncertainties in normalisation since their technique relies on the accuracy of the theoretical calculation of the Bremsstrahlung spectrum intensity. On the other hand, as a magnetic spectrometer was used to define angle, the shapes of their angular distributions are less susceptible to error. The Tokyo experiment employed tagged photons and also used a magnetic spectrometer to measure the proton momentum and angle precisely. It is therefore unlikely to be subject to uncertainties in normalisation or in angular distribution.

In summary; for the total cross section, three of the most recent measurements ie DAPHNE, Bonn and LEGS now agree within the quoted errors, although for energies above 320 MeV the shapes of the DAPHNE and Bonn data disagree in detail. In general, best consistency in total and angular distribution is found between the present data and the LEGS measurements. Clearly, the addition of the DAPHNE data to the pool of experimental measurements contributes significantly to the precision with which the  $D(\gamma, p)n$  cross section is known, and this will prove a valuable asset in comparing experiment with theory.

#### 6.1.4 Comparison with the Existing Data Set above $E_\gamma=440$ MeV

At energies above the peak of the  $\Delta$  resonance the results are compared with the little data that exist in figure 6.10 and figure 6.11. The existing data at higher energy comprises two very incomplete data sets from Lund [31] and Tokyo [32]. Again the measurements were not made at the same photon energies and angles for each of the experiments, therefore some interpolation has been necessary. Total cross sections are given from the Lund data and are included in figure 6.4. There is reasonable agreement between the present data and Lund from 300 to 400 MeV but below and above this energy range the total cross sections disagree significantly. For the differential cross section, the Lund data have fairly large error bars and a detailed comparison is difficult, although in general the data points overlap within errors.

The Tokyo data consists of three points on the angular distribution between  $30^\circ$  and  $72^\circ$  (there is one additional point at  $15^\circ$  at 440 MeV). The error bars are quite large and the measurements show no serious disagreements with DAPHNE. The present results constitute by far the most comprehensive measurement of  $D(\gamma,p)n$  in this energy range.

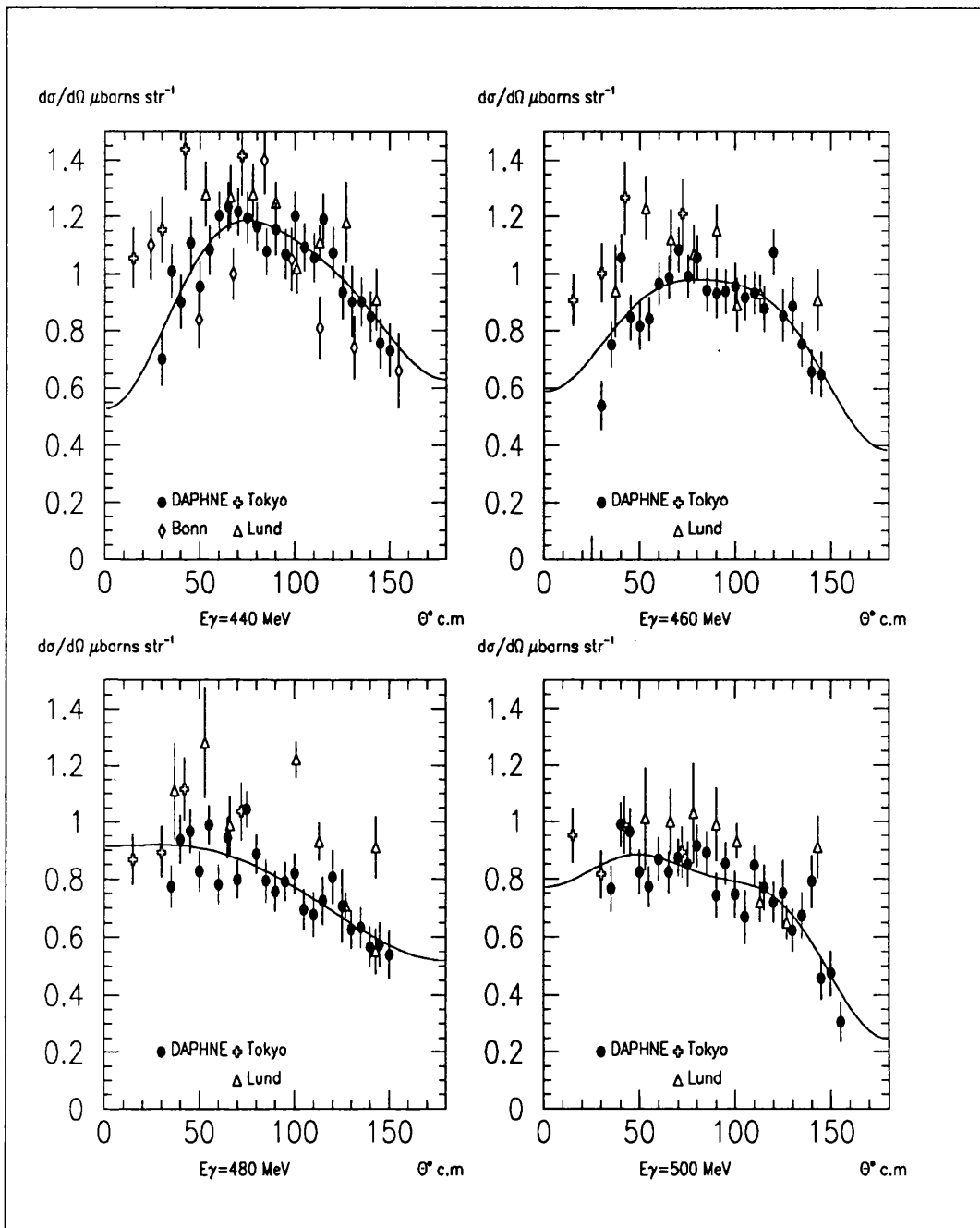


Figure 6.10: *Differential cross sections 440,460,480,500 MeV*

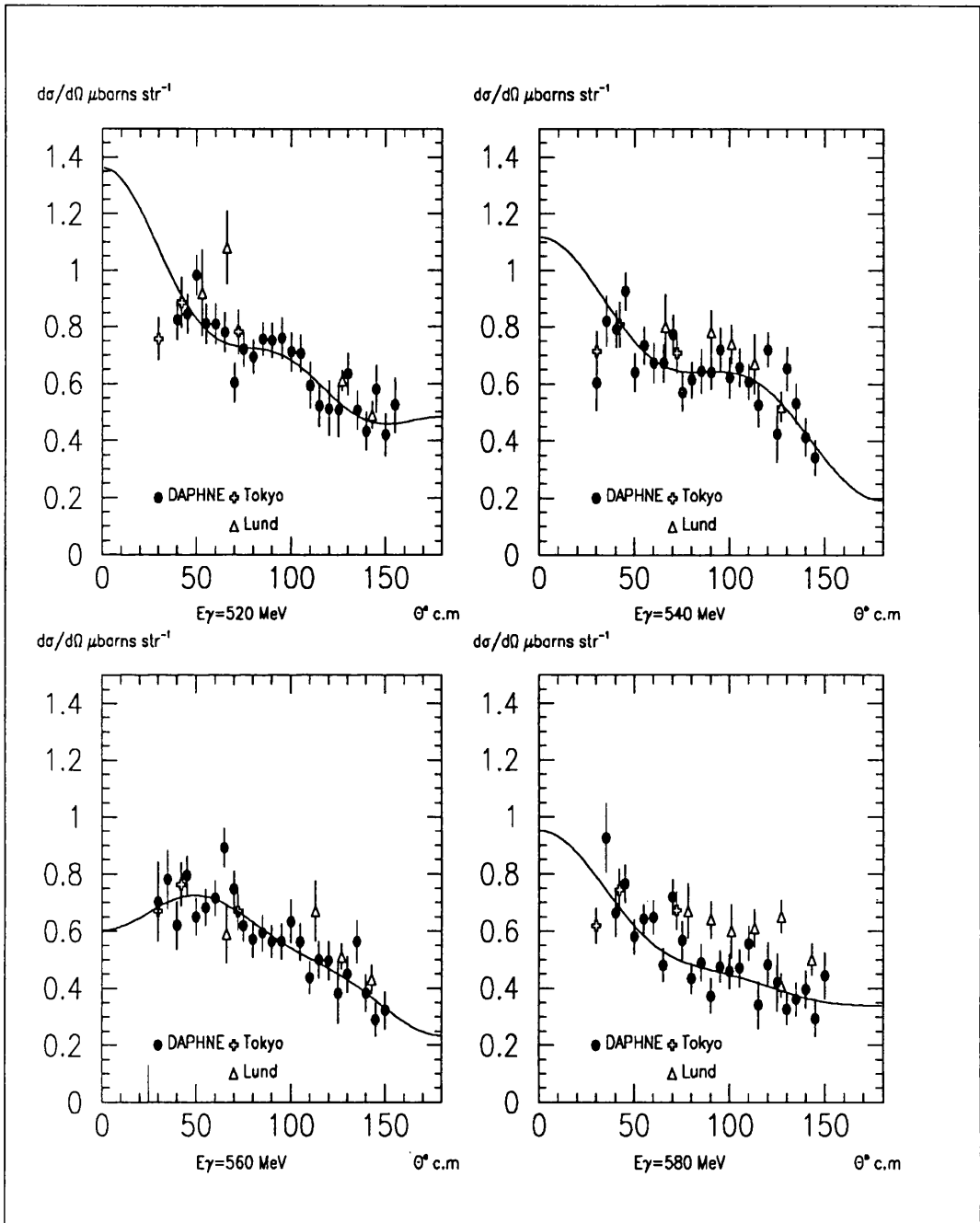


Figure 6.11: *Differential cross sections 520,540,560,580 MeV*

## 6.2 Comparison with Recent Theoretical Calculations

In Chapter 1, section 1.2.5, a brief review of recent theoretical calculations was made. The results from this experiment are now compared with a representative selection of these calculations. Above the  $\Delta$  region there is little previous data and theoretical work is at an early stage of development. Particular attention is paid to a comparison with two recent theoretical calculations by the Mainz group, one an impulse approximation treatment extending up to 800 MeV, and the other, a coupled channel approach for photon energies extending across the  $\Delta$  region to 400 MeV. Total cross section results for these two theoretical approaches are shown in figure 6.12, in comparison to the present results. Differential cross sections are shown in figures 6.13, 6.14, 6.15 and 6.16.

### Comparison with Impulse Approximation

An impulse approximation calculation was recently performed by Arenhövel's group [5]. Referring to figure 6.12, the theoretical results from the impulse approximation overestimate the DAPHNE data above 240 MeV. However, when comparison is made with the angular distributions in figures 6.13–6.16, in general there is a fair to very good reproduction of the shapes of the distributions, but an overestimation in magnitude, which increases systematically with photon energy. For a more quantitative comparison Legendre polynomial coefficients were fitted to each of the theoretical angular distributions. The coefficients are shown along with the DAPHNE data in figure 6.17. An extremely good agreement is found in the comparison of the coefficients  $A_1$  and  $A_2$ . There is also a reasonable agreement for the  $A_3$  coefficient, although the experimental values

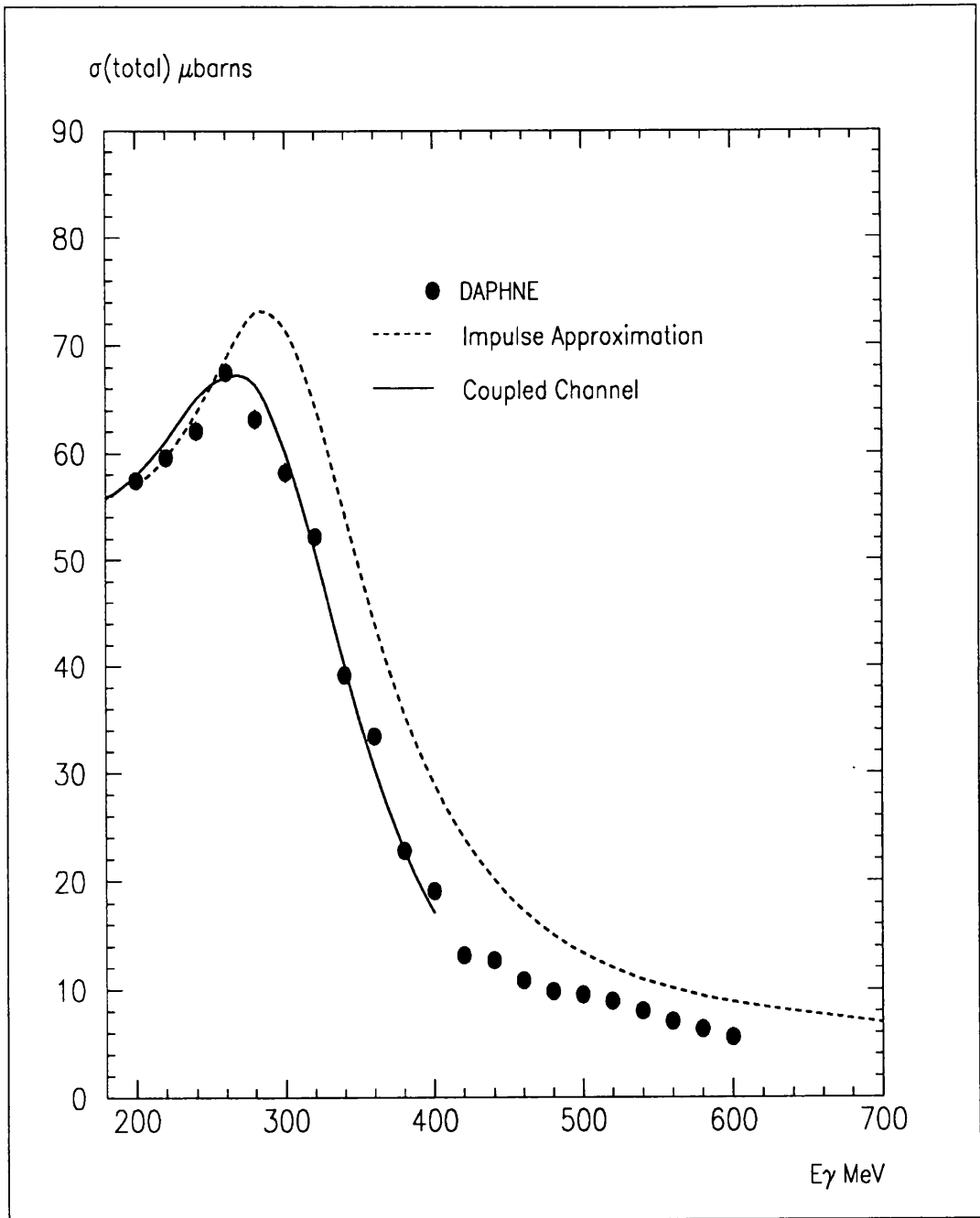


Figure 6.12: Theoretical Calculations of  $\sigma_{tot}$

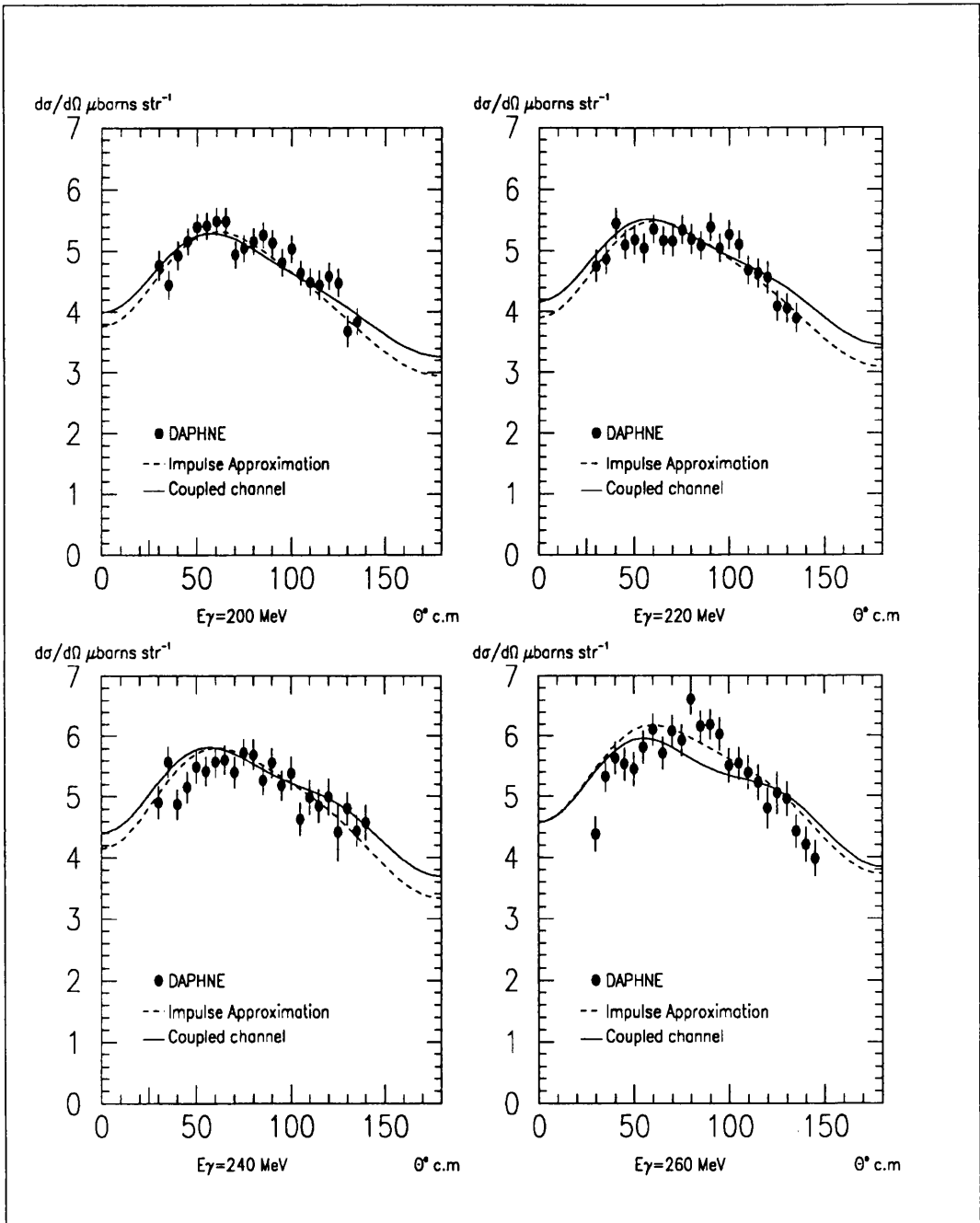


Figure 6.13: *Differential cross sections 200,220,240,260 MeV*

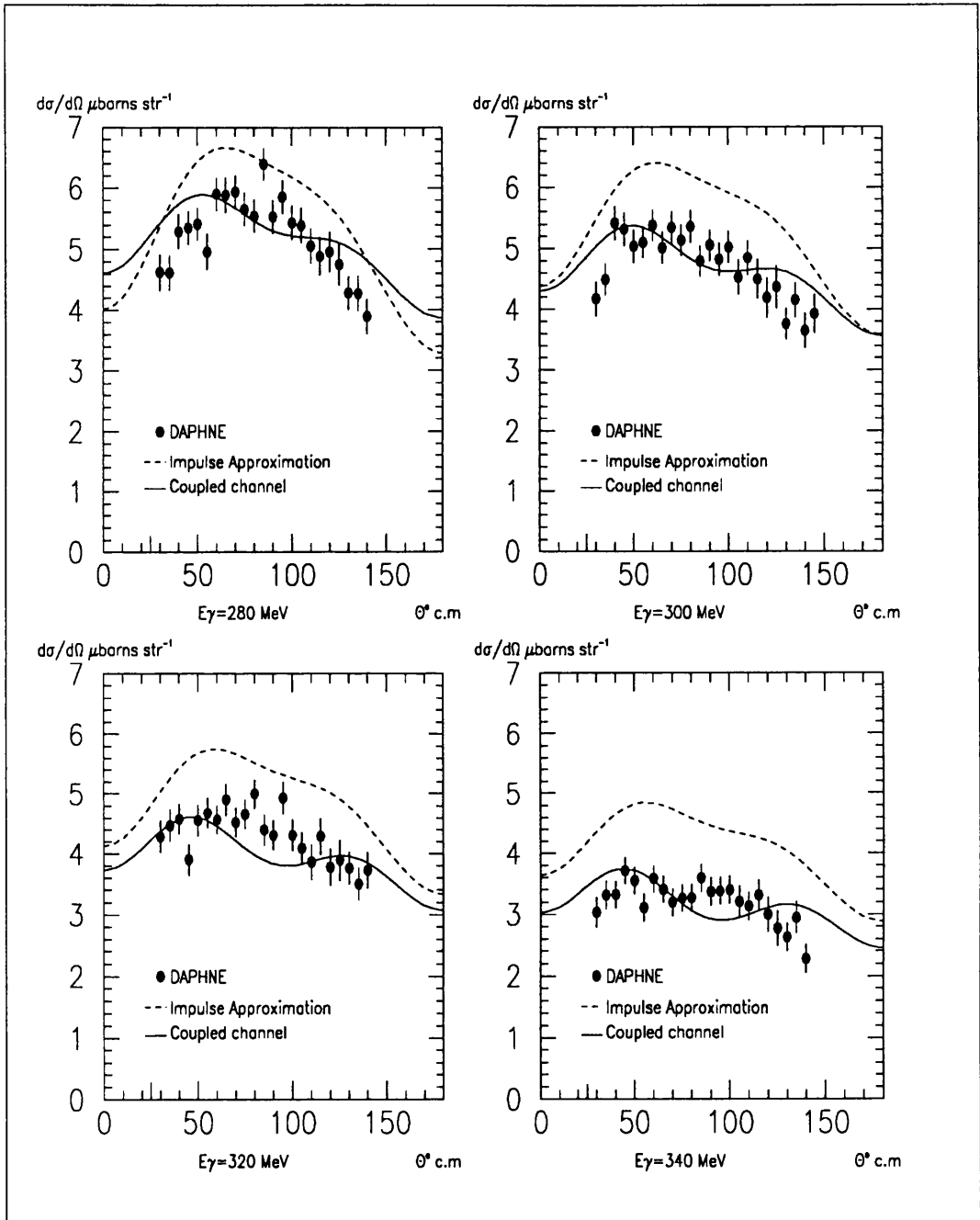


Figure 6.14: *Differential cross sections 280,300,320,340 MeV*

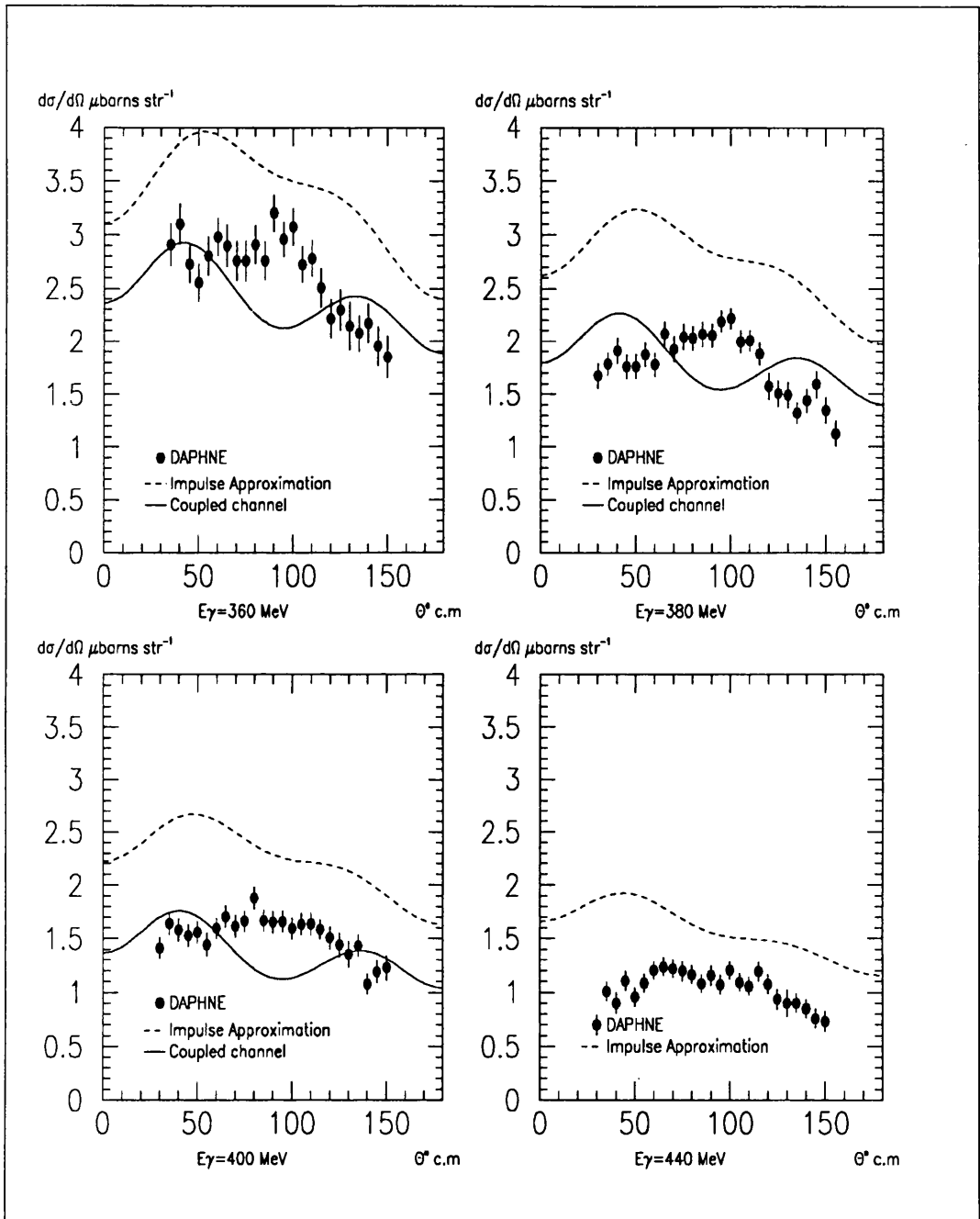


Figure 6.15: *Differential cross sections 360,380,400,440 MeV*

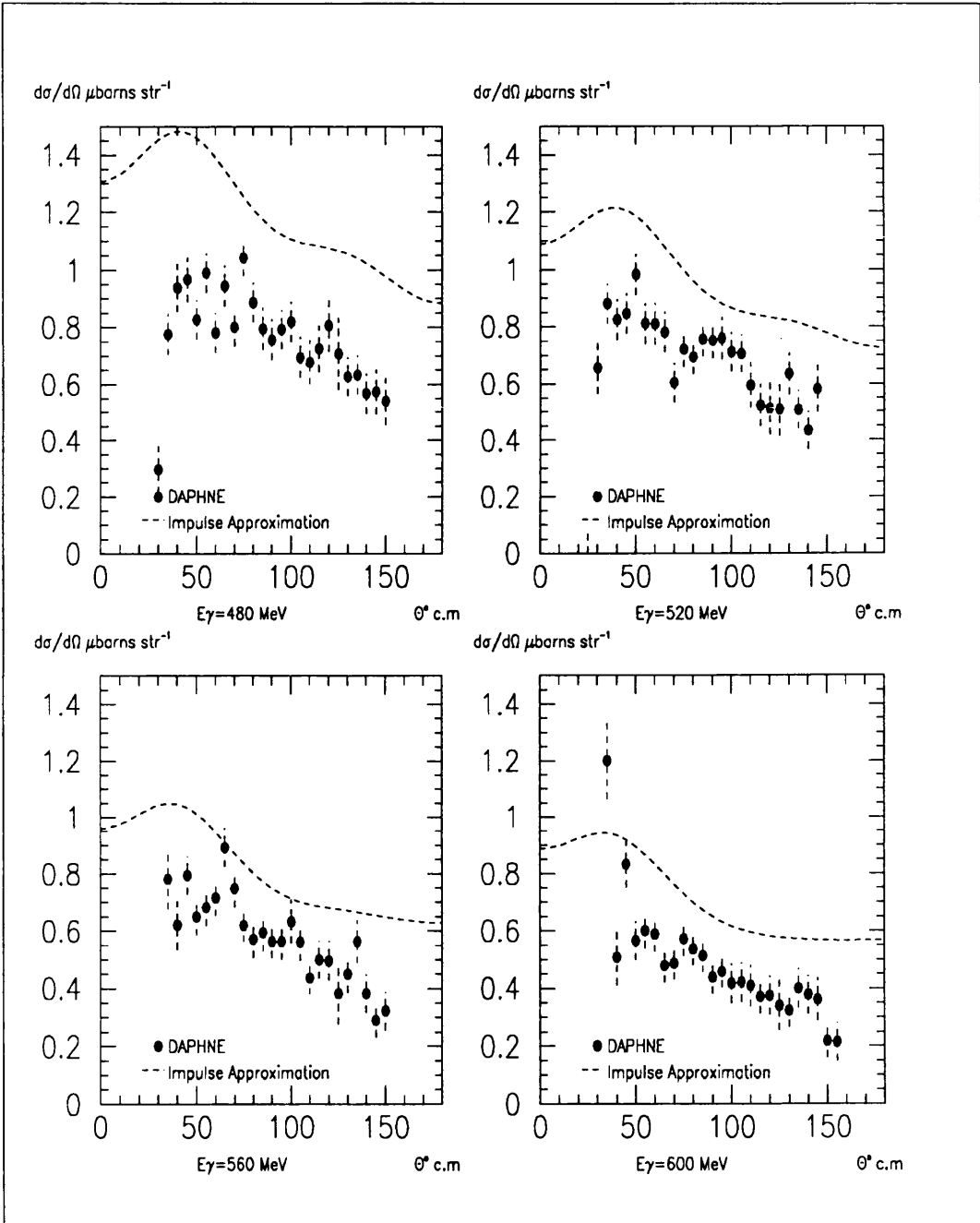


Figure 6.16: *Differential cross sections 480,520,460,600 MeV*

appear to have a more structured appearance with a distinctive change in sign around 300 MeV. There is a significant disagreement for  $A_4$  between 200 and 400 MeV, but rather good agreement above 400 MeV.

## Comparison with Coupled Channel Calculation

The data are also compared to a very recent coupled channel calculation covering the  $\Delta$ -resonance region performed by Arenhövel and Wilhelm [6]. With reference to figure 6.12, the total cross sections from this calculation agree very well in magnitude with the present data, within errors over the whole photon energy range with the exception of below 240 MeV where the theory overestimates the data by about 10 %. Legendre polynomial coefficients fitted to these theoretical angular distributions are shown in figure 6.18. The comparison is less compelling than that for the impulse approximation. There is a consistent discrepancy between the theoretical and experimental  $A_2$  coefficient which manifests itself as the dips seen in the calculations at middle angles in figures 6.14 and 6.15. The theoretical values for the  $A_1$ ,  $A_3$  and  $A_4$  coefficients are very similar for both the impulse approximation and coupled channels calculation.

## Ingredients of Calculations

Both theoretical calculations include:

a) one-body currents plus meson exchange currents as incorporated in the Siegert operators (for NN configurations),

b) explicit meson-exchange currents beyond the Siegert operators for NN,  $N\Delta$ , and  $\Delta\Delta$  configurations,

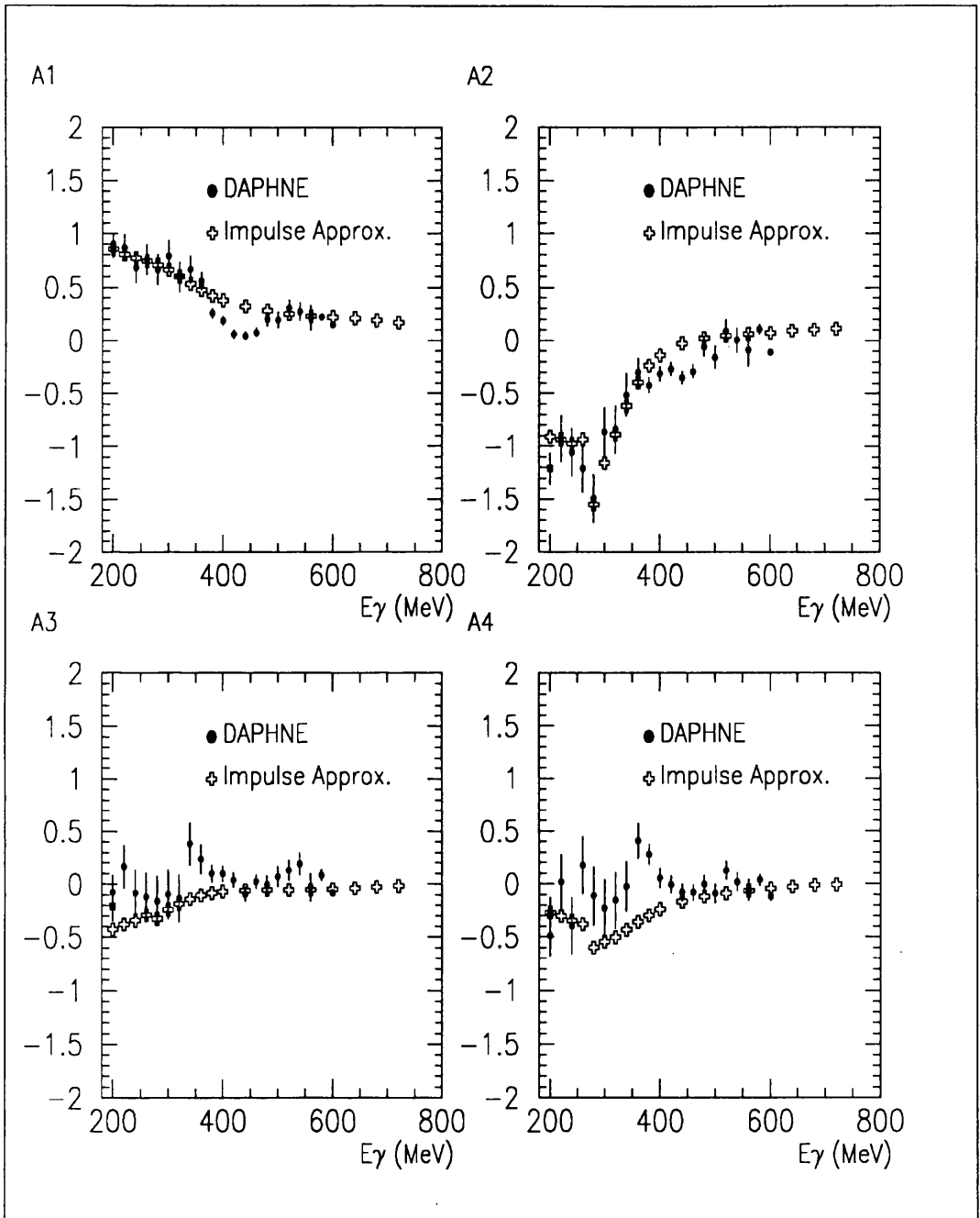


Figure 6.17: Comparison of Legendre coefficients from DAPHNE and the Impulse Approximation calculation

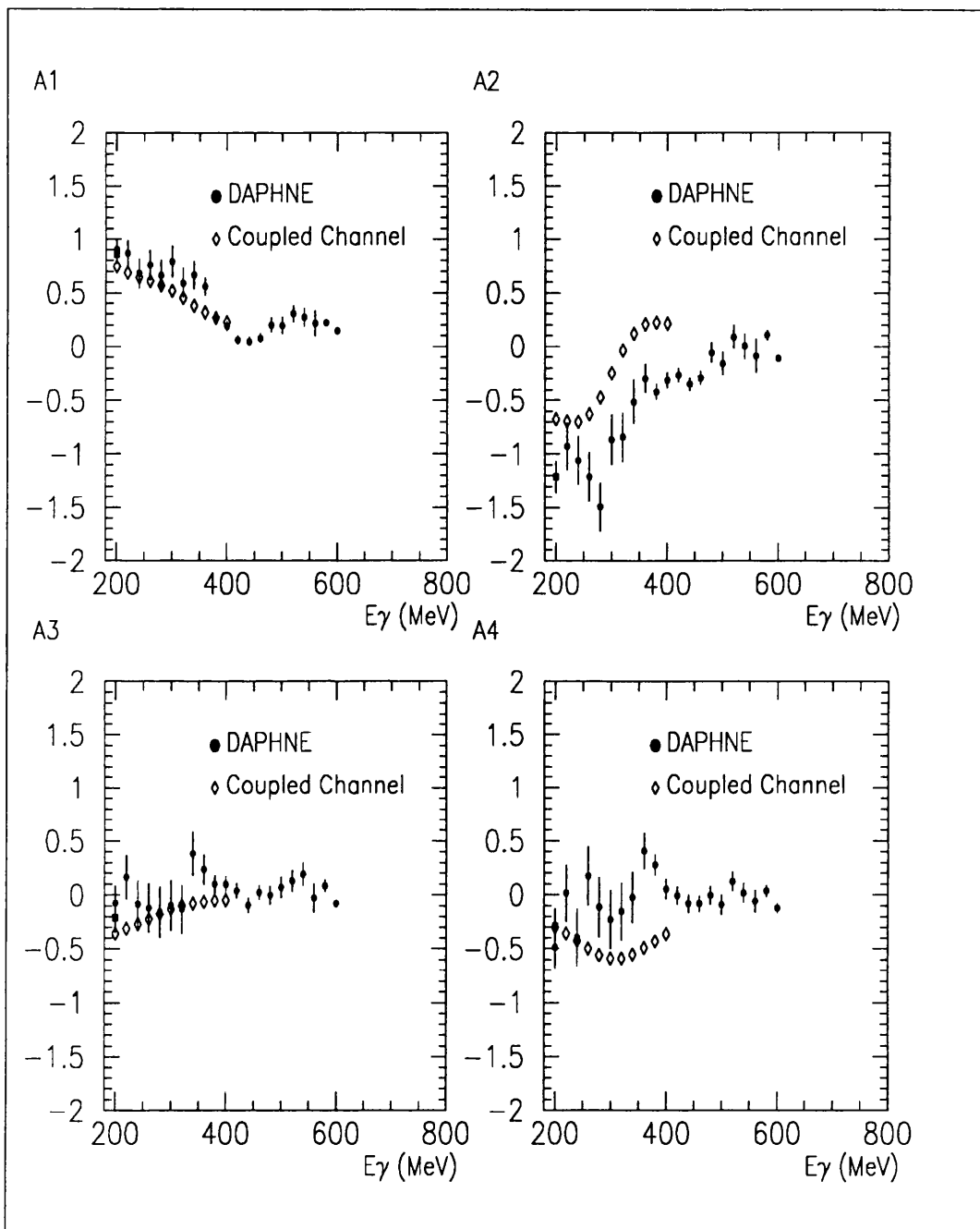


Figure 6.18: Comparison of Legendre coefficients from DAPHNE and the Coupled Channel calculation

c) relativistic corrections (spin-orbit).

The impulse approximation is a perturbative calculation for which the equations defining the nucleon and isobar wavefunctions can be obtained by taking into account only the first order components in the coupled channels representation, for which, the nucleon-nucleon and nucleon-delta transition amplitudes are defined in terms of each other, necessitating the simultaneous solution of a pair of coupled integral equations.

At present, both the theoretical approaches under discussion rely on some degree of phenomenological input. For example, in the coupled channel calculation the  $\pi N\Delta$  vertex is adjusted to fit the  $P_{33}$  phase shifts of  $\pi N$  scattering, and the  $N N$  potential is based on the OBEPR version (a One Boson Exchange potential used in non-relativistic treatments), but requires renormalisation to give a good description of the  $N N$  scattering phase shifts at low energies.

One of the most important considerations for calculations in the  $\Delta$  resonance region is the form of the photoabsorption mechanism which is dominated by magnetic dipole excitation. The corresponding nuclear current is fixed to fit the experimental  $M_{1+}(3/2)$  multipole amplitude of pion photoproduction on the nucleon, by adopting a theoretical amplitude containing a non-resonant Born term and a resonant part describing a  $\Delta$ -isobar excitation. If this amplitude is assumed to be valid for describing photoabsorption in the two nucleon system, as is pointed out by Tanabe and Ohta [50], it gives rise to two different processes, the  $\Delta$ -isobar excitation process and the pion-exchange current process.

It is found that, if the  $\gamma N\Delta$ -coupling is determined using the above procedure, the total cross section is too small, by as much as 30% between 200 and 270 MeV. However, in the approach adopted by Wilhelm and Arenhövel, the

explicit reference to the non-resonant term is omitted and instead it is effectively incorporated into a modified  $\gamma N\Delta$ -coupling. This is the basis of the coupled channel calculation which is compared with the present data, and which gives a very good fit to the experimental total cross section in particular. By implication it appears that a theoretical framework based on static pion exchange currents (described by the non-resonant term) provides an inappropriate description of deuteron photodisintegration in the  $\Delta$  resonance region. Although the modified  $\gamma N\Delta$ -coupling gives a good description of the total cross section, problems with the shape of the angular distribution still remain, since a dip is found at  $90^\circ$  which is not apparent in the data. It seems likely this dip structure is produced by the  $N\Delta$  configurations in high order final state partial waves, which although important for the differential cross section are negligible in the total cross section.

Although the calculations referred to in the foregoing discussion are some of the most comprehensive available, it is recognised they are still incomplete. For example, a complete treatment of retardation effects and relativistic corrections must still be applied. Clearly, developments and improvements in the theory are very dependent on data of good quality and the present data with its high precision and wide range of energy covered, represents a significant addition to the experimental determination of the total and differential two-body photodisintegration cross section of the deuteron.

# **Chapter 7**

## **Conclusions**

## 7.1 Conclusions

The total and differential cross sections for the two-body photodisintegration of deuterium have been measured over the angular range  $25^\circ$ – $155^\circ$  for photon energies 200–600 MeV. The analysis has achieved systematic and statistical errors of a few percent and has extended the range of photon energies for which data are available from 400 to 600 MeV. The data presented by this measurement are more extensive in photon energy and angular acceptance than any previous measurement, the majority of which ranged up to 350 MeV with a few data sets extending higher. The present measurements, which overdetermined the reaction kinematics provided good rejection of competing channels and background over the whole 200–600 MeV photon energy range.

In the previous chapter earlier experimental work was reassessed in the light of the present results and the results compared with recent theoretical calculations by the Mainz group. Three of the most recent measurements ie DAPHNE, Bonn and LEGS now agree within the quoted errors. It was found that there is better consistency amongst the recent data subset than amongst the complete set of existing data as represented by the parameterisation. Clearly, the addition of the DAPHNE data to the pool of experimental measurements contributes significantly to the precision with which the  $D(\gamma,p)n$  cross section is known.

Above the  $\Delta$  region there is little previous data and theoretical work is at an early stage of development. Comparisons were made with two recent theoretical calculations by the Mainz group, one an impulse approximation treatment extending up to 800 MeV, and the other, a coupled channel approach for photon energies extending across the  $\Delta$  region to 400 MeV. The impulse approximation

was seen to show a good agreement for the shapes of the angular distributions, but an overestimation in magnitude, which increases systematically with photon energy. The total cross sections from the coupled channel calculation agree very well in magnitude with the DAPHNE data, whereas the comparison in angular distribution is less convincing than that for the impulse approximation.

Although the calculations referred to in the discussion of Chapter 6 are some of the most comprehensive available, it is recognised they are still incomplete. For example, a complete treatment of retardation effects and relativistic corrections must still be applied. Clearly, developments and improvements in the theory are very dependent on data of good quality and the present data with its high precision and wide range of energy covered, represents a significant addition to the experimental determination of the total and differential two-body photodisintegration cross-section of the deuteron.

The  $D(\gamma,p)n$  cross section data presented in this thesis covered the photon energy range from 200–600 MeV. Data were in fact taken across the whole of the 100–800 MeV energy range and a preliminary analysis of the cross sections at photon energies 600–800 MeV has been undertaken. Methods for particle discrimination and rejection of background are still needed in this energy region, but in the near future the analysis of the DAPHNE data will extend the full range from 100–800 MeV.

As was pointed out in section 1.5, the present facility comprising the microtron, tagging spectrometer and DAPHNE has the potential to measure the photon asymmetry for the  $D(\gamma,p)n$  reaction, and Appendix C confirms that the production of linearly polarised photons from coherent Bremsstrahlung with a useable degree of polarisation, has already been achieved. The measurement of

the photon asymmetry at Mainz is a natural extension to the data presented in this thesis. Should an aligned deuterium target and circularly polarised photon beam, both of which are technically feasible, become available at Mainz, in principle it would then be possible to measure target asymmetries for unpolarised, linearly polarised and circularly polarised photons. The resulting set of polarisation observables would, together with the total and differential cross sections represent the most comprehensive investigation of the  $D(\gamma,p)n$  reaction undertaken to date. Such data would be an invaluable adjunct to future theoretical treatments of deuteron photodisintegration.

# Appendix A

## The Range Method

A RANGE TELESCOPE TECHNIQUE FOR PARTICLE DISCRIMINATION  
AND ENERGY RECONSTRUCTION

**DAPHNE Collaboration**

A. Braghieri <sup>1</sup>, P. Pedroni, T. Pinelli

*INFN, Sezione di Pavia, Via Bassi 6, 27100 Pavia, Italy*

G. Audit, N. D'Hose, V. Isbert <sup>2</sup>, S. Kerhoas, M. Mac Cormick, L. Y. Murphy,

G. Tamas

*SPhN-DAPNIA C.E.N. Saclay, 91191 Gif sur Yvette, France*

R. Crawford

*Kelvin Laboratory, University of Glasgow, UK, Scotland*

---

<sup>1</sup> present address *SPhN-DAPNIA C.E.N. Saclay*

<sup>2</sup> present address *Institut für KERNPHYSIK der Universität MAINZ*

**Abstract**

We present an analysis technique ('Range Method') that optimises particle discrimination and enables energy reconstruction using a sampling detector. The method is a powerful extension of the well known  $dE/dx - E$  technique in which the energy loss rate measured by several scintillator layers is fitted on the theoretical Energy-Range curves. The general features of the method will be discussed and its application to nuclear physics investigations at intermediate energies with the DAPHNE detector. Momentum reconstruction for protons with a resolution of  $\Delta P/P = 2.5 - 10\%$  (FWHM) in the range  $P = 300 - 900 \text{ MeV}/c$  has been obtained.

## 1. General Method

The Range Method is based on the Energy-Range correlation that can be deduced from the Bethe-Bloch equation. For a given particle and a given material the correlation is well known and can be parametrized with a regular function. let us say  $R = g(E)$ . With the help of the  $g$ -function it is easy to calculate the energies deposited in a sampling detector.

We consider a detector consisting of  $N$  layers which are both active and passive (fig. 1), of known thickness and for which the relative Energy-Range functions  $g_i$  are known ( $i = 1, 2, \dots, N$ ). Let us consider a particle of kinetic energy  $E_0$  that enters the detector. We define  $E_i^{in}$  and  $E_i^{out}$  as the energy at the entrance and at the exit of the generic  $i^{th}$  layer respectively. It follows immediately that:

$$E_i^{in} = E_0 \quad \text{for } i = 1 \quad (1a)$$

$$E_i^{in} = E_{i-1}^{out} \quad \text{for } i > 1 \quad (1b)$$

In correspondence to the  $i^{th}$  layer, the particle has a residual range  $R_i$  given by:

$$R_i = g_i(E_i^{in}) \quad (2)$$

Thus, the outgoing energy  $E_i^{out}$  can be easily calculated:

$$E_i^{out} = g_i^{-1}(R_i - \delta_i) \quad (3)$$

where the  $g$ -function has been inverted and  $\delta_i$  is the path inside the layer. The latter can be calculated by knowing the thickness of the layer and the emission angles  $\vartheta$  and  $\varphi$  of the particle, with simple geometrical considerations.

From (2) and (3) it follows that the energy  $\Delta E_i$  released by the particle in the  $i^{th}$  layer is:

$$\Delta E_i = E_i^{in} - g_i^{-1}(g_i(E_i^{in}) - \delta_i) \quad (4)$$

Equation (4) is sequentially applied in order to calculate the energy deposited in each layer, active or passive, until the initial energy  $E_0$  has been distributed.

The layer  $n$  in which the particle comes to rest is given by:

$$g_n(E_n^{in}) - \delta_n < 0 \quad (5)$$

with a deposited energy  $\Delta E_n = E_n^{in}$ .

In order to determine the unknown energy  $E_0$  of a particle using the energy losses measured by the active layers we have to minimize, with respect to  $E_0$ , the quantity:

$$\chi^2 = \frac{1}{N-1} \sum_{\ell=1}^N \frac{|\Delta E_{\ell} - \Delta E_{\ell}^{exp}|^2}{\sigma_{\ell}^2} \quad (6)$$

where  $\Delta E_{\ell}$  is the energy deposited in the  $\ell^{th}$  layer as calculated from (4);  $\Delta E_{\ell}^{exp}$  and  $\sigma_{\ell}$  are respectively the experimental measure and its resolution.

Here the index  $\ell$  only runs over the active layers crossed.  $N$  denotes the last layer in which the particle gave a signal (stopping channel). The presence of the intermediate absorbers is implicitly contained in equation (6) as we have to iterate with equation (4) over all the layers.

The minimization is performed using the standard routines of the Least Square Fit. The only free parameter in (6) is the energy  $E_0$ , therefore the fit needs at least two energy measures. The stopping channel allows a first estimation of  $E_0$ .

We can run the minimisation with different sets of  $g$ -functions appropriate to various particles ( $\pi$ ,  $p$ ,  $d$ ). For each case the  $\chi^2$  value (6) allows a discrimination of the type of particle in that a good fit is expected to yield a low  $\chi^2$ .

The principle of the Range Method is quite general and can be successfully applied to a great variety of layered detectors. There are however some necessary conditions that one must bear in mind:

- a) the measured energies  $\Delta E_{\ell}^{exp}$  are affected by quenching and the corresponding calculated quantity  $\Delta E_{\ell}$  must be corrected for this effect;
- b) the intrinsic energy resolution  $\sigma_{\ell}$  of each layer has to be determined;

- c) particle discrimination requires an appropriate cut on the  $\chi^2$  distribution;
- d) the cut on the  $\chi^2$  distribution determines the discrimination efficiency of a given particle and must be evaluated experimentally or by simulation.

All these parameters are strongly dependent on the detector. As a consequence, the performances of the Range Method (particle discrimination capability and momentum resolution) varies according to the geometry and the intrinsic characteristics of a particular device.

In the following sections we will describe the application of the Range Method to the DAPHNE detector. In particular the problems related to the previous considerations will be pointed out as a guide for other kinds of detectors.

## 2. Application to the DAPHNE detector

The Range Method was specially developed for the DAPHNE detector [1], a large solid angle hadron detector capable of handling multiparticle final states. It consists essentially of three coaxial sections (fig. 2):

- a) a set of 3 cylindrical MWPCs for charged particle tracking,
- b) a three layered scintillator calorimeter, 10 mm, 100 mm and 5 mm thick (A, B and C layer)
- c) a scintillator/lead sandwich for  $\pi^0$  detection, with three active layers (D, E and F), 5 mm thick.

Each layer is segmented into 16 longitudinal bars. It follows that the coverage of the azimuthal angular range is complete; the lengths of the bars are arranged so as to subtend a range of angles in the polar direction  $\vartheta$  from  $21^\circ$  to  $159^\circ$  which corresponds to 94% of  $4\pi$  sr.

The detector operates with the tagged photon beam facility at MAMI [2],

which provides photons up to  $E_\gamma = 800 \text{ MeV}$  and has performed a variety of intermediate photonuclear experiments on light nuclei.

The calorimeter stops protons up to  $P = 500 - 688 \text{ MeV}/c$  and pions up to  $P = 138 - 219 \text{ MeV}/c$  depending on the  $\vartheta$  emission angle ( $\vartheta = 90^\circ - 21^\circ$ ). The thin C layer, in anticoincidence with A and B, allows to select stopped particles ( $ABC$ ).

Particles of higher momenta pass through the B layer and deposit energy also in the subsequent section devoted to  $\pi^0$  detection. An important amount of energy is released in the absorber layers but additional information, other than A, B and C, are available from the 3 thin active layers (D,E,F) placed between the absorbers.

### 2.1. Energy calibration

The light attenuation effects of each scintillator module were determined with cosmic rays. The complete ADC calibration and the energy resolutions were obtained using the following two-body reactions:

$$\gamma + {}^1\text{H} \rightarrow p + \pi^0 \quad (7a)$$

$$\gamma + {}^1\text{H} \rightarrow n + \pi^+ \quad (7b)$$

$$\gamma + {}^2\text{H} \rightarrow p + n \quad (7c)$$

We measure the photon energy and the emission angle  $\vartheta$  of the charged particles with resolutions of  $\Delta E_\gamma = 2 \text{ MeV}$  [3] and  $\Delta\vartheta < 1^\circ$  respectively [1]. Thus, the kinematics of each reaction is determined with great precision and the response of scintillators for protons and pions of a given energy can be studied.

The quenching effects for protons were taken into account using the parametrisation given by Cecil et al. [4], which was found to be accurate for our scintillators.

Figures 3 and 4 shown an example of the energy calibration for a scintillator module, obtained with pions and protons respectively. The ADC value, corrected for attenuation, is reported as a function of the energy loss.

Typical resolutions at the m.i.p. point are  $\sigma/\Delta E = 10\%$  for a B module (100 mm thick) and  $\sigma/\Delta E = 16\%$  for the 5 mm scintillators.

## 2.2. Particle Discrimination with the Range Method

The  $\chi^2$  cut for particle discrimination was determined experimentally from data obtained with a hydrogen target. The Range Method was applied twice to each charged track, using the g-functions for protons (Proton Range) and pions (Pion Range). The correlation between the two values of  $\chi^2$  is shown in fig. 5: the axes are the Proton Range  $\chi^2$  and the Pion Range  $\chi^2$ . Thus we can recognise the pions along the x-axis and the protons along y-axis. The events in the middle are a mixture of protons and pions that have undergone a hadronic interaction inside the detector.

We have chosen the condition  $\chi^2 < 2$ , shown in the outlined regions, in order to unambiguously discriminate protons and pions.

The contaminations were estimated by selecting a clean sample of protons and pions. A subset of protons have been isolated by imposing a coincidence between a charged track and a  $\pi^0$ . The signature of the  $\pi^0$  is given by two photons detected with the lead/scintillator sandwich. Charged events at backward angles allow us to exclusively select pions, as the limit angle of the protons is  $\vartheta \cong 60^\circ$ .

We give as an example the pion contamination for proton identification. The selected pions were reconstructed with the Proton Range and in fig. 6 we show the corresponding  $\chi^2$  distribution. The number of pions that fulfil the Proton Range

(shaded area) is less than 0.5%.

### 2.3. Discrimination for high energy particles

A special treatment was adopted for particles that cross the detector and go out without stopping (ABCDEF events). This case occurs for protons of  $P > 600 \text{ MeV}/c$  and for pions of  $P > 200 \text{ MeV}/c$  (at  $\vartheta = 90^\circ$ ). Relativistic pions and protons have, inside the scintillator resolution, the same energy losses. Thus no discrimination is possible with any technique based on  $dE/dx$ . The discrimination limit depends on the particle and its energy, as well as the detector. In our case, it has been determined experimentally.

If we consider the pion photoproduction on hydrogen below  $E_\gamma = 500 \text{ MeV}$  there are no protons from the reaction (7a) which are energetic enough to escape the detector. Thus, we can exclusively select charged pions from the reaction (7b) and reconstruct them with the Proton Range. Fig. 7 shows the correlation between the reconstructed kinetic energy and the  $\chi^2$  of the fit for pions emitted at  $\vartheta = 80^\circ - 90^\circ$ . It is evident that the condition  $\chi^2 < 2$  is no longer enough to allow a good discrimination and therefore we must also introduce a cut on the reconstructed energy. If we set an upper limit at  $E = 300 \text{ MeV}$  the pion contamination is less than 0.5%.

The energetic limit varies with  $\vartheta$ , as a reflection of the greater amount of material to be traversed at forward angles, and corresponding backward angles. The experimental data, confirmed by a GEANT simulation, allowed us to determine the maximum momentum,  $P_{max}$ , that assure a good discrimination as a function of  $\vartheta$ :

$$P_{max} = 0.025017 \times (\vartheta - 90)^2 + 810 \quad (8)$$

where  $\vartheta$  is in degree. If the reconstructed momentum for protons exceed  $P_{max}$  the discrimination is no longer good. Practically,  $P_{max} = 810 - 900 \text{ MeV}/c$  at

$$\vartheta = 90^\circ - 30^\circ.$$

#### 2.4. Proton efficiency and momentum resolution

The identification efficiency for protons in the entire acceptance of the detector was determined by simulation, using the GEANT code [5]. The geometrical set-up of DAPHNE as well as the energetic and angular resolution were introduced.

Modifications were made to allow a correct treatment of proton hadronic interaction in the domain in which the detector operates [6]. The Range Method was then applied to simulated events with the conditions previously described for proton identification.

We found that the proton efficiency reconstruction depends both on the momentum and on the emission  $\vartheta$  angle (fig. 8). Its reach a maximum value at  $\vartheta = 90^\circ$  ( $> 90\%$ ) and falls at forward and backward angles.

This behaviour can be qualitatively explained by observing that, as  $\vartheta$  decreases:

- a) multiple scattering produces larger variations in the path length of the particle;
- b) for a given momentum the number of scintillators crossed decreases and so fewer constraints are imposed on the fit;
- c) for a given momentum, as the path length inside the scintillators increases, the tail due to hadronic interactions increases.

The minimum momentum that we can reconstruct is determined by the threshold on the B layer, as at least two energy samples of the track are required in order to perform the fit. The maximum momentum is fixed according the relation (8) to prevent pion contamination for protons that escape from the detector.

The resolution was obtained with both experimental data and by simulation (fig. 9). The experimental values come from the analysis of the reaction (7c). The resolution is given by  $\Delta P/P = (P_{theo} - P_{exp})/P_{theo}$ , where  $P_{theo}$  and  $P_{exp}$  are

the values of the proton momentum determined by kinematics and fitted by the Range Method respectively.

The features of the data are well reproduced by simulated events (continuous line). The resolution degrades as the momentum of the particle increases, due to the poorest resolution of the external scintillators and to the greater importance of multiple scattering inside the absorbers layers. It is practically independent of  $\vartheta$  except at the extreme backward and forward angles, where it worsens.

The resolution varies from  $\Delta P/P = 2.5$  to  $\Delta P/P = 10\%$  (FWHM) in the range  $P = 300 - 900 \text{ MeV}/c$ .

One may think to also to calculate the efficiency associated with pions. We remark that this is possible only for the small fraction of the total spectrum of pions that stop inside the detector. Pions that escape the detector are relativistic and their momentum cannot be reconstructed with a reasonable resolution.

### 2.5. Experimental tests

We have carried out an important experimental check of the Range Method by measuring the protons from the reaction (7a). Fig. 10 shows an example of the differential cross section, at  $E_\gamma = 365 \text{ MeV}$ , that we obtained as a function of  $\cos \vartheta_{CM}$ , where  $\vartheta_{CM}$  is the angle of the proton in the center of mass system.

The accessible phase space with these kinematics is restricted due to the angular acceptance of the detector and to the proton momentum threshold imposed by the Range Method.

The curve is the parametrisation of the cross section given in [7] and obtained by fitting all the existing data.

From the good agreement between our data and the best established results, we can conclude that:

- a) the Range Method can discriminate protons with a negligible contamination

of pions;

- b) the proton efficiencies are well calculated with GEANT, providing a good knowledge of the characteristics of the detector.

### 3. Conclusions

The Range Method provides a powerful tool for particle discrimination.

Resolution on the proton momentum is very good if we bear in mind that it is not a magnetic analysis.

The cut on the maximum momentum does not represent, in our case, a strong limitation. In the photon energy range under which the detector operates, the Range Method allows a complete study of proton momentum spectra for the most suitable reactions included in the experimental programs.

The proton efficiency determined with GEANT are realistic and allowed us to reconstruct the differential cross section of the reaction  ${}^1\text{H}(\gamma, p)\pi^0$ .

The Range Method is actually being used in our analysis of the photodisintegration of the Deuteron and  ${}^3\text{He}$ .

## References

- [1] G. Audit et al., Nucl. Instr. and Meth. A301 (1991) 473.
- [2] H. Herminghaus et al., Nucl. Instr. and Meth 138 (1976) 1.
- [3] I. Anthony et al., Nucl. Instr. and Meth. A301 (1991) 230.
- [4] Cecil et al., Nucl. Instr. and Meth. 161 (1979) 439.
- [5] R. Brun et al., GEANT3 User's Guide, CERN DD/EE/ 84-1 (1987).
- [6] P. Pedroni, INFN Report BE-88/3 (1988).
- [7] Landolt-Börnstein, Photoproduction of Elementary Particles, Group 1-Vol. 3. ed. H. Schopper (Springer-Verlag, Berlin, 1973)

## Figure captions

- Fig. 1:* Schematic view of a sampling detector. The labels indicate the energy of the particle at the entrance of each layer.
- Fig. 2:* Transverse view of the DAPHNE detector. The figure shows only one of the 16 azimuthal modules.
- Fig. 3:* Pion Energy calibration for a B scintillator. The ADC value is corrected for the light attenuation effect. The data comes from the reaction  $\gamma + {}^1H \rightarrow n + \pi^+$ .
- Fig. 4:* Proton Energy calibration for a B scintillator. The ADC value is corrected for the light attenuation effect. The energy loss takes into account the quenching. The data comes from the reaction  $\gamma + {}^2H \rightarrow p + n$ .
- Fig. 5:* Particle discrimination with the Range Method. On the x and y axis are reported the  $\chi^2$  from the Proton Range and from the Pion Range respectively.
- Fig. 6:*  $\chi^2$  distribution of pions reconstructed with the Proton Range. The shaded area for  $\chi^2 < 2$  represent the pion contamination for proton identification.
- Fig. 7:* Discrimination limit for high energy particles. The plot shows the correlation between the  $\chi^2$  and the kinetic energy of pions reconstructed as protons.
- Fig. 8:* Reconstruction efficiency for protons obtained with GEANT.
- Fig. 9:* Comparison of experimental and simulated momentum resolution for protons.
- Fig. 10:* Differential cross sections for the reaction  ${}^1H(\gamma, p)\pi^0$  at  $E_\gamma = 365 \text{ MeV}$ . On the x-axis  $\cos\vartheta$  of the proton in the C.M. system. The curve comes from ref. [7].

FIG. 1

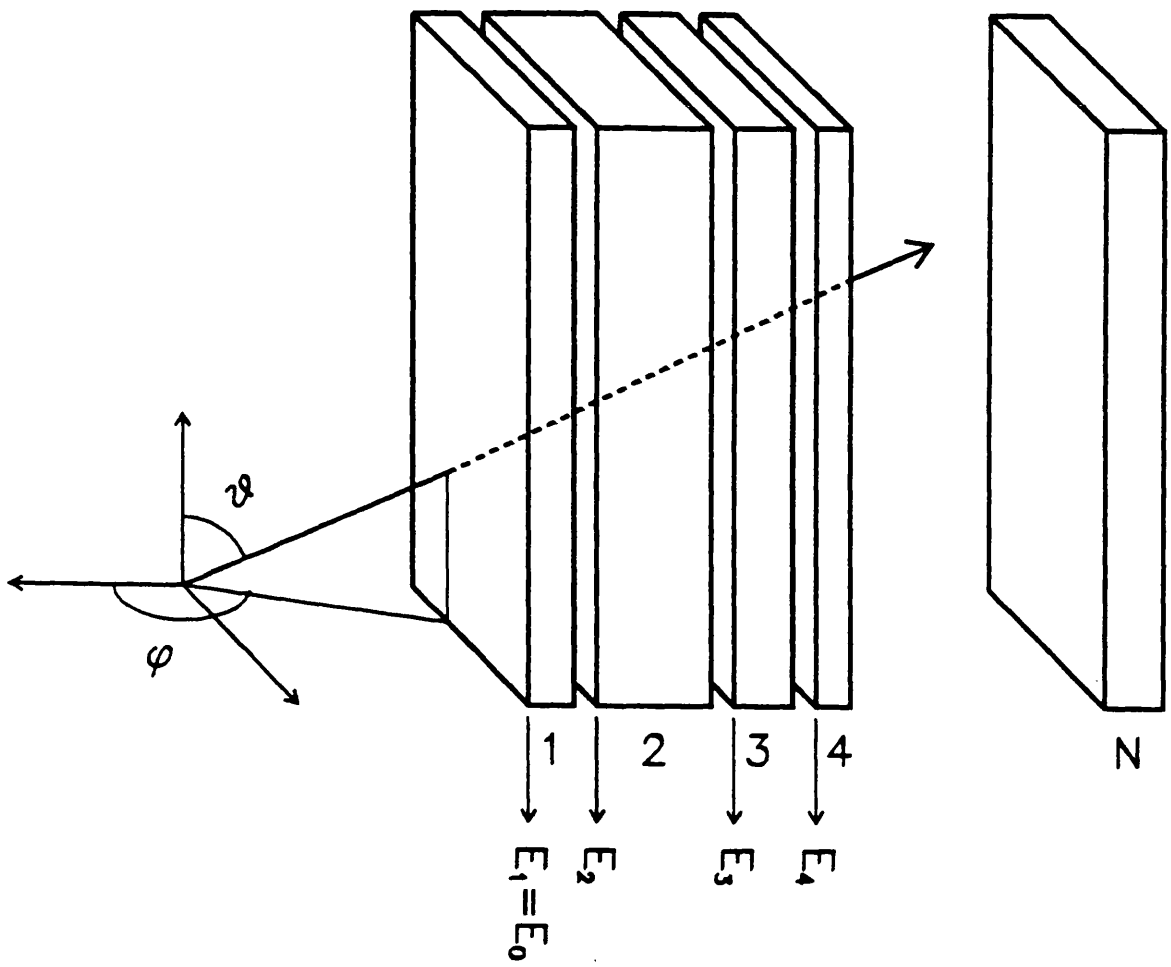


FIG. 2

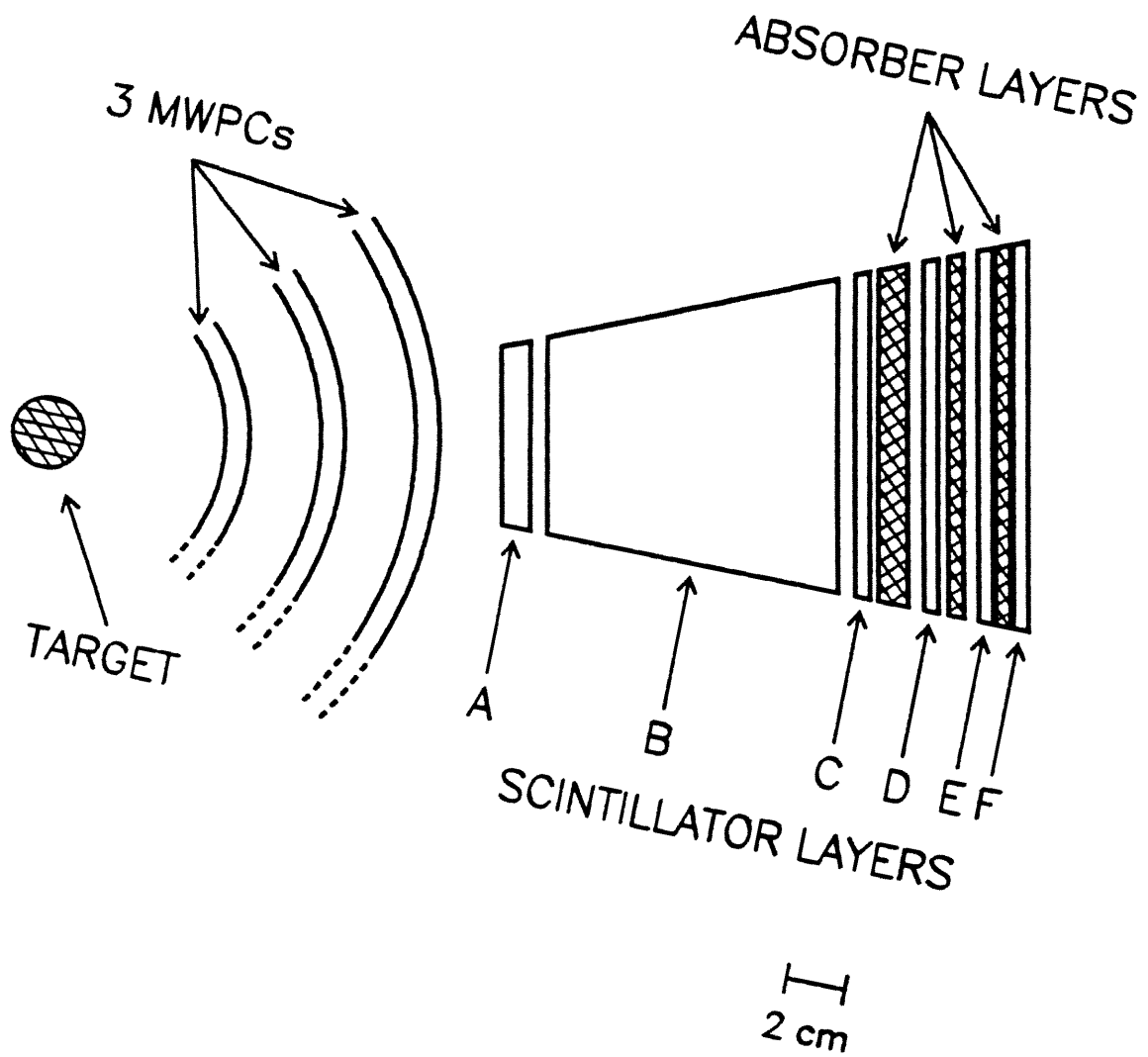


FIG. 3

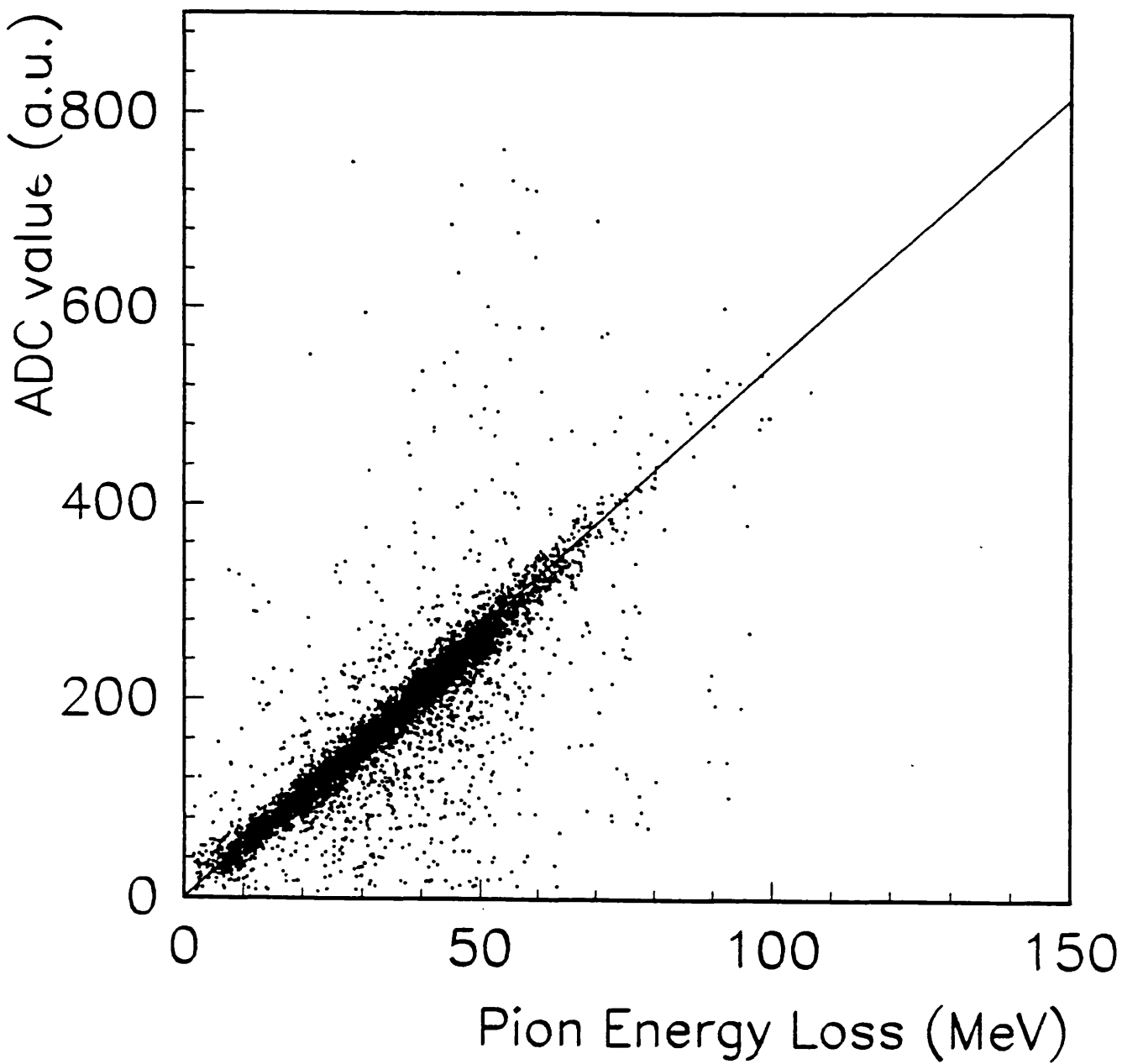


FIG. 4

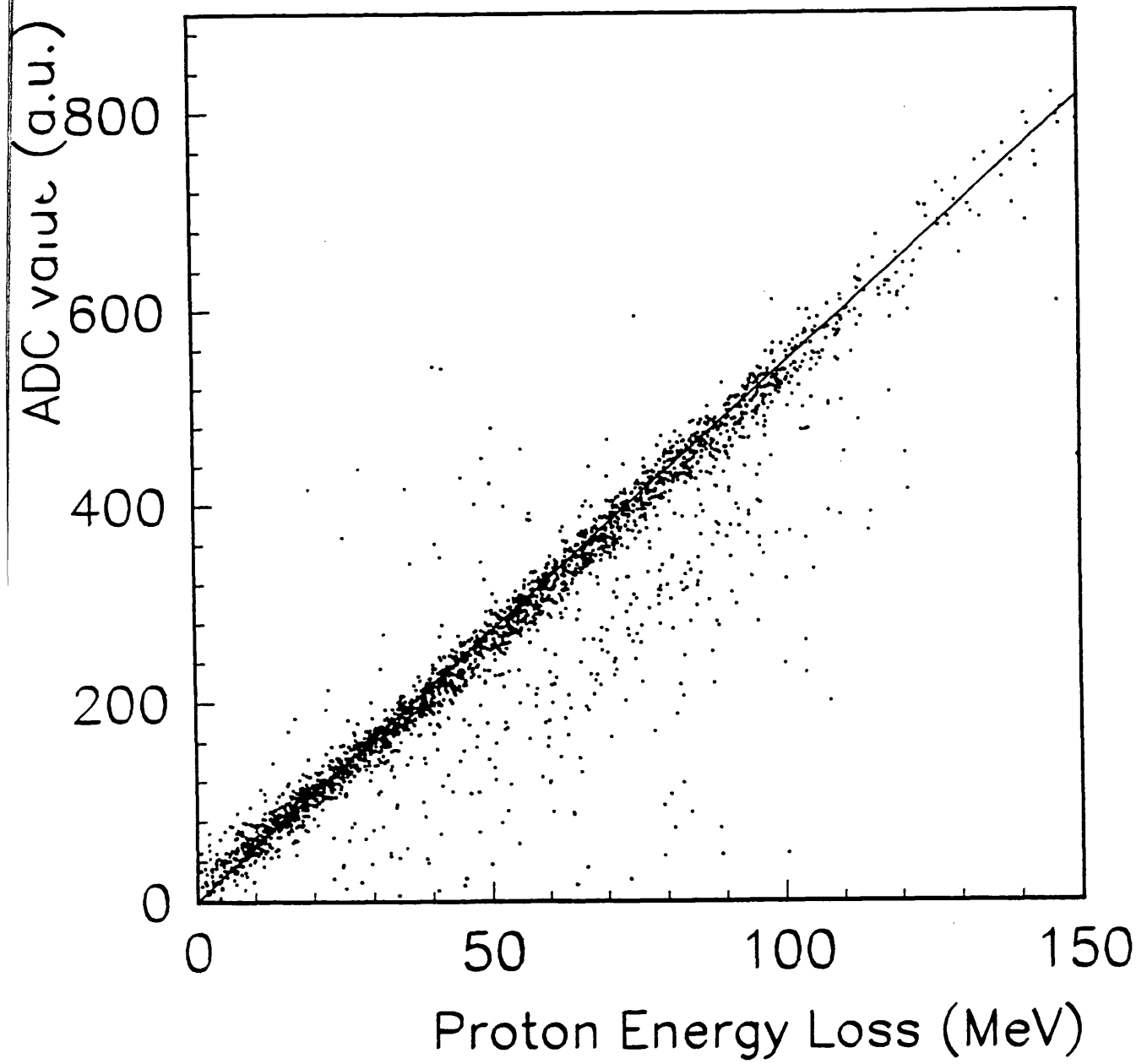


FIG. 5

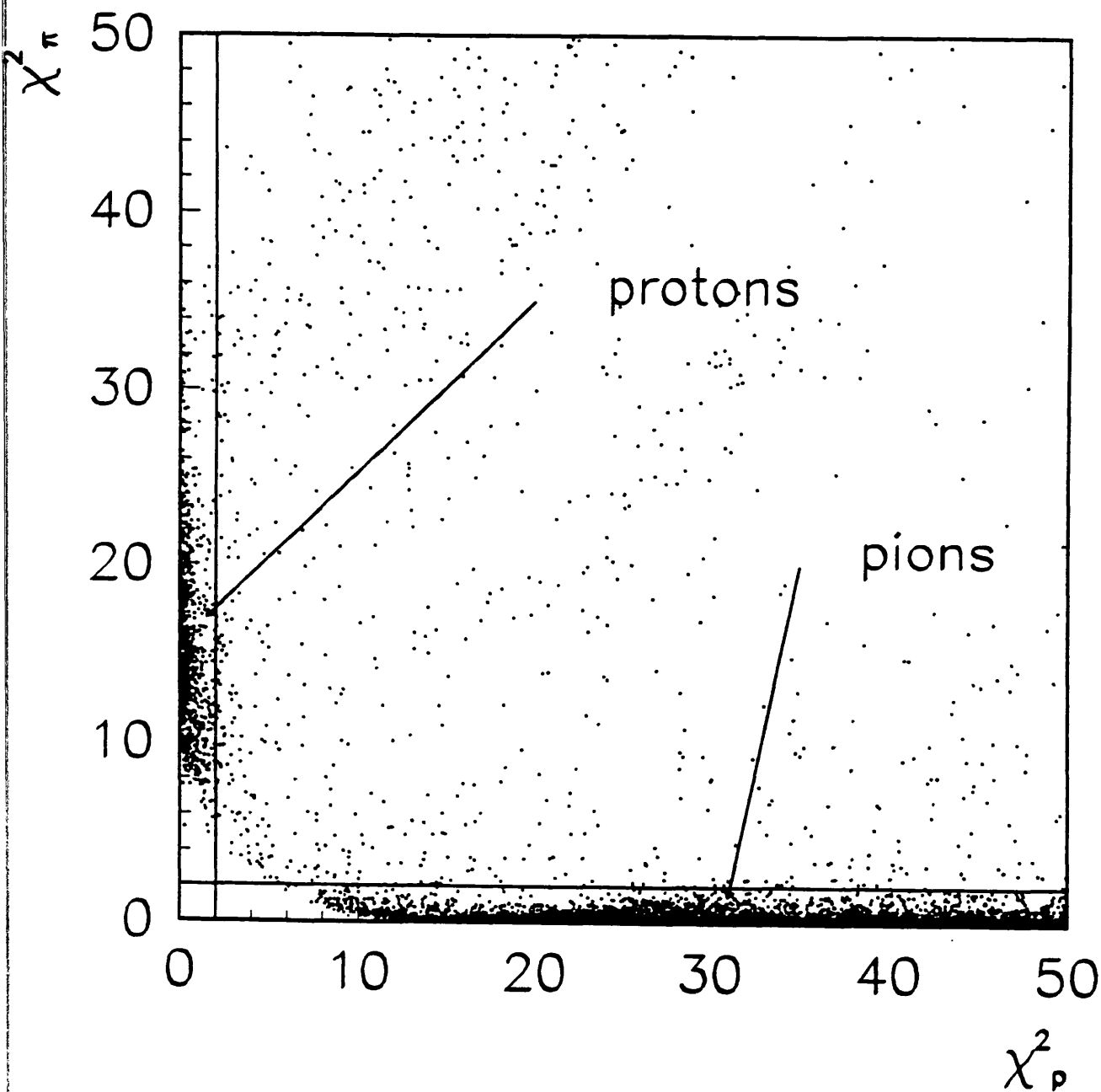


FIG. 6

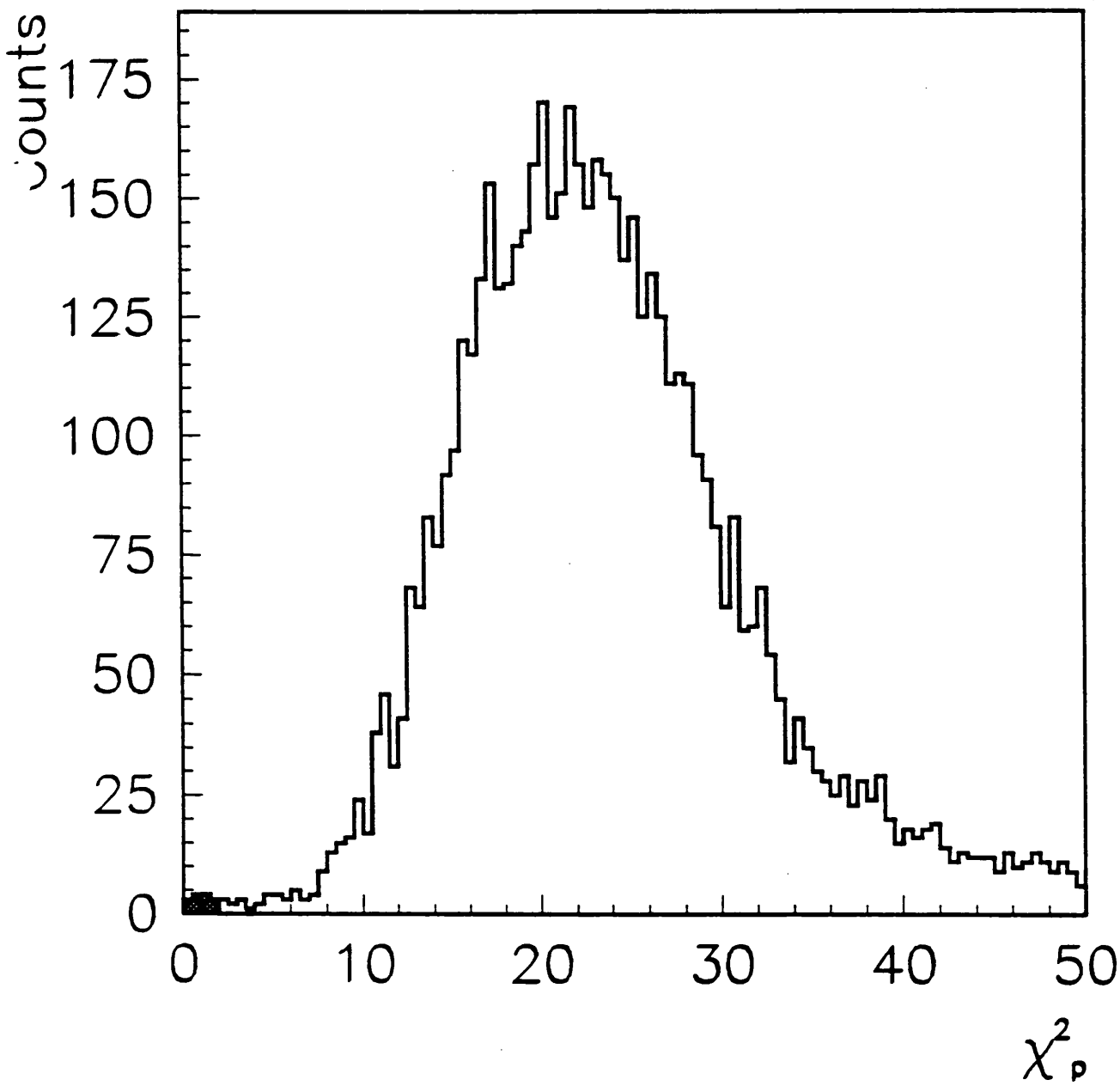


FIG. 7

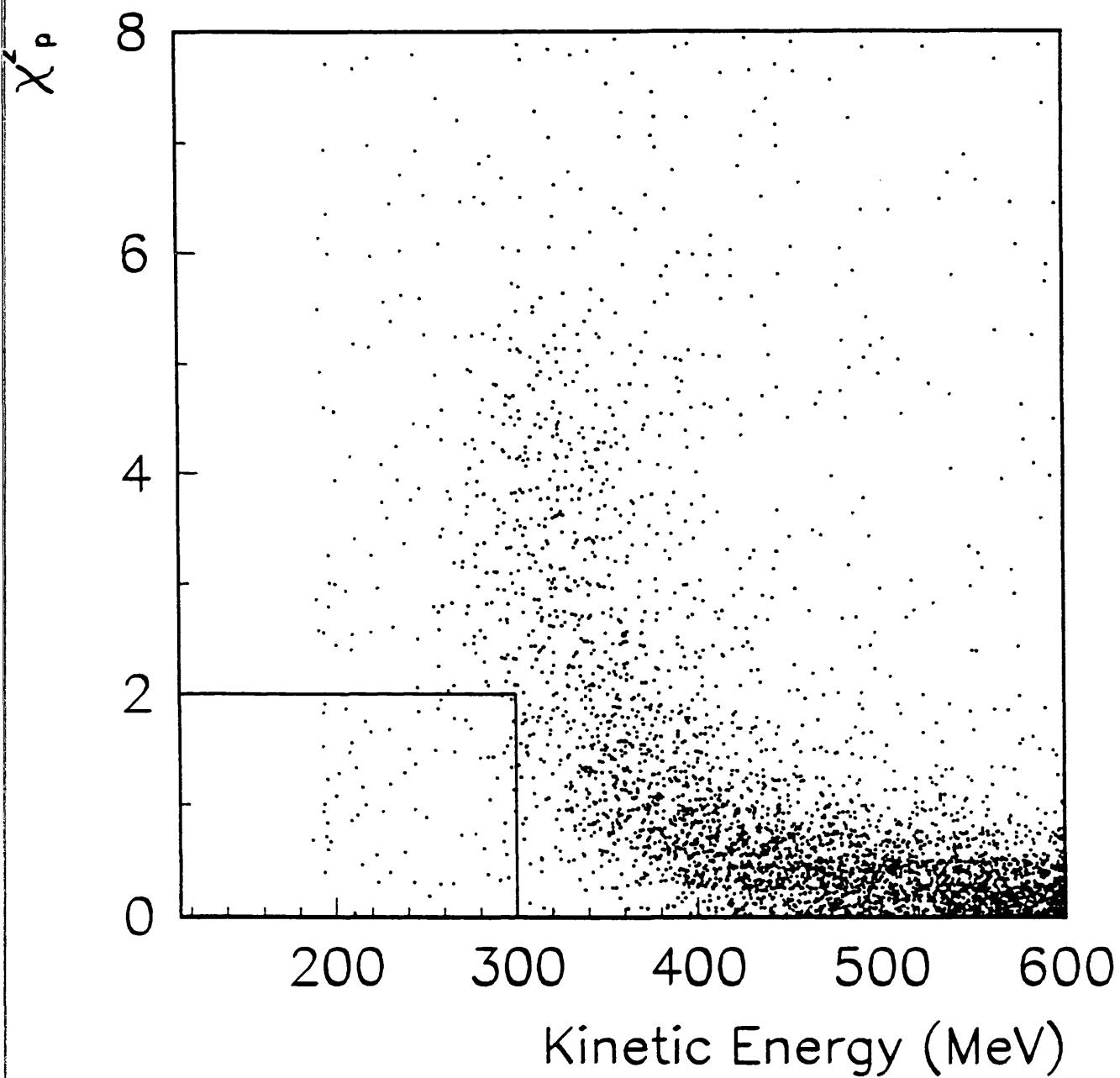


FIG. 8

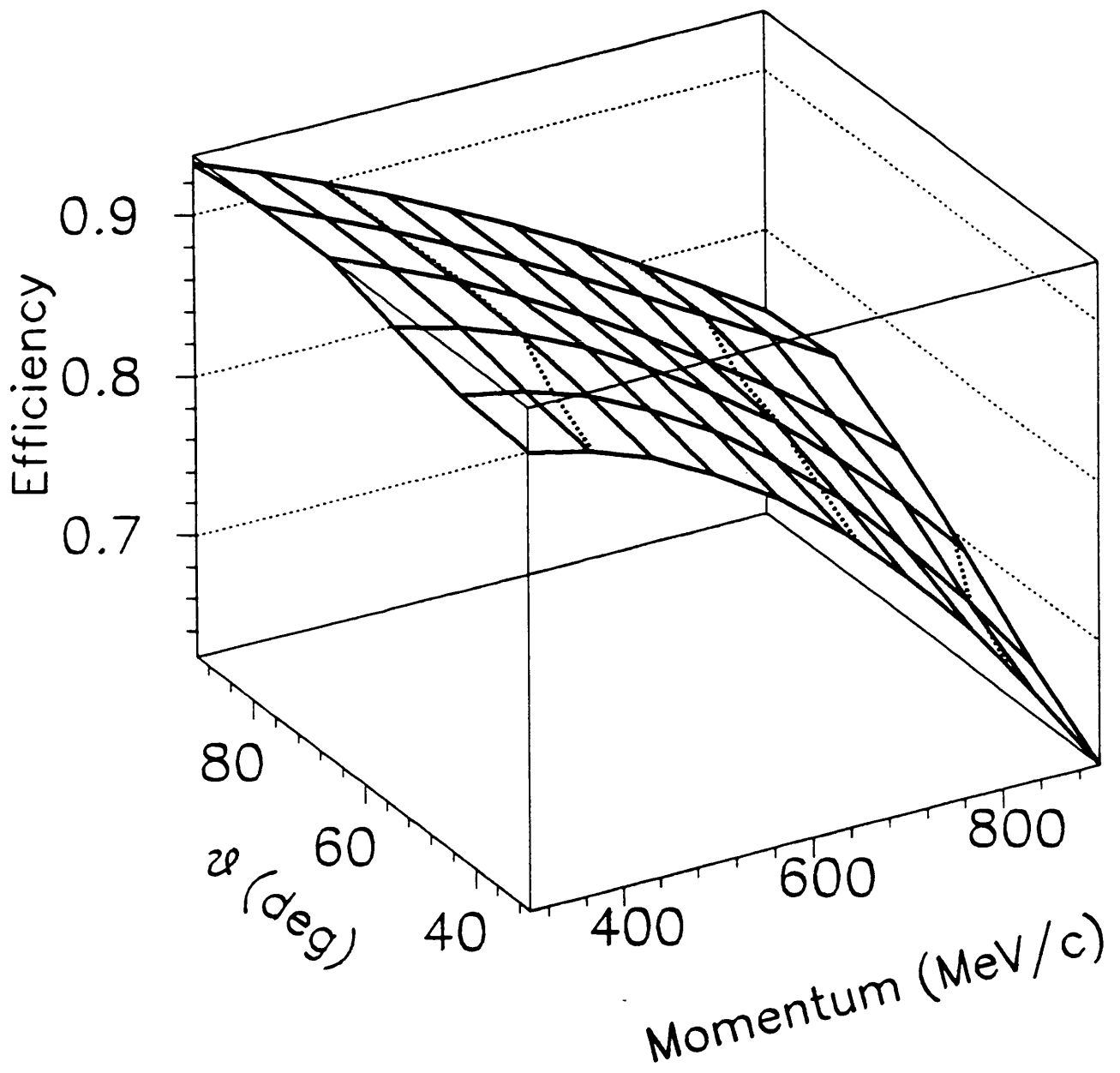


FIG. 9

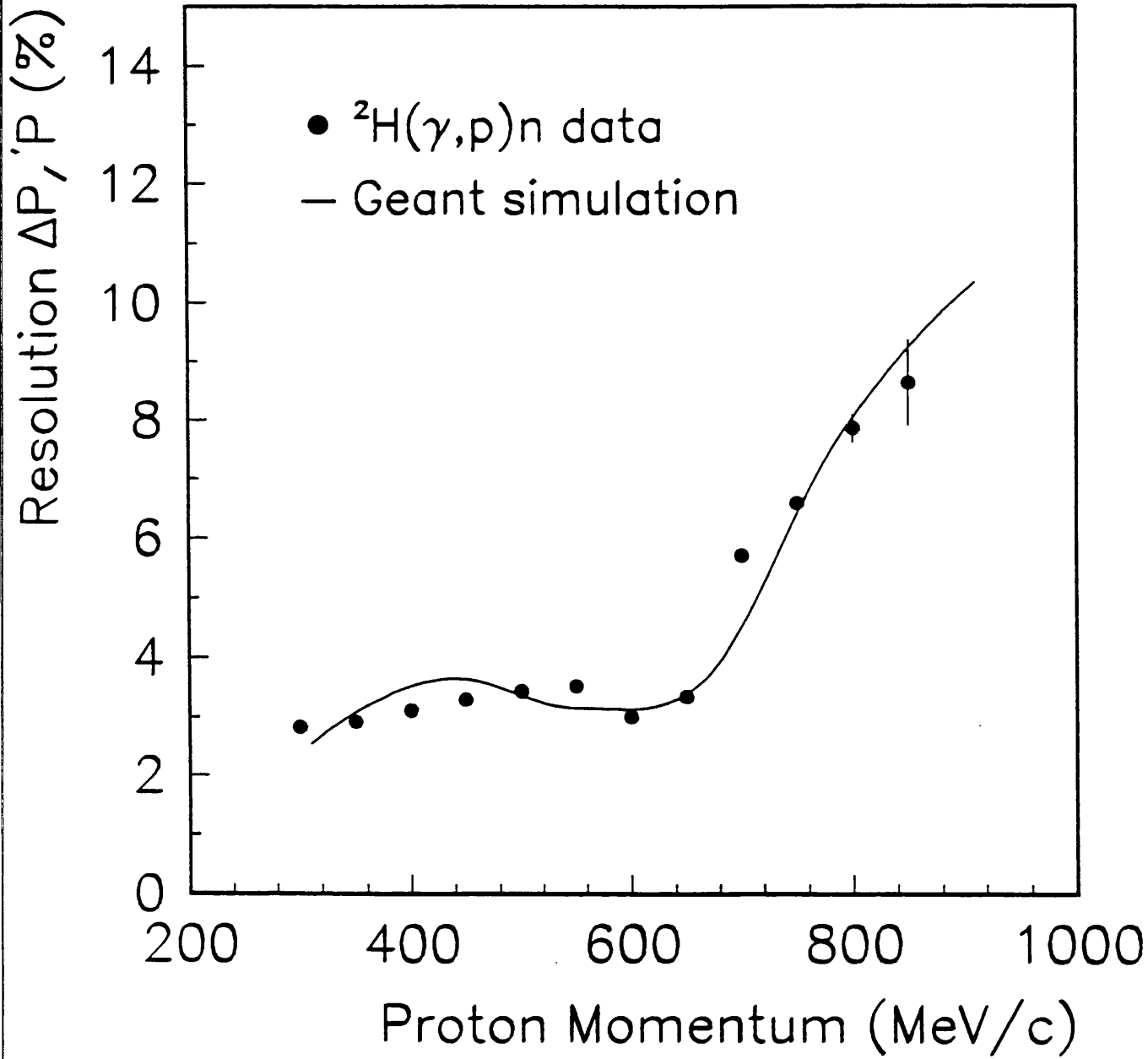
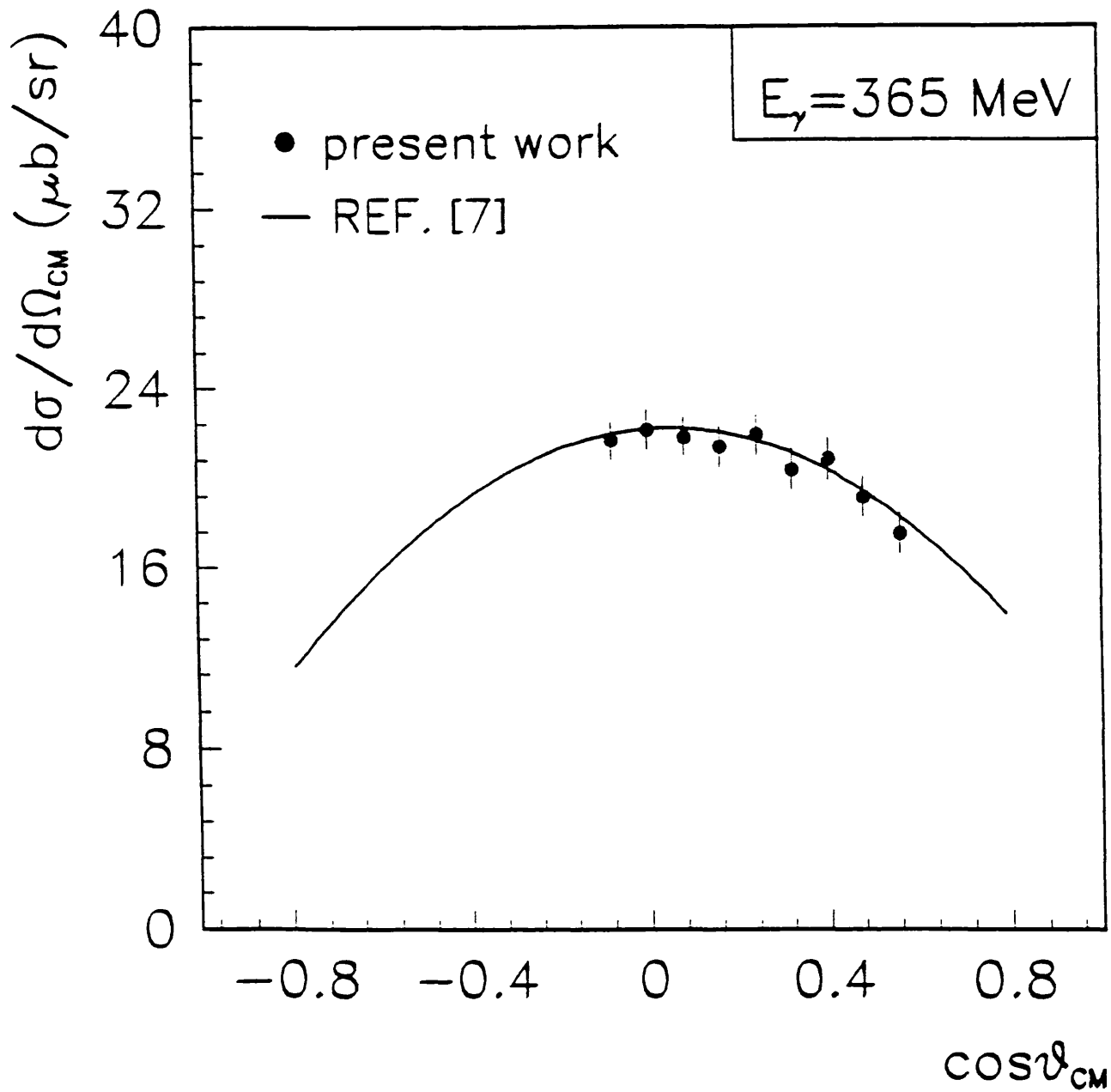


FIG. 10



# Appendix B

## Cross Section Results

The errors quoted in the following tables are the statistical and the systematic errors discussed in section 5.3. In addition, there is a global systematic error of  $\pm 3\%$ .

$E_\gamma=200$ MeV		$E_\gamma=220$ MeV		$E_\gamma=240$ MeV	
$\theta_{cm}^\circ$	$\frac{d\sigma}{d\Omega_{cm}} \mu\text{barns st}^{-1}$	$\theta_{cm}^\circ$	$\frac{d\sigma}{d\Omega_{cm}} \mu\text{barns st}^{-1}$	$\theta_{cm}^\circ$	$\frac{d\sigma}{d\Omega_{cm}} \mu\text{barns st}^{-1}$
30.00	$4.77 \pm 0.24$	30.00	$4.75 \pm 0.27$	30.00	$4.90 \pm 0.27$
35.00	$4.45 \pm 0.24$	35.00	$4.87 \pm 0.26$	35.00	$5.57 \pm 0.26$
40.00	$4.93 \pm 0.24$	40.00	$5.45 \pm 0.24$	40.00	$4.88 \pm 0.26$
45.00	$5.16 \pm 0.23$	45.00	$5.10 \pm 0.25$	45.00	$5.16 \pm 0.25$
50.00	$5.40 \pm 0.21$	50.00	$5.18 \pm 0.24$	50.00	$5.49 \pm 0.26$
55.00	$5.41 \pm 0.21$	55.00	$5.04 \pm 0.23$	55.00	$5.42 \pm 0.26$
60.00	$5.49 \pm 0.22$	60.00	$5.36 \pm 0.24$	60.00	$5.57 \pm 0.24$
65.00	$5.48 \pm 0.22$	65.00	$5.17 \pm 0.23$	65.00	$5.61 \pm 0.25$
70.00	$4.94 \pm 0.22$	70.00	$5.16 \pm 0.23$	70.00	$5.40 \pm 0.24$
75.00	$5.04 \pm 0.21$	75.00	$5.35 \pm 0.24$	75.00	$5.73 \pm 0.25$
80.00	$5.16 \pm 0.22$	80.00	$5.19 \pm 0.23$	80.00	$5.69 \pm 0.23$
85.00	$5.26 \pm 0.21$	85.00	$5.09 \pm 0.24$	85.00	$5.27 \pm 0.24$
90.00	$5.14 \pm 0.21$	90.00	$5.40 \pm 0.24$	90.00	$5.55 \pm 0.25$
95.00	$4.81 \pm 0.21$	95.00	$5.05 \pm 0.23$	95.00	$5.18 \pm 0.26$
100.00	$5.03 \pm 0.22$	100.00	$5.27 \pm 0.23$	100.00	$5.38 \pm 0.24$
105.00	$4.64 \pm 0.22$	105.00	$5.11 \pm 0.23$	105.00	$4.63 \pm 0.27$
110.00	$4.49 \pm 0.20$	110.00	$4.69 \pm 0.22$	110.00	$4.99 \pm 0.27$
115.00	$4.44 \pm 0.22$	115.00	$4.64 \pm 0.23$	115.00	$4.85 \pm 0.29$
120.00	$4.59 \pm 0.23$	120.00	$4.57 \pm 0.24$	120.00	$4.99 \pm 0.27$
125.00	$4.48 \pm 0.22$	125.00	$4.09 \pm 0.26$	125.00	$4.42 \pm 0.30$
130.00	$3.68 \pm 0.22$	130.00	$4.06 \pm 0.25$	130.00	$4.80 \pm 0.47$
135.00	$3.84 \pm 0.25$	135.00	$3.90 \pm 0.23$	135.00	$4.44 \pm 0.27$
140.00	$3.75 \pm 0.22$	140.00	$4.05 \pm 0.24$	140.00	$4.57 \pm 0.27$
145.00	$3.23 \pm 0.23$	145.00	$3.41 \pm 0.26$	145.00	$3.70 \pm 0.29$
150.00	$2.85 \pm 0.22$	150.00	$2.85 \pm 0.25$	150.00	$3.64 \pm 0.27$
155.00	$3.01 \pm 0.22$	155.00	$2.65 \pm 0.24$	155.00	$3.19 \pm 0.30$
160.00	$4.55 \pm 0.25$	160.00	$5.33 \pm 0.27$	160.00	$0.00 \pm 0.47$

Table B.1: *Differential Cross Sections  $E_\gamma = 200, 220,$  and  $240$  MeV*

$E_\gamma=260$ MeV		$E_\gamma=280$ MeV		$E_\gamma=300$ MeV	
$\theta_{cm}^\circ$	$\frac{d\sigma}{d\Omega_{cm}} \mu\text{barns } st^{-1}$	$\theta_{cm}^\circ$	$\frac{d\sigma}{d\Omega_{cm}} \mu\text{barns } st^{-1}$	$\theta_{cm}^\circ$	$\frac{d\sigma}{d\Omega_{cm}} \mu\text{barns } st^{-1}$
30.00	$4.39 \pm 0.28$	30.00	$4.62 \pm 0.27$	30.00	$4.17 \pm 0.28$
35.00	$5.33 \pm 0.28$	35.00	$4.61 \pm 0.29$	35.00	$4.49 \pm 0.29$
40.00	$5.63 \pm 0.26$	40.00	$5.29 \pm 0.28$	40.00	$5.41 \pm 0.27$
45.00	$5.53 \pm 0.27$	45.00	$5.35 \pm 0.28$	45.00	$5.31 \pm 0.27$
50.00	$5.45 \pm 0.26$	50.00	$5.41 \pm 0.27$	50.00	$5.04 \pm 0.26$
55.00	$5.82 \pm 0.28$	55.00	$4.96 \pm 0.27$	55.00	$5.10 \pm 0.27$
60.00	$6.11 \pm 0.27$	60.00	$5.90 \pm 0.29$	60.00	$5.38 \pm 0.25$
65.00	$5.72 \pm 0.27$	65.00	$5.88 \pm 0.27$	65.00	$5.01 \pm 0.26$
70.00	$6.08 \pm 0.27$	70.00	$5.94 \pm 0.28$	70.00	$5.34 \pm 0.25$
75.00	$5.93 \pm 0.26$	75.00	$5.65 \pm 0.27$	75.00	$5.14 \pm 0.26$
80.00	$6.61 \pm 0.26$	80.00	$5.54 \pm 0.27$	80.00	$5.36 \pm 0.25$
85.00	$6.16 \pm 0.26$	85.00	$6.39 \pm 0.27$	85.00	$4.79 \pm 0.27$
90.00	$6.19 \pm 0.26$	90.00	$5.53 \pm 0.27$	90.00	$5.05 \pm 0.26$
95.00	$6.03 \pm 0.25$	95.00	$5.85 \pm 0.28$	95.00	$4.82 \pm 0.26$
100.00	$5.51 \pm 0.27$	100.00	$5.44 \pm 0.28$	100.00	$5.02 \pm 0.27$
105.00	$5.54 \pm 0.28$	105.00	$5.39 \pm 0.27$	105.00	$4.53 \pm 0.26$
110.00	$5.39 \pm 0.27$	110.00	$5.05 \pm 0.28$	110.00	$4.84 \pm 0.29$
115.00	$5.23 \pm 0.28$	115.00	$4.88 \pm 0.29$	115.00	$4.50 \pm 0.28$
120.00	$4.80 \pm 0.29$	120.00	$4.96 \pm 0.32$	120.00	$4.19 \pm 0.32$
125.00	$5.05 \pm 0.33$	125.00	$4.75 \pm 0.33$	125.00	$4.37 \pm 0.32$
130.00	$4.96 \pm 0.35$	130.00	$4.28 \pm 0.34$	130.00	$3.76 \pm 0.35$
135.00	$4.42 \pm 0.28$	135.00	$4.27 \pm 0.27$	135.00	$4.16 \pm 0.26$
140.00	$4.21 \pm 0.27$	140.00	$3.89 \pm 0.28$	140.00	$3.65 \pm 0.29$
145.00	$3.98 \pm 0.28$	145.00	$4.08 \pm 0.29$	145.00	$3.93 \pm 0.28$
150.00	$4.29 \pm 0.29$	150.00	$3.61 \pm 0.32$	150.00	$3.44 \pm 0.32$
155.00	$3.65 \pm 0.33$	155.00	$3.13 \pm 0.33$	155.00	$3.10 \pm 0.32$
160.00	$0.83 \pm 0.35$	160.00	$2.10 \pm 0.34$	160.00	$3.31 \pm 0.35$

Table B.2: Differential Cross Sections  $E_\gamma = 260, 280, \text{ and } 300$  MeV

$E_\gamma=320$ MeV		$E_\gamma=340$ MeV		$E_\gamma=360$ MeV	
$\theta_{cm}^\circ$	$\frac{d\sigma}{d\Omega_{cm}} \mu\text{barns st}^{-1}$	$\theta_{cm}^\circ$	$\frac{d\sigma}{d\Omega_{cm}} \mu\text{barns st}^{-1}$	$\theta_{cm}^\circ$	$\frac{d\sigma}{d\Omega_{cm}} \mu\text{barns st}^{-1}$
30.00	4.29 ± 0.28	30.00	3.03 ± 0.23	30.00	2.92 ± 0.19
35.00	4.47 ± 0.27	35.00	3.31 ± 0.25	35.00	2.91 ± 0.19
40.00	4.58 ± 0.27	40.00	3.32 ± 0.23	40.00	3.10 ± 0.19
45.00	3.90 ± 0.25	45.00	3.71 ± 0.22	45.00	2.73 ± 0.19
50.00	4.56 ± 0.25	50.00	3.55 ± 0.21	50.00	2.55 ± 0.18
55.00	4.68 ± 0.27	55.00	3.11 ± 0.21	55.00	2.81 ± 0.17
60.00	4.57 ± 0.24	60.00	3.58 ± 0.23	60.00	2.98 ± 0.18
65.00	4.90 ± 0.24	65.00	3.40 ± 0.22	65.00	2.90 ± 0.17
70.00	4.53 ± 0.26	70.00	3.19 ± 0.22	70.00	2.76 ± 0.19
75.00	4.66 ± 0.25	75.00	3.26 ± 0.22	75.00	2.76 ± 0.18
80.00	5.00 ± 0.24	80.00	3.26 ± 0.22	80.00	2.91 ± 0.19
85.00	4.40 ± 0.24	85.00	3.59 ± 0.22	85.00	2.76 ± 0.18
90.00	4.32 ± 0.26	90.00	3.37 ± 0.23	90.00	3.20 ± 0.18
95.00	4.93 ± 0.25	95.00	3.38 ± 0.22	95.00	2.96 ± 0.17
100.00	4.31 ± 0.26	100.00	3.40 ± 0.22	100.00	3.07 ± 0.16
105.00	4.10 ± 0.27	105.00	3.20 ± 0.23	105.00	2.72 ± 0.17
110.00	3.86 ± 0.27	110.00	3.13 ± 0.25	110.00	2.78 ± 0.17
115.00	4.29 ± 0.30	115.00	3.31 ± 0.23	115.00	2.51 ± 0.17
120.00	3.78 ± 0.30	120.00	3.00 ± 0.25	120.00	2.22 ± 0.18
125.00	3.89 ± 0.31	125.00	2.77 ± 0.28	125.00	2.30 ± 0.19
130.00	3.76 ± 0.34	130.00	2.63 ± 0.28	130.00	2.14 ± 0.20
135.00	3.51 ± 0.27	135.00	2.95 ± 0.23	135.00	2.07 ± 0.23
140.00	3.73 ± 0.27	140.00	2.28 ± 0.25	140.00	2.17 ± 0.17
145.00	3.43 ± 0.30	145.00	2.20 ± 0.23	145.00	1.95 ± 0.18
150.00	2.97 ± 0.30	150.00	2.26 ± 0.25	150.00	1.85 ± 0.19
155.00	2.85 ± 0.31	155.00	1.88 ± 0.28	155.00	1.92 ± 0.20
160.00	2.47 ± 0.34	160.00	2.16 ± 0.28	160.00	2.14 ± 0.23

Table B.3: Differential Cross Sections  $E_\gamma=320,340,$  and  $360$  MeV

$E_\gamma=380 \text{ MeV}$		$E_\gamma=400 \text{ MeV}$		$E_\gamma=420 \text{ MeV}$	
$\theta_{cm}^\circ$	$\frac{d\sigma}{d\Omega_{cm}} \mu\text{barns st}^{-1}$	$\theta_{cm}^\circ$	$\frac{d\sigma}{d\Omega_{cm}} \mu\text{barns st}^{-1}$	$\theta_{cm}^\circ$	$\frac{d\sigma}{d\Omega_{cm}} \mu\text{barns st}^{-1}$
30.00	$1.67 \pm 0.12$	30.00	$1.41 \pm 0.11$	30.00	$0.90 \pm 0.11$
35.00	$1.79 \pm 0.12$	35.00	$1.64 \pm 0.10$	35.00	$1.03 \pm 0.09$
40.00	$1.91 \pm 0.11$	40.00	$1.58 \pm 0.10$	40.00	$0.96 \pm 0.10$
45.00	$1.76 \pm 0.12$	45.00	$1.53 \pm 0.11$	45.00	$0.97 \pm 0.09$
50.00	$1.76 \pm 0.11$	50.00	$1.56 \pm 0.10$	50.00	$1.19 \pm 0.09$
55.00	$1.88 \pm 0.12$	55.00	$1.44 \pm 0.10$	55.00	$0.99 \pm 0.09$
60.00	$1.78 \pm 0.11$	60.00	$1.59 \pm 0.11$	60.00	$1.14 \pm 0.09$
65.00	$2.07 \pm 0.12$	65.00	$1.70 \pm 0.10$	65.00	$1.12 \pm 0.09$
70.00	$1.93 \pm 0.11$	70.00	$1.61 \pm 0.10$	70.00	$1.20 \pm 0.09$
75.00	$2.04 \pm 0.12$	75.00	$1.66 \pm 0.10$	75.00	$1.24 \pm 0.09$
80.00	$2.03 \pm 0.12$	80.00	$1.88 \pm 0.10$	80.00	$1.09 \pm 0.08$
85.00	$2.07 \pm 0.11$	85.00	$1.66 \pm 0.10$	85.00	$1.09 \pm 0.10$
90.00	$2.05 \pm 0.12$	90.00	$1.65 \pm 0.10$	90.00	$1.17 \pm 0.10$
95.00	$2.19 \pm 0.11$	95.00	$1.66 \pm 0.10$	95.00	$1.15 \pm 0.09$
100.00	$2.21 \pm 0.10$	100.00	$1.59 \pm 0.10$	100.00	$1.06 \pm 0.10$
105.00	$1.99 \pm 0.10$	105.00	$1.63 \pm 0.10$	105.00	$1.28 \pm 0.10$
110.00	$2.01 \pm 0.10$	110.00	$1.63 \pm 0.10$	110.00	$1.29 \pm 0.08$
115.00	$1.88 \pm 0.10$	115.00	$1.59 \pm 0.11$	115.00	$1.11 \pm 0.10$
120.00	$1.57 \pm 0.11$	120.00	$1.51 \pm 0.09$	120.00	$1.20 \pm 0.09$
125.00	$1.50 \pm 0.12$	125.00	$1.44 \pm 0.11$	125.00	$1.17 \pm 0.11$
130.00	$1.49 \pm 0.12$	130.00	$1.35 \pm 0.12$	130.00	$0.77 \pm 0.10$
135.00	$1.32 \pm 0.12$	135.00	$1.43 \pm 0.12$	135.00	$1.03 \pm 0.13$
140.00	$1.44 \pm 0.10$	140.00	$1.08 \pm 0.11$	140.00	$0.78 \pm 0.10$
145.00	$1.59 \pm 0.11$	145.00	$1.19 \pm 0.09$	145.00	$0.92 \pm 0.09$
150.00	$1.35 \pm 0.12$	150.00	$1.23 \pm 0.11$	150.00	$0.80 \pm 0.11$
155.00	$1.13 \pm 0.12$	155.00	$1.06 \pm 0.12$	155.00	$0.95 \pm 0.10$
160.00	$1.18 \pm 0.12$	160.00	$1.24 \pm 0.12$	160.00	$1.09 \pm 0.13$

Table B.4: *Differential Cross Sections  $E_\gamma = 380, 400, \text{ and } 420 \text{ MeV}$*

$E_\gamma=440$ MeV		$E_\gamma=460$ MeV		$E_\gamma=480$ MeV	
$\theta_{cm}^\circ$	$\frac{d\sigma}{d\Omega_{cm}} \mu\text{barns st}^{-1}$	$\theta_{cm}^\circ$	$\frac{d\sigma}{d\Omega_{cm}} \mu\text{barns st}^{-1}$	$\theta_{cm}^\circ$	$\frac{d\sigma}{d\Omega_{cm}} \mu\text{barns st}^{-1}$
30.00	$0.70 \pm 0.09$	30.00	$0.54 \pm 0.08$	30.00	$0.30 \pm 0.08$
35.00	$1.01 \pm 0.09$	35.00	$0.75 \pm 0.08$	35.00	$0.77 \pm 0.08$
40.00	$0.90 \pm 0.09$	40.00	$1.06 \pm 0.08$	40.00	$0.94 \pm 0.07$
45.00	$1.11 \pm 0.09$	45.00	$0.85 \pm 0.08$	45.00	$0.97 \pm 0.08$
50.00	$0.96 \pm 0.09$	50.00	$0.82 \pm 0.08$	50.00	$0.83 \pm 0.08$
55.00	$1.08 \pm 0.09$	55.00	$0.84 \pm 0.08$	55.00	$0.99 \pm 0.07$
60.00	$1.21 \pm 0.09$	60.00	$0.96 \pm 0.08$	60.00	$0.78 \pm 0.07$
65.00	$1.24 \pm 0.08$	65.00	$0.99 \pm 0.07$	65.00	$0.95 \pm 0.07$
70.00	$1.22 \pm 0.08$	70.00	$1.08 \pm 0.08$	70.00	$0.80 \pm 0.07$
75.00	$1.20 \pm 0.08$	75.00	$0.99 \pm 0.08$	75.00	$1.04 \pm 0.06$
80.00	$1.17 \pm 0.09$	80.00	$1.06 \pm 0.08$	80.00	$0.89 \pm 0.06$
85.00	$1.08 \pm 0.08$	85.00	$0.94 \pm 0.08$	85.00	$0.79 \pm 0.07$
90.00	$1.16 \pm 0.08$	90.00	$0.93 \pm 0.08$	90.00	$0.76 \pm 0.07$
95.00	$1.07 \pm 0.09$	95.00	$0.94 \pm 0.09$	95.00	$0.79 \pm 0.07$
100.00	$1.20 \pm 0.09$	100.00	$0.96 \pm 0.08$	100.00	$0.82 \pm 0.07$
105.00	$1.09 \pm 0.08$	105.00	$0.92 \pm 0.08$	105.00	$0.69 \pm 0.07$
110.00	$1.06 \pm 0.08$	110.00	$0.93 \pm 0.08$	110.00	$0.68 \pm 0.07$
115.00	$1.19 \pm 0.09$	115.00	$0.88 \pm 0.07$	115.00	$0.72 \pm 0.08$
120.00	$1.07 \pm 0.09$	120.00	$1.08 \pm 0.08$	120.00	$0.81 \pm 0.08$
125.00	$0.93 \pm 0.09$	125.00	$0.85 \pm 0.08$	125.00	$0.71 \pm 0.09$
130.00	$0.90 \pm 0.09$	130.00	$0.89 \pm 0.09$	130.00	$0.63 \pm 0.13$
135.00	$0.90 \pm 0.12$	135.00	$0.75 \pm 0.10$	135.00	$0.63 \pm 0.07$
140.00	$0.85 \pm 0.09$	140.00	$0.66 \pm 0.08$	140.00	$0.57 \pm 0.07$
145.00	$0.75 \pm 0.09$	145.00	$0.65 \pm 0.07$	145.00	$0.57 \pm 0.07$
150.00	$0.73 \pm 0.09$	150.00	$0.55 \pm 0.08$	150.00	$0.54 \pm 0.08$
155.00	$0.96 \pm 0.09$	155.00	$0.55 \pm 0.08$	155.00	$0.52 \pm 0.08$
160.00	$0.70 \pm 0.12$	160.00	$0.57 \pm 0.09$	160.00	$0.70 \pm 0.09$

Table B.5: *Differential Cross Sections  $E_\gamma = 440, 460,$  and  $480$  MeV*

$E_\gamma=500$ MeV		$E_\gamma=520$ MeV		$E_\gamma=540$ MeV	
$\theta_{cm}^\circ$	$\frac{d\sigma}{d\Omega_{cm}} \mu\text{barns st}^{-1}$	$\theta_{cm}^\circ$	$\frac{d\sigma}{d\Omega_{cm}} \mu\text{barns st}^{-1}$	$\theta_{cm}^\circ$	$\frac{d\sigma}{d\Omega_{cm}} \mu\text{barns st}^{-1}$
30.00	$0.27 \pm 0.09$	30.00	$0.65 \pm 0.09$	30.00	$0.60 \pm 0.12$
35.00	$0.77 \pm 0.08$	35.00	$0.88 \pm 0.09$	35.00	$0.82 \pm 0.10$
40.00	$0.99 \pm 0.08$	40.00	$0.82 \pm 0.07$	40.00	$0.79 \pm 0.09$
45.00	$0.97 \pm 0.08$	45.00	$0.85 \pm 0.07$	45.00	$0.93 \pm 0.07$
50.00	$0.82 \pm 0.08$	50.00	$0.98 \pm 0.07$	50.00	$0.64 \pm 0.07$
55.00	$0.77 \pm 0.08$	55.00	$0.81 \pm 0.07$	55.00	$0.73 \pm 0.07$
60.00	$0.87 \pm 0.07$	60.00	$0.81 \pm 0.07$	60.00	$0.67 \pm 0.07$
65.00	$0.82 \pm 0.08$	65.00	$0.78 \pm 0.07$	65.00	$0.67 \pm 0.07$
70.00	$0.87 \pm 0.07$	70.00	$0.60 \pm 0.07$	70.00	$0.77 \pm 0.07$
75.00	$0.85 \pm 0.07$	75.00	$0.72 \pm 0.07$	75.00	$0.57 \pm 0.07$
80.00	$0.91 \pm 0.08$	80.00	$0.69 \pm 0.06$	80.00	$0.61 \pm 0.07$
85.00	$0.89 \pm 0.07$	85.00	$0.76 \pm 0.06$	85.00	$0.64 \pm 0.06$
90.00	$0.74 \pm 0.07$	90.00	$0.75 \pm 0.06$	90.00	$0.64 \pm 0.08$
95.00	$0.85 \pm 0.08$	95.00	$0.76 \pm 0.06$	95.00	$0.72 \pm 0.06$
100.00	$0.75 \pm 0.07$	100.00	$0.71 \pm 0.07$	100.00	$0.62 \pm 0.08$
105.00	$0.67 \pm 0.08$	105.00	$0.71 \pm 0.07$	105.00	$0.66 \pm 0.07$
110.00	$0.85 \pm 0.09$	110.00	$0.59 \pm 0.07$	110.00	$0.61 \pm 0.07$
115.00	$0.77 \pm 0.07$	115.00	$0.52 \pm 0.08$	115.00	$0.53 \pm 0.06$
120.00	$0.72 \pm 0.08$	120.00	$0.51 \pm 0.07$	120.00	$0.72 \pm 0.08$
125.00	$0.75 \pm 0.07$	125.00	$0.51 \pm 0.10$	125.00	$0.43 \pm 0.06$
130.00	$0.62 \pm 0.11$	130.00	$0.63 \pm 0.09$	130.00	$0.65 \pm 0.10$
135.00	$0.67 \pm 0.07$	135.00	$0.51 \pm 0.07$	135.00	$0.53 \pm 0.08$
140.00	$0.79 \pm 0.08$	140.00	$0.43 \pm 0.07$	140.00	$0.41 \pm 0.07$
145.00	$0.46 \pm 0.09$	145.00	$0.58 \pm 0.07$	145.00	$0.34 \pm 0.07$
150.00	$0.47 \pm 0.07$	150.00	$0.42 \pm 0.08$	150.00	$0.42 \pm 0.06$
155.00	$0.31 \pm 0.08$	155.00	$0.53 \pm 0.07$	155.00	$0.21 \pm 0.08$
160.00	$0.52 \pm 0.07$	160.00	$0.37 \pm 0.10$	160.00	$0.40 \pm 0.06$

Table B.6: *Differential Cross Sections  $E_\gamma = 500, 520,$  and  $540$  MeV*

$E_\gamma=560 \text{ MeV}$		$E_\gamma=580 \text{ MeV}$		$E_\gamma=600 \text{ MeV}$	
$\theta_{cm}^\circ$	$\frac{d\sigma}{d\Omega_{cm}} \mu\text{barns st}^{-1}$	$\theta_{cm}^\circ$	$\frac{d\sigma}{d\Omega_{cm}} \mu\text{barns st}^{-1}$	$\theta_{cm}^\circ$	$\frac{d\sigma}{d\Omega_{cm}} \mu\text{barns st}^{-1}$
30.00	$0.70 \pm 0.13$	30.00	$0.46 \pm 0.23$	30.00	$1.14 \pm 0.02$
35.00	$0.78 \pm 0.14$	35.00	$0.93 \pm 0.12$	35.00	$1.20 \pm 0.18$
40.00	$0.62 \pm 0.10$	40.00	$0.66 \pm 0.12$	40.00	$0.51 \pm 0.14$
45.00	$0.80 \pm 0.08$	45.00	$0.77 \pm 0.08$	45.00	$0.83 \pm 0.10$
50.00	$0.65 \pm 0.07$	50.00	$0.58 \pm 0.07$	50.00	$0.56 \pm 0.08$
55.00	$0.68 \pm 0.07$	55.00	$0.64 \pm 0.06$	55.00	$0.60 \pm 0.07$
60.00	$0.72 \pm 0.06$	60.00	$0.65 \pm 0.05$	60.00	$0.59 \pm 0.06$
65.00	$0.89 \pm 0.06$	65.00	$0.48 \pm 0.06$	65.00	$0.48 \pm 0.06$
70.00	$0.75 \pm 0.07$	70.00	$0.72 \pm 0.06$	70.00	$0.49 \pm 0.06$
75.00	$0.62 \pm 0.06$	75.00	$0.57 \pm 0.06$	75.00	$0.57 \pm 0.06$
80.00	$0.57 \pm 0.06$	80.00	$0.43 \pm 0.07$	80.00	$0.54 \pm 0.06$
85.00	$0.59 \pm 0.06$	85.00	$0.49 \pm 0.05$	85.00	$0.51 \pm 0.06$
90.00	$0.56 \pm 0.06$	90.00	$0.37 \pm 0.06$	90.00	$0.44 \pm 0.06$
95.00	$0.56 \pm 0.06$	95.00	$0.48 \pm 0.06$	95.00	$0.46 \pm 0.06$
100.00	$0.63 \pm 0.06$	100.00	$0.46 \pm 0.05$	100.00	$0.42 \pm 0.06$
105.00	$0.56 \pm 0.08$	105.00	$0.47 \pm 0.06$	105.00	$0.42 \pm 0.07$
110.00	$0.44 \pm 0.07$	110.00	$0.56 \pm 0.07$	110.00	$0.41 \pm 0.07$
115.00	$0.50 \pm 0.06$	115.00	$0.34 \pm 0.06$	115.00	$0.37 \pm 0.07$
120.00	$0.50 \pm 0.07$	120.00	$0.48 \pm 0.08$	120.00	$0.37 \pm 0.06$
125.00	$0.38 \pm 0.07$	125.00	$0.42 \pm 0.08$	125.00	$0.34 \pm 0.07$
130.00	$0.45 \pm 0.10$	130.00	$0.33 \pm 0.10$	130.00	$0.32 \pm 0.09$
135.00	$0.56 \pm 0.06$	135.00	$0.36 \pm 0.05$	135.00	$0.40 \pm 0.06$
140.00	$0.38 \pm 0.08$	140.00	$0.40 \pm 0.06$	140.00	$0.38 \pm 0.07$
145.00	$0.29 \pm 0.07$	145.00	$0.29 \pm 0.07$	145.00	$0.36 \pm 0.07$
150.00	$0.32 \pm 0.06$	150.00	$0.44 \pm 0.06$	150.00	$0.22 \pm 0.07$
155.00	$0.27 \pm 0.07$	155.00	$0.32 \pm 0.08$	155.00	$0.22 \pm 0.06$
160.00	$0.43 \pm 0.07$	160.00	$0.40 \pm 0.08$	160.00	$0.27 \pm 0.07$

Table B.7: *Differential Cross Sections  $E_\gamma = 560, 580, \text{ and } 600 \text{ MeV}$*

Photon Energy $E_\gamma$ [MeV ]	$\Delta E_\gamma$ [MeV ]	Cross Section $\sigma$ [ $\mu$ barns]	$\Delta\sigma$ [ $\mu$ barns]
200	20	57.45	0.63
220	20	59.55	0.83
240	20	62.07	0.87
260	20	67.48	0.89
280	20	63.10	0.90
300	20	58.17	0.90
320	20	52.11	0.88
340	20	39.17	0.79
360	20	33.47	0.55
380	20	22.77	0.33
400	20	19.09	0.31
420	20	13.19	0.27
440	20	12.72	0.26
460	20	10.82	0.26
480	20	9.83	0.34
500	20	9.54	0.39
520	20	8.92	0.41
540	20	7.99	0.45
560	20	7.07	0.61
580	20	6.33	0.17
600	20	5.57	0.16

Table B.8: *Total Cross Section Results*

$E_\gamma$ (MeV)	$A_0$	$\Delta A_0$	$A_1$	$\Delta A_1$	$A_2$	$\Delta A_2$	$A_3$	$\Delta A_3$	$A_4$	$\Delta A_4$
200	4.57	0.05	0.90	0.09	-1.21	0.15	-0.07	0.00	-0.48	0.16
220	4.74	0.07	0.87	0.12	-0.93	0.22	0.16	0.00	0.02	0.20
240	4.94	0.07	0.68	0.14	-1.06	0.23	-0.08	0.00	-0.40	0.22
260	5.37	0.07	0.76	0.14	-1.21	0.23	-0.12	0.00	0.18	0.23
280	5.02	0.07	0.66	0.14	-1.49	0.23	-0.16	0.00	-0.11	0.23
300	4.63	0.07	0.79	0.15	-0.87	0.23	-0.10	0.00	-0.23	0.23
320	4.15	0.07	0.59	0.14	-0.84	0.23	-0.13	0.00	-0.15	0.23
340	3.12	0.06	0.67	0.13	-0.51	0.20	0.38	0.00	-0.03	0.20
360	2.66	0.04	0.56	0.08	-0.30	0.13	0.24	0.00	0.41	0.14
380	1.81	0.03	0.26	0.05	-0.42	0.08	0.10	0.00	0.28	0.08
400	1.52	0.02	0.19	0.05	-0.31	0.07	0.10	0.00	0.05	0.08
420	1.05	0.02	0.06	0.04	-0.27	0.07	0.04	0.00	-0.01	0.07
440	1.01	0.02	0.05	0.04	-0.35	0.06	-0.10	0.00	-0.08	0.07
460	0.86	0.02	0.08	0.04	-0.29	0.06	0.02	0.00	-0.08	0.07
480	0.78	0.03	0.20	0.06	-0.06	0.09	0.00	0.00	-0.01	0.09
500	0.76	0.03	0.19	0.08	-0.16	0.10	0.07	0.00	-0.09	0.10
520	0.71	0.03	0.31	0.08	0.09	0.11	0.13	0.00	0.12	0.10
540	0.64	0.04	0.27	0.09	0.00	0.12	0.19	0.00	0.02	0.11
560	0.56	0.05	0.22	0.12	-0.09	0.15	-0.03	0.00	-0.06	0.14
580	0.50	0.01	0.22	0.02	0.11	0.05	0.08	0.00	0.04	0.05
600	0.44	0.01	0.15	0.02	-0.11	0.03	-0.08	0.00	-0.12	0.03

Table B.9: Legendre Polynomial Coefficients

## **Appendix C**

# **Coherent Bremsstrahlung Trials**

## Coherent Bremsstrahlung Trials

Although measurement of polarisation observables in deuteron photodisintegration yields valuable information with which to investigate various theoretical models very few such experiments have been undertaken. In particular there exists no detailed information above 300 MeV on the photon asymmetry for the two-body photodisintegration of deuterium using linearly polarised photons. The large angular acceptance of DAPHNE, in particular the complete coverage of azimuthal angles, is ideally suited to this type of measurement. Furthermore, by employing the ability of the new Mainz facility to produce linearly polarised photons (in the energy range above 300 MeV) from coherent Bremsstrahlung from a thin diamond radiator, it will be possible to extend the data to higher energies.

Linearly polarised photons can be produced using the coherent Bremsstrahlung process in a crystal radiator. The degree of linear polarisation and the shape of the photon energy spectrum depend critically on the orientation of the crystal used to produce the coherent Bremsstrahlung and the direction of the incident electron beam. Several trials have taken place, using a diamond radiator, and after optimising its orientation, strongly enhanced coherent contributions to the Bremsstrahlung spectrum were observed. The crystal was mounted on a goniometer which was capable of rotation about 3 orthogonal axes with sensitive resolution. The crystal was aligned initially to within approximately 2 degrees of its optimum orientation by setting it azimuthally with respect to a known direction in the crystal lattice determined by an X-ray analysis, and mounting it normal to the incident electron beam using a laser. Sensitive scans with first horizontal and then vertical rotations were carried out, in which electron

spectra in the tagger were recorded as a function of goniometer angle. This allowed a determination of when the electron beam was parallel to the principal crystal planes which were defined when the diamond was cut. The crystal was then rotated by a predetermined angle (to select the coherent Bremsstrahlung energy) about an axis normal to the beam followed by a scan through azimuthal angle. This scan was used to confirm that coherent Bremsstrahlung was being produced by a single reciprocal lattice vector in the crystal. An example of this scan through azimuthal angle is shown in figure C1.

The results have been very encouraging, although multiple scattering effects and imperfections in the crystal tended to smear out the structure in the spectra. However, the intensity of the coherent radiation normalised to the incoherent compares well with what is expected from calculations. The relative intensity of coherent to incoherent contributions for an optimised orientation is shown as a function of photon energy in figure C2.

If the Bremsstrahlung photon beam is collimated, the incoherent contribution, which is contained within a broader cone about the incident electron beam direction is reduced relative to the coherent contribution. Trials with a collimator having half the acceptance of the usual collimator have been carried out with very encouraging results. Techniques for setting up the crystal in a more reliable and reproducible way are being investigated. It is hoped a tagged photon beam with a (55-65)% degree of linear polarisation at  $\sim 300$  MeV will be available in the near future.

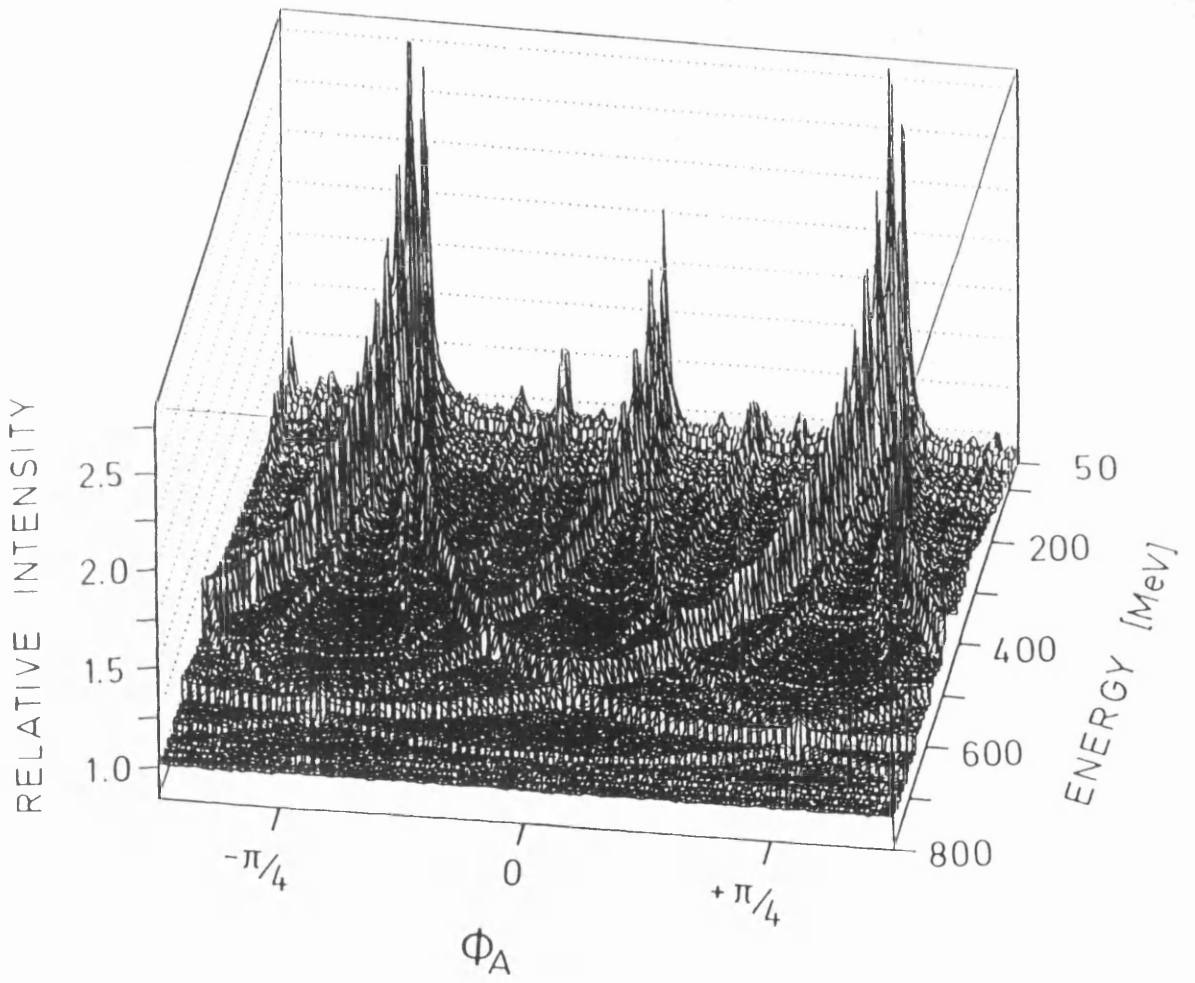


Figure C.1: Scan through azimuthal angle

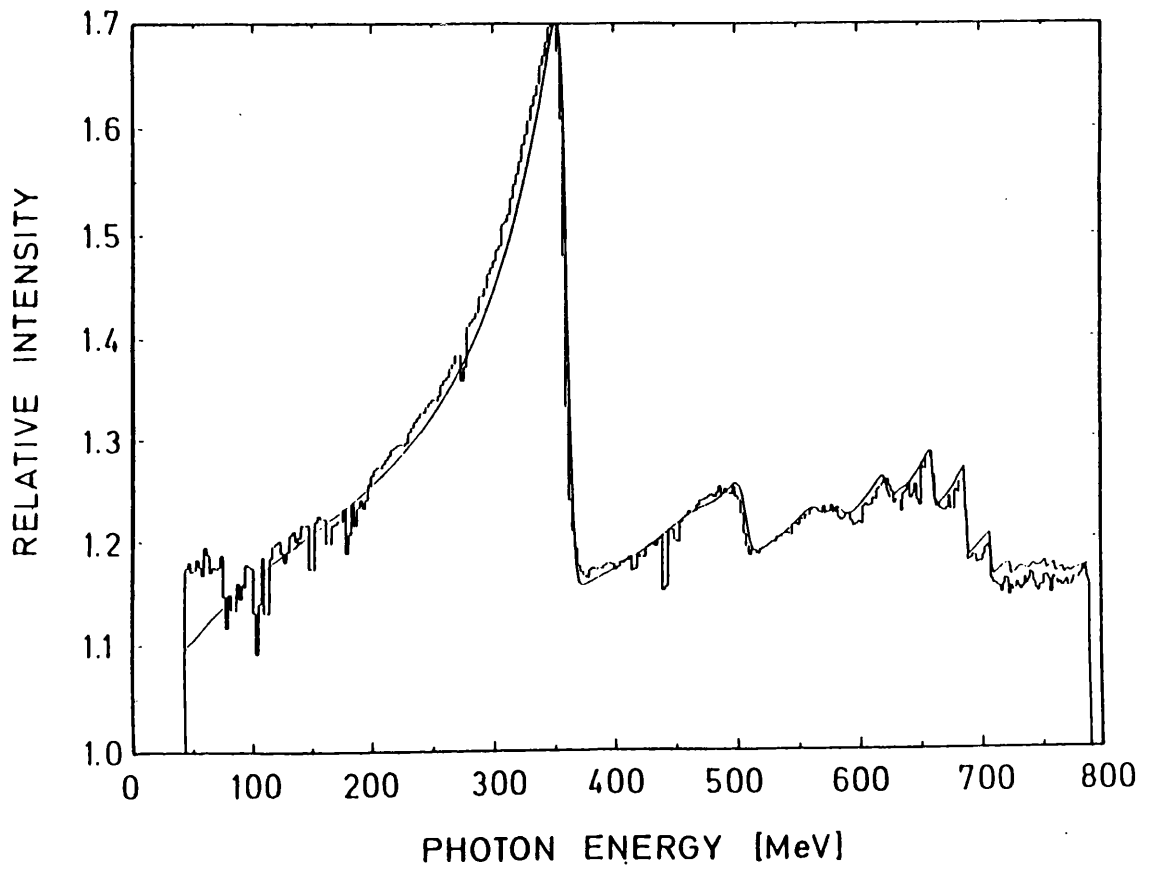
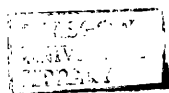


Figure C.2: *Relative intensity of coherent to incoherent contributions*

# Bibliography

- [1] J.CHADWICK *and* M.GOLDHABER: *Nature* **134** (1934) 237
- [2] H.ARENHÖVEL: *Nuc.Phys* **A374** (1982) 521c
- [3] H.ARENHÖVEL: *Nuc.Phys* **A384** (1982) 287
- [4] J.M.LAGET: *Can.J.Phys* **62** (1984) 1046
- [5] H.ARENHÖVEL AND M.SCHWAMB: *private communication*
- [6] P.WILHELM AND H.ARENHÖVEL: *Phys.Lett.* **318B** (1993) 410
- [7] P.WILHELM AND H.ARENHÖVEL: *Mainz Preprint MKPH-T-93-15*
- [8] P.A.WALLACE: *PhD Thesis, University of Glasgow. 1989.*
- [9] A.BETHE *and* R.PEIERLS: *Proc.Roy.Soc. A* **148** (1935) 146
- [10] L.HULTHEN: *Handbuch der Physik* ed. S.Flugge
- [11] F.PARTOVI: *Ann. Phys. (N.Y.)* **27** 79 (1964)
- [12] W.JAUS AND W.S.WOOLCOCK: *Nuovo Cim* **97A** 103 (1987)
- [13] K.-M.SCHMITT AND H.ARENHÖVEL: *Few-Body Syst.* **6** 117 (1989)
- [14] E.HADJMICHAEL, M.L.RUSTGI, L.N. PANDEY: *Phys.Rev* **C36** 44 (1987)
- [15] E.A.WHALIN *et.al.* : *Phys.Rev* **101** (1956) 377
- [16] J.C.KECK *and* A.V.TOLLESTRUP: *Phys.Rev* **101** (1956) 360
- [17] D.R.DIXON *and* K.C.BANDTEL: *Phys.Rev* **104** (1956) 1730

- [18] C.A.TATRO *et.al.* : *Phys.Rev* **112** (1958) 932
- [19] R.KOSE *et.al.* : *Z.Phys* **202** (1967) 365
- [20] J.BUON *et.al.* : *Phys.Lett.* **26B** (1968) 595
- [21] A.M.SMITH *et.al.* : *J.Phys* **A1** (1968) 553
- [22] R.L.ANDERSON *et.al.* : *Phys.Rev Lett* **13** (1969) 651
- [23] D.I.SOBER *et.al.* : *Phys.Rev Lett* **9** (1969) 430
- [24] P.DOUGAN *et.al.* : *Z.Phys. A* **280** (1977) 341
- [25] ARENDS *et.al.* : *Nuc.Phys* **a412** (1984) 509
- [26] E.DESANCTIS *et.al.* : *Phys.Rev. C* **34** (1986) 413
- [27] LEVI SANDRI *et.al.* : *Phys.Rev. C* **39** (1989) 1701
- [28] J.MATTHEWS *et.al.* : *private communication*
- [29] BLANPIED *et.al.* : *private communication*
- [30] H.MYERS *et.al.* : *Phys.Rev* **121** (1961) 630
- [31] P.DOUGAN *et.al.* : *Z.Phys. A* **276** (1976) 55
- [32] BABA *et.al.* : *Phys.Rev Lett* **48** (1982) 729
- [33] BABA *et.al.* : *Phys.Rev. C* **28** (1983) 286
- [34] K.H.ALTHOFF *et.al.* : *Z.Phys.C* **21** (1983) 149
- [35] L.I.SCHIFF: *Phys.Rev* **83** 252 (1951)
- [36] H.BETHE AND W.HEITLER: *Proc.Roy.Soc (London)* **A146** (1934) 83.
- [37] D.F.BARTLETT *et.al.* : *Phys.Rev Lett* **13** (1971) 881
- [38] B.L.SCHROCK *et.al.* : *Phys.Rev Lett* **26** (1971) 1659
- [39] W.DUTTY *et.al.* : *Preprint*
- [40] H.HERMINGHAUS *et.al.* : *Nucl.Inst.Meth.* **138** (1976) 1



- [41] H.HERMINGHAUS *et.al.* : *Nucl.Inst.Meth.* **187** (1981) 103
- [42] I.ANTHONY *et.al.* : *Nucl.Inst.Meth.* **A301** (1991) 230
- [43] G.AUDIT *et.al.* : *Nucl.Inst.Meth.* **A301** (1991) 473
- [44] S.KERHOAS: *PhD Thesis, CEA Saclay 1993.*
- [45] A.BRAGHIERI *etal:* *to be published*
- [46] P.PEDRONI: *Simulation of inelastic hadron collisions below 5 GeV*  
INFN/BE-88/3 1988
- [47] CERN LIBRARY:
- [48] P.ROSSI *et.al.* : *Phys.Rev. C* **40** (1989) 2412
- [49] D.A.JENKINS *et.al.* : *Preprint*
- [50] H.TANABE AND K.OHTA: *Phys.Rev. C* **40** (1989) 1905